UNIVERSITY OF SOUTHAMPTON

FACULTY OF ENGINEERING AND APPLIED SCIENCE

SOUND RADIATION FROM SOURCES IN CIRCULAR MOTION WITH APPLICATION TO HELICOPTER ROTOR NOISE

BY

HIMAT K. TANNA B.Sc. (Eng.)

Thesis submitted for the degree of Doctor of Philosophy in the Institute of Sound and Vibration Research.

November, 1970.

PREFACE

The work described in this thesis was done in the course of the programme on rotor noise research conducted at Southampton University with the joint resources of N.A.S.A., U.K. Ministry of Technology, and U.S. Army grants.

(a) The computational study of rotational noise was carried out jointly by Dr. S.E. Wright and the author, and the findings were published in a series of three reports as follows.

(1) Computer program : ISVR Technical Report No. 13 by Tanna,

(2) Computed results : ISVR Technical Report No. 15 by Wright and Tanna,

(3) Interpretation of results : ISVR Technical Report No. 14 by Wright.

The computed results were presented in Wright's thesis, and in order to avoid duplication, they are not included in the present thesis.

(b) The theory for sound radiation from a point force in circular motion (Chapters 5 and 6) was developed by Dr. C.L. Morfey and the author as a joint effort; it will appear shortly as a joint paper in the Journal of Sound and Vibration.

ABSTRACT

FACULTY OF ENGINEERING AND APPLIED SCIENCE

INSTITUTE OF SOUND AND VIBRATION RESEARCH

Doctor of Philosophy

SOUND RADIATION FROM SOURCES IN CIRCULAR MOTION WITH APPLICATION TO HELICOPTER ROTOR NOISE

by Himatlal Keshavji Tanna

A characteristic feature of most of the thrust producing devices used in the present day vertical and short takeoff-and-landing aircraft technology is that noise is radiated from steady and fluctuating sources executing circular motion. Helicopter rotors, compressor fans and tip jet rotors are examples where sound is generated by rotating sources of cyclic and/or arbitrary time dependent source strength. The radiation properties of these sources are studied here, and in particular, noise from the rotating blades of open rotors is investigated in detail.

The effects of chordwise and spanwise differential-pressure profiles, and their variations with azimuth, on higher harmonic rotational noise from helicopter rotors are established. Previous theories are modified to include these profiles and it is shown computationally that fluctuating loading profiles must be included in the radiation analysis for accurate prediction of rotational noise. Computer programs for noise prediction from various loading models are available for future use. A detailed study of available measured aerodynamic loading data reveals several interesting

points; in particular, it appears that the asymmetry of blade loading under any particular flight condition can be explained qualitatively.

In order to establish the effects of acceleration of sound sources due to steady rotation in a circle, expressions are derived for the far-field sound radiation from random singularities in circular motion, using the moving-source approach. The overall results are obtained in exact closed form, and a series approximation has been developed to show how the radiation spectrum is influenced by rotation. The point force theory provides good correlation with experimental results. It is suggested that the use of rotating point acoustic stress analysis provides a model for representing distributed blade forces.

ACKNOWLEDGEMENTS

I would like to express my sincere acknowledgements to my supervisor, Dr. C.L. Morfey, for all his help and guidance throughout the investigation reported in this thesis.

The financial support for the work described in this thesis was provided by,

(a) U.S. National Aeronautics and Space Administration (Langley Research Center),

(b) U.K. Ministry of Technology (St. Giles Court),

and (c) U.S. Army (European Research Office, Frankfurt).

I am also very grateful to Mrs. Lampard and Mrs. Wells who typed the manuscript so efficiently.

CONTENTS

	Page Number
LIST OF SYMBOLS	(i)
LIST OF FIGURES	(vi)
CHAPTER 1. INTRODUCTION	1
1.1 Helicopter rotor noise	2
1.2 Analysis of sound radiation from moving sources	3
1.3 Radiation from periodic rotating forces (rotational noise)	5
1.4 Helicopter rotor aerodynamics	8
1.5 Radiation from random rotating forces (broadband noise)	8
1.6 Radiation from point sources in circular motion	10
CHAPTER 2. ROTATIONAL NOISE THEORY	12
2.1 General theory	12
2.2 Point span loading models	19
2.2.1 Actual chordwise loading profile model	19
2.2.2 Equivalent rectangular chordwise loading profile model	21
2.3 Radiation from single blade loading harmonic with arbitrary chordwise loading profile	23
2.4 Computer programs	25
2.4.1 Computation procedure	27
2.4.2 Integration method	27
2.4.3 Computation time	28
2.4.4 Blade loading data	28
2.5 Conclusions	28
CHAPTER 3. ROTATIONAL NOISE RESULTS AND DISCUSSION	34
3.1 Single blade loading harmonic radiation with arbitrary chordwise loading profile	34
3.2 Composite blade loading harmonics radiation	36

3.3 Radiation from fluctuating chordwise and spanwise loading profiles 37

3.3.1 Blade loading data 38

3.3.2 Computed output 39

3.3.2.1 mB spectra 39

3.3.2.2 Polar plots 41

3.4 Conclusions 43

CHAPTER 4. ROTOR AERODYNAMICS STUDY

4.1 Effect of flight condition on asymmetry of blade loading 65

4.1.1 Conclusions 70

4.2 Blade differential-pressure harmonics 71

4.2.1 Harmonic representation of blade differential-pressures 71

4.2.2 Amplitude fall-offs of differential-pressure harmonics 72

4.2.3 Conclusions 74

CHAPTER 5. OVERALL SOUND RADIATION FROM A POINT FORCE IN CIRCULAR MOTION 83

5.1 Power output from point sources in uniform straight-line motion 84

5.2 Point force in uniform circular motion 88

5.2.1 Mean square far-field sound pressure 90

5.2.2 Overall sound power output 94

5.3 Pure rotation of a point force 95

5.3.1 Single-frequency rotating force 95

5.4 Conclusions 97

CHAPTER 6. SPECTRAL DENSITY OF SOUND RADIATION FROM BROADBAND ROTATING FORCES 109

6.1 Spectral density of sound pressure 109

6.1.1 Ensemble-averaged pressure auto-correlation 109

6.1.2 Transformation to instantaneous spectral density 113

6.1.3 Time-averaged spectrum 114

6.1.4 Radiation spectrum in particular cases 116

6.1.5 Comparison with previous work 118

6.2 Spectral density of total sound power 119

6.3 Comparison with experimental results 121

6.4 Conclusions 125

CHAPTER 7. SOUND RADIATION FROM POINT VOLUME-VELOCITY SOURCES IN CIRCULAR MOTION 138

7.1 Overall sound radiation 139

7.1.1 Mean square far-field sound pressure 141

7.1.2 Overall sound power output 142

7.2 Spectral density of sound radiation from broadband rotating volume-velocity sources 143

7.2.1 Spectral density of sound pressure 143

7.2.2 Spectral density of total sound power 145

7.3 Conclusions 146

CHAPTER 8. SOUND RADIATION FROM POINT VOLUME-DISPLACEMENT SOURCES IN CIRCULAR MOTION 155

8.1 Sound field of a point volume displacement source in arbitrary motion 156

8.2 Overall sound radiation from uniform circular motion 157

8.2.1 Mean square far-field sound pressure 158

8.2.2 Overall sound power output 161

8.3 Conclusions 162

CHAPTER 9. SOUND RADIATION FROM POINT ACOUSTIC STRESSES IN CIRCULAR MOTION 163

9.1 Power output from point acoustic stresses in uniform straight-line motion 164

9.2 Overall sound radiation from point acoustic stresses in uniform circular motion 166

9.2.1 Zero rotation, finite M 168

9.2.1.1 Mean square far-field sound pressure 169

9.2.1.2 Overall sound power output 172

9.2.2 Effect of rotation 173

9.2.2.1 Mean square far-field sound pressure 174

9.2.2.2 Overall sound power output 178

9.3 Spinning point acoustic stresses 178

9.3.1 Single-frequency spinning acoustic stresses 179

9.4 Conclusions 181

CHAPTER 10. CONCLUSIONS 191

10.1 Main conclusions 192

10.1.1 Rotational noise from helicopter rotors 192

10.1.2 Rotor aerodynamics 192

10.1.3 Radiation from random rotating forces 193

10.1.4 Radiation from random rotating volume-velocity sources 195

10.1.5 Overall radiation from random rotating volume-displacement sources 196

10.1.6 Overall radiation from random rotating point acoustic stresses 196

10.2 Research recommendations 197

10.3 Final comment 200

REFERENCES 202

APPENDIX I. COMPUTER PROGRAM FOR THE PREDICTION OF ROTATIONAL NOISE 206

1. Quoted formulae and simplification 206

2. Computation procedure 207

3. Program nomenclature 208

4. Input parameters 211

5. Input format for data cards 212

6. Notes regarding the input data format 214

7. Control cards and card sequence 215

8. Computation time on ICT Atlas computer 216

9. Integration details 217

9.1 Method of integration 217

9.2 Importance of integration interval 218

9.3 Relation between integration interval and computing time 219

APPENDIX II. PRELIMINARY COMPUTATIONAL STUDY OF ROTATIONAL NOISE - SUMMARY 225

APPENDIX III. COMPUTER PROGRAM A 234

APPENDIX IV. COMPUTER PROGRAM B 240

APPENDIX V. COMPUTER PROGRAM C 246

APPENDIX VI. COMPUTER PROGRAM D 252

APPENDIX VII. CALCULATION OF TIME AVERAGES FOR CIRCULAR MOTION 256

APPENDIX VIII. CORRELATION-SPECTRAL DENSITY TRANSFORMATION 257

APPENDIX IX. PURE ROTATION EFFECT ON FORCE RADIATION SPECTRUM 259

APPENDIX X. RADIATION SPECTRUM FROM BROADBAND FORCES IN UNIFORM STRAIGHT-LINE MOTION 261

APPENDIX XI. RADIATION SPECTRUM FROM BROADBAND SOURCES IN UNIFORM STRAIGHT-LINE MOTION 263

APPENDIX XII. CORRELATION FUNCTIONS 264

LIST OF SYMBOLS

For easier reference, it is convenient to define the symbols used under two separate headings:

Analysis of harmonic rotating sources (Chapters 2 to 4)

a blade chord, inches

a_p distance of p^{th} chord section from leading edge, inches

$A_p(r,\psi)$ differential-pressure on p^{th} chord section at point (r,ψ) on on the rotor disc, pounds/in^2

A_{po}, A_{pg}, $\bar{A}_{pg}$ steady, cosine and sine coefficients of g^{th} harmonic of differential-pressure on p^{th} chord section, pounds/in^2

B rotor blade number

c_o speed of sound

C_m, D_m; C'_m, D'_m differential-pressure (pounds/in^2), loading (pounds/in) coefficients

D observer-source separation $|R_i - x_i|$

$\underset{\sim}{f}$ force per unit volume

g blade differential-pressure or loading harmonic number

$J_n(x)$ Bessel function of order n and argument x

k acoustic wave-number $= mB\,\Omega/c_o$

L_T total loading on rotor $= L'_o\,aB$, pounds

$L'(r_e,\psi)$ blade loading at point (r_e,ψ) on the rotor disc, pounds/in (equivalent rectangular chordwise loading)

L'_o, L'_g, $\bar{L}'_g$ steady, cosine and sine coefficients of g^{th} harmonic of blade loading, pounds/in (Equivalent rectangular chordwise loading)

$L'_p(r_e,\psi)$ blade loading on p^{th} chord section at point (r_e,ψ) on the rotor disc, pounds/in (actual chordwise loading)

L'_{po}, L'_{pg}, $\bar{L}'_{pg}$	steady, cosine and sine coefficients of g^{th} harmonic of blade loading on p^{th} chord section, pounds/in (actual chordwise loading)
m	rotational noise harmonic number
M_e, M_T	effective, tip Mach number
n	number of blade chord sections
N	rotor frequency, Hz.
p	acoustic pressure; subscript, denotes chord section,
P, P'	Fourier series representation of differential-pressure, loading
r	distance from rotor centre of element on rotor disc
rdrdψ	area of element on rotor disc
r_e, r_T	rotor effective radius, tip radius
$\underset{\sim}{R}$	observer position
SP_{mB}	sound pressure - m^{th} harmonic of B-bladed rotor
SP_{mBg}	sound pressure from single blade loading harmonic g
t	time
T	period for blade passage frequency $= 2\pi/B\Omega$
w_p	width of p^{th} chord section, inches
$\underset{\sim}{x}$	source position
α_{pg}	$= L'_{pg}(r_e) \;/\; L'_{po}(r_e)$
β	resultant force angle, degrees
β_o	steady pitch angle, degrees
β_1, $\bar{\beta}_1$	cosine, sine coefficient of cyclic pitch, degrees
γ	blade twist rate, degrees/inch
γ_μ	directivity function $= mBJ_\mu (mBM_e \cos\sigma)$

$\Delta\psi$ integration interval for azimuthal integration

θ observer azimuth angle, 0^o at tail, positive in the direction of rotation

$\mu_{\pm}$ $= (mB \pm g)$

σ observer elevation angle, 0^o in rotor plane, positive above rotor plane

χ spectrum function for distributive chordwise loading

ψ blade azimuth angle

Ω rotor angular frequency

$\hat{}$ peak value

i co-ordinate directions (i = 1,2,3).

Analysis of random rotating sources (Chapters 5 to 9)

a radius of circular path

A(M), B(M), C(M) coefficients in the sound power expression

c_o speed of sound

$d(t)$, $\dot{d}(t)$, $\ddot{d}(t)$ time-varying volume displacement, volume velocity, volume acceleration

D drag (or longitudinal) force

f harmonically varying force

e, f, g, h periodic functions of $[\theta]$

F fluctuating point force

F_r component of F in the $\underset{\sim}{r}$ direction

$G_x(\omega)$, $G_x(\nu)$ auto-spectral density of a random function x(t)

$G_{xy}(\omega)$, $G_{xy}(\nu)$ cross-spectral density of two random functions x, y

$\overline{G}_p(\omega)$ time-averaged spectral density of sound pressure

I acoustic intensity

$J_n(z)$ Bessel function of order n and argument z

M	convection or rotation Mach number
M_r, M_R	components of M in the $\underset{\sim}{r}$, $\underset{\sim}{R}$ directions
p'	acoustic pressure
$\langle p'^2 \rangle$	mean-square sound pressure
$q(t)$	point acoustic source strength
$Q(t)$	time-varying point volume velocity source strength (mass per unit time)
$\underset{\sim}{r}$	vector position of observation point
$\underset{\sim}{R}$	source-observer vector
$R_x(\tau)$, $R_x(\sigma)$	auto-correlation function of x(t)
$R_{xy}(\tau)$, $R_{xy}(\sigma)$	cross-correlation function of x and y
$S(t)$	time-varying point volume displacement source strength (mass)
t	time
T	thrust (or transverse force)
T_{ij}	fluctuating point acoustic stress tensor, i, j = x (axial), θ (circumferential), σ (radial)
T_{rr}, T_{RR}	components of T_{ij} in the $\underset{\sim}{r}$, $\underset{\sim}{R}$ directions
W, $dW/d\omega$	sound power output, spectral density
$\underset{\sim}{x}$	vector position of source point
X	$= T\cos\psi$, $= T_{xx}\cos^2\psi$
Y	$= D\sin\psi$, $= T_{x\theta}\sin\psi\cos\psi$
Z	$= T_{\theta\theta}\sin^2\psi$
α	$= M\sin\psi$
ϵ	drag-thrust force ratio (constant)
θ	azimuth angle about the line of uniform straight-line motion; source azimuth angle for uniform circular motion
ν	source radian frequency
ρ_o	undisturbed fluid density

σ $= \tau / \left[1 - M_r\right]_1$

τ observer time delay

ϕ $= [\theta]$;

observer azimuth angle for uniform straight-line motion and for pure rotation of acoustic stresses

ψ observer angle, 0^o on axis of rotation

ω observed radian frequency

Ω rotation radian frequency

$[\ ]$ evaluation at retarded time $[t] = t - [R]/c_o$

$\dot{}$ differentiation with respect to time

$|\ |$ modulus

$'$ differentiation of a function with respect to the variable

$< >_t$ time-averaged value

$< >_\Omega$ ensemble-averaged value

$\hat{}$ Fourier transform;

peak amplitude

$*$ complex conjugate

i subscript denotes three co-ordinate directions ($i = 1,2,3$)

$1,2$ subscripts indicate values at observer times t_1, $t_2 = t_1 + \tau$.

LIST OF FIGURES

Page Number

CHAPTER 1

1.1 Forces on rotating blades. 11

CHAPTER 2

2.1 Rotor and field point geometry 30

2.2 Differential-pressure geometry. 31

2.3 Pressure-time history on rotor disc element. 32

2.4 Loading-time history for equivalent rectangular chordwise loading model 33

CHAPTER 3

3.1 g = 0. Effect of shape of chordwise loading profile. 45

3.2 g = 12. Effect of shape of chordwise loading profile. 46

3.3 g = 48. Effect of shape of chordwise loading profile. 47

3.4 Spectrum functions for various chordwise loading profiles. 48

3.5 NH-3A. Hover in ground effect. 0.95 span station. 49

3.6 NH-3A. 190 Knots, low wing lift. 0.85 span station. 50

3.7 NH-3A. 165 Knots, high wing lift. 0.85 span station. 51

3.8 Blade stations for differential-pressure data. 52

3.9 mB spectra: point span loading models. 53

3.10 mB spectra; distributive span loading models. 54

3.11 Polar elevation: point chord, point span loading model. 55

3.12 Polar elevation: point span, distributive chord loading model. 56

3.13 Polar elevation: point span, equivalent rectangular chord loading model. 57

3.14 Polar elevation: point chord, distributive span loading model. 58

3.15 Polar elevation: distributive chord, distributive span loading model. 59

3.16 Polar plan: point chord, point span loading model. 60

3.17 Polar plan: point span, distributive chord loading model. 61

3.18 Polar plan: point span, equivalent rectangular chord loading model. 62

3.19 Polar plan: point chord, distributive span loading model. 63

3.20 Polar plan: distributive chord, distributive span loading model. 64

CHAPTER 4

4.1 Blade loading variation with azimuth for different flight conditions ($r = 0.9\ r_T$) 76,77

4.2 Loading fluctuations due to blade-tip vortex intersection. 78

4.3 Variation of blade differential-pressure harmonics amplitude fall-off along blade chord. 79

4.4 Variation of blade differential-pressure harmonics amplitude fall-off along blade span (near leading edge). 80

4.5 Variation of blade differential-pressure harmonics amplitude fall-off along blade span (near trailing edge). 81

4.6 Variation of blade differential-pressure harmonics amplitude fall-off with flight condition. 82

CHAPTER 5

5.1 Source and observer geometry for moving point sources. 98

5.2 Point source in uniform straight-line motion. 98

5.3 Effect of uniform straight-line convection Mach number (M) on sound power output from (a) point acoustic source, (b) point volume velocity source and (c) point volume displacement source. 99

5.4 Effect of uniform straight-line convection Mach number (M) on sound power output from (d) fluctuating longitudinal force and (e) fluctuating transverse force. 100

5.5 Point force in uniform circular motion. 101

5.6 Effect of rotation Mach number (M) on the directivity of overall mean-square pressure from steady rotating point force. 102

5.7 Effect of force orientation ($\varepsilon = D/T$) on the directivity of overall mean-square pressure from steady rotating point force. 103

5.8 Effect of rotation Mach number (M) on the directivity of overall mean-square pressure from fluctuating rotating point force. 104

5.9 Effect of force orientation ($\varepsilon = D/T$) on the directivity of overall mean-square pressure from fluctuating rotating point force. 105

5.10 Comparison of series expansions of coefficients (a) $A_o(M)$, (b) $B_o(M)$, (c) $B_1(M)$ and (d) $A_1(M)$, terminated at M^4 terms, with their closed-form expressions. 106,107

5.11 Harmonic point force spinning in its own plane. 108

5.12 Observation point geometry. 108

CHAPTER 6

6.1 Effect of rotation Mach number (M) on the spectral density of sound pressure in the rotor plane. 126

6.2 Effect of rotation (Ω/ω) of the force on the directivity of the sound pressure spectral density. 127

6.3 Effect of force orientation (ε) on the directivity of the sound pressure spectral density. 128

6.4 Effect of rotation Mach number (M) on the directivity of the sound pressure spectral density. 129

6.5 Effect of rotation Mach number (M) of the pure thrust (T) force on the directivity of sound pressure spectral density. 130

6.6 Effect of rotation Mach number (M) of the pure drag (D) force on the directivity of sound pressure spectral density. 131

6.7 Effect of rotation (Ω/ω) and force orientation (ε) on the sound power spectral density. 132

6.8 Effect of rotation (Ω/ω) and Mach number (M) on the sound power spectral density. 133

6.9 Comparison between theoretical and measured directivities (Rolls-Royce fan). 134

6.10 Comparison between theoretical and measured directivities (I.S.V.R. fan). 135

6.11 Comparison between theoretical and measured directivities (I.S.V.R. model rotor). 136,137

CHAPTER 7

7.1 Point source in uniform circular motion. 148

7.2 Effect of rotation Mach number (M) on the directivity of overall mean-square pressure from steady rotating volume velocity source. 149

7.3 Effect of rotation Mach number (M) on the directivity of overall mean-square pressure from fluctuating rotating volume velocity source. 150

7.4 Comparison of series expansions of coefficients (a) A(M) and (b) B(M), terminated at M^4 terms, with their closed-form expressions. 151

7.5 Effect of rotation (Ω/ω) of the source on the directivity of the sound pressure spectral density. 152

7.6 Effect of rotation Mach number (M) on the directivity of the sound pressure spectral density. 153

7.7 Effect of rotation (Ω/ω) and Mach number (M) on the sound power spectral density. 154

CHAPTER 9

9.1 Point acoustic stress in uniform straight-line motion. 182

9.2 Point acoustic stress in uniform circular motion. 182

9.3 Effect of Mach number (M) on the directivity of overall mean-square pressure (point span, distributive chord loading model). 183

9.4 Effect of acoustic stress orientation (ε) on the directivity of overall mean-square pressure (point span, distributive chord loading model). 184

9.5 Effect of Mach number (M) on the directivity of overall mean-square pressure (point chord, distributive span loading model). 185

9.6 Effect of acoustic stress orientation (ε) on the directivity of overall mean-square pressure (point chord, distributive span loading model). 186

9.7 Comparison of series expansions of coefficients (a) $C_1(M)$, (b) $C_2(M)$ and (c) $C_3(M)$, terminated at M^4 terms, with their closed form expressions. 187

9.8 Effect of rotation (Ω/ν) and Mach number (M) on the mean-square sound pressure in the plane of rotation. 188

9.9 Effect of rotation (Ω/ν) of the acoustic stress on the directivity of overall mean-square pressure (point span, distributive chord loading model). 189

9.10 Observation point geometry for spinning point acoustic stresses. 190

APPENDIX I

1. Flow diagram for the program. 220

2. Computer program (HARTRAN). 221

3. Input format for data cards. 222

4. Control cards and card sequence for ICT Atlas Computer. 223

5. Effect of integration interval $\Delta\psi$ on computed spectrum. 224

APPENDIX II

6. The standard cases. 230

7. Observer definition around rotor. 231

8. Span distribution definitions. 232

9. Blade loading azimuth functions. 233

APPENDIX III

10. Flow diagram for Program A. 237

11. Input Format for Program A. 238

12. Computer Program A. 239

APPENDIX IV

13. Flow diagram for Program B. 243

14. Input Format for Programs B and D. 244

15. Computer Program B. 245

APPENDIX V

16. Flow diagram for Program C. 249

17. Input Format for Program C. 250

18. Computer Program C. 251

APPENDIX VI

19. Flow diagram for Program D. 254

20. Computer Program D. 255

CHAPTER 1

INTRODUCTION

Throughout the history of man-kind, every human invention has brought along with it some sort of disadvantage or discomfort to our everyday lives. In the case of technological progress, the biggest penalty we are paying can be summed up by the single phrase "pollution of our environment". In recent years, the technologically advanced nations are beginning to realize the increasing magnitude of this problem and are setting up separate ministries and organizations in order to control the pollution of the environment we live in,

The major unwanted by-product from the present day air transport vehicles which causes most concern is the high levels of noise produced by these vehicles. In particular, noise from helicopters, V/STOL aircraft and ground effect machines is causing a variety of problems ranging from hearing damage on the one hand, to community acceptability on the other.

In civilian operations, high levels of noise from these vehicles are defeating the very purpose of city centre transportation for which these vehicles are designed. In the military use (for those who are interested), the far-field noise levels are such that they give early warning of approach to the enemy. Internal noise levels are also high; long-term exposure causes a very serious health hazard to flight crews. In addition, the manufacturers are faced with the problem of designing better components, to resist the fatigue failure of structures and malfunction of electronic and sensitive mechanical equipment due to vibrations induced by high intensity noise within the vehicle. Clearly, there is urgent need for developing new

methods of controlling the noise levels.

Noise from helicopters, V/STOL aircraft and ground effect machines is generated by a multiplicity of sources of sound, each of which is a complicated process in itself. It is impossible to eliminate all these sources completely, and therefore the object must be to understand the radiating properties of all the mechanisms involved in order to develop accurate prediction methods; once these become available, the noise producing devices used on these vehicles can be designed from the start to satisfy any noise limitation.

Aim of the investigation

A characteristic feature of most of the thrust producing devices used in the present day V/STOL aircraft technology is that noise is radiated from steady and fluctuating sources executing circular motion. Helicopter rotors, compressors fans and tip jet rotors are examples where sound is generated by rotating sources of cyclic and/or arbitrary time dependent source strength. The object of the work reported in this thesis is to study the radiation properties of these sources. In particular, effort is concentrated in investigating the noise from rotating blades of open rotors.

1.1 Helicopter rotor noise

In the present generation of turbine powered helicopters, the subjectively dominant noise sources are aerodynamic in nature; these include the radiation from rotating blades of main and tail rotors of a helicopter. It is also well established that the most important factor in the generation of noise from helicopter rotors is the presence of fluctuating blade forces due to non-uniform inflow [1-15].

These fluctuating forces on the rotor blades arise from a number of causes, which are discussed fully in chapter 4. The force-time history on a rotating blade can be conveniently separated into two parts for the purpose of evaluating the resulting sound field; forces which are repetitive for each blade revolution and forces which vary randomly with time (see Fig. 1.1). The periodic force-time history can be Fourier analyzed into harmonic components (at multiples of rotational frequency) which give rise to the discrete tones, at multiples of the rotor blade passage frequency; this is known as the "rotational" noise. Random blade forces contribute a continuous spectrum of radiated sound pressure, normally referred to as the "broadband" noise in literature.

The two methods used for analyzing the sound field from moving sources are described below.

1.2 Analysis of sound radiation from moving sources

An important part of aerodynamic noise theory [1] is concerned with sound radiation from moving sources. In evaluating the sound radiated from rotating singularities, it is convenient to describe the excitation initially in a moving frame of reference; rotating blades is an example in which the excitation (forces) is rotating with the blades. The sound field can then be derived by using two alternative approaches.

(1) The source description may be transformed immediately into fixed co-ordinates before proceeding to calculate the sound field. This procedure was adopted by Gutin [2] for the excitation associated with steady blade forces, and by Gutin [3] and Embleton and Thiessen [4] for steady mass sources as a model for rotor thickness noise. For the excitation associated with harmonic blade forces, Wright [5] used the same approach,

and is described in the book by Morse and Ingard [6, section 11.3] . It has since been generalized by Ffowcs Williams and Hawkings [7] for sources of arbitrary time dependence in circular motion.

(2) Alternatively, the simplicity of the moving-frame source description may be retained in the acoustic analysis, but at the expense of having to allow for the source motion. Lilley [8] used this approach to estimate the overall mean square pressure radiated from a fluctuating point force in circular motion, but acceleration effects (due to the finite radius of curvature of the path) were neglected. The general theory of sound radiation from moving singularities was developed from this viewpoint by Lowson [9], who has used it [10,11,12,13] to give alternative derivations of the steady and harmonic rotating-force results mentioned above.

Both approaches are used in the present thesis. The rotational noise analysis (chapter 2) is developed by using the first approach, and the sound radiated by rotating sources of arbitrary time dependence is evaluated by using the moving-source approach (chapters 5 to 9).

The moving-source approach offers two advantages. First, simple results for the overall radiation can be obtained directly, without involving the radiation spectrum. Second, the spectrum result takes the form of a series expansion about the linear-motion case; this enables us to establish the effects of source acceleration due to circular motion on the linear-motion results conveniently.

The following sections describe the areas of research on radiation from rotating sources that are tackled in the thesis.

1.3 Radiation from periodic rotating forces (rotational noise)

Although the importance of fluctuating ordered blade loads in the generation of rotational noise was established as a result of two computational studies by Schlegel, King and Mull [14] and Loewy and Sutton [15], the necessary analytical treatment of the subject was given separately by Lowson and Ollerhead [10] and Wright [5] at Southampton. An extensive computational study of rotational noise following these theories [5,10] was carried out as a joint effort between Wright and the author at Southampton. The computer program for this study was developed by the author [16] and is described in detail in Appendix I. The results of the computational study are reported in reference [17], and were included in Wright's thesis [18]. In order to avoid duplication, a summary only of the computational investigation is given in the present thesis - see Appendix II.

The four basic assumptions involved in the rotational noise theories [5,10,14] quoted above are:

(a) The rotor or propellor system is assumed to be stationary. As a result, the solution's accuracy decreases as the rotor system translational speed increases.

(b) Steady conditions are assumed. That is, what happens in one revolution happens in every other revolution, and in fact, what happens to one blade at a particular azimuth is repeated on every other blade when it is at that azimuth.

(c) The loading profile across the blade span is neglected and the total loading on the blade is supposed to be acting over a small span length Δr (point loading) at an effective radius r_e, usually taken to be around 0.8 of the tip radius r_T.

† For a flat plate aerofoil the local differential pressure equals the loading but for any other shape of aerofoil section the local pressures on the top and bottom surfaces must strictly be resolved in a direction normal to the chord before subtraction. The term 'differential pressure' is used loosely throughout the thesis to indicate the loading.

(d) The chordwise differential-pressure† profile is assumed to be rectangular. That is, the actual differential-pressure profile across the chord is approximated by equivalent rectangular distribution for easier harmonic analysis.

Now although assumption (b) appears to be justified (this is supported by the fact that the contribution from discrete tones at multiples of the rotor shaft frequency is negligible in the case of helicopter rotor noise spectrum), the other three do not. In fact Schlegel [14] has eliminated assumption (d) in his analysis, and Lowson and Ollerhead [10] have modified their analysis to include the effect of forward velocity of the rotor system. The last assumption (d) has not been properly examined in any of the previous theories, and together with spanwise distributed loading effects it forms a part of the present investigation. The investigation seems to be justified for the following reasons.

(1) The relative importance of broadband noise and discrete-frequency noise from a helicopter rotor has been in question for a long time, but the situation is fairly clear now. At low tip Mach numbers, broadband noise is subjectively as important as rotational noise, if not more important [37]. (It is treated separately in chapters 5 and 6). On the other hand, at high tip Mach numbers (say greater than 0.5), rotational noise becomes more important subjectively. Experimental data show that discrete-frequency peaks at multiples of the rotor blade passage frequency could be detected well into the region of the spectrum where broadband noise exists [10,37], especially at higher tip Mach numbers. Thus it is essential to explore all the possible mechanisms for the generation of rotational noise.

(2) When a helicopter rotor is being translated at high forward speed, the large differences in effective angle of attack between the advancing and the retreating half cycles of the blade revolution produce large variations in the blade loading, as well as in the loading profiles across the chord and span. This is only one example out of a number of situations and causes which lead to large fluctuations in the profiles. Under such flight conditions, it is obvious that the available theories may give misleading results, and it is considered essential to modify the present theories in order to investigate the consequences of such changes in loading profiles on the radiation of noise.

(3) Aerodynamic measurements of the blade loads indicate that in various situations, especially when blade stall occurs, the differential-pressure across the blade chord has a very peculiar profile, having negative lift over a part of the chord (usually near the trailing edge). This will affect rotational noise harmonics predicted by previous theories at frequencies whose wavelengths are comparable to or shorter than the blade chord.

To summarize, modifications of the previous theories to include chordwise and spanwise differential-pressure profiles and their variations with azimuth are required at

(1) high tip Mach numbers, say $M_T > 0.6$,

(2) high forward speeds,

and (3) higher frequencies of the acoustic spectra.

A detailed account of the work which results from the above arguments is given in chapters 2 and 3.

1.4 Helicopter rotor aerodynamics

In order to calculate the noise radiated from a helicopter rotor, the most vital information which must be known is the magnitudesof fluctuating forces acting on the blades. Unfortunately, this information is not easily available, either experimentally or theoretically, at the present time. On the experimental side, measurement of blade airloads is a very complicated and expensive instrumentation problem, where the magnitudes of the high frequency harmonic airloads are so small (but vital for noise calculations) that the available accuracy of the measuring instruments renders them unreliable. So far, it is impossible to include all the factors which produce the loading asymmetries in the computer solutions for airloads prediction - see White [19].

As a result, the best one can do at the present time is to study all the available measured loading data in detail and look for any trends that exist. This is done here in chapter 4. In addition to gaining some information on the variation of blade loading harmonic fall-offs along the blade chord and span, the study reveals several other interesting features. In particular, it appears that the loading asymmetry at a particular flight condition can be explained with reasonable success, by combining all the factors which produce the non-uniform flow through the rotor under this flight condition.

1.5 Radiation from random rotating forces (broadband noise)

Helicopter rotor blades experience random forces, which give rise to the broadband part of the acoustic spectrum, basically for three possible reasons; (a) random vortex shedding at the trailing edge (hence broadband noise is referred to as "vortex noise" by some investigators), (b) boundary

layer turbulence on the surface of the blades, and (c) interaction of a blade with turbulence in the wake shed by the previous blades. The relative magnitudes of these will vary from one rotor geometry to another, as well as with the operating conditions.

The analysis for sound radiation from sources of arbitrary time dependence in circular motion was given by Ffowcs Williams and Hawkings [7], but it is limited to spectral results only. Moreover, since their result for the radiation spectrum takes the form of an infinite series of Bessel functions, it makes it necessary to use a computer program in order to use it in practice.

It was decided to tackle the problem from first principles (chapters 5 and 6), using the moving-source approach described before. Lowson's general result [9] for the sound field of a point force in arbitrary motion is applied to the special case of uniform circular motion, and the resulting radiation properties are established in detail. In order to study the effects of distributing the forces over the rotating blades, a parallel analysis is developed in chapter 9, where the sound field from point acoustic stresses† in uniform circular motion at subsonic speeds is derived.

The rotating acoustic stresses analysis has two further applications in practice. The first one refers to the noise from tip jet rotors, where the quadrupole effects of the acoustic stresses in the turbulence are responsible for jet noise at high subsonic Mach numbers. The second application refers to the noise measurement techniques used for simulating steady fly-over of a jet by rotating it at the end of a rod in a controlled environment; within the limits of Lighthill's compact-quadrupole model for jet noise, the theory gives all the information required about how the linear-motion results are affected by finite rotation.

† For distributed blade forces, the moments of the forces can be represented by point acoustic stresses (or quadrupoles). This is discussed fully in Chapter 9.

1.6 Radiation from point sources in circular motion

Finally, the moving-source approach is used again to calculate the sound radiated from rotating point volume-velocity sources (mass flow introduction) and point volume-displacement sources (mass displacement), in chapters 7 and 8 respectively.

The volume-velocity source analysis has direct application to the noise from tip jet rotors. Here, at low jet exhaust speeds (approx. $M < 0.4$), the noise is dominated by the monopole effects of the jet mass flow fluctuations induced by (a) irregular combustion and (b) jet pipe boundary layer turbulence, as shown by Ffowcs Williams and Gordon [20].

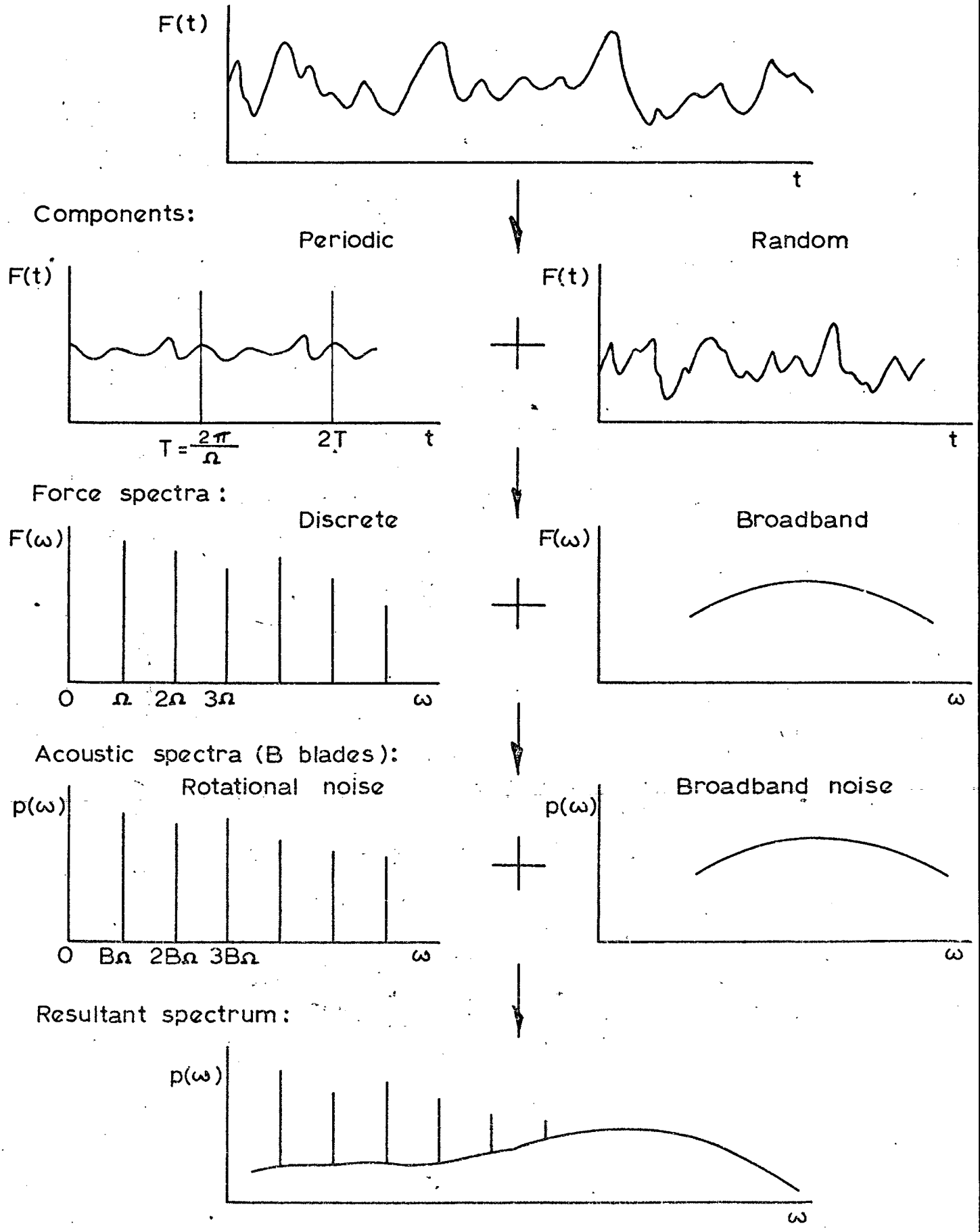

Fig. 1.1 Forces on rotating blades.

CHAPTER 2

ROTATIONAL NOISE THEORY

Expressions for the sound radiation from harmonically fluctuating forces distributed over rotating blades are derived here. Since the purpose of the investigation is to evaluate the effects of the shapes of chordwise and spanwise differential-pressure profiles, and their variations with azimuth, on the generation of rotational noise, it is convenient to make the following two assumptions:

(a) The rotor or propeller system is assumed to be stationary. As a result, the solution's accuracy decreases as the rotor system translational speed increases.

(b) Steady conditions are assumed. That is, what happens to one blade at a particular azimuth is repeated on every other blade when it is at that azimuth.

These assumptions reduce the mathematical complexity of the problem considerably.

2.1 General theory

The structure of the analysis is similar to those by previous investigators [2, 5, 14]. Since the sound field from rotating forces over the blades is equivalent to the sound field due to stationary dipoles over the rotor disc which arise from force fluctuations at each element ($rd\psi$, dr) of the disc, the analysis can basically be divided into three stages;

(1) To determine the sound pressure at a point $\underset{\sim}{R}$ due to a fluctuating force acting at point $\underset{\sim}{x}$ on the rotor disc.

(2) To define the time history of the force per unit disc area acting at each element ($rd\psi$, dr) of the rotor disc in terms of the force per unit blade area.

(3) To evaluate the total radiation from the entire disc by azimuthal and radial integrations.

The acoustic pressure p due to a point force $\underset{\sim}{F}(t)$ acting at $\underset{\sim}{x}$ is given by Lighthill [1] as

$$p(\underset{\sim}{R}, t) = -\frac{\partial}{\partial R_i}\left\{\frac{F_i(t-D/c_o)}{4\pi D}\right\} \tag{2.1}$$

where D is the observer-source separation,

$$D = |R_i - x_i| \tag{2.2}$$

and i signifies the three co-ordinate directions $i = 1, 2, 3$. Equation (2.1) thus gives

$$p(\underset{\sim}{R},t) = \frac{(R_i-x_i)}{4\pi D^2}\left\{\frac{1}{c_o}\frac{\partial}{\partial t}F_i(t-D/c_o) + \frac{1}{D}F_i(t-D/c_o)\right\}. \tag{2.3}$$

The fluctuating force $\underset{\sim}{f}$ per unit disc area acting at any point (r,ψ) on the rotor disc varies periodically at integral multiples of the rotor blade passage angular frequency $B\Omega$ and so it can be represented by the Fourier series

$$\underset{\sim}{f}(r,\psi;\ t) = \sum_{m=1}^{\infty} \underset{\sim}{C}_m(r,\psi)\ \exp j(mB\Omega t) \tag{2.4}$$

where the period T of the force variation is the time interval between the passage of successive ~~blades~~ blades over point (r,ψ) and is given by

$$T = \frac{2\pi}{B\Omega}. \tag{2.5}$$

It should be noted that the steady coefficient (m=0) is omitted because it does not make any contribution to the acoustic pressure field. If the force is distributed over an element of disc area $dS = rdrd\psi$, so that

$$\underset{\sim}{f}\, rdrd\psi = \underset{\sim}{F}, \tag{2.6}$$

then the resulting m^{th} harmonic of sound pressure is obtained from (2.3) as

$$dSP_{mB}(\underset{\sim}{R},t) = \frac{(R_i - x_i)}{4\pi D^2} C_{mi}(r,\psi) \left(\frac{jmB\Omega}{c_o} + \frac{1}{D}\right)$$

$$\exp j(mB\Omega t - \frac{mB\Omega D}{c_o})\, rdrd\psi. \tag{2.7}$$

It is convenient to take the origin at the centre of the rotor. Since the ~~differential pressure~~ force is acting in the plane normal to the radius vector, $x_i C_{mi} = 0$. With reference to the geometries defined in figures (2.1) and (2.2),

$$x_i = (r\cos\psi,\ r\sin\psi,\ 0), \tag{2.8}$$

$$R_i = (R\cos\sigma\cos\theta,\ R\cos\sigma\sin\theta,\ R\sin\sigma), \tag{2.9}$$

$$C_{mi} = (-C_m\sin\beta\sin\psi,\ C_m\sin\beta\cos\psi,\ -C_m\cos\beta), \tag{2.10}$$

giving

$$D = |R_i - x_i| = \left\{R^2 + r^2 - 2rR\cos\sigma\cos(\theta - \psi)\right\}^{\frac{1}{2}} \tag{2.11}$$

and $$R_i C_{mi} = -RC_m\left\{\sin\beta\cos\sigma\sin(\psi - \theta) + \sin\sigma\cos\beta\right\}. \tag{2.12}$$

The sound pressure equation (2.7) can now be written as

$$dSP_{mB}(\underset{\sim}{R},t) = -\frac{R}{4\pi D^2} C_m(r,\psi)\left\{\sin\beta\cos\sigma\sin(\psi - \theta) + \sin\sigma\cos\beta\right\}\left(\frac{jmB\Omega}{c_o} + \frac{1}{D}\right) x$$

$$\exp j(mB\Omega t - \frac{mB\Omega D}{c_o})\, r\, dr\, d\psi\ . \tag{2.13}$$

If the blade is twisted and the rotor is operating with cyclic pitch

†† Here it is assumed that the chord width projected on the rotor disc is identical to the actual blade chord width. This is valid for small values of β. On the other hand, for large values of β, the projected chord width is $\cos\beta$ times the actual blade chord width.

variation, then the resultant pitch angle at any point (r,ψ) on the rotor disc is given by

$$\beta(r,\psi) = \beta_o + \beta_1 \cos\psi + \bar{\beta}_1 \sin\psi - \gamma(r-r_o) , \qquad (2.14)$$

where β_o = steady pitch angle,

β_1 = cosine coefficient of cyclic pitch,

$\bar{\beta}_1$ = sine coefficient of cyclic pitch,

γ = blade twist rate ,

and r_o = radius at which blade twist begins.

Thus once the ~~differential-pressure~~ coefficient C_m of the force per unit disc area acting on the element $(rd\psi, dr)$ of the disc can be defined, in terms of the force per unit blade area the radiation may be obtained from equation (2.13). The actual spanwise and chordwise differential-pressure profiles acting on the blades can be introduced as follows.

The blade chord is divided into a number of sections, the number depending upon the number of transducer positions across the chord at which measured differential-pressure data are available. The loading on each of these elements is considered as a rotating fluctuating force. Retaining the appropriate time delays between one chord section and every other chord section enables us to define the ~~pressure~~ time history of the force per unit disc area at each azimuthal element of the rotor disc at a fixed span station. This process is then repeated at several radial stations and in this manner, it is also possible to introduce a span loading profile as well as its variation with azimuth.

The ~~pressure~~ time history of the force per unit disc area as the blades pass over element $(rd\psi, dr)$ is shown in Fig. 2.3.†† If a_p represents the distance from the leading edge of the chord station representing the p^{th} chord section, then the ~~pressure~~ spectrum of the assumed rectangular disc loading P_p due to ~~on~~ the p^{th} strip can be written in the

† If the number of blade chord sections is large, the loading on each strip can be approximated by point loading.

Fourier series form as

$$P_p(r,\psi;t) = \sum_{m=1}^{\infty} D_{pm}(r,\psi) \cos\left\{ mB\Omega t - mB\psi - \frac{mB(a_p - a_1)}{r} \right\} \tag{2.15}$$

where

$$D_{pm}(r,\psi) = \frac{2}{T} \int_{-t_p/2}^{t_p/2} A_p(r,\psi) \cos \frac{2m\pi t}{T}\, dt \tag{2.16}$$

$$= 2 \frac{A_p(r,\psi) t_p}{T} \frac{\sin(m\pi t_p/T)}{(m\pi t_p/T)} \,. \tag{2.17}$$

If w_p† represents the projected width of the p^{th} section, given approximately by

$$w_p \doteq \frac{1}{2}(a_{p+1} - a_{p-1}) \,, \tag{2.18}$$

then

$$t_p = \frac{w_p}{\Omega r} \,, \quad \frac{t_p}{T} = \frac{w_p B}{2\pi r} \tag{2.19}$$

and so (2.17) can be written as

$$D_{pm}(r,\psi) = \frac{2A_p(r,\psi)}{m\pi} \sin\left(\frac{mw_p B}{2r}\right) \,. \tag{2.20}$$

The ~~differential-pressure~~ loading spectrum (2.15) then becomes

$$P_p(r,\psi;t) = \sum_{m=1}^{\infty} \frac{2A_p(r,\psi)}{m\pi} \sin\left(\frac{mw_p B}{2r}\right) \cos mB\left\{ \Omega t - \psi - \frac{(a_p - a_1)}{r} \right\}. \tag{2.21}$$

Note that $A_p(r,\psi)$ is the differential-pressure on the p^{th} chord section at point (r,ψ) and is given by

$$A_p(r,\psi) = A_{po}(r) + \sum_{g=1}^{\infty} \left\{ A_{pg}(r) \cos g\psi + \bar{A}_{pg}(r) \sin g\psi \right\} \tag{2.22}$$

where $A_{po}(r)$, $A_{pg}(r)$, $\bar{A}_{pg}(r)$ are the steady, cosine and sine coefficients

† See second footnote on page 15. For large β, projected $w_p \doteq \frac{1}{2}(a_{p+1} - a_{p-1}) \cos\beta$.

respectively of the Fourier analyzed stationary differential-pressure on the blade station. The resultant ~~pressure~~ loading spectrum due to n chord sections can be written into complex form, from (2.21) as

$$P(r,\psi;t) = \sum_{p=1}^{n} \sum_{m=1}^{\infty} \frac{2A_p(r,\psi)}{m\pi} \sin\left(\frac{mw_p B}{2r}\right) \exp jmB\left\{\Omega t - \psi - \frac{(a_p - a_1)}{r}\right\} . \quad (2.23)$$

Comparing this with equation (2.5), the ~~differential-pressure~~ coefficient $C_m(r,\psi)$ ~~becomes~~ of the force per unit disc area can be written in terms of the force per unit blade area as

$$C_m(r,\psi) = \sum_{p=1}^{n} \frac{2A_p(r,\psi)}{m\pi} \sin\left(\frac{mw_p B}{2r}\right) \exp - jmB\left\{\psi + \frac{(a_p - a_1)}{r}\right\} . \quad (2.24)$$

Substituting this into (2.13), the radiation from the entire disc is given by

$$SP_{mB}(\underset{\sim}{R},t) = \int_0^{r_T} \int_0^{2\pi} - \exp j(mB\Omega t) \frac{R}{2\pi^2 mD^2} \left\{\sin\beta \cos\sigma \sin(\psi-\theta) + \sin\sigma \cos\beta\right\}\left(\frac{jmB\Omega}{c_o} + \frac{1}{D}\right) x$$

$$\left[\sum_{p=1}^{n} A_p(r,\psi) \cdot \sin\left(\frac{mw_p B}{2r}\right) \exp - jmB\left\{\frac{\Omega D}{c_o} + \psi + \frac{(a_p - a_1)}{r}\right\}\right] r \, d\psi \, dr . \quad (2.25)$$

Writing $$mB\left\{\frac{\Omega D}{c_o} + \psi + \frac{(a_p - a_1)}{r}\right\} = \bar{U}_p(r,\psi) , \quad (2.26)$$

and taking the real and imaginary parts of the resulting equation, the root-mean-sqaure value of the m^{th} harmonic of sound pressure is given by

$$SP_{mB} = \frac{1}{\sqrt{2}} \hat{SP}_{mB} = \frac{R}{2\sqrt{2}\pi^2 m} \left\{(Re)^2 + (Im)^2\right\}^{\frac{1}{2}} \quad (2.27)$$

where

$$Re = \int_0^{r_T} \int_0^{2\Pi} \frac{1}{D^2} \left\{ \sin\beta \cos\sigma \sin(\psi-\theta) + \sin\sigma \cos\beta \right\} x$$

$$\left[\sum_{p=1}^{n} \left\{ A_p(r,\psi) \cdot \sin\left(\frac{mw_p B}{2r}\right) \cdot \left(\frac{\cos U_p}{D} + \frac{mB\Omega}{c_o} \sin U_p\right) \right\} \right] r d\psi dr \qquad (2.27a)$$

and

$$Im = \int_0^{r_T} \int_0^{2\pi} \frac{1}{D^2} \left\{ \sin\beta \cos\sigma \sin(\psi-\theta) + \sin\sigma \cos\beta \right\} x$$

$$\left[\sum_{p=1}^{n} \left\{ A_p(r,\psi) \cdot \sin\left(\frac{mw_p B}{2r}\right) \cdot \left(\frac{mB\Omega}{c_o} \cos U_p - \frac{\sin U_p}{D}\right) \right\} \right] r d\psi \, dr \qquad (2.27b)$$

and where

$$U_p(r,\psi) = mB\left\{ \frac{\Omega D}{c_o} + \psi + \frac{(a_p - a_1)}{r} \right\} , \qquad (2.27c)$$

$$A_p(r,\psi) = A_{po}(r) + \sum_{g=1}^{\infty} \left\{ A_{pg}(r) \cos g\psi + \bar{A}_{pg}(r) \sin g\psi \right\} , \qquad (2.27d)$$

$$\beta(r,\psi) = \beta_o + \beta_1 \cos\psi + \bar{\beta}_1 \sin\psi - \gamma(r-r_o) , \qquad (2.27e)$$

$$D = \left\{ R^2 + r^2 - 2rR \cos\sigma \cos(\theta-\psi) \right\}^{\frac{1}{2}} , \qquad (2.27f)$$

$$w_p \doteq \frac{1}{2} (a_{p+1} - a_{p-1}) . \qquad (2.27g)$$

The above result gives the r.m.s. value of the m^{th} harmonic of sound pressure at any observer position from the rotor centre, in terms of the fluctuating spanwise and chordwise differential-pressure distributions on the rotor blades. The quantities required to evaluate this final result are

(1) rotor geometry and operating conditions,

(2) field point distance, azimuth angle, elevation angle, and

(3) rotor blade differential-pressures, in the form of steady and harmonic sine and cosine coefficients at several chordwise and spanwise stations.

2.2 Point span loading models

In order to establish the effects of chordwise differential-pressure profiles on the generation of noise, the spanwise loading profile is now reduced to point loading. Expressions for sound radiation in the far field from two such point span loading models are derived from the general result (2.25) as follows.

2.2.1 Actual chordwise loading profile model

Consider the general sound pressure equation (2.25). In the far field,

$$\frac{jmB\Omega}{c_o} >> \frac{1}{D} \quad , \quad D \doteq R - r\cos\sigma\cos(\theta-\psi) \quad \text{in the exponential term,}$$

$$\text{and} \quad D \rightarrow R \quad \text{elsewhere.} \tag{2.28}$$

Equation (2.25) then reduces, writing $\Omega = 2\pi N$, to

$$SP_{mB}(\underset{\sim}{R},t) = \frac{-jBN}{\pi R c_o} \exp jmB\Omega(t-R/c_o) \int_o^{r_T} \int_o^{2\pi} \left\{ \sin\beta\cos\sigma\sin(\psi-\theta) + \sin\sigma\cos\beta \right\} x$$

$$\left[\sum_{p=1}^{n} A_p(r,\psi) \cdot \sin\left(\frac{mw_p B}{2r}\right) \cdot \exp jmB\left\{ \frac{\Omega r}{c_o}\cos\sigma\cos(\theta-\psi) - \psi - \frac{(a_p-a_1)}{r} \right\} \right] r\, d\psi dr. \tag{2.29}$$

If the loading on the blade is now assumed to be concentrated over span Δr at effective radius r_e , then writing

$$A_p(r_e,\psi) \cdot \Delta r = L_p'(r_e,\psi) \tag{2.30}$$

as the loading per unit chord width at r_e, the sound pressure equation becomes

$$SP_{mB}(\underset{\sim}{R},t) = \frac{-jBNr_e}{\pi Rc_o} \exp jmB\Omega\,(t-R/c_o) \int_o^{2\pi} \left\{ \sin\beta \cos\sigma \sin(\psi-\theta) + \sin\sigma \cos\beta \right\} x$$

$$\left[\sum_{p=1}^{n} L_p'(r_e,\psi) \cdot \sin\left(\frac{mw_p B}{2r_e}\right) \cdot \exp jmB\left\{ M_e \cos\sigma \cos(\theta-\psi) - \psi - \frac{(a_p-a_1)}{r_e} \right\} \right] d\psi \,. \tag{2.31}$$

Taking the real and imaginary parts of the above equation, the r.m.s. value of m^{th} harmonic of sound pressure is given by

$$SP_{mB} = \frac{1}{\sqrt{2}} \hat{SP}_{mB} = \frac{BNr_e}{\sqrt{2}\pi Rc_o} \left\{ (Re)^2 + (Im)^2 \right\}^{\frac{1}{2}} \tag{2.32}$$

where

$$Re = \int_o^{2\pi} \left\{ \sin\beta \cos\sigma \sin(\psi-\theta) + \sin\sigma \cos\beta \right\} x$$

$$\left[\sum_{p=1}^{n} L_p'(r_e,\psi) \cdot \sin\left(\frac{mw_p B}{2r_e}\right) \cdot \sin V_p(\psi) \right] d\psi \tag{2.32a}$$

and

$$Im = \int_o^{2\pi} \left\{ \sin\beta \cos\sigma \sin(\psi-\theta) + \sin\sigma \cos\beta \right\} x$$

$$\left[\sum_{p=1}^{n} L_p'(r_e,\psi) \cdot \sin\left(\frac{mw_p B}{2r_e}\right) \cdot \cos V_p(\psi) \right] d\psi \tag{2.32b}$$

and where

$$V_p(\psi) = mB\left\{ M_e \cos\sigma \cos(\theta-\psi) - \psi - \frac{(a_p-a_1)}{r_e} \right\} \,, \tag{2.32c}$$

$$L'_p(r_e,\psi) = L'_{po}(r_e) + \sum_{g=1}^{\infty} \left\{ L'_{pg}(r_e)\cos g\psi + \bar{L}'_{pg}(r_e)\sin g\psi \right\}. \qquad (2.32d)$$

The above result predicts the radiation from the point span loading model when the chordwise loading profile is continuously changing with azimuth. The spectrum so obtained is to be compared with the spectrum obtained by replacing the actual chordwise loading profile by an equivalent rectangular profile at every azimuth. (The word "equivalent" means that the areas under the actual profile and the rectangular profile are equal, at all azimuthal points.) Expressions for the radiation from such a model are now derived below.

2.2.2 Equivalent rectangular chordwise loading profile model

Here the loading-time history as the blades pass over points (r_e,ψ) is as shown in Fig. 2.4 and the corresponding spectrum in the Fourier series form can be written as

$$P'(r_e,\psi;t) = \sum_{m=1}^{\infty} D'_m(r_e,\psi)\cos(mB\Omega t - mB\psi) \qquad (2.33)$$

where

$$D'_m(r_e,\psi) = \frac{2}{T}\int_{-t_{o/2}}^{t_{o/2}} L'(r_e,\psi)\cos\frac{2m\pi t}{T}\,dt$$

$$= \frac{2\,L'(r_e,\psi)}{m\pi}\sin\left(\frac{maB}{2r_e}\right). \qquad (2.34)$$

Writing (2.33) into complex form, the loading coefficient $C'_m(r_e,\psi)$ is then obtained as

$$C'_m(r_e,\psi) = \frac{2\,L'(r_e,\psi)}{m\pi}\sin\left(\frac{maB}{2r_e}\right)\exp -j(mB\psi) \qquad (2.35)$$

and the resulting sound pressure in the far field can be derived to be

$$SP_{mB}(\underset{\sim}{R},t) = \frac{-jBNr_e}{\pi Rc_o} \exp jmB\Omega\left(t - \frac{R}{c_o}\right) \cdot \sin\left(\frac{maB}{2r_e}\right) x$$

$$\int_o^{2\pi} \left\{ \sin\beta \cos\sigma \sin(\psi-\theta) + \sin\sigma \cos\beta \right\} L'(r_e,\psi)\, x$$

$$\exp jmB\left\{ M_e \cos\sigma \cos(\theta-\psi) - \psi \right\} d\psi \quad . \tag{2.36}$$

As before, taking the real and imaginary parts of the above equation, the r.m.s. value of m^{th} harmonic of sound pressure is given by

$$SP_{mB} = \frac{1}{\sqrt{2}} \hat{SP}_{mB} = \frac{BNr_e}{\sqrt{2}\pi Rc_o} \sin\left(\frac{maB}{2r_e}\right) \left\{ (Re)^2 + (Im)^2 \right\}^{\frac{1}{2}} \tag{2.37}$$

where

$$Re = \int_o^{2\pi} \left\{ \sin\beta \cos\sigma \sin(\psi-\theta) + \sin\sigma \cos\beta \right\} L'(r_e,\psi) \cdot \sin V(\psi)\, d\psi \tag{2.37a}$$

and

$$Im = \int_o^{2\pi} \left\{ \sin\beta \cos\sigma \sin(\psi-\theta) + \sin\sigma \cos\beta \right\} L'(r_e,\psi) \cdot \cos V(\psi)\, d\psi \tag{2.37b}$$

and where

$$V(\psi) = mB\left\{ M_e \cos\sigma \cos(\theta-\psi) - \psi \right\}, \tag{2.37c}$$

$$L'(r_e,\psi) = L'_o(r_e) + \sum_{g=1}^{\infty} \left\{ L'_g(r_e) \cos g\psi + \bar{L}'_g(r_e) \sin g\psi \right\}$$

or

$$L'(r_e,\psi) = \frac{1}{a} \sum_{p=1}^{n} L'_p(r_e,\psi) \cdot w_p \quad . \tag{2.37d}$$

The above equation predicts the radiation from the point span loading model when the chordwise loading profile at each azimuthal station is replaced by the equivalent rectangular profile.

2.3 Radiation from single blade loading harmonic with arbitrary chordwise loading profile

Consider equation (2.31) for radiation in the far field from the point span loading model. The radiation from a single harmonic (g) blade loading of the form

$$L'_p(r_e,\psi) = L'_{pg}(r_e)\cos g\psi = L'_{pg}(r_e)\left(\frac{e^{jg\psi} + e^{-jg\psi}}{2}\right) \qquad (2.38)$$

is then given by

$$SP_{mBg}(\underset{\sim}{R},t) = \frac{-jBNr_e}{\pi Rc_o}\exp jmB\Omega\left(t - \frac{R}{c_o}\right)\int_o^{2\pi}\left\{\sin\beta\cos\sigma\sin\psi + \sin\sigma\cos\beta\right\} x$$

$$\left[\sum_{p=1}^{n}\frac{\alpha_{pg}(r_e)}{2}L'_{po}(r_e)\cdot(e^{jg\psi} + e^{-jg\psi})\cdot\sin\left(\frac{mw_pB}{2r_e}\right) x\right.$$

$$\left.\exp jmB\left\{M_e\cos\sigma\cos\psi - \psi - \frac{(a_p - a_1)}{r_e}\right\}\right] d\psi \ , \qquad (2.39)$$

where

$$\alpha_{pg}(r_e) = \frac{L'_{pg}(r_e)}{L'_{po}(r_e)} \ , \qquad (2.40)$$

and the observer azimuth angle θ is put equal to zero since the radiation is symmetrical about the rotor axis. Now Wright [5] has shown that a single loading harmonic of this form produces two sets of rotating modes μ, defined as

$$\mu_+ = mB + g \ , \quad \mu_- = mB - g \ . \qquad (2.41)$$

The radiation from the slower rotating modes μ_+ can be neglected in comparison to the radiation from the faster rotating modes μ_-. The radiation equation (2.39) can thus be written approximately as

$$SP_{mBg}(\underset{\sim}{R},t) = \frac{-jBNr_e}{\pi Rc_o} \exp\ jmB\Omega(t-\frac{R}{c_o}) \left[\sum_{p=1}^{n} \frac{\alpha_{pg}(r_e)}{2} L'_{po}(r_e).\sin(\frac{mw_p B}{2r_e}) \exp -jmB\frac{(a_p-a_1)}{r_e} \right] x$$

$$\int_0^{2\pi} \left\{ \sin\beta\ \cos\sigma\ \sin\psi + \sin\sigma\ \cos\beta \right\}.\exp\ j\left\{ mBM_e \cos\sigma\ \cos\psi - (mB-g)\psi \right\} d\psi \ . \tag{2.42}$$

Using the Bessel function relationships

$$\int_0^{2\pi} \exp\ j(mBM_e\cos\sigma\ \cos\psi - \mu_-\psi)d\psi = 2\pi j^{\mu_-} J_{\mu_-}(mBM_e\cos\sigma) \tag{2.43}$$

$$\text{and} \int_0^{2\pi} \sin\psi\ .\ \exp\ j(mBM_e\cos\sigma\ \cos\psi - \mu_-\psi)d\psi = -\frac{\mu_-}{mBM_e\cos\sigma} 2\pi j^{\mu_-} J_{\mu_-}(mBM_e\cos\sigma) \tag{2.44}$$

this becomes

$$SP_{mBg}(\underset{\sim}{R},t) = -j^{\mu_-+1} \frac{Nr_e}{mRc_o} \exp\ jmB\Omega(t-\frac{R}{c_o}).\left\{ \cos\beta\ \sin\sigma - \frac{\sin\beta}{M_e}\ \frac{\mu_-}{mB} \right\}\ x$$

$$mB\ J_{\mu_-}(mBM_e\cos\sigma)\ .\ \left[\sum_{p=1}^{n} \alpha_{pg}(r_e).L'_{po}(r_e).\sin(\frac{mw_p B}{2r_e}).\exp\ -jmB\frac{(a_p-a_1)}{r_e} \right]. \tag{2.45}$$

Taking the real and imaginary parts of the above equation, the peak value of the sound pressure is given by

$$\hat{SP}_{mBg} = \frac{N}{2Rc_o}\left\{ \cos\beta\ \sin\sigma - \frac{\sin\beta}{M_e}\frac{\mu_-}{mB} \right\} mB\ J_{\mu_-}(mBM_e\cos\sigma)\ x$$

$$\frac{2r_e}{m}\left[\left(\sum_{p=1}^{n} \alpha_{pg}(r_e)\ .\ L'_{po}(r_e).\ \sin(\frac{mw_p B}{2r_e}).\ \cos\left\{ \frac{mB(a_p-a_1)}{r_e} \right\} \right)^2 \right.$$

$$\left. + \left(\sum_{p=1}^{n} -\alpha_{pg}(r_e).\ L'_{po}(r_e).\ \sin(\frac{mw_p B}{2r_e}).\ \sin\left\{ \frac{mB(a_p-a_1)}{r_e} \right\} \right)^2 \right]^{\frac{1}{2}} . \tag{2.46}$$

The above equation can be used to investigate the radiation properties of a single blade loading harmonic g with arbitrary shape of chordwise profile. (It should be noted that the profile remains unaltered with azimuth.)

When the loading profile is rectangular,

$$n = 1 \ , \quad \alpha_{pg} = \alpha_g \quad , \quad w_p = a \quad \text{and} \quad L'_{po} = L'_o \ . \tag{2.47}$$

The general radiation equation (2.46) then reduces to

$$\hat{SP}_{mBg} = \frac{\alpha_g N}{2Rc_o} \left\{ \cos\beta \sin\sigma - \frac{\sin\beta}{M_e} \frac{\mu_-}{mB} \right\} mB \, J_{\mu_-}(mBM_e \cos\sigma). \ L'_o aB \, \frac{2r_e}{maB} \sin\left(\frac{maB}{2r_e}\right) \ . \tag{2.48}$$

Now $L'_o \, aB = L_T$, the total steady lift on the rotor and so equation (2.48) can be written as

$$\hat{SP}_{mBg} = \frac{\alpha_g}{2} \frac{NL_T}{Rc_o} \left\{ \cos\beta \sin\sigma - \frac{\sin\beta}{M_e} \frac{\mu_-}{mB} \right\} mB \, J_{\mu_-}(mBM_e \cos\sigma). \ \frac{\sin\left(\frac{maB}{2r_e}\right)}{\left(\frac{maB}{2r_e}\right)} \ . \tag{2.49}$$

This result is in agreement with Wright's result [5].

2.4 Computer programs

Having obtained the sound radiation equations for various loading models, the results were programmed so that numerical answers can be obtained if the blade loading information is available. The four programs written in the HARTRAN version of 1900 FORTRAN for use at the Atlas Computer Laboratory, Chilton, Berkshire, are as follows:

Program A : Equation (2.46)

To investigate the properties of single blade loading harmonic radiation, for point span loading but distributed chordwise loading of any profile desired (i.e. arbitrary shape but unaltered with azimuth).

Program B : Equation (2.32).

To investigate the effect of shape of chordwise differential-pressure profile, and its variation with azimuth on rotational noise harmonics. In order to study the effect of this mechanism, all other parameters must be held constant and so the span loading profile is replaced by point loading at effective radius r_e.

Program C : Equation (2.27)

To calculate harmonics of rotational noise as predicted by the final result of the general theory. That is, when both the chordwise and the spanwise loading profiles are continuously changing with azimuth.

Program D : Equation (2.37)

To evaluate the difference in radiation due to actual chordwise profiles and equivalent rectangular distributions. Thus this program is written to predict the radiation from the point span loading model when the chordwise differential-pressure profiles are replaced by equivalent rectangular profiles.

These programs were checked against the previous rotational noise program [16] (described in Appendix I) and against one another, in several ways, and identical input quantities gave identical computed results in all cases. The programs are described in Appendices III to VI, where the details are kept to a minimum since they are already described for the

previous program given in Appendix I. Nevertheless, sufficient detail has been included so that other investigators can use the programs without much difficulty. A few general comments concerning all four programs are given below.

2.4.1 Computation procedure

The method used repeatedly evaluates the basic sound pressure equations which include either a single integration or a double integration. One integration is around the rotor azimuth (ψ) with the sample points (azimuth angles) chosen at constant intervals. The other integration is along the blade span where sample stations are unevenly spaced. In the case of point span loading models, the effective radius r_e is chosen to be 0.8 of the tip radius r_T ; the effective radius point can be shifted to any other desired fraction of the tip radius simply by altering the value of r_T appropriately.

In the programs, the quantities included in the integrands are evaluated first and then the values of integrands are calculated at each source point (r,ψ). Azimuthal integration at each radial station is performed next and this is followed by radial integration to obtain real and imaginary parts of the sound pressure.

2.4.2 Integration method

The integrand is evaluated at several points and the area under the integrand curve is determined by the "trapezoidal rule" approximation. The details of this method are given in Appendix I. The most important point to bear in mind here is that the angular increment ($\Delta\psi$) of integration must be small enough to obtain a valid computation.

2.4.3 Computation time

For any particular computation case (a case here means a set of rotor geometry and operating conditions), it is clear that the computing time is approximately proportional to the number of observation points and the number of harmonics of rotational noise desired.

The execution time increases as the number of radial stations increases and the execution time decreases as the azimuthal integration interval increases. The relationship is approximately linear in both the cases.

2.4.4 Blade loading data

The blade loading data for the noise calculations is fed into the programs in the form of steady and harmonic coefficients of Fourier analysed fluctuating loading at various spanwise and/or chordwise stations on the blade.

For measured loading data which is not Fourier analyzed, but is available at equally spaced azimuthal points around the rotor disc, the programs were modified to accept the data in this alternative form.

2.5 Conclusions

(1) This chapter has developed the theory needed to establish the effects of chordwise and spanwise differential-pressure profiles, and their fluctuations with azimuth, on higher harmonic rotational noise of a helicopter rotor. Previous point loading theories are modified to include distributed blade loads, and expressions for radiation from various loading models are derived.

(2) Radiation equations have been programmed in the HARTRAN version of 1900 FORTRAN language. Rotational noise harmonics at any point in the near-field or far-field can be computed in terms of rotor geometry, operating

conditions and fluctuating chordwise and spanwise load distributions.

The findings of the computational study are discussed in detail in the next chapter.

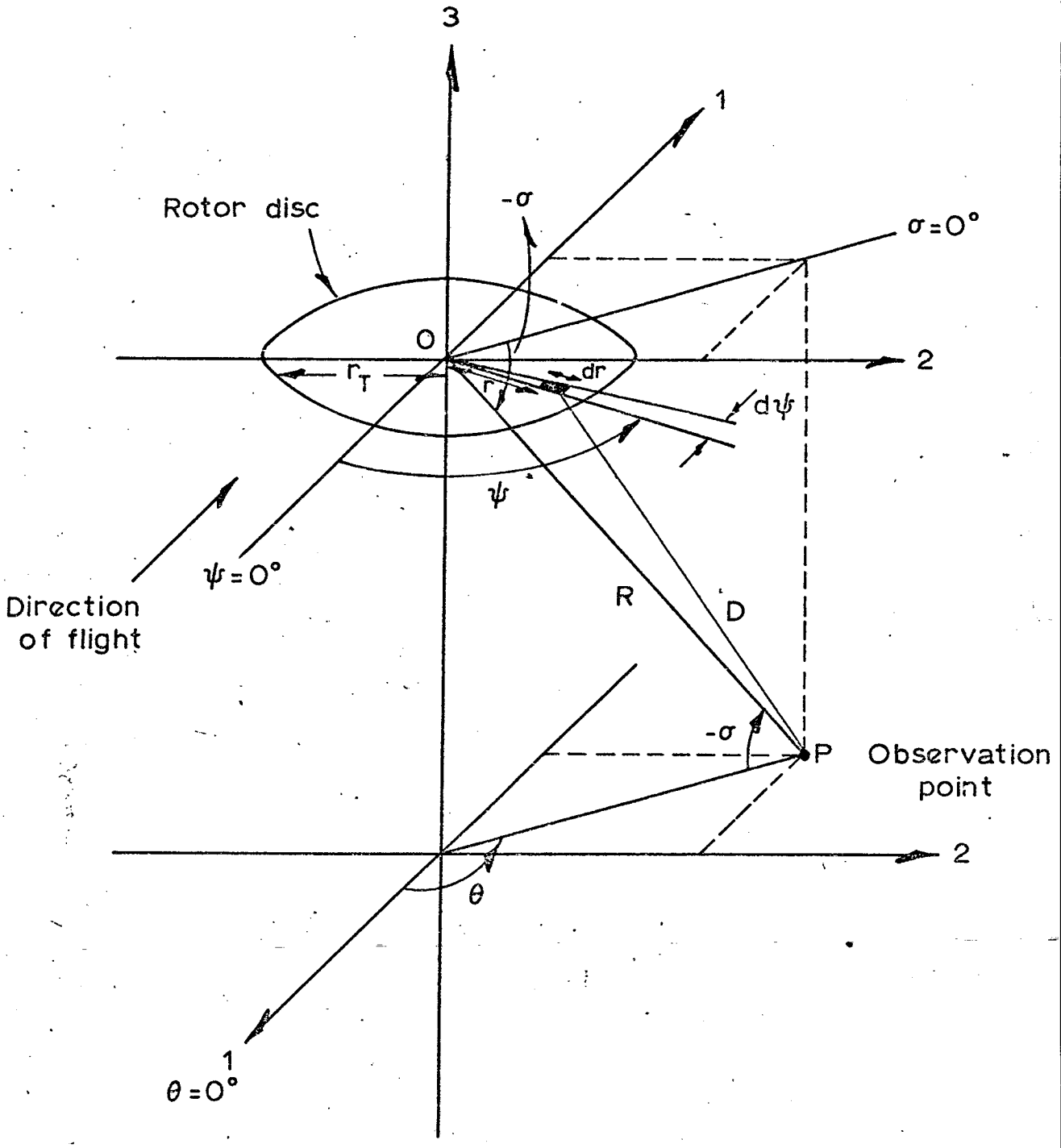

Fig. 2.1. Rotor and field point geometry.

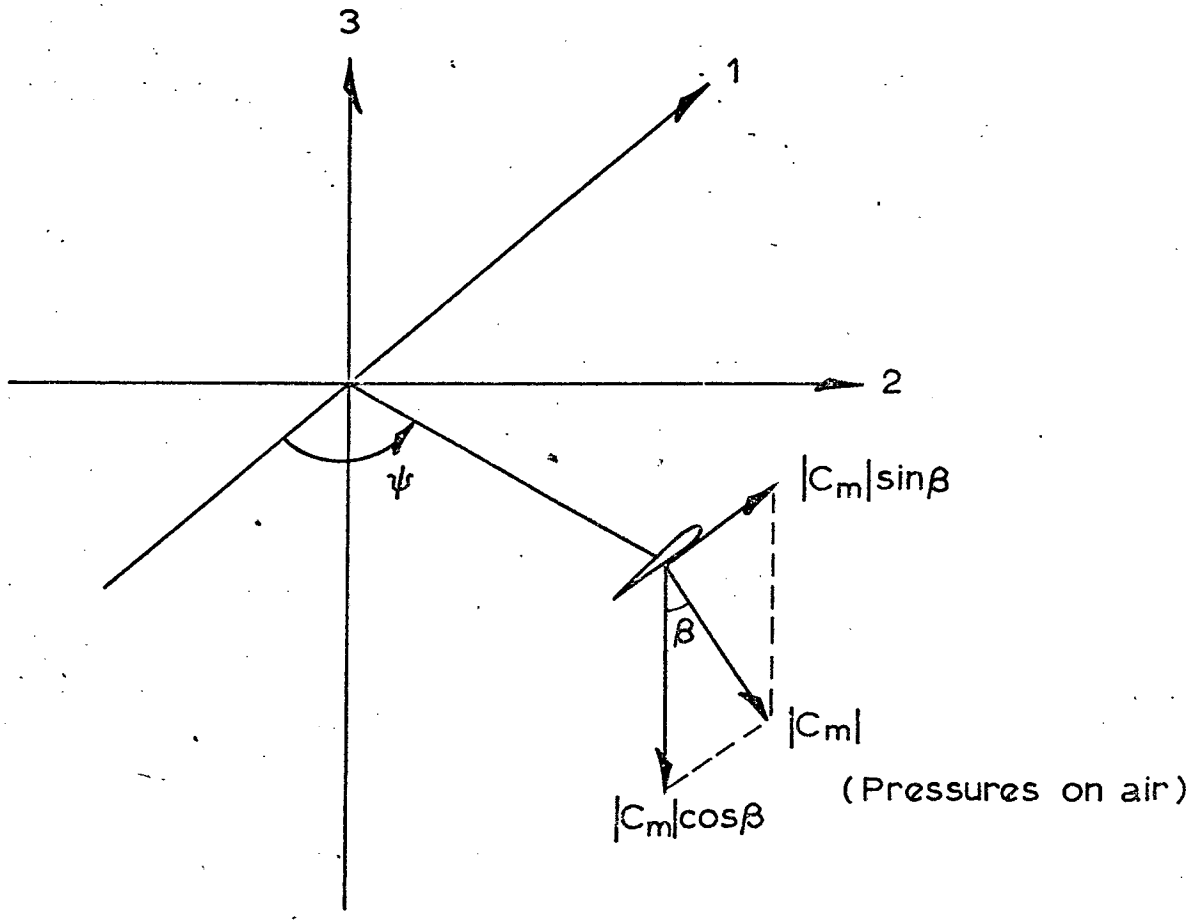

Fig. 2.2. Differential-pressure geometry.

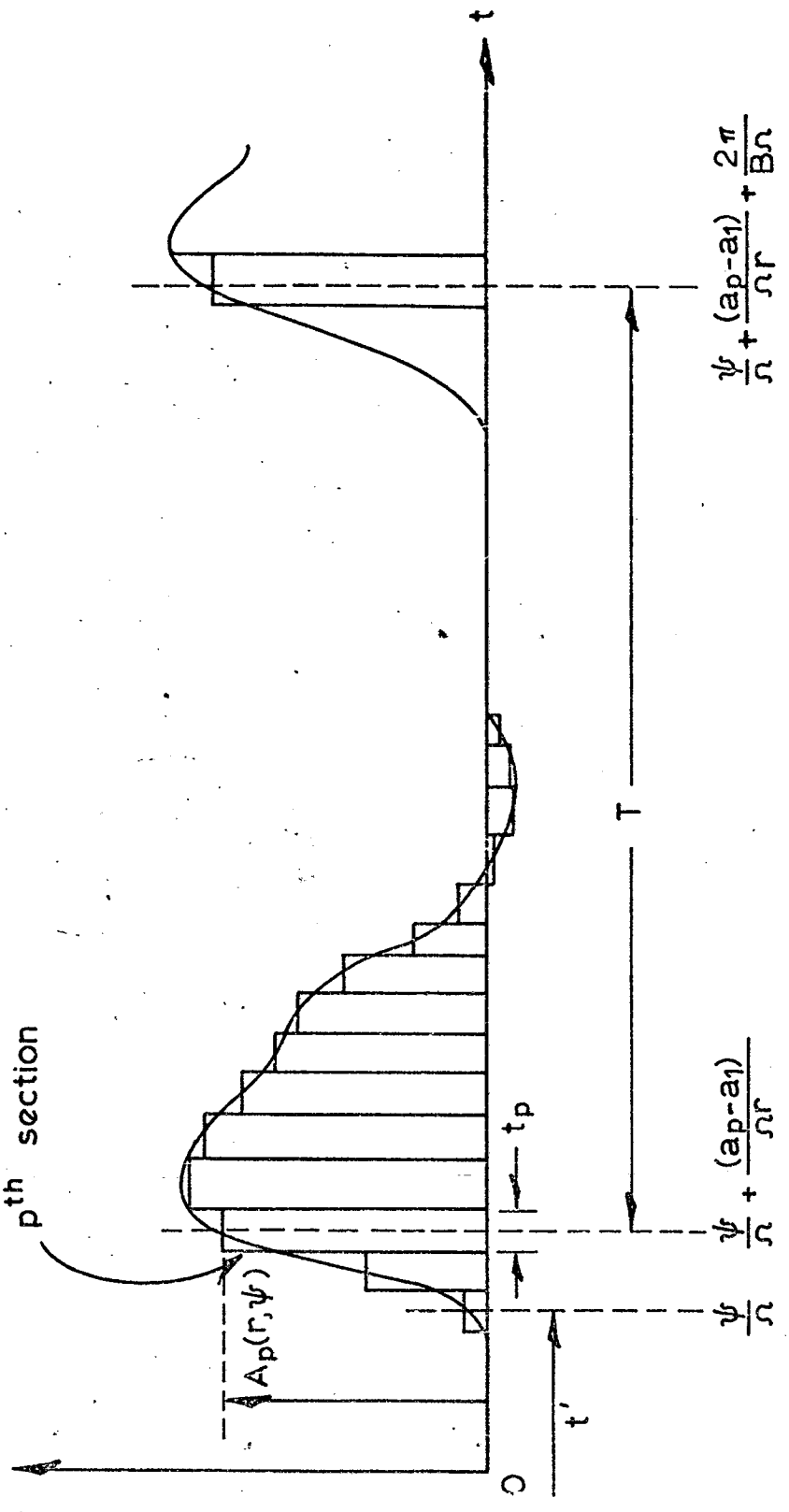

Fig. 2.3. Pressure-time history on rotor disc element.

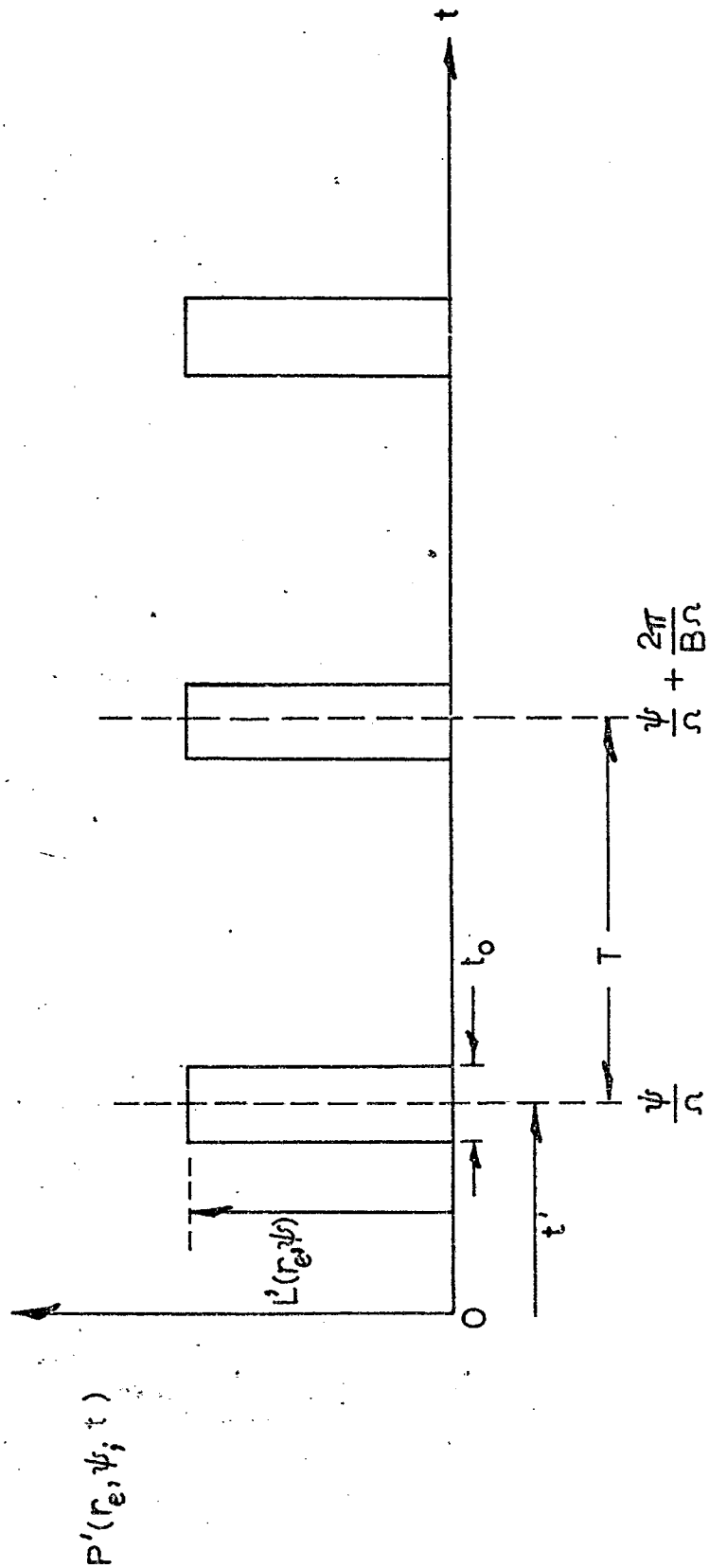

Fig. 2.4. Loading-time history for equivalent rectangular chordwise loading model.

CHAPTER 3

ROTATIONAL NOISE RESULTS AND DISCUSSION

The computer programs developed to compute the radiation from various loading models were used to investigate the differences in radiation properties between the models and the results are described in this chapter. Radiation from a single blade loading harmonic g with distributed chordwise loading is considered first.

3.1 Single blade loading harmonic radiation with arbitrary chordwise loading profile

The radiation equation (2.46) for this model can be written as

$$\hat{SP}_{mBg} = K \cdot \gamma_{\mu_-} \cdot \chi \quad , \tag{3.1}$$

where $$K = \frac{N}{2Rc_o} \left\{ \cos\beta \sin\sigma - \frac{\sin\beta}{M_e} \frac{\mu_-}{mB} \right\} , \tag{3.2}$$

$$\gamma_{\mu_-} = mB\, J_{\mu_-}(mBM_e \cos\sigma) \qquad \text{(directivity function)}, \tag{3.3}$$

and $$\chi = \frac{2r_e}{m} \left[\left(\sum_{p=1}^{n} L'_{pg}(r_e) \cdot \sin\left(\frac{mw_p B}{2r_e}\right) \cdot \cos\left\{ \frac{mB(a_p - a_1)}{r_e} \right\} \right)^2 \right.$$

$$\left. + \left(\sum_{p=1}^{n} - L'_{pg}(r_e) \cdot \sin\left(\frac{mw_p B}{2r_e}\right) \cdot \sin\left\{ \frac{mB(a_p - a_1)}{r_e} \right\} \right)^2 \right]^{\frac{1}{2}} \tag{3.4}$$

(spectrum function for distributed chordwise loading).

For distributed chordwise loading, the spectrum function χ appears as a basic multiplier; since it is independent of the observer angle σ, it affects the radiation spectrum at all observer angles identically. For point loading, the spectrum function is flat whereas if the loading is distributed, sound waves arriving at a fixed point from various parts of the blade chord interfere with each other, thus producing a non-flat spectrum

function. For well-defined loading profiles (e.g. rectangular, triangular, etc.) the spectrum functions can be derived by pulse-train analysis and are shown by Wright [21]. Equation (3.4) now enables us to compute the spectrum function for any loading profile desired.

Figures 3.1, 3.2 and 3.3 show the sound pressure spectra for steady ($g = 0$) and fluctuating ($\bar{g} = 12$, $g = 48$) blade loading harmonics respectively, for various chordwise loading profiles. The gross loading on the rotor (that is, the area under the loading profile) is 12,000 pounds in each case, and the spectra are computed for the standard case defined as follows:

Standard case:

Observation point distance $R = 300$ ft.,

elevation angle $\sigma = -30^{\circ}$,

rotor tip radius $r_T = 30$ ft.,

effective Mach number $M_e = 0.5$,

rotor blade number $B = 4$,

blade force angle (constant) $\beta = 6^{\circ}$,

blade chord width $a = 16$ in.,

and number of chord sections $n = 10$.

Clearly, the mB spectra for various loading profiles differ from one another by the spectrum functions χ for these profiles. Computed spectrum functions for the seven chordwise loading profiles chosen are shown in Fig. 3.4.

Consider the radiation spectra from the three zero net lift type distributions (square-wave type, N-type and sinusoidal). The spectra for steady ($g = 0$) and harmonically ($g = 12$, 48) fluctuating zero-lift type pressure distributions are shown in Figs. 3.1, 3.2 and 3.3 respectively.

The spectra show that a finite blade with equal positive and negative regions of differential-pressure can still radiate because the different path lengths prevent complete cancellation. It should be noted that the point loading model would predict zero radiation in this situation.

The computed spectra illustrate the importance of including chordwise loading profiles in the radiation analysis, especially when there is negative lift acting over a part of the blade chord. At higher frequencies of the acoustic spectrum, sound pressure levels from zero-lift type distributions can in fact be higher than these from positive-lift type distributions, as is shown in Fig. 3.3.

3.2 Composite blade loading harmonics radiation

(Point span loading models)

So far in this chapter we have considered radiation from a single blade loading harmonic with fixed chordwise profile. In practice rotor blades generate a complete spectrum of blade loading harmonics. Moreover the chordwise differential-pressure profile fluctuates with azimuth. Here the composite spectrum functions will mask each other and the effect of including fluctuating chordwise loading profile on the radiation spectrum can be established computationally.

Figures 3.5, 3.6 and 3.7 show the effect of the shape of chordwise differential-pressure profile and its variation with azimuth on rotational noise for three different flight conditions. The loading data used in the computation are obtained from reference [22] (30 blade loading harmonics). The rotational noise spectra are computed by using the point span loading model, and the figures show the differences in radiation between the actual chordwise profiles and equivalent rectangular profiles.

The spectra computed by using the actual chordwise loading profiles are higher in level than those computed by using equivalent rectangular profiles, especially at the higher harmonics where the wavelength of the sound radiated is comparable to the blade chord. For the rotor system considered, the blade chord a = 18.2 in. and rotational frequency N = 3.4 Hz. Thus for accurate noise prediction, chordwise profile becomes important when

$$ka > 1 \quad \text{or} \quad \frac{2\pi N.\ mBa}{c_o} > 1 \ , \qquad (3.5)$$

giving mB > 35. The difference in levels is as high as 8-10 dB at some harmonics, and it would increase if blade loading harmonics greater than 30 were available. The steady fall-off of the spectra after about mB = 56 is purely because of lack of blade loading harmonics greater than 30 - see Lowson [10], Wright [5].

To summarize, the main conclusion here is that the variation of chordwise blade loading profiles alone accounts for a significant part of the high-frequency rotational noise from helicopter rotors, according to available data. Since the existing theories predict spectra which fall short of the measured spectra at higher harmonics, it is clear that the present modification to include loading profiles will help considerably in bridging that gap.

3.3 Radiation from fluctuating chordwise and spanwise loading profiles

In the previous two sections, we have considered radiation from point span loading models; that is, the differential-pressure profile across the blade span is replaced by point loading at effective radius point r_e. In reality, the loading on the blades is distributed across the chord as well as across the span. In addition, the spanwise loading profile does not remain constant with azimuth, especially at high forward speeds. Its effect on the noise radiation must therefore be established.

This is done computationally for only one comprehensive set of measured loading data [22] available at the present time. In order to compute the radiation (spectrum, polar elevation and polar plan) from various loading models, the data had to be processed appropriately and the details are given below.

3.3.1 Blade loading data

(S-61F Compound Helicopter, 190 Knots)

Differential-pressures in pounds/in^2 were recorded at 144 azimuth positions (every 2.5^o of azimuth) at five chordwise and five spanwise stations (as shown in Fig. 3.8), and the readings were averaged over ten consecutive rotor revolutions. The rotor geometry and operating conditions are as follows.

Blade chord $a = 18.2$ in.,

tip radius $r_T = 31$ ft.,

number of blades $B = 5$,

rotational frequency $N = 3.4$ Hz.,

radius at start of twist $r_o = 74$ in.,

blade twist rate $\gamma = 0.0134$ degrees/in.,

steady pitch angle $\beta_o = 7.366^o$,

cosine coefficient of cyclic pitch $\beta_1 = 0.776^o$,

sine coefficient of cyclic pitch $\bar{\beta}_1 = -9.99^o$.

For point loading models, the profiles at all azimuth positions were integrated using the trapezoidal rule, noting that the differential-pressure at any point on the edge of the blade is always zero. Keeping rest of the parameters constant, sound pressure levels from the following five loading

models were computed.

(1) Distributive chordwise and distributive spanwise loading model.

(2) Point chord, distributive spanwise loading model - by reducing the chordwise loading at each azimuth station to point loading.

(3) Point span, distributive chordwise loading model - by reducing the spanwise loading at each azimuth station to point loading.

(4) Point span, equivalent rectangular chordwise loading model - by reducing the spanwise loading at each azimuth station to point loading and replacing the resultant chordwise profile by its equivalent rectangular distribution.

(5) Point chord and point span loading model - by reducing the chordwise as well as spanwise loading at each azimuth station to point loading.

3.3.2 Computed output

The computed results are presented in Figs. 3.9 to 3.20. Since the differential-pressure data is available at 144 azimuth positions, Fourier analysis of the loading data enables us to determine approximately 70 blade loading harmonics accurately. It should therefore be noted that computed acoustic spectra are valid for mB numbers upto approximately 60 - 65 only.

3.3.2.1 mB spectra (Figs. 3.9 and 3.10)

Sound pressure level spectra at a point in the far field are shown in figures 3.9 (for point span loading models) and 3.10 (for distributive span loading models). Unfortunately, no sound pressure level measurements for this flight condition are available in order to establish which of the five models produces the best correlation with the measured spectrum. Nevertheless, we can at least describe the differences between radiation from different loading models. It should also be realised that since the levels

of the spectra from the point span loading models could be varied by varying the effective radius r_e (taken to be 0.8 of the tip radius r_T for computation purposes), they cannot be compared directly with the spectrum levels from the distributive span loading models.

Let us consider the spectra from the point span loading models (Fig. 3.9) first. The point chord loading has a flat spectrum function $\chi = 1$ whereas the equivalent rectangular loading has a spectrum function which varies as $\frac{\sin (maB/2r_e)}{(maB/2r_e)}$. Since the loading profile (but not the level) remains constant with azimuth, the mB spectra differ by this spectrum function only. The result is that the mB spectrum from the point loading model is higher in level than the spectrum from equivalent rectangular loading model. The difference increases as mB number increases. For the actual chordwise profile model, since the profile is changing with azimuth, a fixed spectrum function cannot be assigned. But on average, the spectrum function in this case takes a value somewhere in between the spectrum function levels for point loading and rectangular loading. The resulting mB spectrum then follows as shown in Fig. 3.9.

In the case of distributive span loading models (Fig. 3.10), there is no appreciable difference in spectra between point chord loading and distributive chord loading, except at the higher harmonics where the levels from point chord loading are higher than those from distributive chord loading. This is again due to the fact that at higher harmonics, the envelope of the spectrum functions from point chord loading (distributed across the span) is higher than the envelope of spectrum functions from distributive chord loading (also distributed across the span).

For the sake of comparison, if the spectra from all five loading models are superimposed, it is interesting to note that the general shape of the spectrum from the most complicated model (distributed chord, distributed span) is resembled most by the spectrum from the least complicated model (point chord, point span); the biggest difference occurs at the first harmonic, where the point span loading model underestimates the radiation by as much as 15 dB. This difference is partly a result of the position of effective radius point. Since the first rotational noise harmonic is dominated by steady loading (low solidity rotors), the level is very sensitive to the Mach number M_e of the effective radius point. Simple calculations show that if r_e is taken to be say 0.9 of the tip radius instead of 0.8 r_T as in the present case, the first harmonic will increase in level by 6 dB.

3.3.2.2 Polar plots (Figs. 3.11 to 3.20)

Because of the limit on computation time and the cost involved, the aim was to obtain a maximum amount of information from a minimum amount of computation. Polar elevations (σ) and polar plans (θ) for the five loading models were investigated at 1° intervals over a limited range of angles: σ from -22° to -38° ($\theta = 0^\circ$), where the far field radiation is usually maximum; and θ from -8° to $+8^\circ$ ($\sigma = -30^\circ$).

The computed polar plots do not show any sign of sharp fluctuations with angle, as observed in measured directivities, even though the computed directivity plots use actual measured blade loading harmonic amplitudes and phases. This suggests that the sharp fluctuations with angle observed in directivity measurements are time fluctuations and not angular fluctuations. The existence of these time fluctuations was demonstrated experimentally by Stainer [32].

Polar elevation plots (Figs. 3.11 to 3.15)

As described before, the radiation from the three point span loading models differ from one another by their spectrum functions only. These spectrum functions are independent of the observer elevation angle σ and so for any particular harmonic m, the polar elevations shown in Figs. 3.11, 3.12 and 3.13 are similar in shape. The only difference present is in the levels of various harmonics; the first rotational noise harmonic remains nearly unaffected, and the levels of higher harmonics start to decrease as the extent of source distribution becomes comparable with the radiated sound wavelength (or in other words, as the chordwise loading becomes more distributive).

On the other hand, for distributive span loading models, the envelope of the spectrum functions for fluctuating spanwise loading profile is a function of σ (as shown by Wright [21] for the special case when the span loading profile remains constant with azimuth). Thus, depending on the spanwise loading profile and its variation with azimuth, the polar elevation plots from the distributive span loading model (Fig. 3.14) could differ considerably from those for the point span loading model (Fig. 3.11). This is true in the present case, as shown in Figs. 3.11 and 3.14. The elevation plots for the two distributive span loading models are roughly similar in shape. The main difference is in the levels of higher harmonics, where distributive chord loading suppresses these higher harmonics.

Once again, it is rather unfortunate that no measured directivity results for this flight condition are available, in order to establish which one of the five loading models fits best with measurements. The only conclusion that can be derived at this stage is that different loading models give different results, and that the spanwise loading profile together with its variation around the azimuth produces the biggest effect on the radiated noise.

Polar plan plots (Figs. 3.16 to 3.20.)

The polar plan plots in the far field are basically circular around the rotor axis for the three point span loading models, where the spectrum function (for constant profile) or the envelope of spectrum functions (for varying profile) is not sensitive to the observer azimuth angle θ. The levels of various harmonics differ in a manner similar to that described for polar elevation plots - distributed chordwise loading suppresses the levels of higher harmonics.

The effect of distributive spanwise loading is similar to that observed for polar elevations; the variation of sound pressure level with azimuth for any harmonic is sensitive to spanwise profile and its fluctuations. The rest of the comments made for polar elevation plots apply here.

3.4 Conclusions

(1) The limited amount of computation has shown that different loading models give different radiation results. The spanwise loading profile and its variation with azimuth produces the biggest effect over the point loading assumption.

(2) The above statement is based on only one set of loading data (S-61F, 190 knots) used in the present investigation. It needs to be verified for other cases when measured blade loading data become available. In addition, any future blade air-loads measurement programme must include simultaneous noise measurements, so that the relative usefulness of various theoretical loading models for noise prediction can be established.

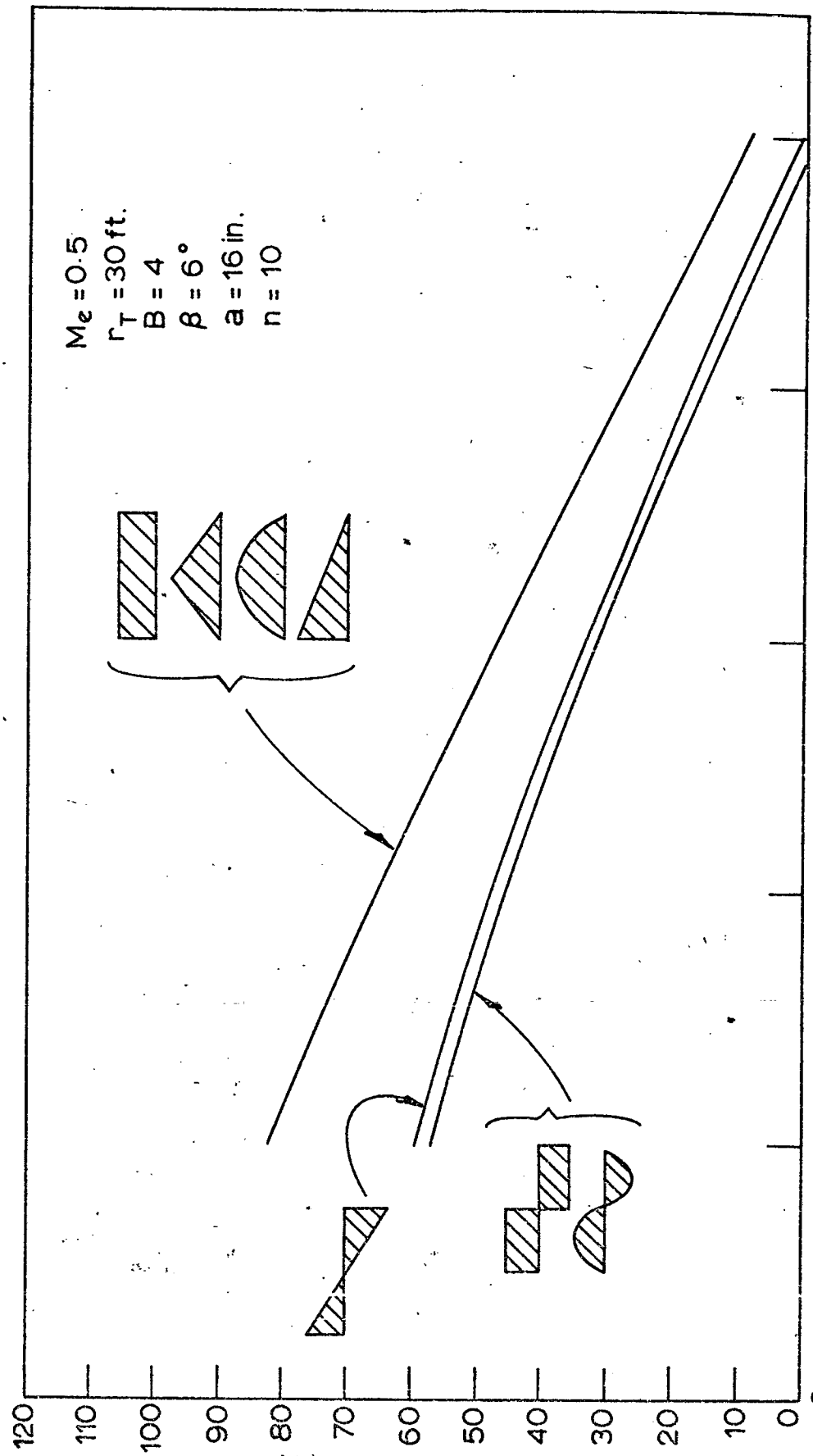

Fig. 3.1. g=0. Effect of shape of chordwise loading profile. R = 300 ft., $\sigma = -30°$.

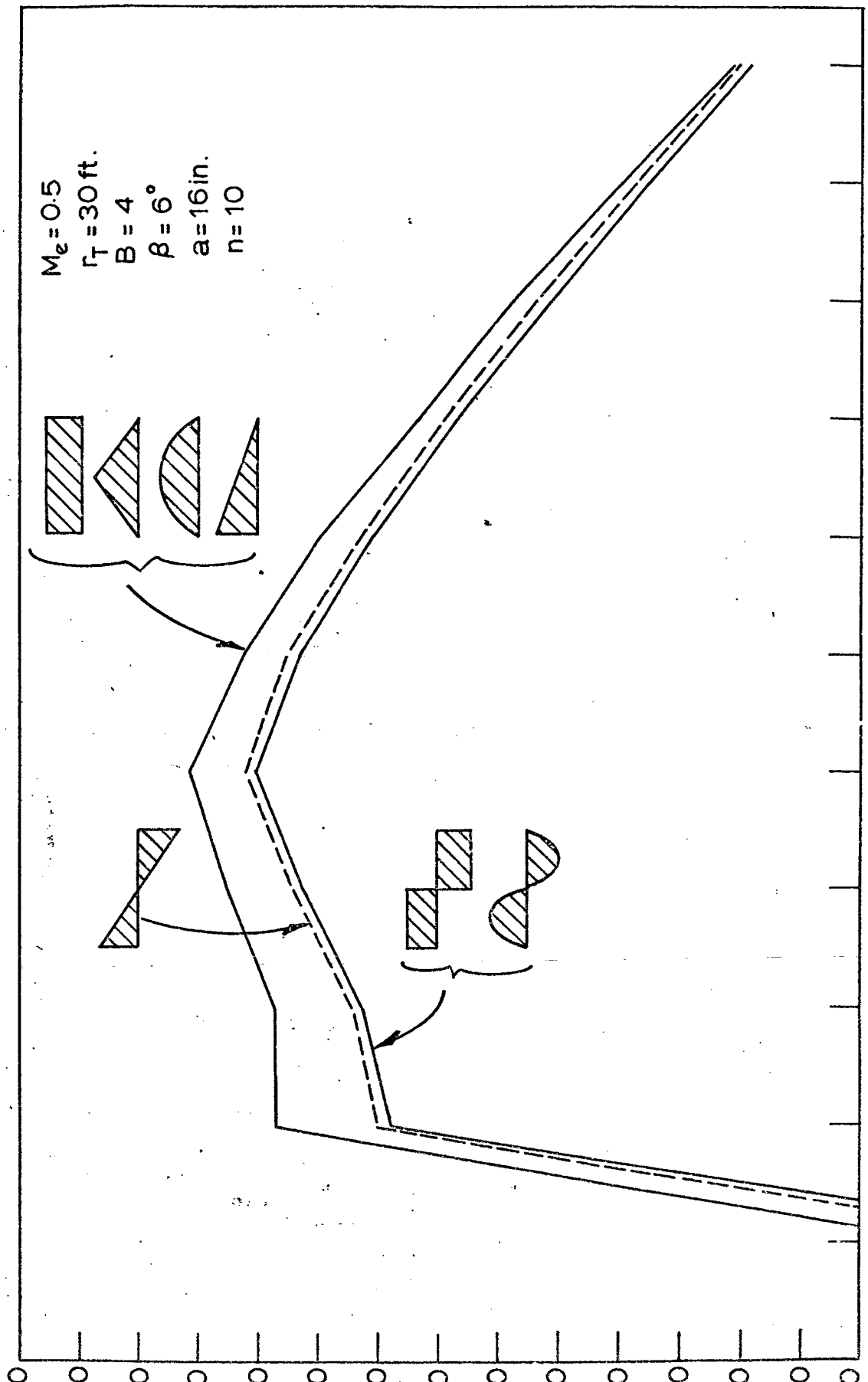

Fig. 3.2. g=12. Effect of shape of chordwise loading profile. R=300 ft., σ=-30°.

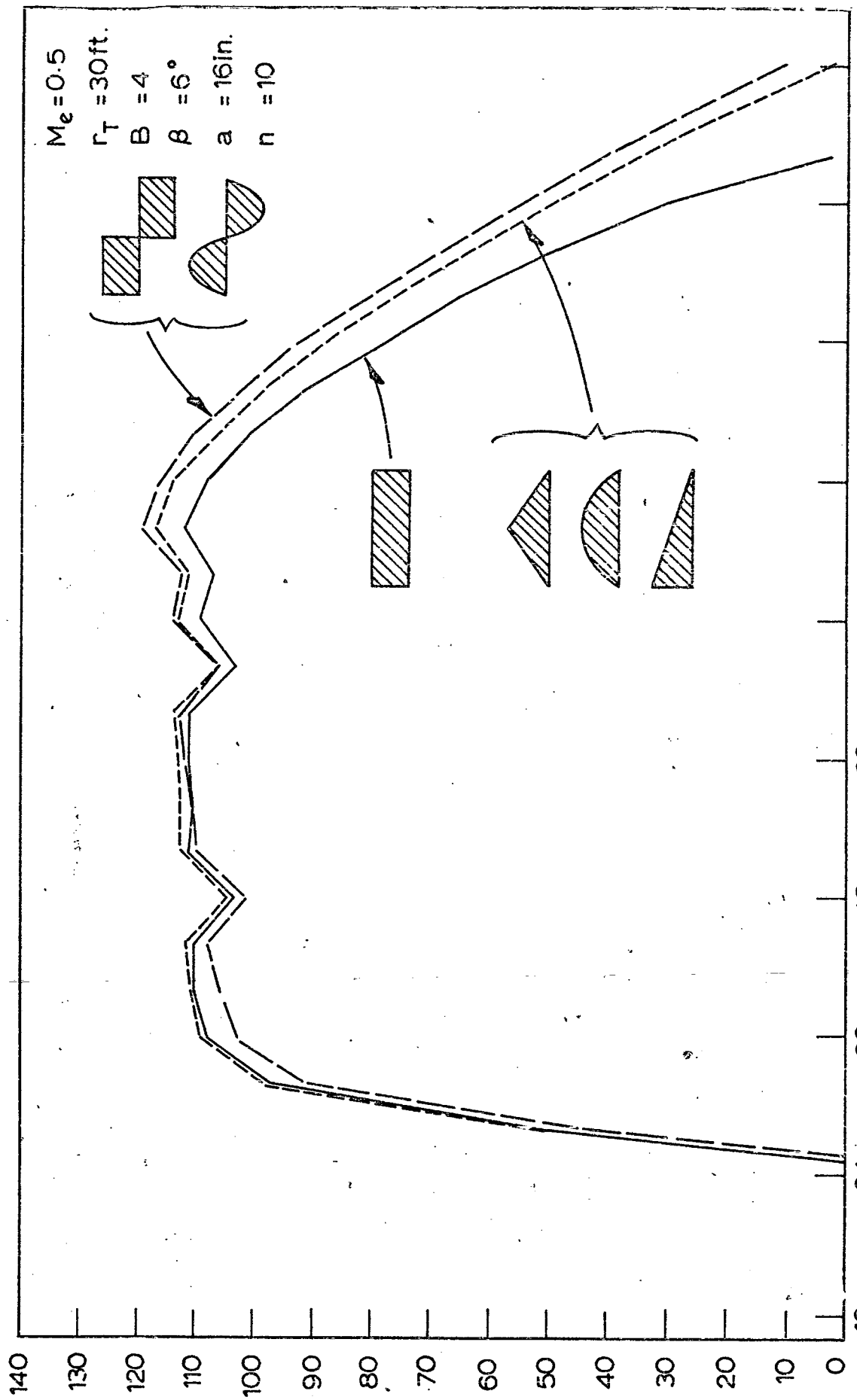

Fig. 3.3 g=48 Effect of shape of chordwise loading profile. R=300ft., σ=-30°.

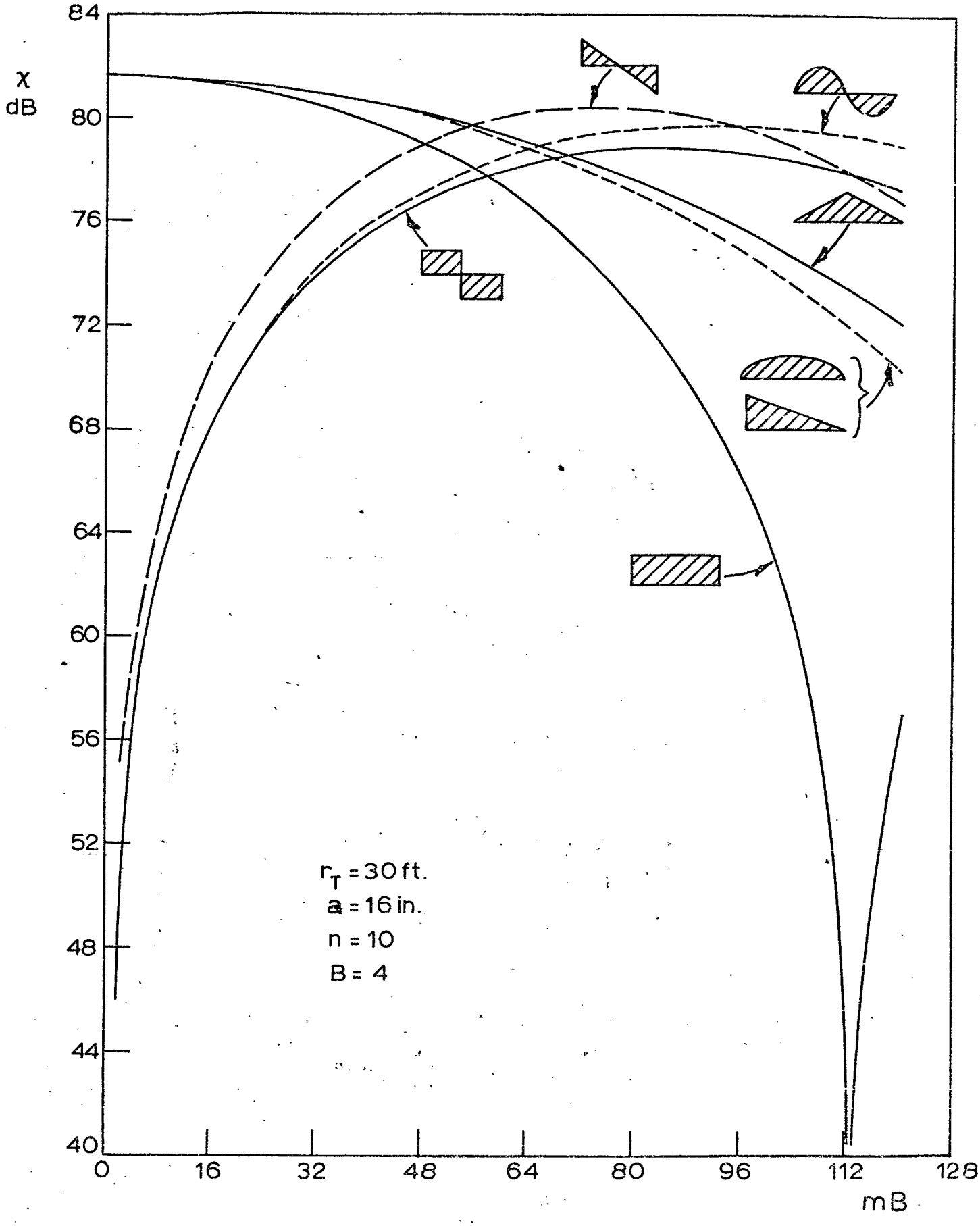

Fig. 3.4. Spectrum function for various chordwise loading profiles. Gross loading on rotor equals 12,000 pounds.

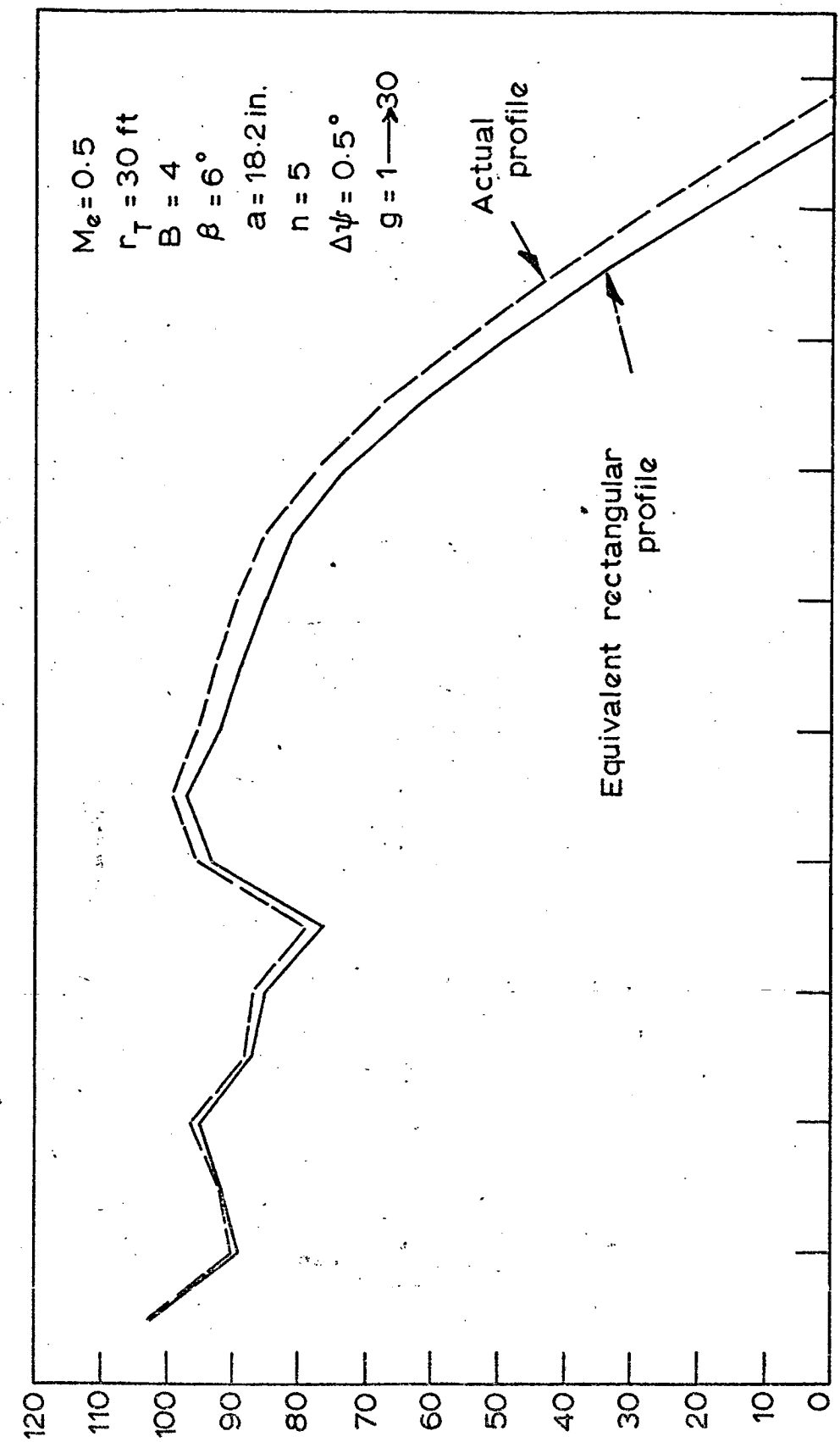

Fig. 3.5. NH-3A. Hover in ground effect. 0.95 span station. $R = 300$ ft., $\sigma = -30°$, $\theta = 0°$.

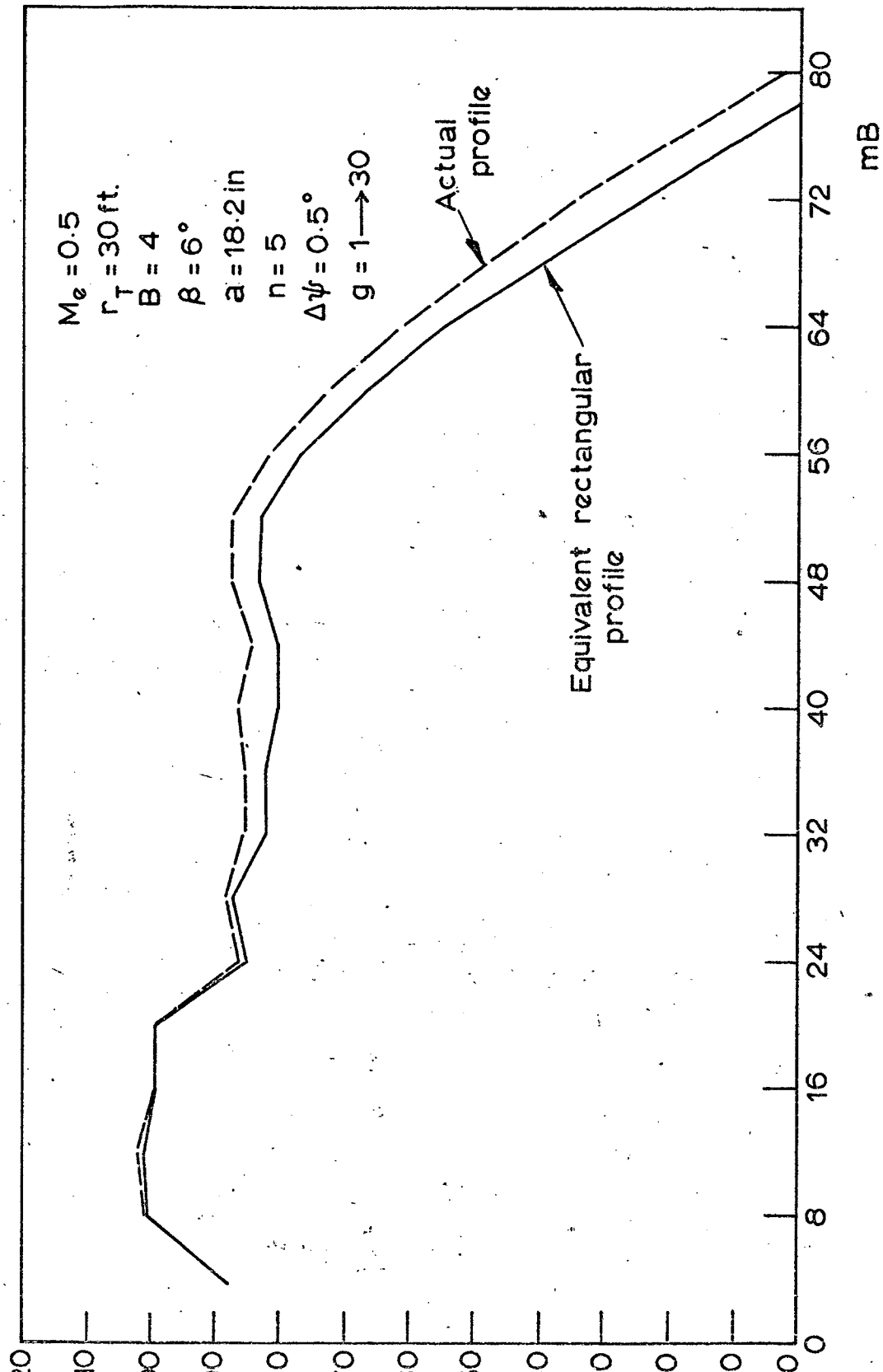

Fig. 3.6. NH-3A. 190 Knots, low wing lift. 0.85 span station. R = 300 ft., $\sigma = -30°$; $\theta = 0°$.

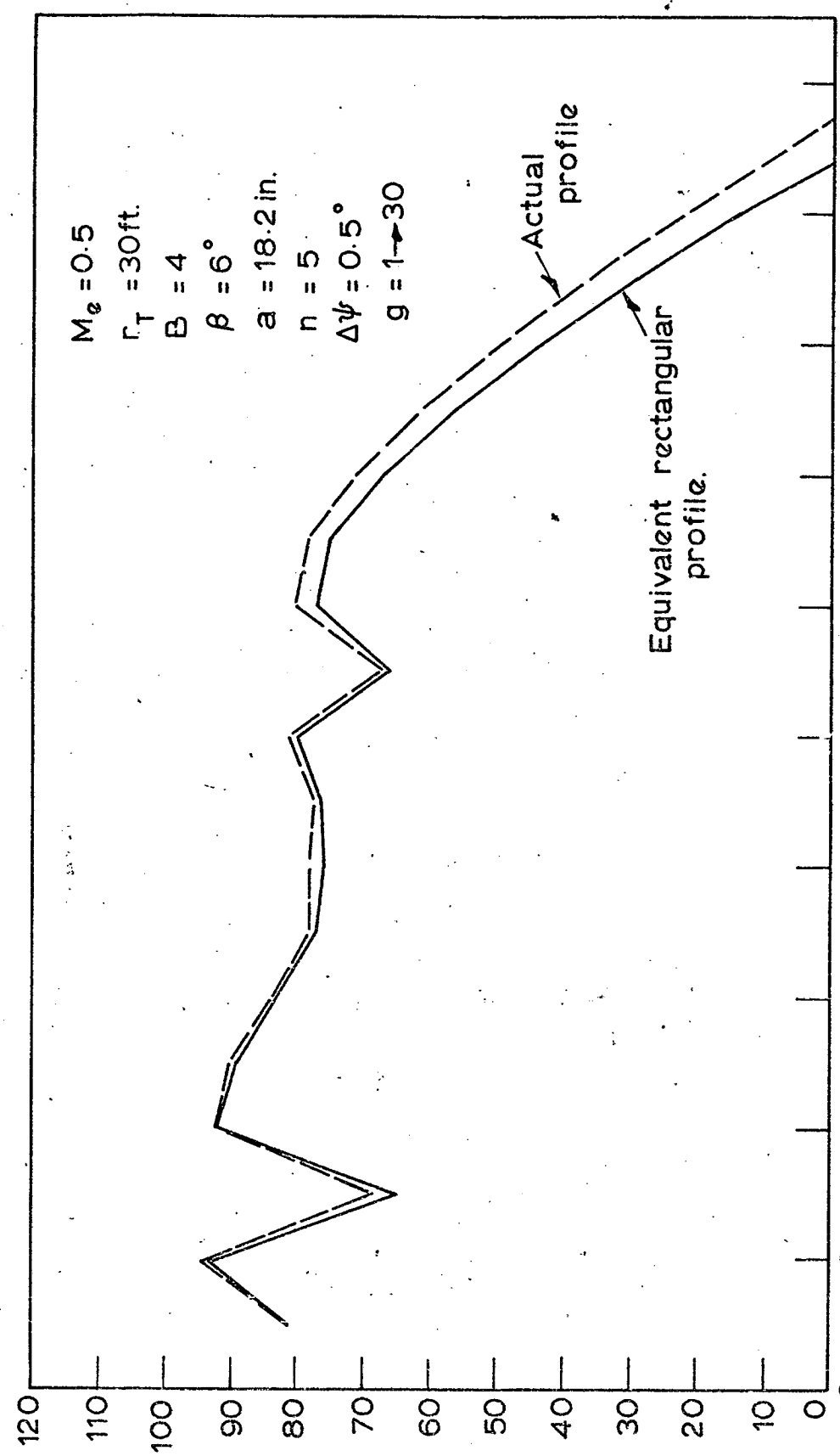

Fig. 3.7. NH-3A. 165 Knots, high wing lift. 0.85 span station. R = 300 ft., σ = -30°, θ = 0°.

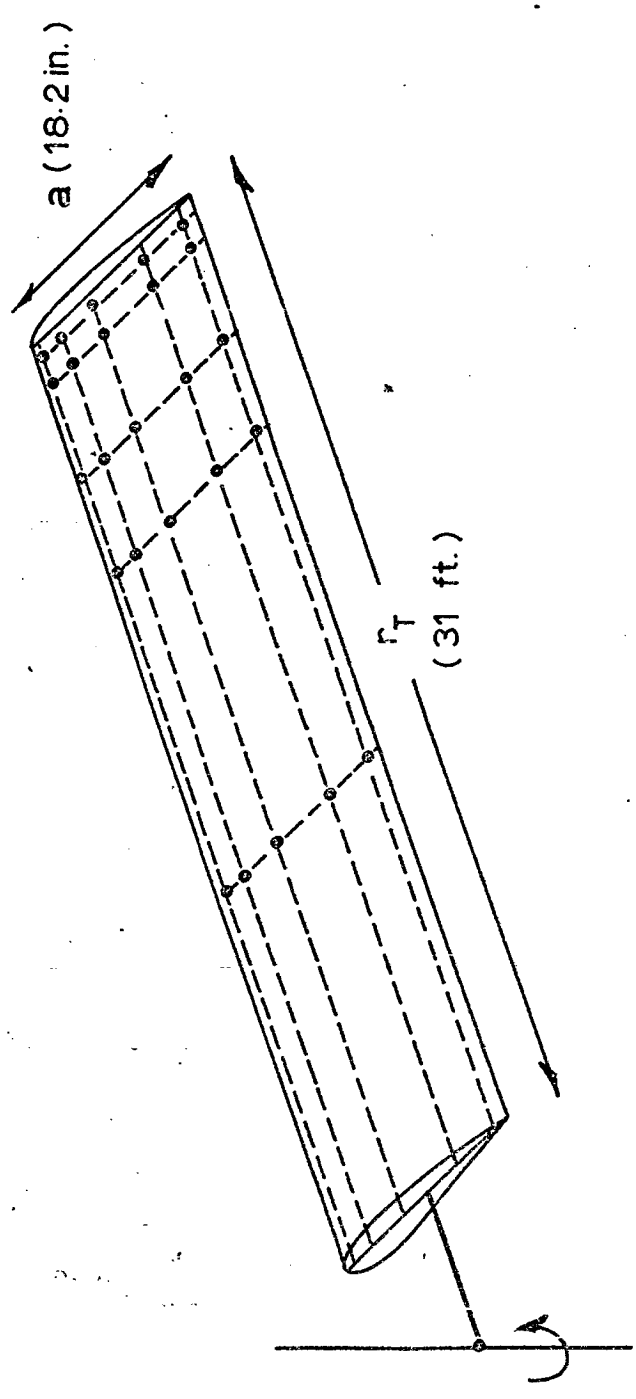

Span stations at $0.40r_T$, $0.75r_T$, $0.85r_T$, $0.95r_T$, $0.98r_T$.

Chord stations at 0.42a, 0.158a, 0.30a, 0.60a, 0.91a.

Fig. 3.8. Blade stations for differential-pressure data.

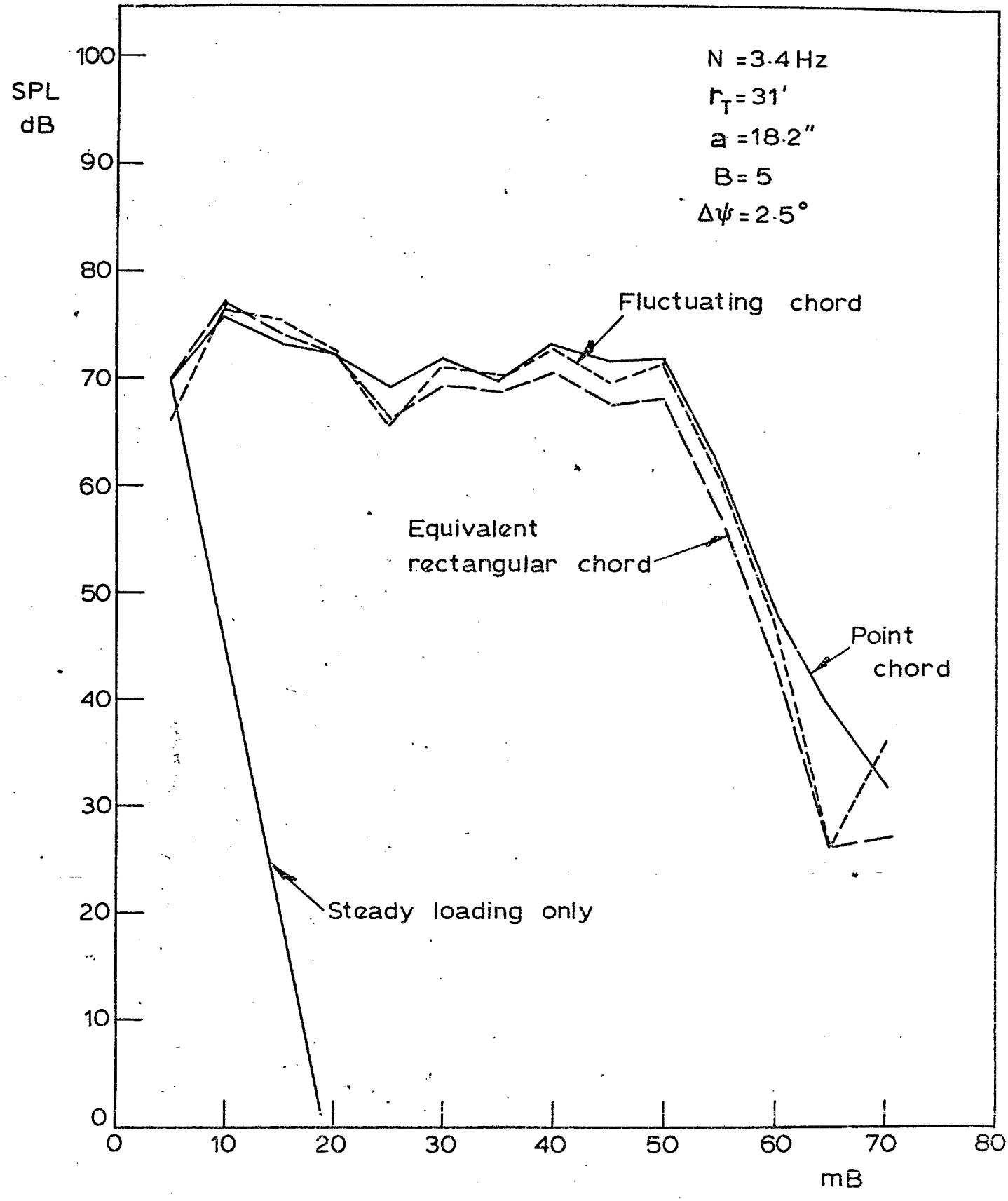

Fig. 3.9. mB spectra: point span loading ($0.8 r_T$) models. R = 300 ft., $\sigma = -30°$, $\theta = 0°$.

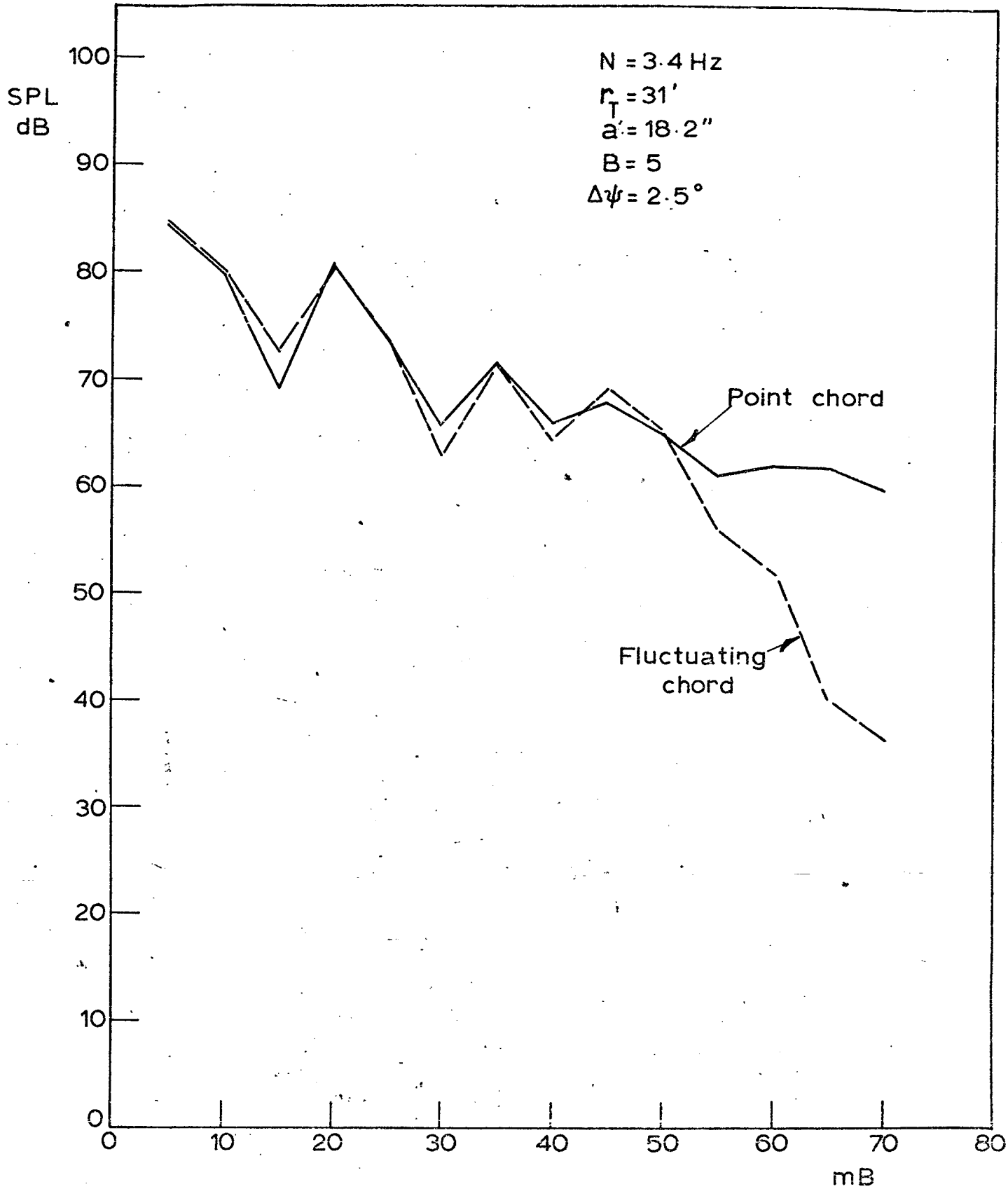

Fig. 3.10. mB spectra: distributive span loading models. R = 300 ft., σ = -30°, θ = 0°.

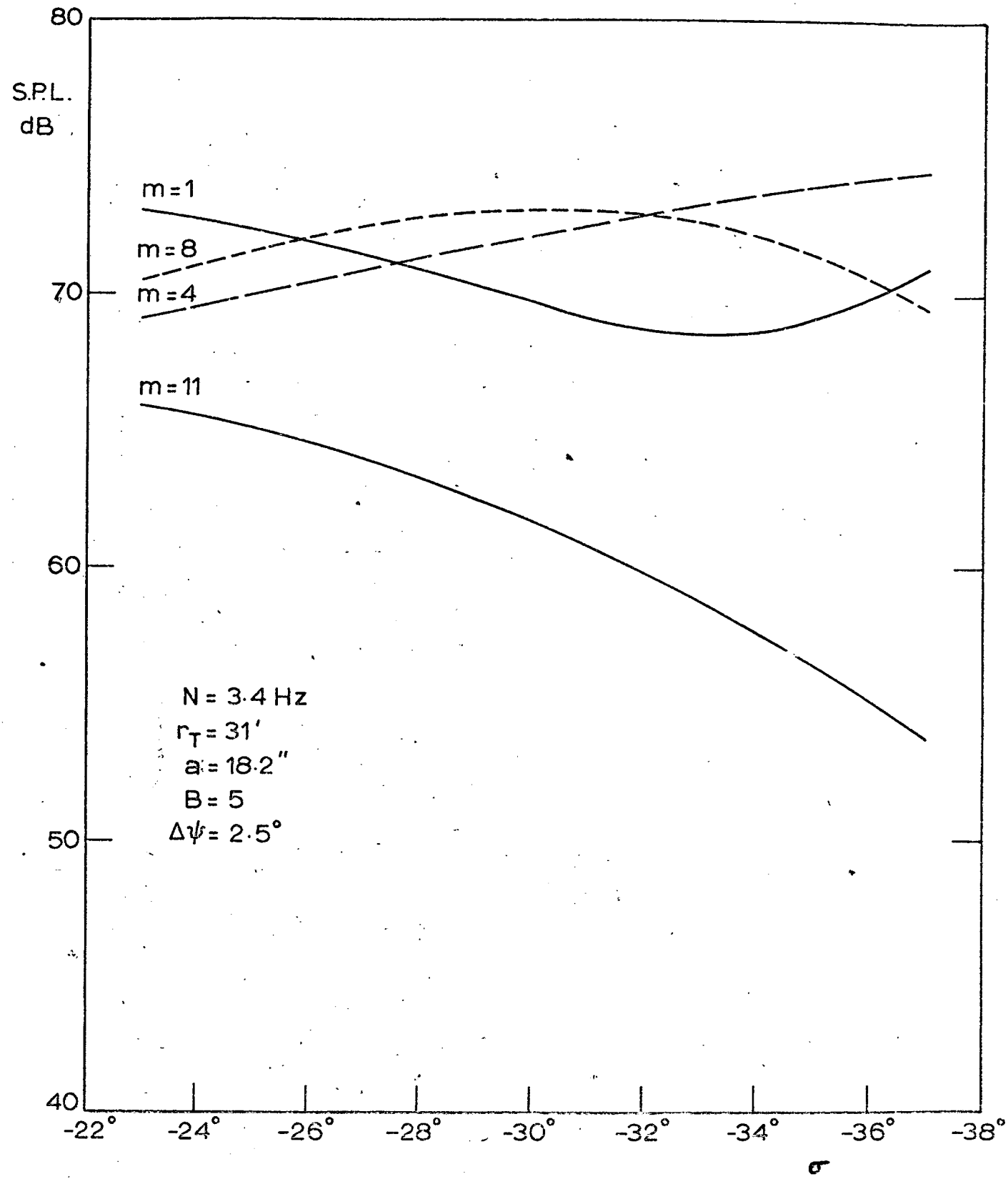

Fig. 3.11. Polar elevation: point chord, point span loading model. R = 300 ft., $\theta = 0°$.

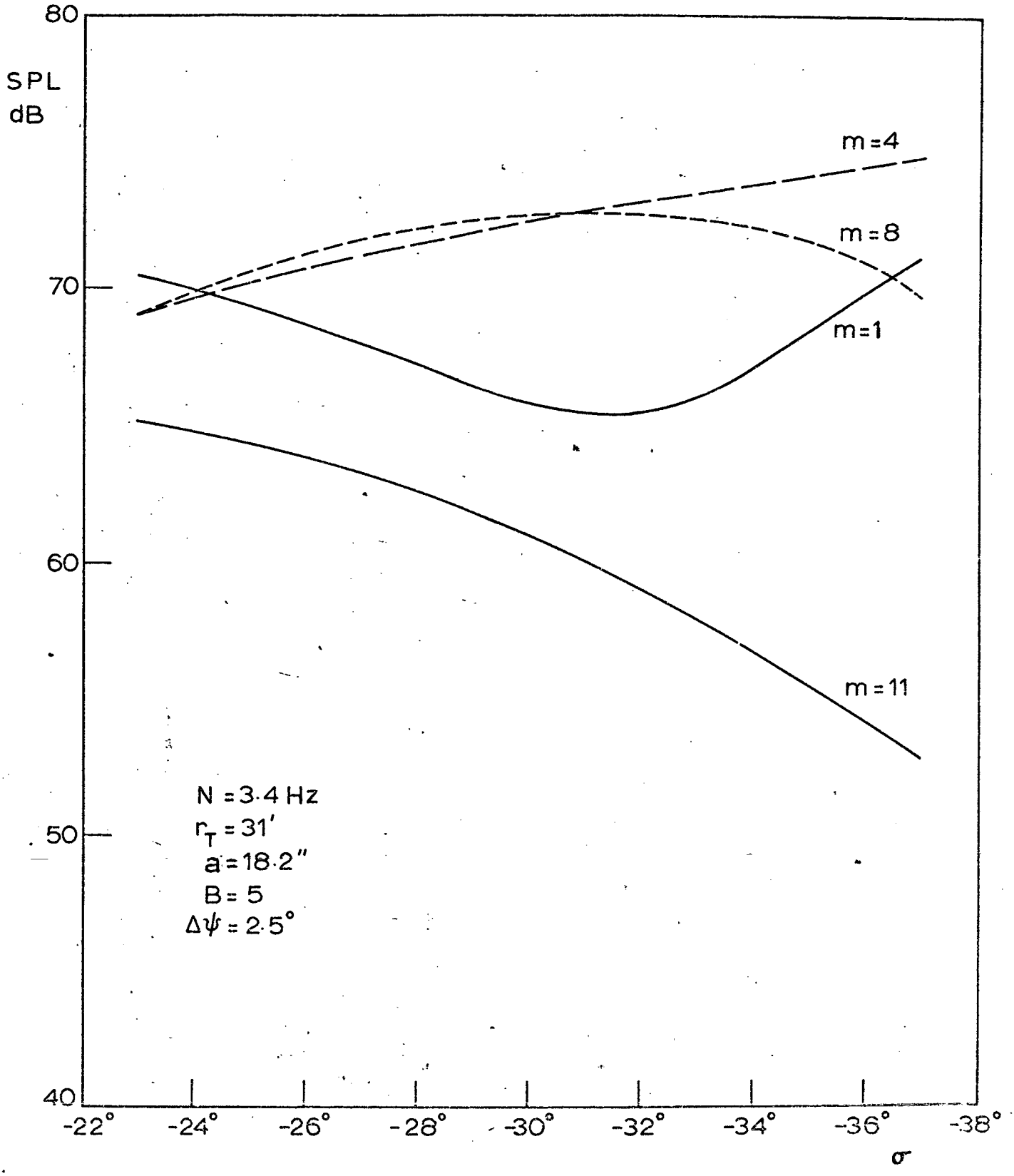

Fig. 3.12. Polar elevation: point span, distributive chord loading model. R=300 ft., θ=0°.

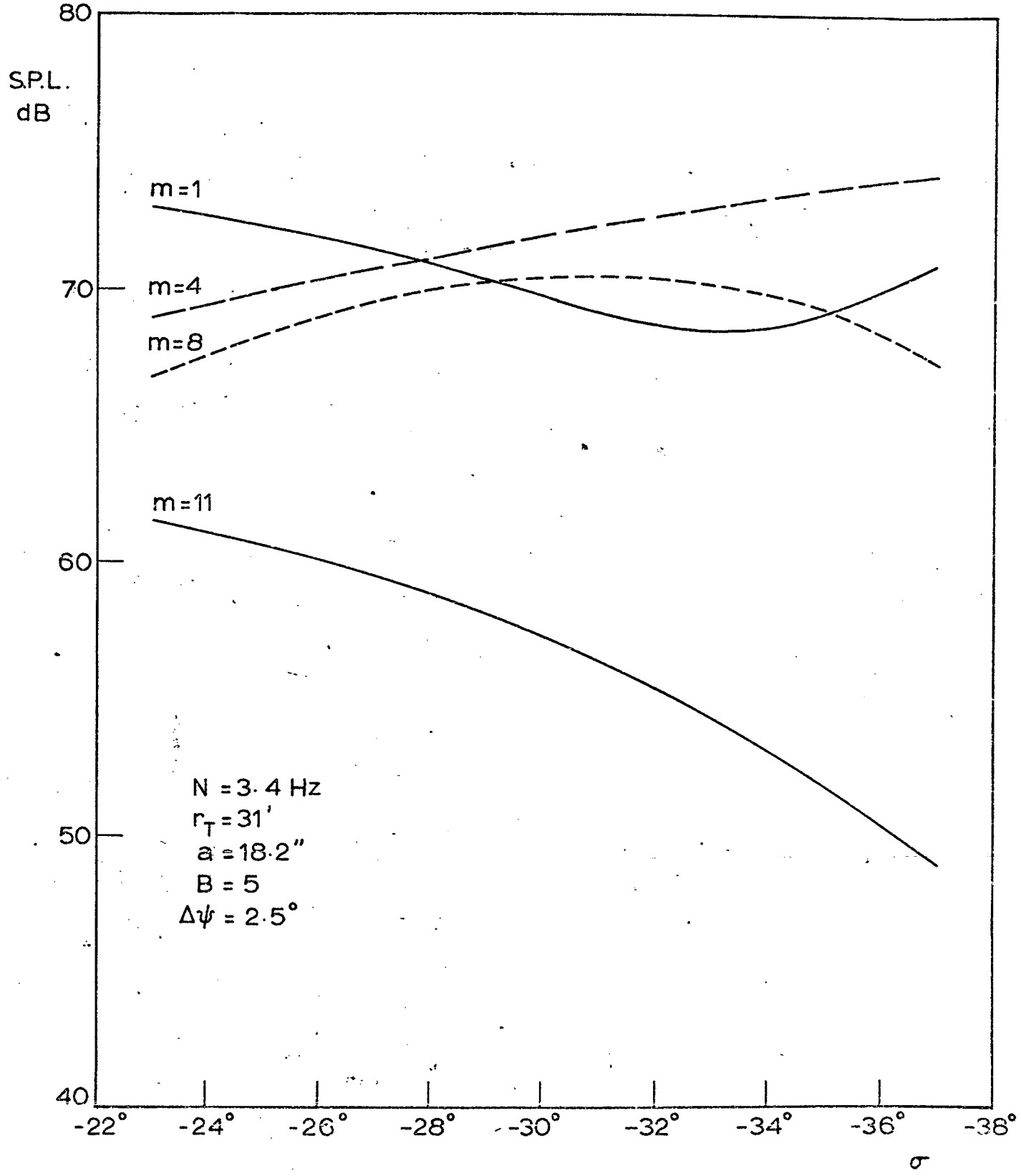

Fig. 3.13. Polar elevation: point span, equivalent rectangular chord loading model. R = 300 ft., $\theta = 0°$.

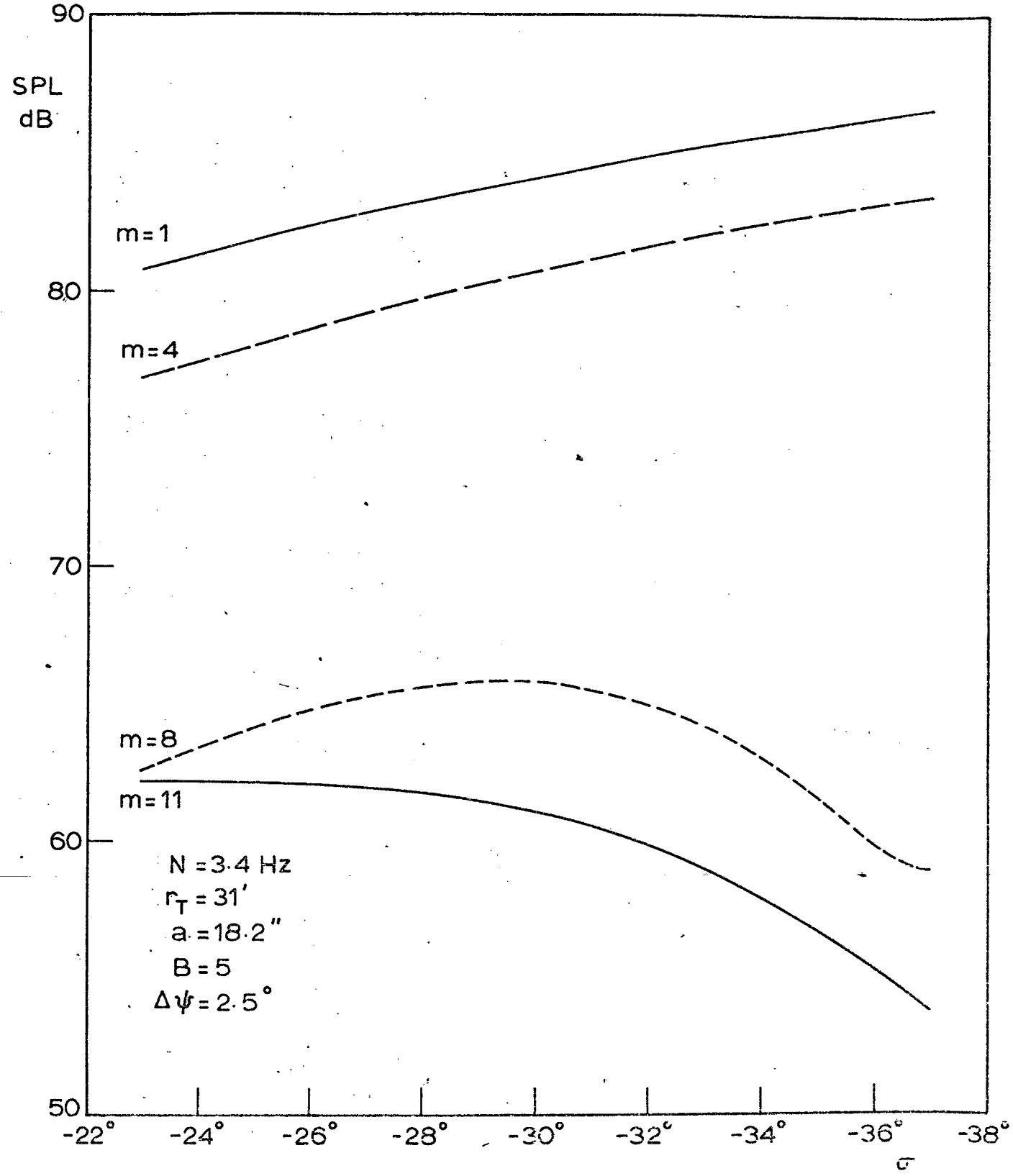

Fig. 3.14. Polar elevation: point chord, distributive span loading model. R = 300 ft., $\theta = 0°$.

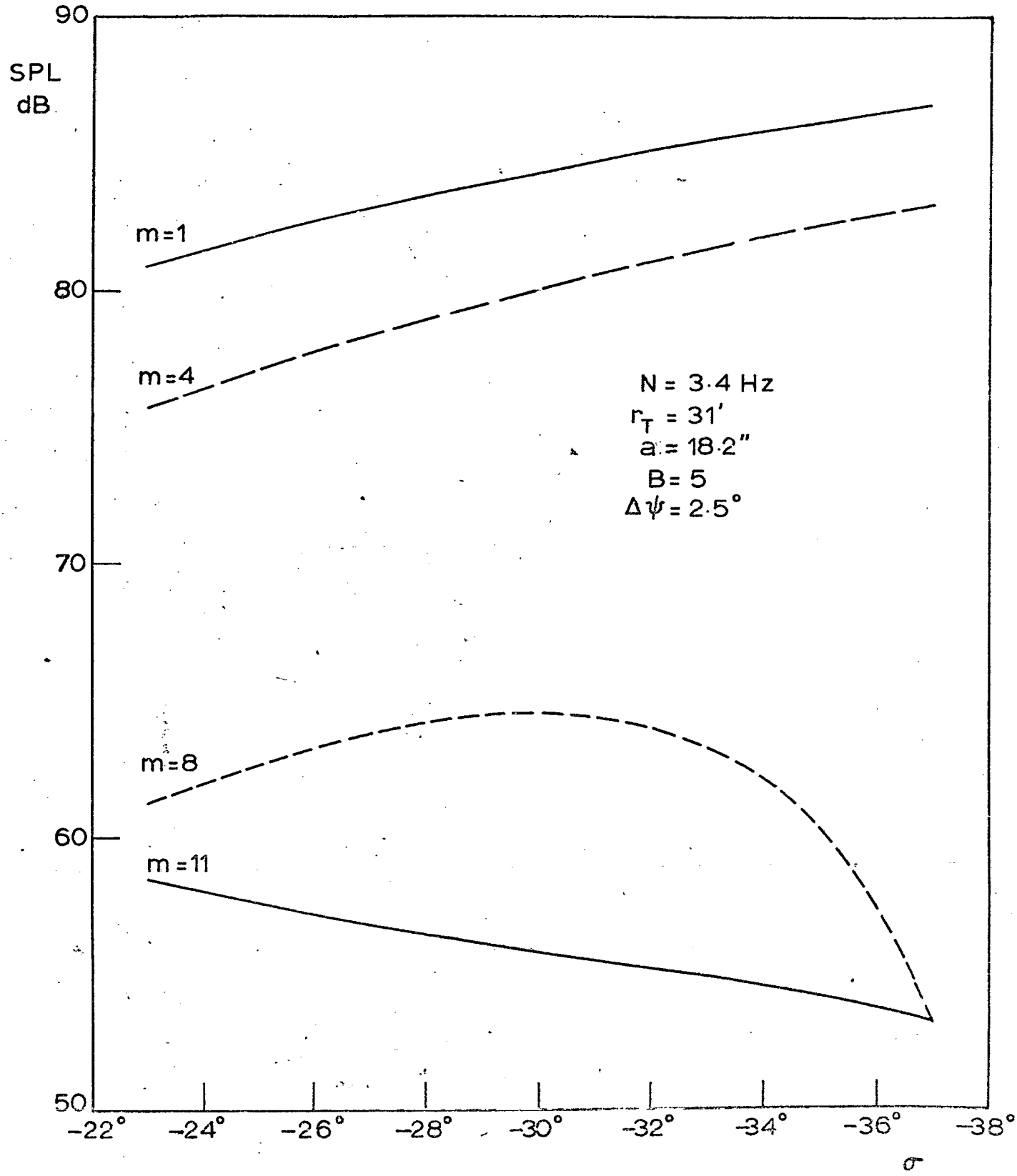

Fig. 3.15. Polar elevation : distributive chord, distributive span loading model. R = 300 ft., $\theta = 0°$.

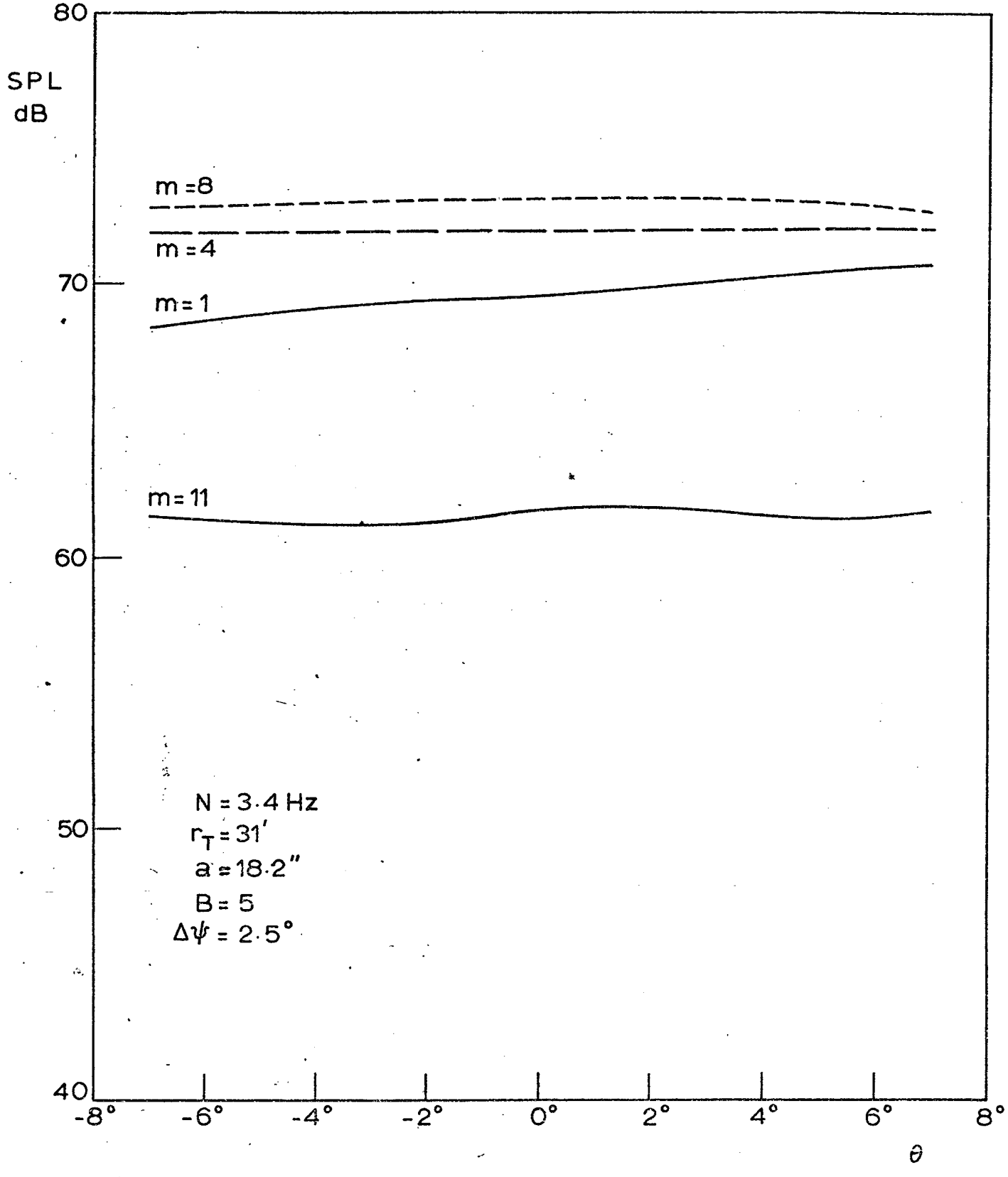

Fig. 3.16. Polar plan: point chord, point span loading model. R = 300 ft., σ = -30°.

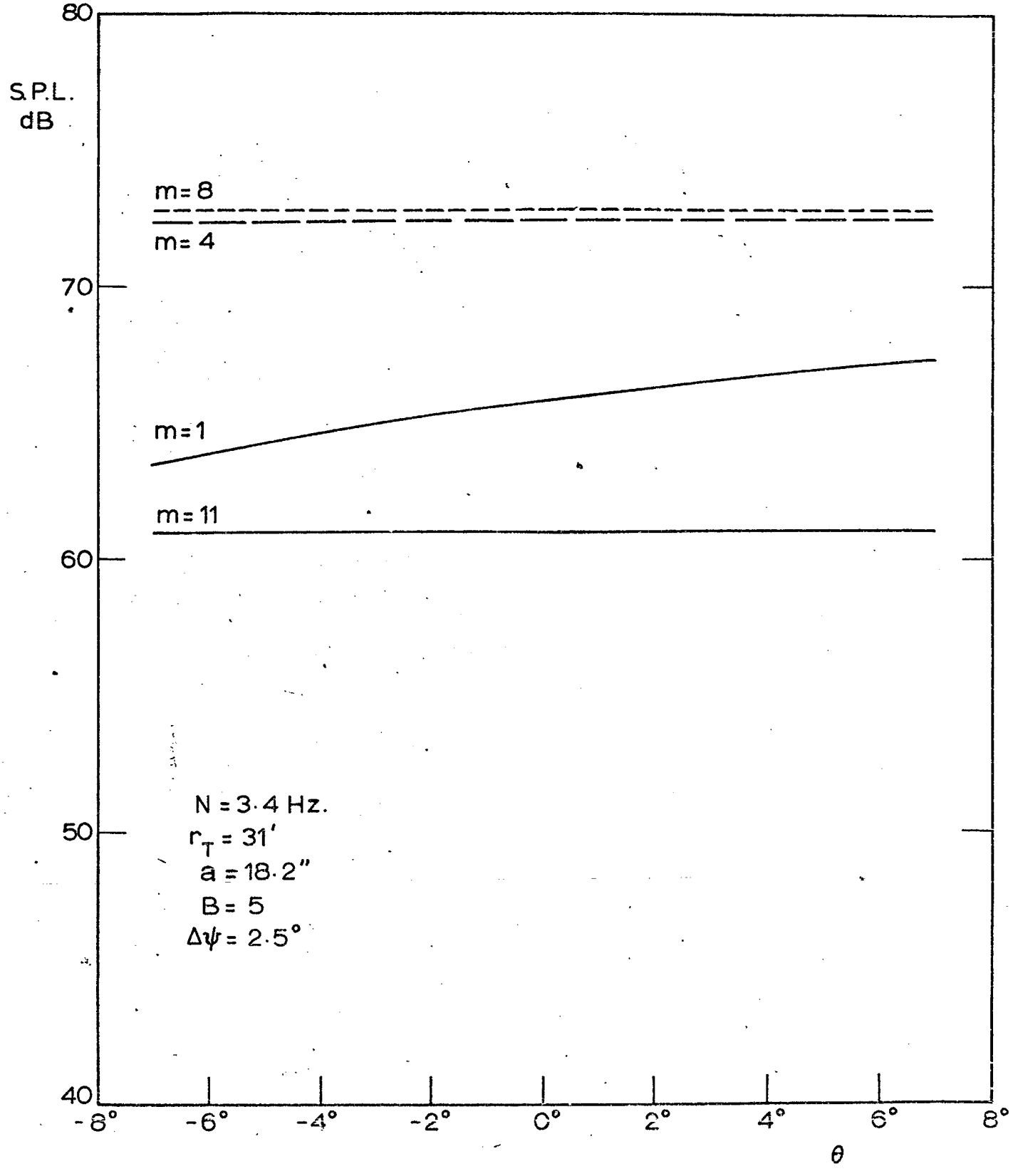

Fig. 3.17. Polar plan: point span, distributive chord loading model. R = 300 ft., σ=-30°.

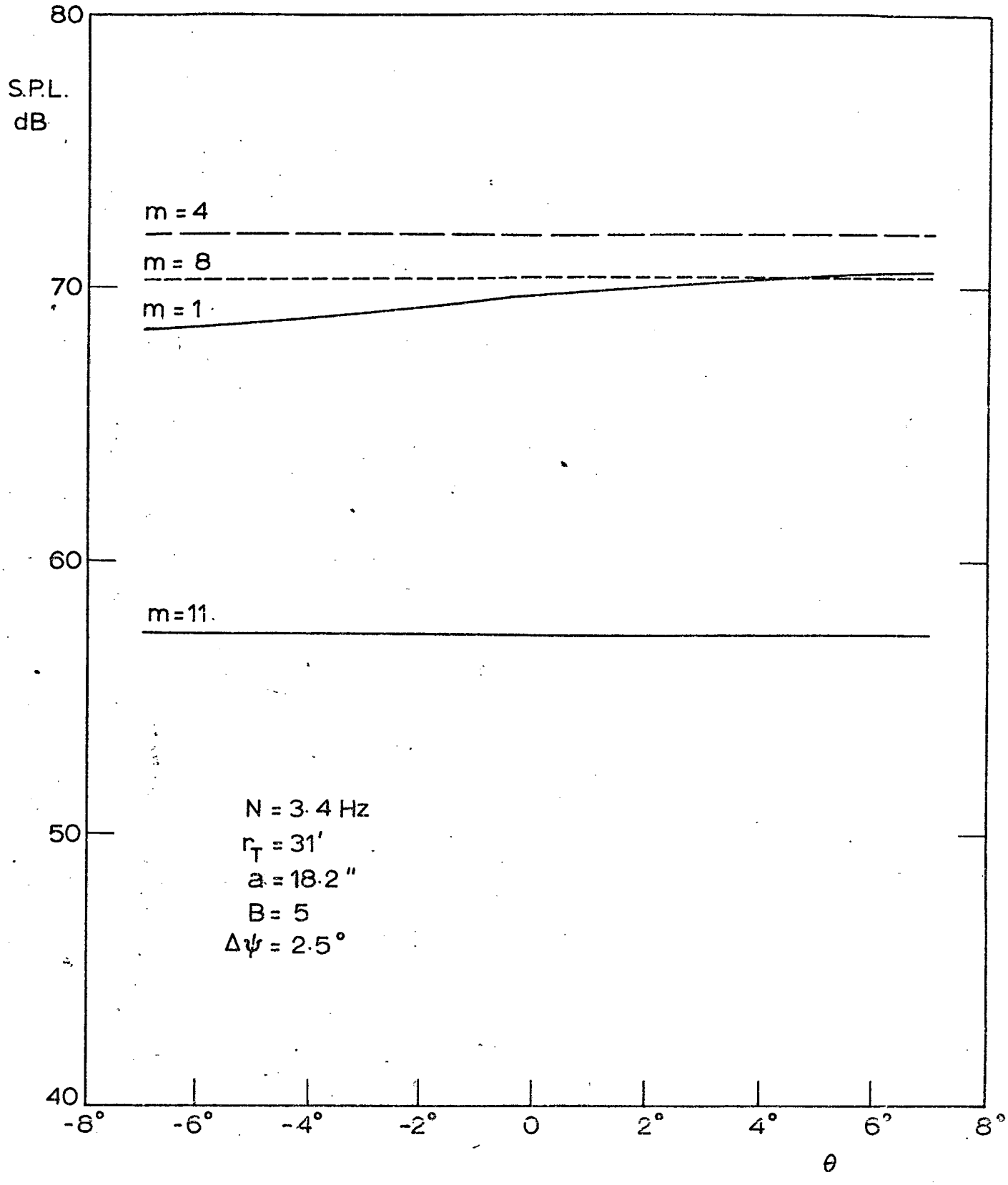

Fig. 3.18. Polar plan: point span, equivalent rectangular chord loading model. R = 300 ft., σ = - 30°.

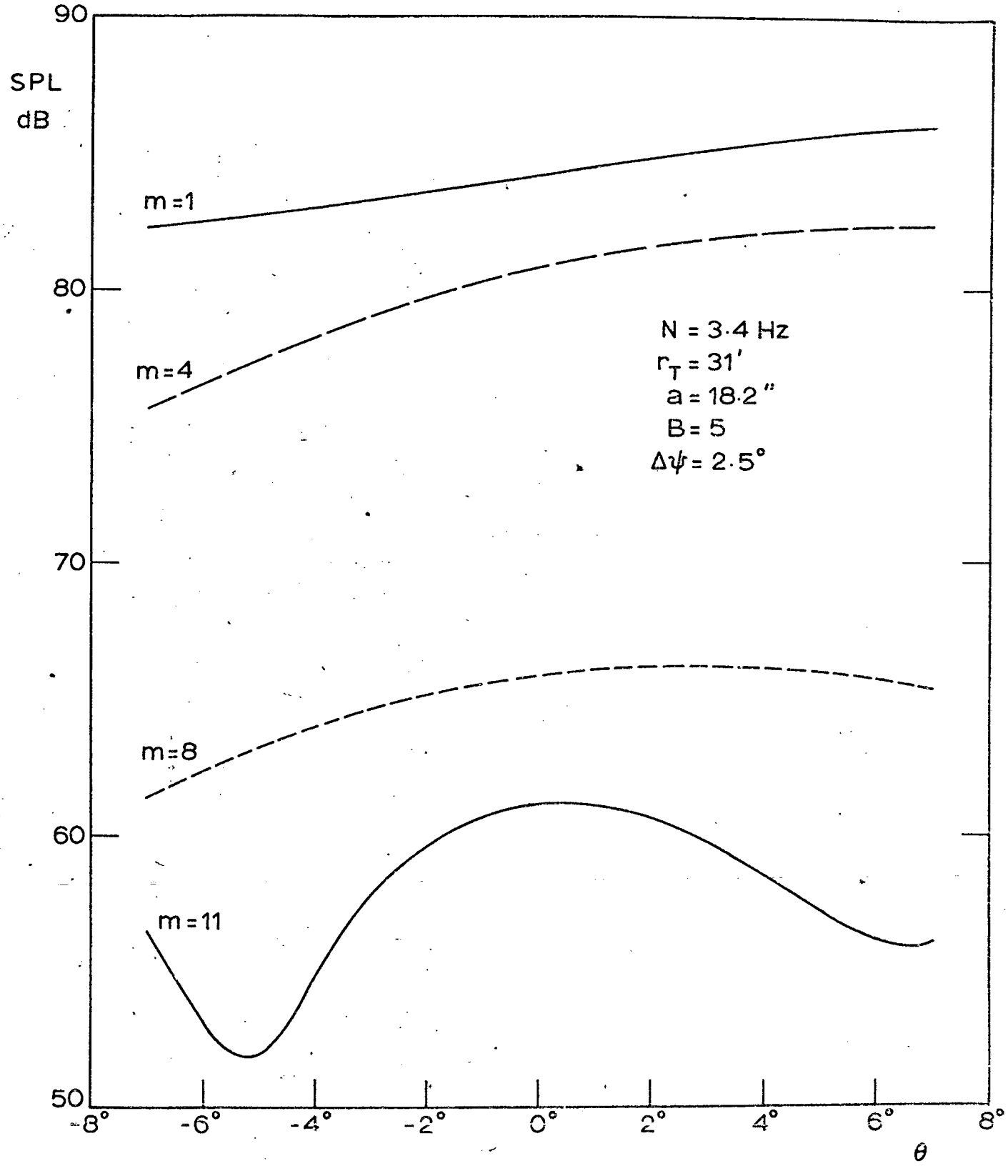

Fig. 3.19. Polar plan: point chord, distributive span loading model. R = 300 ft., σ = -30°.

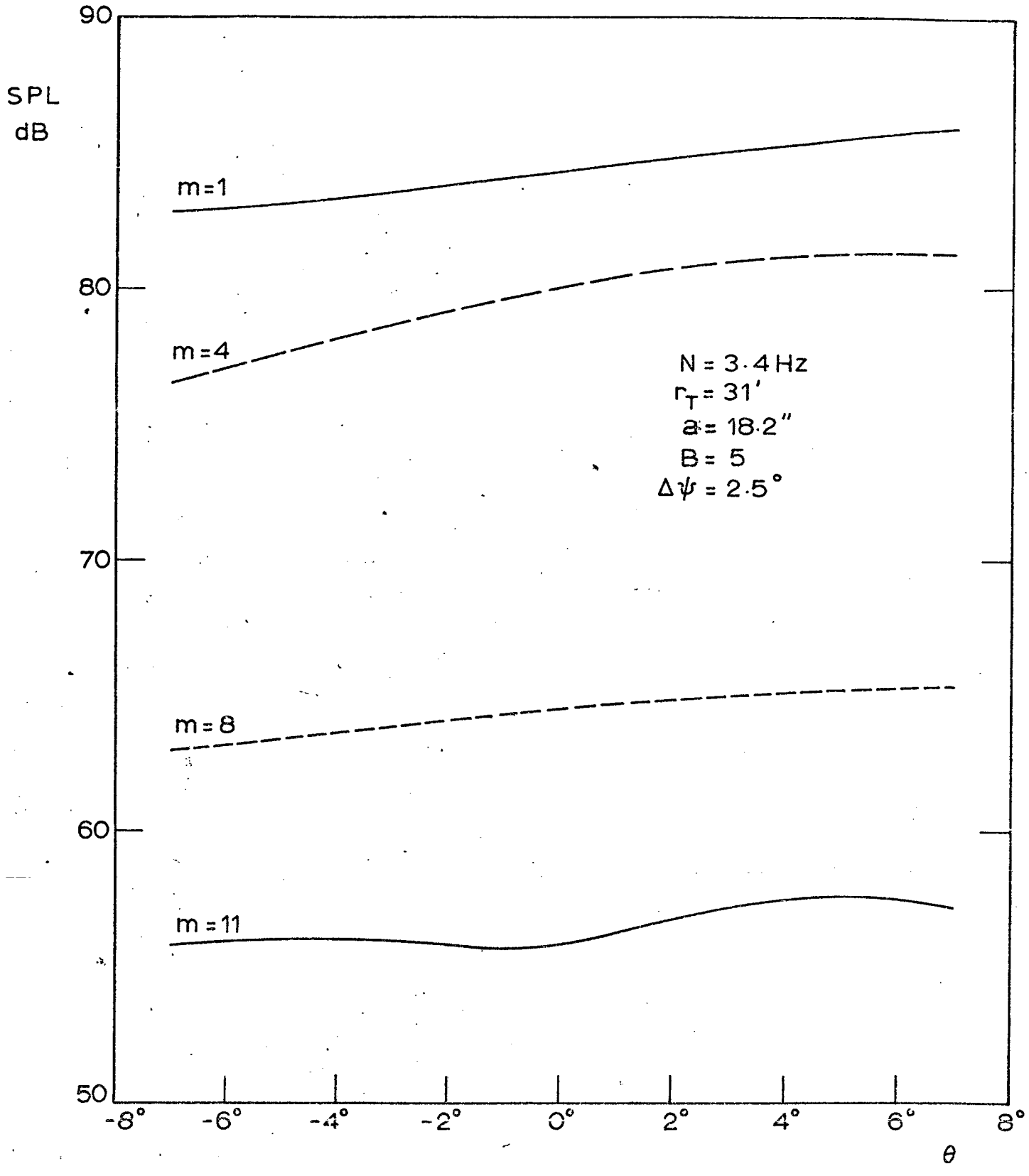

Fig. 3.20. Polar plan : distributive chord, distributive span loading model. R = 300 ft., σ = -30°.

CHAPTER 4

ROTOR AERODYNAMICS STUDY

Once the theory and computer programs for rotational noise are available, it is tempting to compute a large number of hypothetical cases by feeding hypothetical loading data and profiles and computing the radiation. This would be interesting as an academic exercise, but because of the computing time and the cost involved, the amount of computation must be limited. Any future cases to be computed must therefore be chosen carefully so that the loadings and profiles assumed are fairly representative of those that occur in practice on helicopter rotors.

Bearing this in mind, the obvious thing to do at this stage is to study the available measured aerodynamic loading data and to look for any trends that exist. The main drawback here is that there is very little measured blade loading data available to date; this is because of the fact that measurement of rotor blade airloads is a very complicated and expensive instrumentation problem where the readings depend critically on the accuracy of the measuring instruments. Nevertheless, an attempt was made to study in detail the data reported by Scheiman [23] for an S-58 helicopter and by Schlegel and Bausch [22] for an S-61F compound helicopter. The findings are discussed in the following sections.

4.1 Effect of flight condition on asymmetry of blade loading

The asymmetry of integrated loading across the chord near the blade tip (0.9 r_T, where the loading is usually maximum) is studied as a function of flight condition. From Scheiman's [23] measured aerodynamic loading data, ten flight conditions were chosen at random and the loading variations with azimuth for these flight conditions are shown in Fig. 4.1, where the loading $L'(r,\psi)$ is recorded at every 15^o of azimuth, averaged over three

consecutive rotor revolutions. An attempt was made to explain to some extent the asymmetry at a particular flight condition by considering factors like blade-tip vortex intersection, blade stall, effect of fuselage, vortex pattern shed by the blades, and so on, that exist at this flight condition. The study reveals that each flight regime has a characteristic asymmetry of blade loading around the azimuth.

An experimental program, carried out by Lehman [24], to study the tip vortex patterns from a model helicopter rotor in a water tunnel by injecting air bubbles at the blade tips was found to be very interesting here. The model used was a scaled version of the Bell UH-1D rotor. Discrete tip vortex patterns were observed for forward flight advance ratio (μ = forward speed/tip speed) regimes in the general ranges of $\mu = 0$ to 0.025 (V = 0 to 10 Knots), $\mu = 0.025$ to 0.13 (V = 10 Knots to 50 Knots) and μ above 0.13 (V = 50 Knots). His findings can be summarized as follows:

(1) The tip vortex wake can be characterized as possessing three separate and distinct pattern sequences as the advance ratio goes from 0 (hover) to above 0.13 (V = 50 to 60 Knots range).

(2) At hover and below $\mu = 0.025$ (V = 10 Knots), the vortex pattern is a helix trail. The helix can have radial contraction, and changes in the axial spacing of succeeding helixes could occur. The vortex trail from one blade can intersect with other following blades, specially when the rotor is operating in ground effect.

(3) For advance ratios over 0.13 (V = 50 to 60 Knots), the helix pattern has coarse pitch such that interaction of one trail with a preceding or succeeding one is not possible.

(4) In the $\mu = 0.025$ to 0.13 (V = 10 Knots to 60 Knots) range, the wake arrangement is most complex. Mass flow through the rotor disc is

deflected downwards. Tip vortices shed over the front half of the rotor disc coalesce and form a pair of parallel vortex trails which move downstream much in the manner of the tip vortex trails shed by fixed-wing aircraft. The arc segment of the tip vortex trail formed during the forward portion of the rotor revolution loses its identity (strength) rapidly, usually disappearing by the time it reaches the centre of the rotor as it travels downstream. On the other hand, the arc segment of the tip vortex trail formed during the rear portion of a rotor revolution retains its identity and its ends join the parallel tip vortex trails mentioned earlier. The latter segments of the tip vortex trails retain their identity for perhaps two rotor diameters downstream. In the $\mu = 0.025$ to 0.13 range, the tip vortices shed by the rotor blade during the forward portion of a rotor revolution cycle pass above the rotor blade, and thus the following blade intersects with one or more of the following trails.

These observations and other factors which produce loading asymmetries will now be combined to explain the loading variations shown in Fig. 4.1.

Fig. 4.1(a). Hover in light wind, out of ground effect

The first thing to be noticed here is that the loading is nearly symmetrical about the 0° - 180° line. This is to be expected because the velocities of the advancing blade and the retreating blade relative to air are nearly the same since the rotor system is stationary. A slight asymmetry may be the result of light wind. The tip vortex pattern is a helix trail and since the rotor is operating out of ground effect, intersection of the vortex trail from one blade with the following blade is unlikely. Thus there are no abrupt changes in lift around the azimuth. The gradual change in loading

observed (rise in lift just before 90° azimuth and fall in lift just after 270° azimuth) may be the result of changes in angle of attack due to the presence of fuselage, tail wings and the flow through the tail rotor.

The flow through the main rotor is smoother in this flight condition than in any other flight condition and so any asymmetry in loading observed here will be present in all other flight regimes together with load variations brought about by other factors, as described later on.

Figs. 4.1(b) to 4.1(e). Forward flight, out of ground effect

The symmetry about 0° - 180° line is bound to be destroyed here because of the difference in velocities, relative to the air, between the advancing and the retreating halves of the blade revolution cycle. The loading, in fact, becomes more asymmetric as the forward velocity increases. In all forward flight regimes, in addition to the asymmetry produced by the presence of fuselage, tail wings and tail rotor, sharp changes in loading will occur when a blade encounters a tip-vortex trail.

In the $\mu = 0.025$ to 0.13 range, Lehman (see (4) above) has observed that tip vortices shed by one blade are likely to intersect with the following blades, and this results in blade load fluctuations as shown in Figs. 4.1(b) and 4.1(c). The strength of the tip vortex appears to be higher at 48 knots (Fig. 4.1(c)) than at 23 knots (Fig. 4.1(b)). Cox and Lynn [25] have also shown that a sudden increase and decrease in differential-pressure occur during low forward speeds due to blade-tip vortex intersection, just before the 90° azimuth position and just after the 270° azimuth position respectively, as shown in Fig. 4.2. The indicated tip vortices would cause sudden inflow changes near azimuth positions A and B. Thus the passage of a blade through the trailing vortices would result in a sudden lift variation

on the blade elements near the tip. These abrupt changes in loading near the blade tips result in the impulsive type of noise (blade slap) [10,25,38] commonly observed at these low forward speeds.

As the forward speed of the helicopter is increased above 60 knots, Lehman (see (3) above) has shown that the tip-vortex pattern is a helix with coarse pitch such that interaction of one trail with a preceding or succeeding one is not possible. Thus the strength of the tip vortex decreases as the advance ratio μ increases and so the change in loading due to blade-tip vortex intersection is hardly noticeable at the high forward speed (Fig. 4.1(e)) of 108 knots. At such high forward speeds, because there are no sudden changes in loading, blade slap is rarely encountered in practice.

The asymmetry in loading about the 0° - 180° line in the case of 108 knots forward flight (Fig. 4.1(e)) is entirely due to changes in inflow angle of attack resulting from difference in velocities of the blade (relative to air) between the advancing half cycle and the retreating half cycle of the blade revolution. The loading around 90° azimuth (advancing side) is less because the angle of attack is less here. On the retreating side, the angle of attack increases as the 180° azimuth is crossed, but around 270° azimuth, the angle of attack becomes so high that blade stall occurs [39] and this accounts for the dip in loading around 270° - 300° azimuth.

Fig. 4.1(f). Low forward speed, in ground effect

Because of the ground effect, the flow through the rotor in this case will not be as smooth as that when the rotor is out of ground effect [24,40]. Thus the blade-tip vortex intersection will be more severe in this case. This explains the sharper load fluctuations in Fig. 4.1(f) compared to those

in Fig. 4.1(b), where the helicopter is flying at similar forward speed but is out of ground effect.

Fig. 4.1(g). Climb

If the rate of climb is fast enough for the tip-vortex trail to be left in the flow so that blade-tip vortex intersection cannot take place, then there would be no sharp fluctuations of loading on the blade. This is so in Fig. 4.1(g) and it also explains why blade slap is rarely encountered at high rates of climb.

Fig. 4.1(j). Partial power descent

Since the forward velocity is zero, the rotor is flying straight into its flow thereby making the blades intersect the tip vortices several times in one revolution. This results in sharp changes in blade loading observed in Fig. 4.1(j), giving rise to blade slap so prominently noticed in such a flight regime.

4.1.1 Conclusions

Thus it can be concluded that each flight regime has characteristic low frequency blade loading fluctuations which can be explained qualitatively by combining the factors which produce the asymmetry. Such low frequency force fluctuations will give rise to lower harmonics of rotational noise.

Measured helicopter rotor noise spectra show that rotational noise is rich in higher harmonic content even when it is hovering; as many as 30 harmonics can be detected by narrow-band analysis in some cases. This suggests that in all flight conditions, in addition to the low frequency harmonic force fluctuations described above, there are higher frequency harmonic force fluctuations present which can be detected only if the differential-pressure

measurements are recorded at smaller azimuth intervals. Acoustic spectra suggest that these higher frequency force fluctuations are present in all flight regimes and a study of the mechanisms which give rise to these fluctuations should prove very useful.

4.2 Blade differential-pressure harmonics

Before investigating the amplitude fall-offs of measured blade differential-pressure harmonics, it might be useful to summarize the definitions of these quantities as follows.

4.2.1 Harmonic representation of blade differential-pressures

If the differential-pressure on a blade element is periodic with period $2\pi/\Omega$, i.e. if the loading is reproducible every cycle of blade rotation (stationary loading), then it can be analyzed into harmonic components by writing it in the Fourier series form as

$$A_p(r,\psi) = A_{po}(r) + \sum_{g=1}^{\infty} \left\{ A_{pg}(r)\cos g\psi + \bar{A}_{pg}(r) \sin g\psi \right\}, \qquad (4.1)$$

where the coefficients are

$$A_{po}(r) = \frac{1}{2\pi} \int_0^{2\pi} A_p(r,\psi)\, d\psi \quad , \qquad (4.2)$$

$$A_{pg}(r) = \frac{1}{2\pi} \int_0^{2\pi} A_p(r,\psi) \cos g\psi \quad d\psi \quad , \qquad (4.3)$$

and

$$\bar{A}_{pg}(r) = \frac{1}{2\pi} \int_0^{2\pi} A_p(r,\psi) \sin g\psi \quad d\psi \quad . \qquad (4.4)$$

In equation (4.1),

r = spanwise station distance from rotor centre,

ψ = rotor azimuth angle,

p = blade chordwise station number,

and g = differential-pressure harmonic number.

The above series can also be expressed in terms of amplitudes and phases of harmonic components as

$$A_p(r,\psi) = A_{po}(r) + \sum_{g=1}^{\infty} \hat{A}_{pg}(r) \cos\left\{ g\psi + \phi_{pg}(r) \right\} , \qquad (4.5)$$

where $$\hat{A}_{pg}(r) = \left\{ A_{pg}(r)^2 + \bar{A}_{pg}(r)^2 \right\}^{\frac{1}{2}} \qquad (4.6)$$

and $$\phi_{pg}(r) = \tan^{-1}\left\{ \frac{-\bar{A}_{pg}(r)}{A_{pg}(r)} \right\} . \qquad (4.7)$$

4.2.2 Amplitude fall-offs of differential-pressure harmonics

Reference [22] gives the steady and the sine and cosine coefficients of 30 harmonics of differential-pressure, at 5 spanwise and 5 chordwise stations (as shown in Fig. 3.8) for five different flight conditions. These blade loading harmonics are plotted to investigate how the spectrum fall-offs vary across the chord (Fig. 4.3) and the span (Figs. 4.4 and 4.5), and with the flight condition (Fig. 4.6). Ideally, in order to derive general trends, one should investigate several sets of loading data for different rotor geometries, but unfortunately these are not available at the present time. Nevertheless, it is hoped that such investigation of this particular set of loading data will give some useful information.

In figures 4.3 to 4.6, peak amplitudes of differential-pressure harmonics are plotted as the ratio $\left(\frac{A_{pg}}{A_{po}}\right)^2$ in dB against g (log scale). The first

point to be noticed from all the plots is that the fall-off lines do not pass through the origin in most cases and so laws of the form

$$\hat{A}_{pg} = A_{po} \cdot g^{-n} \quad , \tag{4.8}$$

as suggested by Lowson and Ollerhead [10], are not appropriate. The loading harmonic fall-off is better described by laws of the form

$$\hat{A}_{pg} = \hat{A}_{p1} \cdot g^{-n} \quad , \tag{4.9}$$

and the steady loading A_{po} should be considered entirely on its own. The total radiation spectrum is then the sum of the contributions from steady blade forces and harmonic fluctuating forces.

(a) Variation of loading fall-off along blade chord (Fig. 4.3)

The spanwise station chosen here is near the blade tip (0.95 r_T) because the loading near the tip contributes most towards the radiation of noise. For the particular flight condition considered, the blade differential-pressure harmonic amplitude fall-off is higher at the leading edge and it decreases progressively towards the trailing edge. The values are

chord station	0.042a	0.158a	0.30a	0.60a	0.91a
fall-off (dB/octave)	13	10	7	6	6

This suggests that there are more higher frequency force fluctuations near the trailing edge than near the leading edge. Also the general level of the spectrum appears to be higher at the trailing edge than at the leading edge.

(b) Variation of loading fall-off along blade span (Figs. 4.4, 4.5)

Here the variation of fall-off along the span is investigated at two chord stations, one near the leading edge (0.042a , Fig. 4.4) and one near the trailing edge (0.91a , Fig. 4.5). The values obtained for the same

flight condition are

span station	0.40 r_T	0.75 r_T	0.85 r_T	0.95 r_T	0.98 r_T
fall-off (dB/octave) 0.042 a	10	9	13	13	10
fall-off (dB/octave) 0.91a	9	10.5	10	6	8.5

Clearly there is no obvious trend as in (a) above, but the fall-offs near the trailing edge are lower than those near the leading edge, at most span stations; this suggests that the higher frequency force fluctuations are dominant near the trailing edge of the blade at all points along the span.

(c) Variation of loading fall-off with flight condition (Fig. 4.6)

The loading fall-offs here are investigated at a fixed point on the blade (0.95 r_T , 0.042a). For the five different flight conditions considered, the fall-offs vary between 7 dB/octave and 13 dB/octave.

It is interesting to note that the level of the loading harmonics spectrum is higher in the "Hover in ground effect" case than in the other four flight regimes. This suggests that the airflow through the rotor in this flight condition is rougher than in the other four flight conditions and this would in fact produce more noise, provided such a difference in the loading spectra was observed at all transducer positions.

4.2.3 Conclusions

In general, considering all the differential-pressure harmonics amplitude fall-offs plotted in Figs. 4.3 to 4.6, it can be said that the fall-offs lie roughly between 6 dB per octave and 14 dB per octave, the levels of the spectra varying along the chord and the span and with the flight condition. This suggests loading harmonics fall-off laws in the limits

$$\hat{A}_{pl} \cdot g^{-2.3} \lesssim \hat{A}_{pg} \lesssim \hat{A}_{pl} \cdot g^{-1} \quad . \tag{4.10}$$

The loading spectra near the blade tip, which cause the dominant sound radiation, fall off at approximately 6 dB per octave near the trailing edge in many cases and so

$$\hat{A}_{pg} = \hat{A}_{pl} \cdot g^{-1} \tag{4.11}$$

may be taken as the standard power law for loading harmonics amplitude fall-off over all flight regimes of the S-61F compound helicopter.

The above deductions are strictly valid for this particular set of loading data only, and it remains to be seen whether they can be applied to other similar rotor configurations.

$r = 0.90\, r_T$

Table 4
$L'(r, \psi)$
lb/in

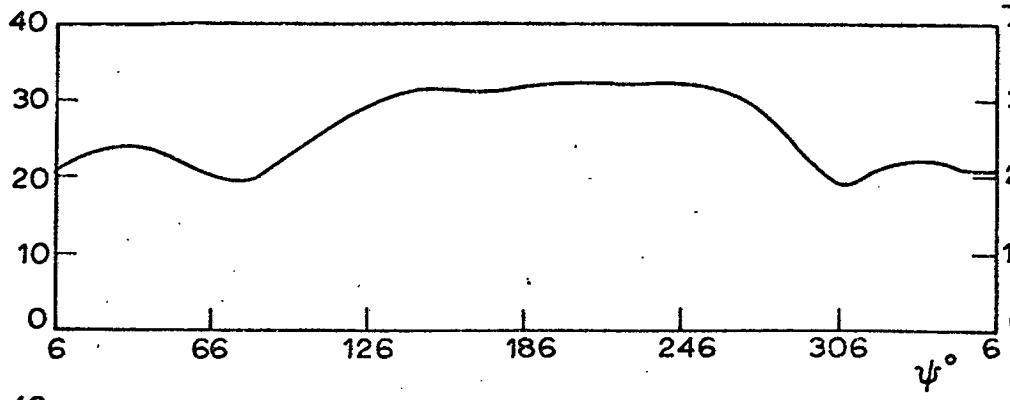

a) Hover in light wind O.G.E. V = 0 knots

Table 6
$L'(r, \psi)$
lb/in

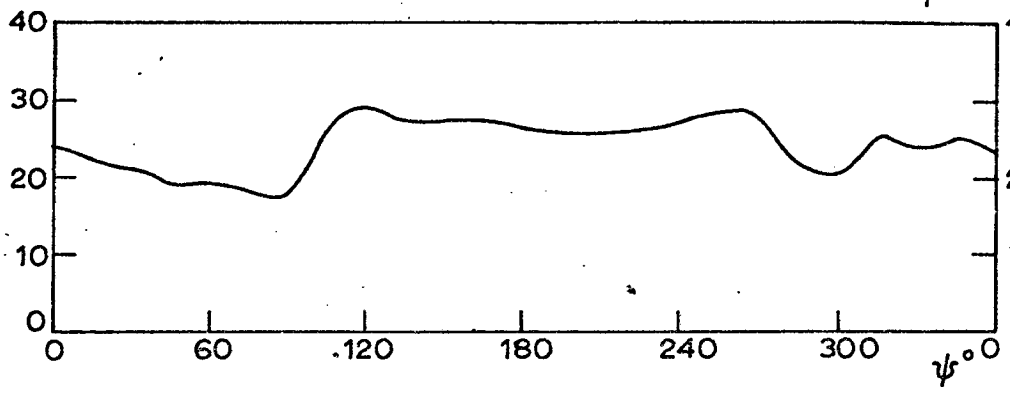

b) Foward speed V = 23 knots O.G.E.

Table 9
$L'(r, \psi)$
lb/in.

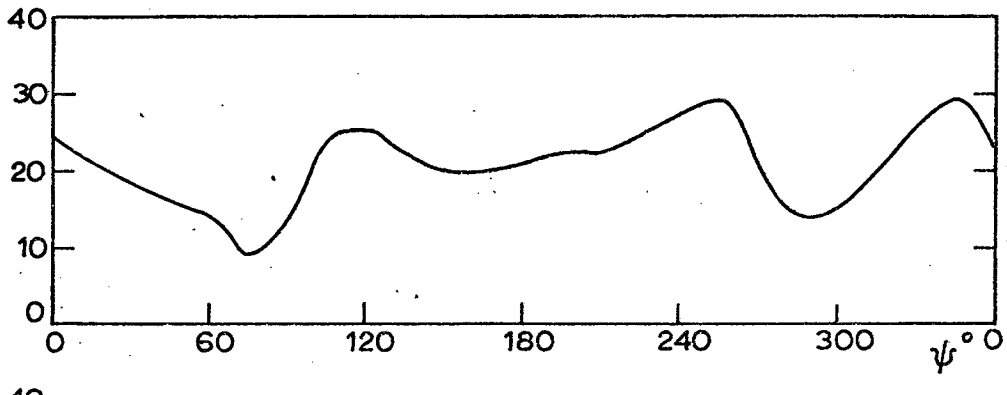

c) Foward speed V = 48 knots O.G.E.

Table 14
$L'(r, \psi)$
lb/in

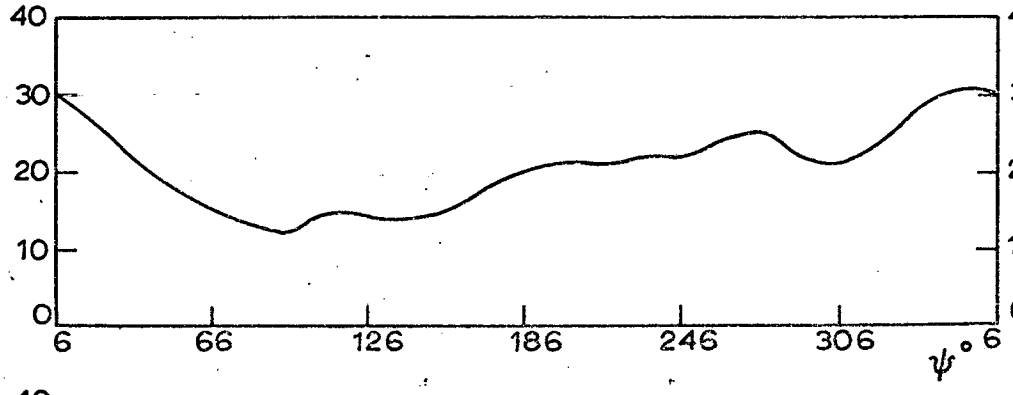

d) Foward speed V = 88 knots O.G.E.

Table 19
$L'(r, \psi)$
lb./in.

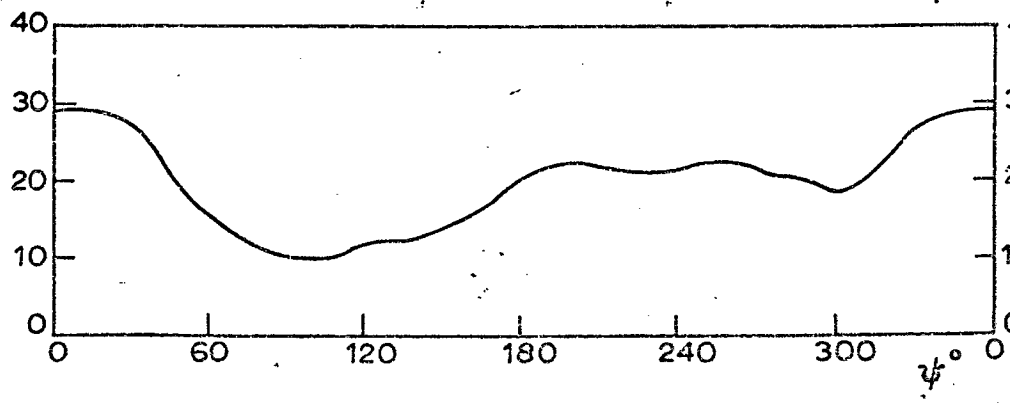

e) Foward speed V = 108 knots O.G.E.

Table 27
$L'(r,\psi)$
lb/in.

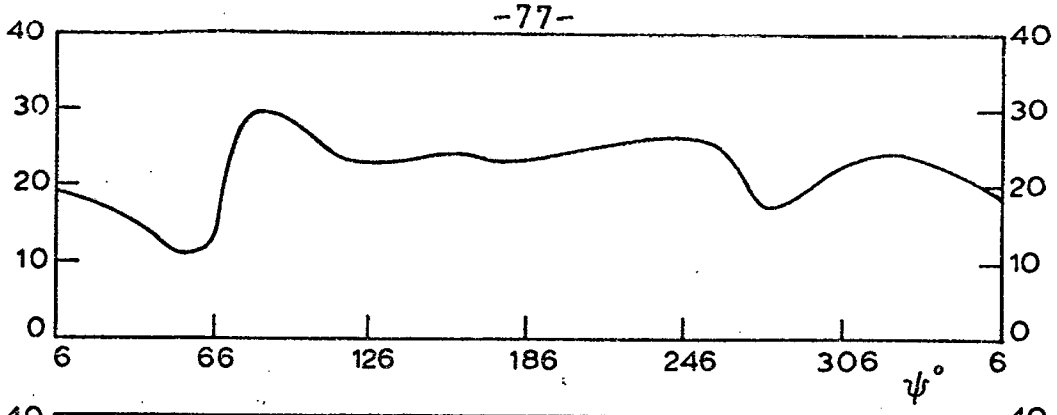

f) Foward speed
V = 27 knots
I.G.E.

Table 32
$L'(r,\psi)$
lb/in

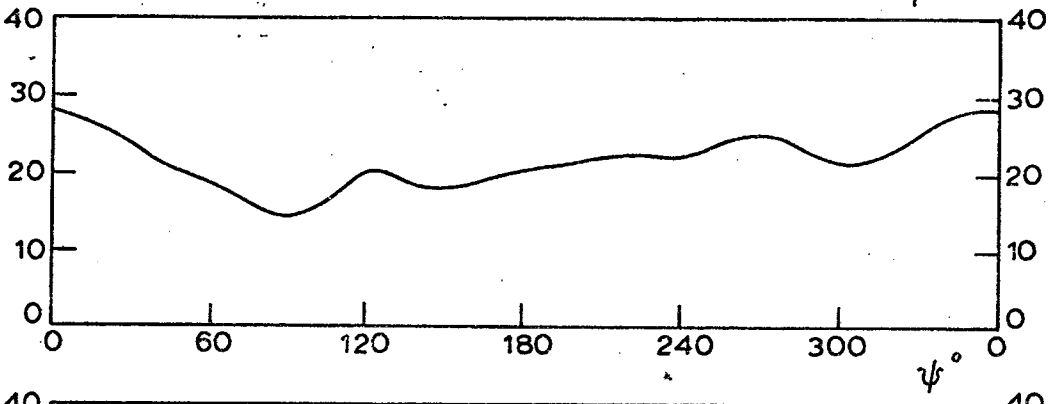

g) Climb
V = 65 knots
V_c = 1000 ft/min.

Table 35
$L'(r,\psi)$
lb/in

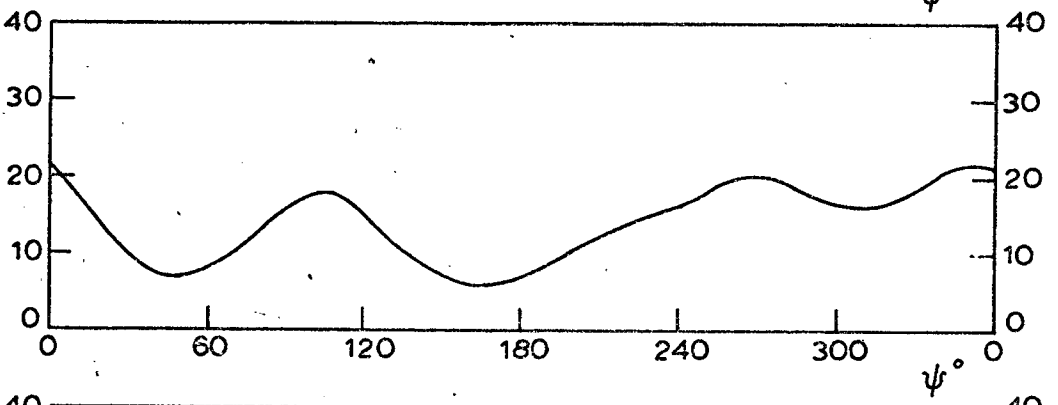

h) Autorotation
V = 76 knots
V_d = 1800 ft/min.

Table 42
$L'(r,\psi)$
lb/in

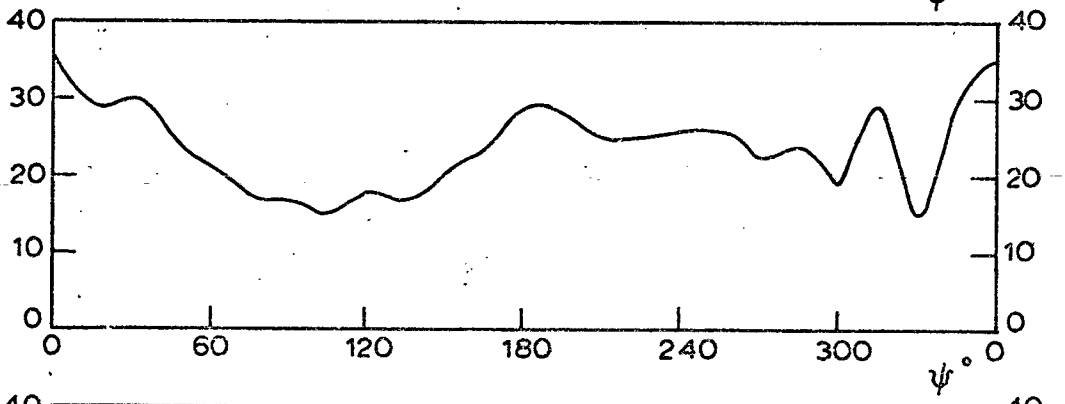

i) Steady turn
V = 89 knots
Right turn

Table 74
$L'(r,\psi)$
lb/in

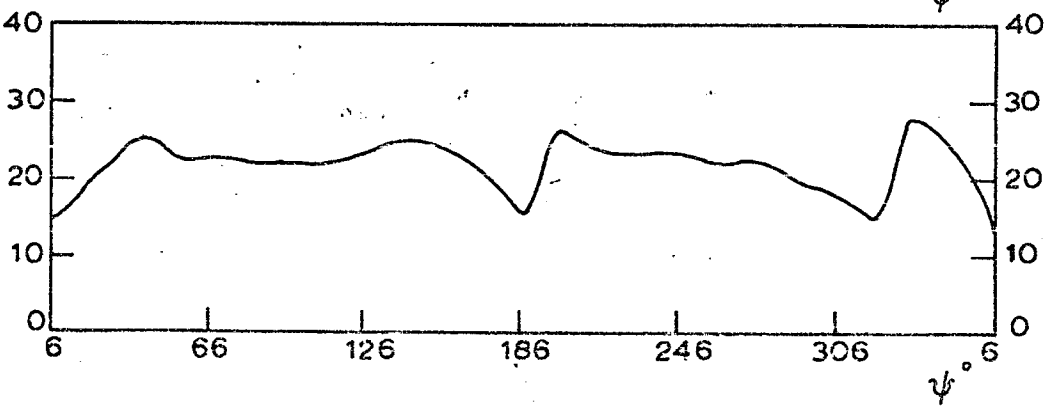

j) Partial power descent.
V = 0 knots
V_d = 900 ft/min

Fig. 4.1. Blade loading variation with azimuth for different flight conditions ($r = 0.9r_T$). (Loading data from Scheiman, S-58 helicopter)

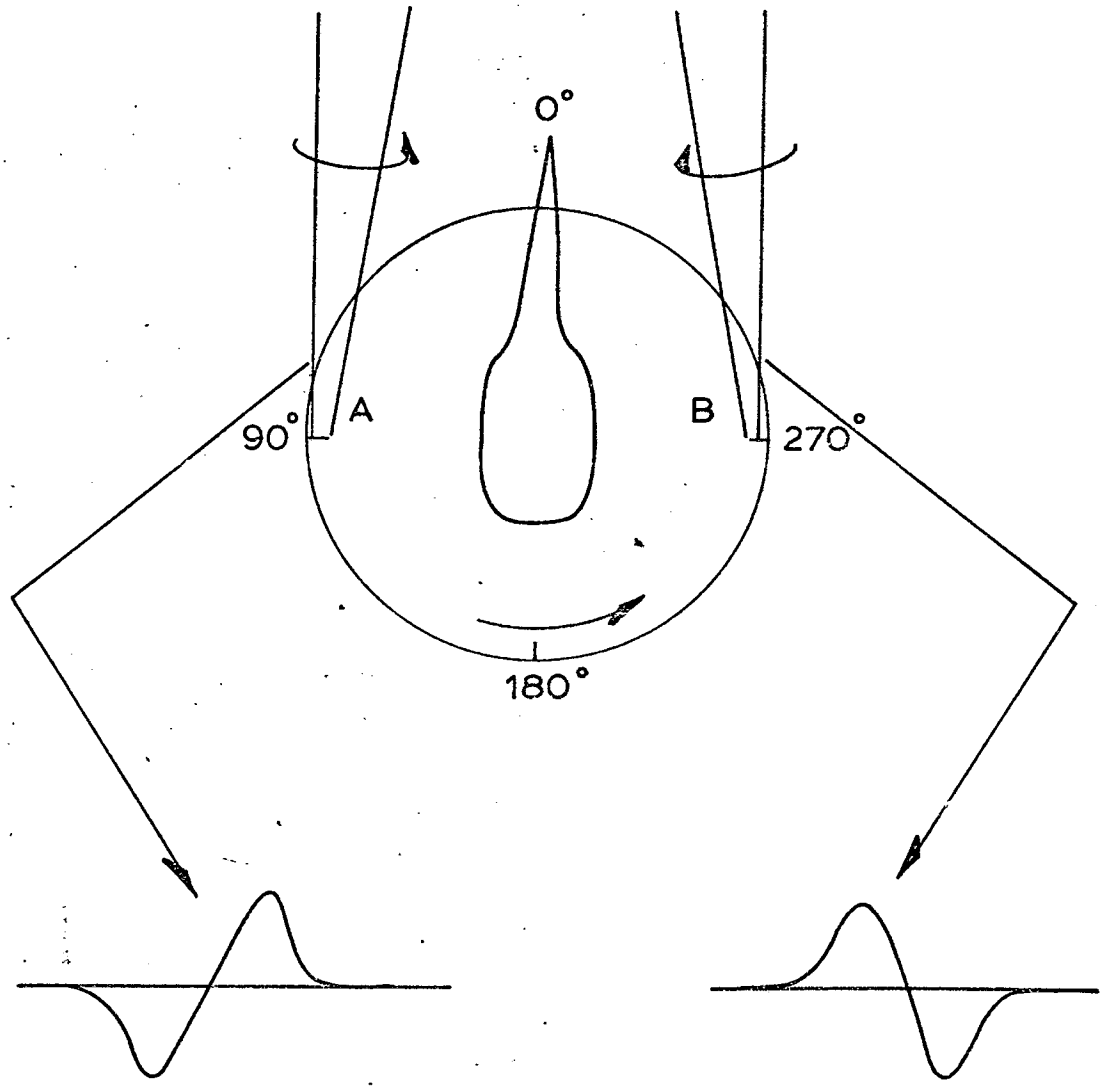

Change in loading due to upward flow over blade.

Change in loading due to downward flow over blade.

Fig. 4.2. Loading fluctuations due to blade-tip vortex intersection.

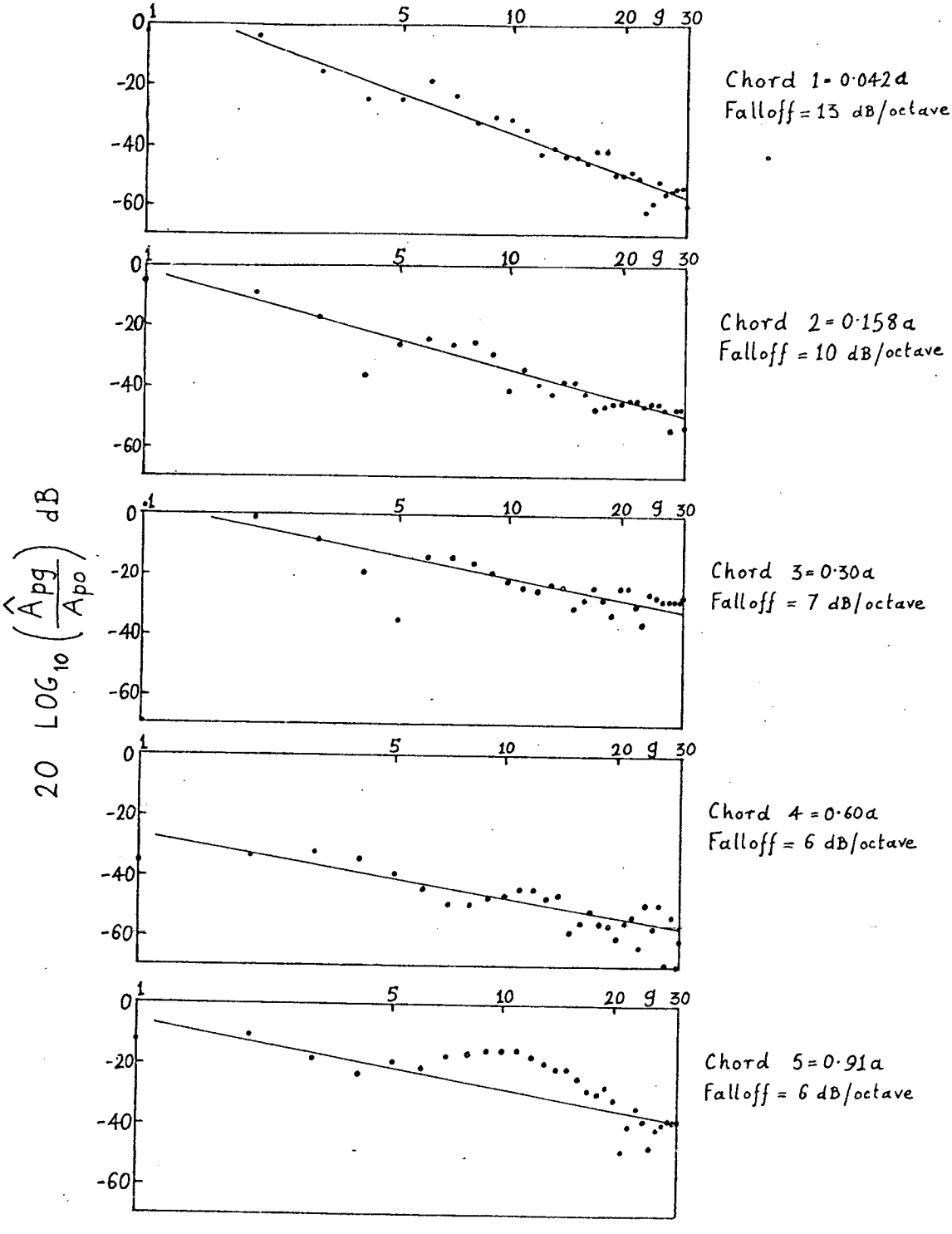

FIG. 4.3. Variation of blade differential-pressure harmonics amplitude fall-off along blade chord.
(190 Knots, low wing lift, span 4 = 0·95r_T)

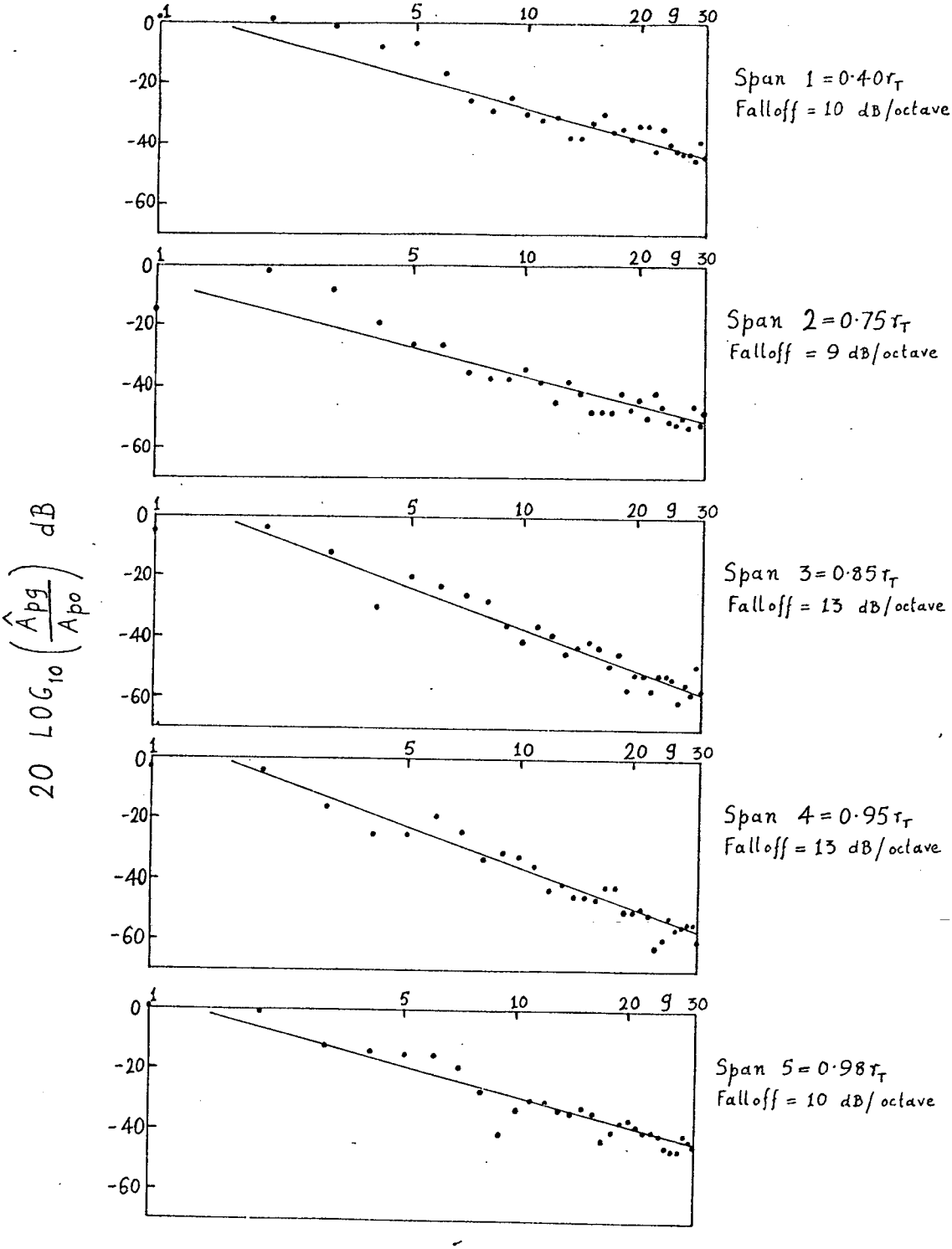

FIG. 4.4. Variation of blade differential-pressure harmonics amplitude fall-off along blade span (near leading edge). (190 Knots, low wing lift, chord 1 = 0·042 a)

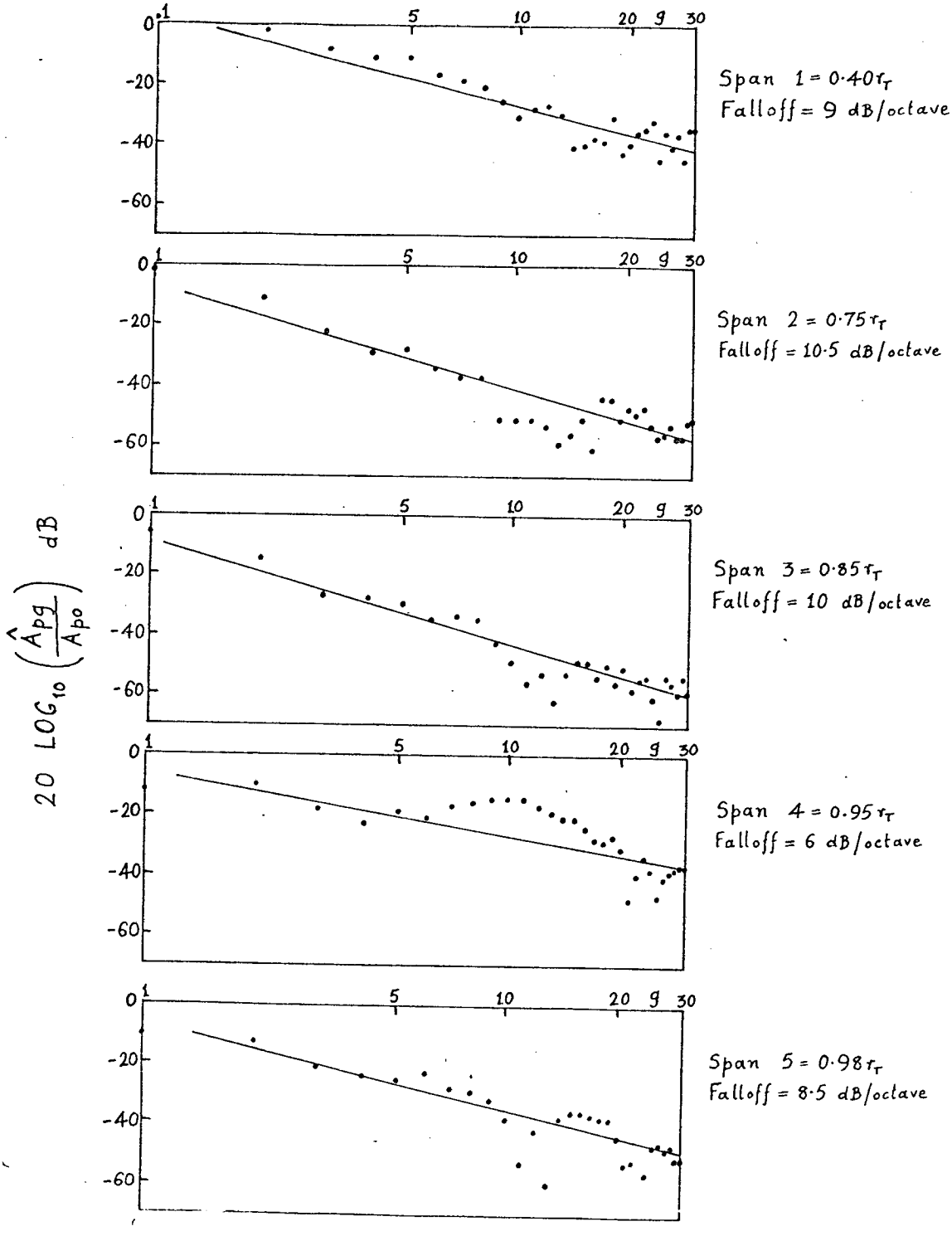

FIG. 4.5. Variation of blade differential-pressure harmonics amplitude fall-off along blade span (near trailing edge).
(190 Knots, low wing lift, chord 5 = 0·91 a)

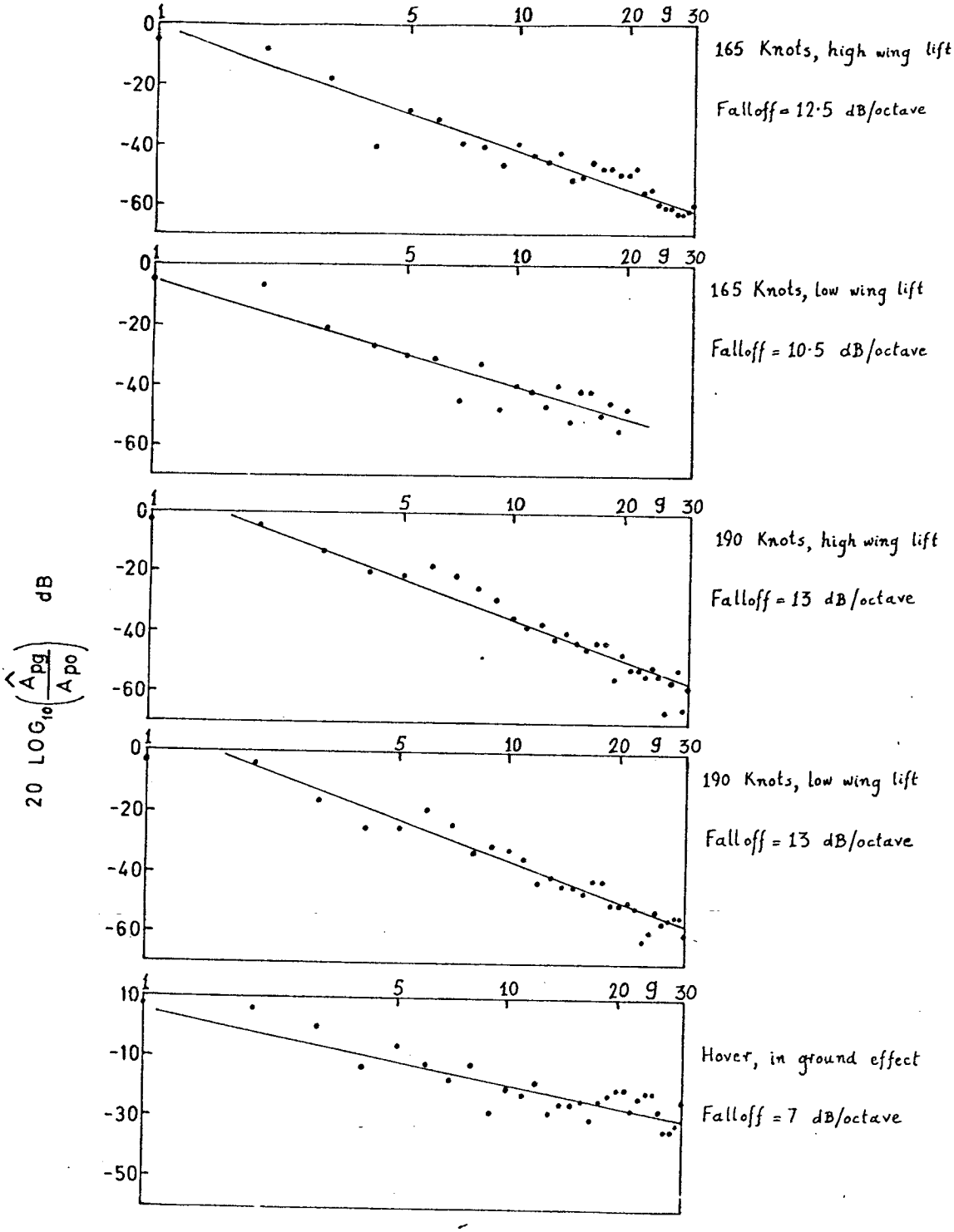

FIG. 4.6. Variation of blade differential-pressure harmonics amplitude fall-off with flight condition.
(Span $4 = 0.95 r_T$, chord $1 = 0.042a$)

CHAPTER 5

OVERALL SOUND RADIATION FROM A POINT FORCE IN CIRCULAR MOTION

So far we have considered the radiation from periodic forces acting on rotating blades; they give rise to rotational noise harmonics at frequencies which are multiples of rotor blade passage frequency. In reality, the acoustic spectra from machinery containing rotating blades (e.g. helicopter rotors, compressor fans, etc.) also contain contributions from random forces, which give rise to the broadband (or continuous) part of the spectrum. Three possible causes of random forces on helicopter rotor blades were given in section 1.5. Depending on the rotor geometry and operating conditions, the contribution from these random forces may dominate the radiation spectrum subjectively, and so the radiation properties of such forces must be established.

Exact expressions in closed-form for the overall far field radiation (directivity and total sound power) from a point force in uniform circular motion are derived in this chapter. The point force model is valid provided the wavelength of the sound radiated is larger than the blade dimensions. The investigation allows us to study the effects of accelerative motion (where the acceleration arises from steady rotation in a circle) of the point force on the sound field it radiates; the significance of such effects in fan or helicopter rotor noise at subsonic tip speeds is established here.

The two alternative approaches which can be used to analyze the sound field of moving sources were described in chapter 1. The moving-source approach is used here and Lowson's general theory [9] of sound radiation from singularities in arbitrary motion is applied to Lilley's problem [8] of broadband sound radiation from a point force moving uniformly in a

circular path. For the special case of linear motion, closed-form solutions for the overall radiation are available for various types of source and are reviewed in section 5.1; corresponding spectral results are obtainable from section 11.2 of Morse and Ingard's book [6], as will be indicated in Chapter 6. In view of this, the main interest is in establishing how the linear-motion results are modified by acceleration perpendicular to the source path.

One way to demonstrate the effect of circular as opposed to linear motion would have been to calculate a number of cases numerically, using the general result given by Ffowcs Williams and Hawkings [7] which takes the form of an infinite series of Bessel functions. It was decided instead to start from first principle using Lowson's moving-source approach [9], for two reasons. First, simple closed-form results are obtained for the overall radiation directly, without involving the radiation spectrum.

The other advantage of the moving-source approach relates to the spectrum calculation, where it leads to a series expansion in the ratio (Ω/ω) of the angular rotation rate to the radian frequency of the radiated sound. Linear source motion corresponds to $(\Omega/\omega) = 0$, so the result is an expansion about the linear-motion case which is valid for small values of this ratio. The effects of finite frequency ratio (Ω/ω), combined with finite source Mach number M, on the spectral properties of the radiation are investigated in Chapter 6.

5.1 Power output from point sources in uniform straight-line motion

The effects of source motion are introduced here in their simplest form, by considering steady motion in a straight line. The overall sound power output is studied as a function of convection Mach number, for various types of source. Most of the results are well known, but the analysis

serves to introduce some important ideas about retarded time.

Because of the finite speed of sound c_o, an acoustic signal emitted from point $\underset{\sim}{x}$ reaches an observation point $\underset{\sim}{r}$ after a finite time interval. In the case of a moving source, the time interval is

$$t - [t] = [R]/c_o \qquad \text{(see Fig. 5.1);} \qquad (5.1)$$

i.e. the observation time t differs from the emission time $[t]$ by an amount which depends on the source-observer separation R, evaluated at the time of emission. The bracket notation, $[f(t)] = f([t])$, is used throughout the rest of the thesis to denote the retarded-time value of any function f(t).

Differentiating equation (5.1) gives

$$dt = [1 - M_R]\, d[t], \qquad (5.2)$$

where

$$M_R = -\frac{1}{c_o}\frac{dR}{dt} \qquad (5.3)$$

is the approach Mach number of the source towards the observer. Equation (5.2) is the basis of much of the analysis which follows.

In considering the sound power output of a moving source, the distinction between dt and $d[t]$ is important. The instantaneous energy acoustic flux in the far field is $p'^2/\rho_o c_o$, directed radially outwards from the point of emission; so in time dt, the energy per unit area crossing a large sphere centred on this point is

$$\left(\frac{p'^2}{\rho_o c_o}\right) dt = \left(\frac{p'^2}{\rho_o c_o}\right) [1 - M_R]\, d[t]. \qquad (5.4)$$

To get the source power output, defined as the average rate at which energy

is emitted by the source, equation (5.4) is divided by $d[t]$, then time-averaged and integrated over the spherical surface.

The result is

$$W = \int_S I\left[1 - M_R\right] dS \; ; \tag{5.5}$$

in this equation the acoustic intensity, defined by

$$I = \left\langle p'^2/\rho_o c_o \right\rangle \quad , \tag{5.6}$$

is strictly an ensemble average taken for a single source position, rather than a time average (which would involve changes in source orientation and position relative to the observer). The ensemble averaging process is carried out explicitly for circular motion in Chapter 6. For straight-line motion, as considered in this section, the ensemble average is equivalent to a time average.

To calculate the power output W for a moving source from equation (5.5) the far-field intensity must be specified as a function of direction; the result then follows by straight-forward integration. Some examples are given below.

(a) Point acoustic source

A point acoustic source of strength q(t) may be represented physically by $q = \rho_o \ddot{d}$, where d(t) represents a time-varying volume displacement and $\ddot{d}$ is its second derivative (the volume acceleration). In this and the following cases source motion multiplies the far-field intensity I by a factor $\left[1 - M_R\right]^{-k}$, provided M_R is constant; $k = 2$ for the point acoustic source [26]. If the observation point is at a polar angle ψ from the line of motion (Fig. 5.2), the approach Mach number $M_R = M \cos\psi$; thus equation (5.5) gives for the point acoustic source

$$\frac{W(M)}{W(0)} = \tfrac{1}{2} \int_0^{\pi} \frac{\sin\psi \cdot d\psi}{1 - M\cos\psi} = \frac{1}{2M} \ln\left(\frac{1 + M}{1 - M}\right) . \qquad (5.7)$$

(b) Point volume velocity source

Lowson [9] has shown that for a source of specified volume velocity $\dot{d}(t)$, the index $k = 4$. It follows from (5.5) that

$$\frac{W(M)}{W(0)} = \tfrac{1}{2} \int_0^{\pi} \frac{\sin\psi \cdot d\psi}{(1 - M\cos\psi)^3} = (1 - M^2)^{-2} . \qquad (5.8)$$

(c) Point volume displacement source

A straightforward extension of Lowson's analysis (see Chapter 8) shows that for a source of specified volume displacement $d(t)$, the index $k = 6$. Thus

$$\frac{W(M)}{W(0)} = \tfrac{1}{2} \int_0^{\pi} \frac{\sin\psi \cdot d\psi}{(1 - M\cos\psi)^5} = \frac{1 + M^2}{(1 - M^2)^4} . \qquad (5.9)$$

(d) Fluctuating longitudinal force

The basic directional factor $\cos^2\psi$ in this case is multiplied by a source motion factor as in (b) above, with $k = 4$ [9]. Thus

$$\frac{W(M)}{W(0)} = \frac{3}{2} \int_0^{\pi} \frac{\sin\psi \cos^2\psi \cdot d\psi}{(1 - M\cos\psi)^3}$$

$$= \frac{3}{2} \frac{1}{M^3} \left\{ \frac{2M(2M^2 - 1)}{(1 - M^2)^2} + \ln\left(\frac{1 + M}{1 - M}\right) \right\} . \qquad (5.10)$$

(e) Fluctuating transverse force

The basic directional factor $\sin^2\psi \cos^2\theta$ (where θ is the azimuth angle about the line of motion) is multiplied by the same factor for source motion as the longitudinal force. The sound power ratio is therefore

$$\frac{W(M)}{W(O)} = \frac{3}{4\pi} \int_0^{2\pi} \cos^2\theta \, d\theta \int_0^{\pi} \frac{\sin^3\psi \cdot d\psi}{(1 - M\cos\psi)^3}$$

$$= \frac{3}{2}\frac{1}{M^3}\left\{ \frac{M}{1 - M^2} - \tfrac{1}{2}\ln\left(\frac{1 + M}{1 - M}\right)\right\}. \qquad (5.11)$$

Values of the sound power ratio in dB are plotted for the various types of source in Figures 5.3 and 5.4.

5.2 Point force in uniform circular motion

The far field sound pressure from a point force $\underset{\sim}{F}(\underset{\sim}{x},t)$ in arbitrary motion is given by Lowson [9] as

$$p'(\underset{\sim}{r},t) = \left[\frac{r_i - x_i}{4\pi c_o R^2 (1-M_R)^2}\left\{\frac{\partial F_i}{\partial t} + \frac{F_i}{1-M_R}\frac{\partial M_R}{\partial t}\right\}\right] \qquad (5.12)$$

where r_i, x_i $(i = 1,2,3)$ are the Cartesian co-ordinates of observer and source respectively, and M_R is the component of convection Mach number in the direction $\underset{\sim}{R}$ of the observer;

$$M_R = \frac{\underset{\sim}{M} \cdot \underset{\sim}{R}}{R} = \frac{M_j(r_j - x_j)}{R} \quad . \qquad (5.13)$$

The square brackets again imply evaluation of retarded time $[t] = t - [R]/c_o$, where t is the time of observation and $R = |\underset{\sim}{r} - \underset{\sim}{x}|$ is the observer-source separation.

For a point force rotating in a circle about a fixed point, it is convenient to take the centre of the circle as origin. Then $M_j x_j = 0$; also if the force is normal to the radius vector, $F_i x_i = 0$ (see Fig. 5.1). Equation (5.12) thus reduces, at distances large compared with the radius of the circle ($r \gg a$), to

$$p'(\underset{\sim}{r},t) = \frac{1}{4\pi c_o r}\left[\frac{\partial F_r}{\partial t}(1 - M_r)^{-2} + F_r \frac{\partial M_r}{\partial t}(1 - M_r)^{-3}\right]. \qquad (5.14)$$

It should be noted that in equation (5.14), $M_r = M_i r_i / r$ is the Mach number component parallel to the line from the origin to the observation point. The force component F_r is defined similarly. In terms of the rotating force geometry defined in Fig. 5.5, where the force is resolved into thrust (T) and drag (D)† components (the terminology arises from the use of this model for propeller and helicopter rotor noise calculations),

$$M_r = - M \sin\psi \sin\theta \qquad (5.15)$$

and

$$F_r = - T \cos\psi - D \sin\psi \sin\theta \; ; \qquad (5.16)$$

these are the Mach number and force components parallel to $\underset{\sim}{r} = \overrightarrow{OP}$.

Since ψ and M are constant,

$$\frac{dM_r}{dt} = - \Omega M \sin\psi \cos\theta \qquad (5.17)$$

and

$$\frac{dF_r}{dt} = - \frac{dT}{dt}\cos\psi - \Omega D \sin\psi \cos\theta - \frac{dD}{dt}\sin\psi \sin\theta \; . \qquad (5.18)$$

Equation (5.14) then gives, writing $M \sin\psi = \alpha$, $T \cos\psi = X$, and $D \sin\psi = Y$,

$$4\pi c_o r p' = \left[- (1+ \alpha\sin\theta)^{-2} (\dot{X} + \dot{Y} \sin\theta) + (1+ \alpha\sin\theta)^{-3} \Omega\cos\theta \, (\alpha X - Y)\right] . \qquad (5.19)$$

This general result is used below to find the mean square radiated pressure and sound power for a rotating random force. It should be noted that the word <u>random</u> here means with no periodic components; the only restriction essential to this chapter, in fact, is that the rotating force should contain no periodic components at multiples of the rotational frequency.

† Throughout the thesis, the tangential force component in the plane of rotation is referred to as the "drag force".

5.2.1 Mean square far-field sound pressure

Equation (5.19) may be written as

$$4\pi c_o r p' = - f\left[\dot{X}\right] - g\left[\dot{Y}\right] + \Omega h\left[\alpha X - Y\right] \qquad (5.20)$$

where $f = \left[(1 + \alpha\sin\theta)^{-2}\right]$,

$g = \left[(1 + \alpha\sin\theta)^{-2} \sin\theta\right]$, (5.21)

and $h = \left[(1 + \alpha\sin\theta)^{-3} \cos\theta\right]$.

If $\dot{X}$ and $\dot{Y}$ are stationary random functions of time, they will contribute a continuous spectrum of radiated sound pressure which can be calculated by forming the pressure covariance from (5.20). Note that (f, g, h) are all periodic functions of time, with period $2\pi/\Omega$, while $(\dot{X},\dot{Y})$ are assumed to be stationary random functions of time; the two types of function are uncorrelated. Moreover, $\langle h \rangle = 0$, so h is uncorrelated with (X,Y) even though $\langle X \rangle$, $\langle Y \rangle$ are not zero. This means that the auto-correlation of the right hand side of equation (5.20) may be written in terms of products of the auto-correlations R_f , R_g , R_h of the periodic functions and the auto-correlations R_X , R_Y , $R_{\dot{X}}$, $R_{\dot{Y}}$ derived for the force components.

From equation (5.20), the auto-correlation $R_p(\tau)$ of the sound pressure is given by time-averaging the product

$$(4\pi c_o r)^2 \, p_1' p_2' = \left(f\left[\dot{X}\right] + g\left[\dot{Y}\right] - \Omega h\left[\alpha X - Y\right]\right)_1 \left(f\left[\dot{X}\right] + g\left[\dot{Y}\right] - \Omega h\left[\alpha X - Y\right]\right)_2$$

where the subscripts (1,2) denote values at observer times t_1, t_2 $(= t_1 + \tau)$. The overall mean square pressure is simply $R_p(0)$.

Expanding the product gives

$$(4\pi c_o r)^2\, p_1' p_2' = f_1 f_2 [\dot{X}]_1 [\dot{X}]_2 + g_1 g_2 [\dot{Y}]_1 [\dot{Y}]_2 + f_1 g_2 [\dot{X}]_1 [\dot{Y}]_2 + g_1 f_2 [\dot{Y}]_1 [\dot{X}]_2$$

$$- \Omega \Big\{ f_1 h_2 [\dot{X}]_1 [\alpha X - Y]_2 + h_1 f_2 [\alpha X - Y]_1 [\dot{X}]_2$$

$$+ g_1 h_2 [\dot{Y}]_1 [\alpha X - Y]_2 + h_1 g_2 [\alpha X - Y]_1 [\dot{Y}]_2 \Big\}$$

$$+ \Omega^2 h_1 h_2 [\alpha X - Y]_1 [\alpha X - Y]_2 \quad . \qquad (5.22)$$

When this is time-averaged with $\tau = 0$, the Ω terms disappear since $R_{fh}(0) = R_{gh}(0) = 0$; thus the mean square far-field pressure is given in terms of T and D by

$$(4\pi c_o r)^2 R_p(0) = R_f(0)\cos^2\psi \, \langle \dot{T}^2 \rangle + 2R_{fg}(0)\cos\psi \, \sin\psi \, \langle \dot{T}\dot{D} \rangle + R_g(0)\sin^2\psi \, \langle \dot{D}^2 \rangle$$

$$+ \Omega^2 R_h(0) \Big\{ \alpha^2 \cos^2\psi \, \langle T^2 \rangle - 2\alpha \, \cos\psi \, \sin\psi \, \langle TD \rangle + \sin^2\psi \, \langle D^2 \rangle \Big\}. \qquad (5.23)$$

The effect of source acceleration is clearly displayed in the Ω^2 term, which also contains the contribution of steady thrust and drag forces to the overall radiation.

The correlation functions R_f , R_{fg} , R_g , R_h for $\tau = 0$ may be evaluated as follows. By definition,

$$R_f(0) = \frac{1}{2\pi} \int_0^{2\pi} f^2 \, . \, d\theta$$

$$= \frac{1}{2\pi} \int_0^{2\pi} f^2 \, . \, (1 + \alpha\sin\phi) \, . \, d\phi \qquad (\phi = [\theta]) \, ,$$

where the variable of integration has been changed from θ to ϕ as indicated in Appendix VII. It follows from (5.21) that provided $\alpha < 1$,

$$R_f(0) = \frac{1}{2\pi}\int_0^{2\pi} (1 + \alpha\sin\phi)^{-3}.d\phi = \frac{1 + \frac{1}{2}\alpha^2}{(1-\alpha^2)^{5/2}} \quad ;$$

Similarly

$$R_{fg}(0) = \frac{1}{2\pi}\int_0^{2\pi} (1 + \alpha\sin\phi)^{-3}\sin\phi.d\phi = \frac{-\frac{3}{2}\alpha}{(1-\alpha^2)^{5/2}} \quad ,$$

$$R_g(0) = \frac{1}{2}\int_0^{2\pi} (1 + \alpha\sin\phi)^{-3}\sin^2\phi.d\phi = \frac{\frac{1}{2} + \alpha^2}{(1-\alpha^2)^{5/2}} \quad ,$$

and

$$R_h(0) = \frac{1}{2\pi}\int_0^{2\pi} (1 + \alpha\sin\phi)^{-5}\cos^2\phi.d\phi = \frac{\frac{1}{2} + \frac{1}{8}\alpha^2}{(1-\alpha^2)^{7/2}} \quad . \qquad (5.24)$$

The integrals in (5.24) above were evaluated by contour integration in the complex plane $z = e^{i\phi}$.

Equations (5.23) and (5.24) are the main results of this chapter. Taken together they give an exact expression for the mean square far-field sound pressure at the observation point (r, ψ), due to a point force with random time variation rotating uniformly in a circle.

Steady force

In the special case where the thrust and drag components are both constant with time,

$$\langle p'^2 \rangle = \left\{ \frac{\Omega}{2\pi c_o r} (T\cos\psi - \frac{D}{M}) \right\}^2 . \frac{\alpha^2(1 + \frac{1}{4}\alpha^2)}{8(1 - \alpha^2)^{7/2}}$$

(steady thrust and drag, $\alpha < 1$). (5.25)

This result can be compared with Gutin's propeller noise calculation [2] by putting the number of blades equal to 1. Gutin gives the n^{th}-harmonic

amplitude of the radiated pressure as n $J_n(n\alpha)$ times the bracketed factor in (5.25), so adding the mean square contributions from all harmonics (n = 1 to ∞) gives

$$\langle p'^2 \rangle = \left\{ \frac{\Omega}{2\pi c_o r}(T\cos\psi - \frac{D}{M}) \right\}^2 \tfrac{1}{2} \sum_{n=1}^{\infty} n^2 J_n^2 (n\alpha). \qquad (5.26)$$

Equation (5,25) and (5.26) are identical - see Watson [27, p.573] .

Fluctuating force

The contribution from fluctuations in the thrust and drag forces can be written more simply using the further assumption that these are related by

$$\dot{D} = \varepsilon \dot{T} \quad , \qquad (\varepsilon = \text{constant}). \qquad (5.27)$$

Equation (5,27) implies that the resultant fluctuating force has a fixed orientation in the rotating frame of reference. With equations (5.23) and (5.24) it gives

$$(4\pi c_o r)^2 \frac{\langle p'^2 \rangle}{\langle \dot{T}^2 \rangle} = \left\{ (1+\tfrac{1}{2}\alpha^2)\cos^2\psi - 3\varepsilon\alpha \sin\psi \cos\psi + \varepsilon^2(\tfrac{1}{2}+\alpha^2)\sin^2\psi \right\} / (1-\alpha^2)^{5/2}, \qquad (\alpha < 1). \qquad (5.28)$$

Figures 5.6 to 5.9 show the effects of Mach number M and drag-thrust ratio ε on the overall radiated sound field, for both steady and fluctuating forces. For this purpose the mean square sound pressures are normalized by F^2 and $\langle \dot{F}^2 \rangle$ respectively, where $F = (1 + \varepsilon^2)^{\frac{1}{2}}T$ is the resultant force. The standard values $\varepsilon = 0.1$ and $M = 0.5$ are chosen to be characteristic of helicopter rotors.

5.2.2 Overall sound power output

The overall radiated power corresponding to (5.23) follows by integrating the intensity over a spherical surface r = constant;

$$W = \int_S I(r,\psi)\, dS \ . \tag{5.29}$$

Here $I(r,\psi)$ is a time-average value, as distinct from the ensemble average for the linearly-moving source defined in (5.6).

When the integral above is evaluated using (5.23) and (5.24) for the intensity, the TD and $\dot{T}\dot{D}$ cross-product terms vanish and the power output from a rotating point force is obtained in the form

$$12\pi\rho_o c_o^3 \ . \ W = \langle \dot{T}^2 \rangle \ A_o(M) + \langle \dot{D}^2 \rangle \ B_o(M) + \Omega^2 \left\{ \langle T^2 \rangle \ A_1(M) + \langle D^2 \rangle \ B_1(M) \right\} . \tag{5.30}$$

In equation (5.30), the A_o and B_o terms are independent of the rotational frequency Ω, they give the sound power radiated from a point force in uniform linear motion, which was calculated directly in section 5.1. Thus $A_o(M)$ is given by equation (5.11), and $B_o(M)$ by equation (5.10).

The effects of finite rotational frequency are contained in the A_1 and B_1 terms in (5.30); these are the only terms which remain when the thrust and drag are steady. The thrust function is

$$A_1(M) = \frac{1}{16M^3} \left\{ 3 \ \ln\left(\frac{1+M}{1-M}\right) - \frac{2M(3-5M^2)}{(1-M^2)^2} \right\} \tag{5.31}$$

and the drag function is

$$B_1(M) = (1 - M^2)^{-3} \ . \tag{5.32}$$

This last result was obtained by Dokuchaev [28], by considering the case of a steady drag force moving in a circle.

For low Mach number applications, it may be useful to approximate A_o , B_o , A_1 , B_1 by the first few terms of a series. Expansion in powers of M gives

$$A_o(M) = 1 + \frac{6}{5}M^2 + \frac{9}{7}M^4 + \ldots \quad , \tag{5.33}$$

$$B_o(M) = 1 + \frac{18}{5}M^2 + \frac{45}{7}M^4 + \ldots \quad , \tag{5.34}$$

$$A_1(M) = \frac{1}{5}M^2 + \frac{3}{7}M^4 + \ldots \quad , \tag{5.35}$$

$$B_1(M) = 1 + 3M^2 + 6M^4 + \ldots \quad . \tag{5.36}$$

Figure 5.10 shows the effect of terminating the series expansions at the M^4 term.

5.3 Pure rotation of a point force

If the radius of the circular path is now reduced to zero, then M = 0 although Ω remains finite. The resulting overall mean square pressure due to pure rotation of the point force is given by the general equations (5.23) and (5.24) as

$$(4\pi c_o r)^2 \ \langle p'^2 \rangle = \langle \dot{T}^2 \rangle \cos^2\psi + \tfrac{1}{2}(\langle \dot{D}^2 \rangle + \Omega^2 \langle D^2 \rangle) \sin^2\psi \ . \tag{5.37}$$

Integration over a spherical surface gives the corresponding sound power output as

$$12\pi\rho_o c_o^3 \ . \ W = \langle \dot{T}^2 \rangle + \langle \dot{D}^2 \rangle + \Omega^2 \langle D^2 \rangle \ . \tag{5.38}$$

5.3.1 Single-frequency rotating force

A particular case is that of a harmonically varying drag force, with radian frequency ν; then $\langle \dot{D}^2 \rangle = \nu^2 \langle D^2 \rangle$ and the ratio of the sound power output due to pure rotation to the power output without rotation is given by

$$\frac{W(\Omega)}{W(0)} = 1 + \left(\frac{\Omega}{\nu}\right)^2 \ . \tag{5.39}$$

This result, obtained as a special case of (5.38), can alternatively be derived by direct calculation following Sretenskii's method [29] as shown below.

If the force $f = f_o \cos \nu t$ rotates in its own plane at Ω radians/second as shown in Fig. 5.11, then at any instant of time its components in the y and z directions are

$$f_y = f_o \cos \Omega t \cos \nu t , \quad f_z = f_o \sin\Omega t \cos\nu t . \tag{5.40}$$

The resultant sound pressure at a point $\underset{\sim}{r}$ in the far field is given by

$$p' = \frac{1}{4\pi c_o r} \left[\frac{\partial f_r}{\partial t}\right]. \tag{5.41}$$

In terms of the geometry defined in Fig. 5.12,

$$\underset{\sim}{r} = (r\cos\psi , r\sin\psi\cos\theta , r\sin\psi\sin\theta) ;$$

so

$$f_r = f_o \sin\psi\cos(\Omega t - \theta)\cos\nu t , \tag{5.42}$$

and the mean square pressure in the far field follows from (5.41) as

$$(4\pi c_o r)^2 \langle p'^2 \rangle = f_o^2 \sin^2\psi \langle \Omega^2 \sin^2(\Omega t-\theta)\cos^2\nu t + \tfrac{1}{2}\Omega\nu \sin 2(\Omega t-\theta)\sin 2\nu t + \nu^2\cos^2(\Omega t-\theta)\sin^2\nu t \rangle . \tag{5.43}$$

Provided Ω and ν are not integrally related, this reduces to

$$(4\pi c_o r)^2 \langle p'^2 \rangle = \tfrac{1}{4}(\Omega^2 + \nu^2) f_o^2 \sin^2\psi . \tag{5.44}$$

It is clear from the above equation that rotation of the point force, at angular speed Ω in its own plane, increases the sound power output by a factor

$$\frac{W(\Omega)}{W(0)} = 1 + \left(\frac{\Omega}{\nu}\right)^2 \quad . \tag{5.45}$$

5.4 Conclusions

Exact expressions have been obtained in closed form for the overall far-field radiation (directivity and total sound power) from a point force moving uniformly in a circle. The only restriction on the force spectrum is that it contain no discrete components at multiples of the rotation rate.

The effects of source acceleration due to circular motion on the radiation spectrum are established in the next chapter.

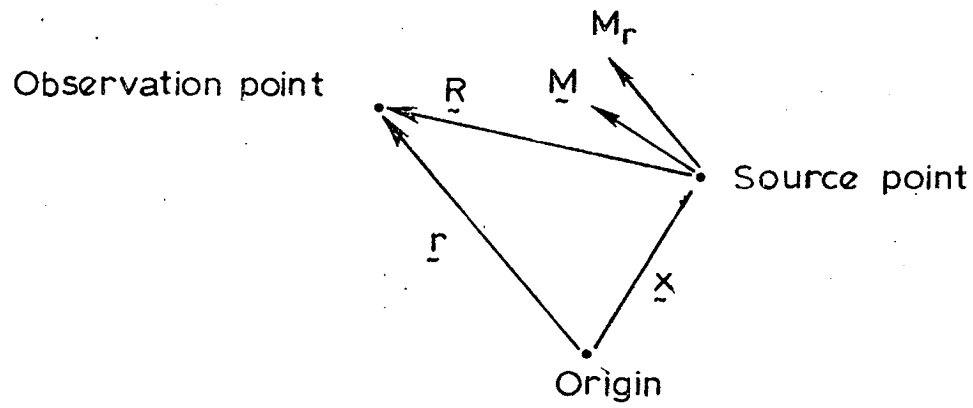

Fig. 5.1 Source and observer geometry for moving point sources.

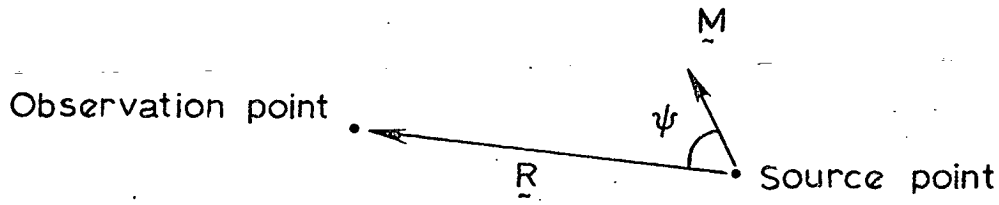

Fig. 5.2 Point source in uniform straight-line motion.

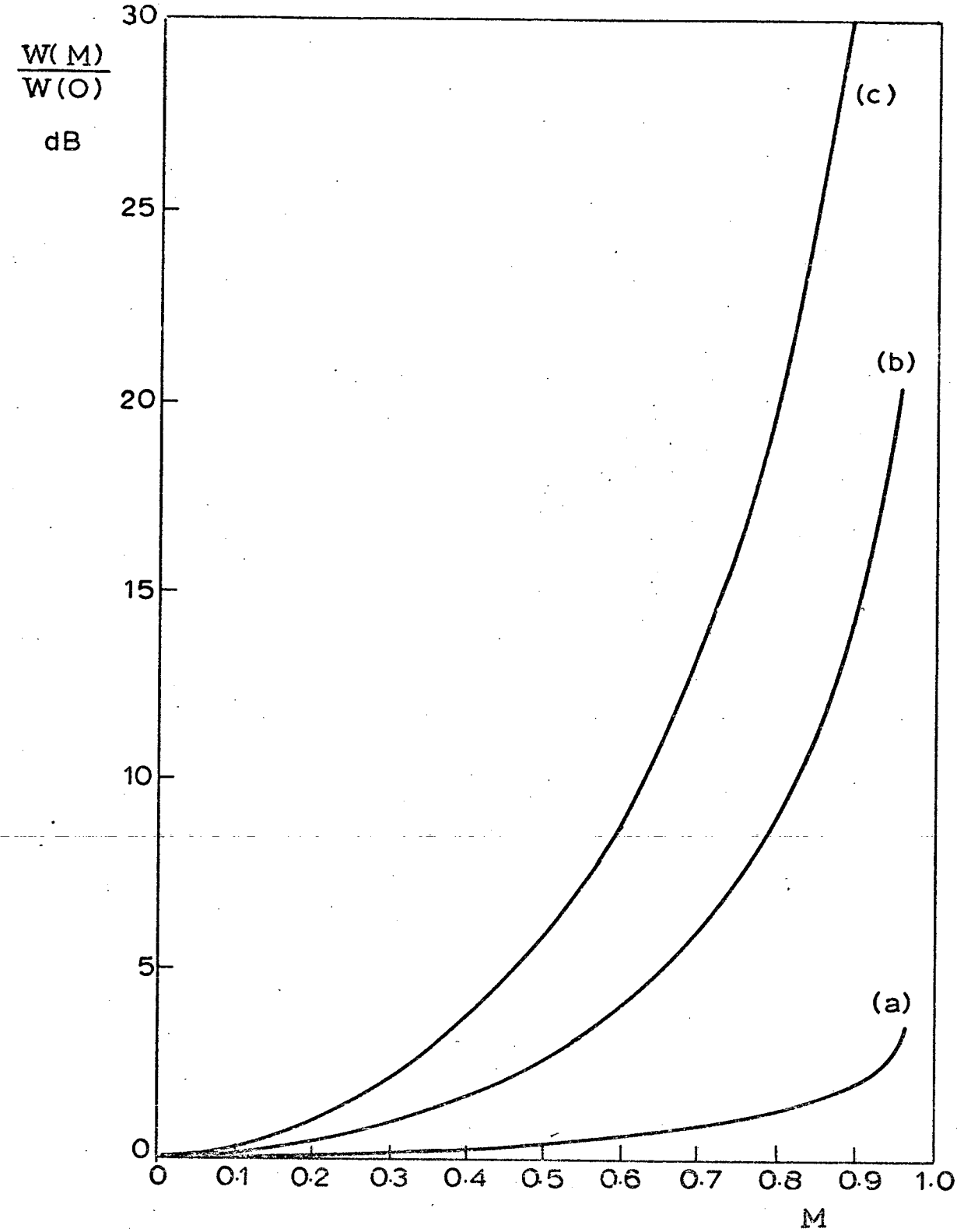

Fig. 5.3. Effect of uniform straight-line convection Mach number (M) on sound power output from (a) point acoustic source, (b) point volume velocity source and (c) point volume displacement source.

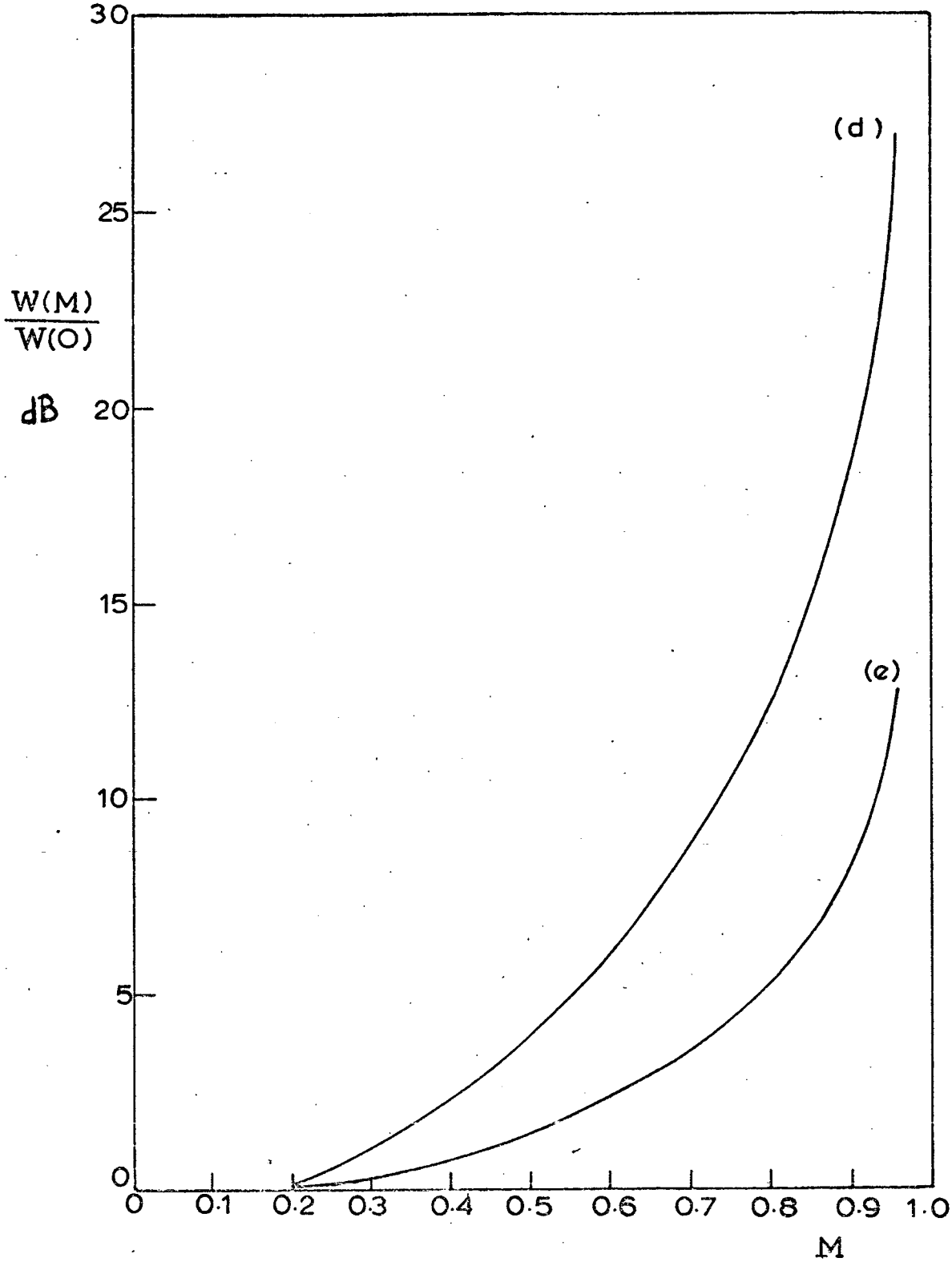

Fig.5.4 Effect of uniform straight-line convection Mach number (M) on sound power output from (d) fluctuating longitudinal force and (e) fluctuating transverse force.

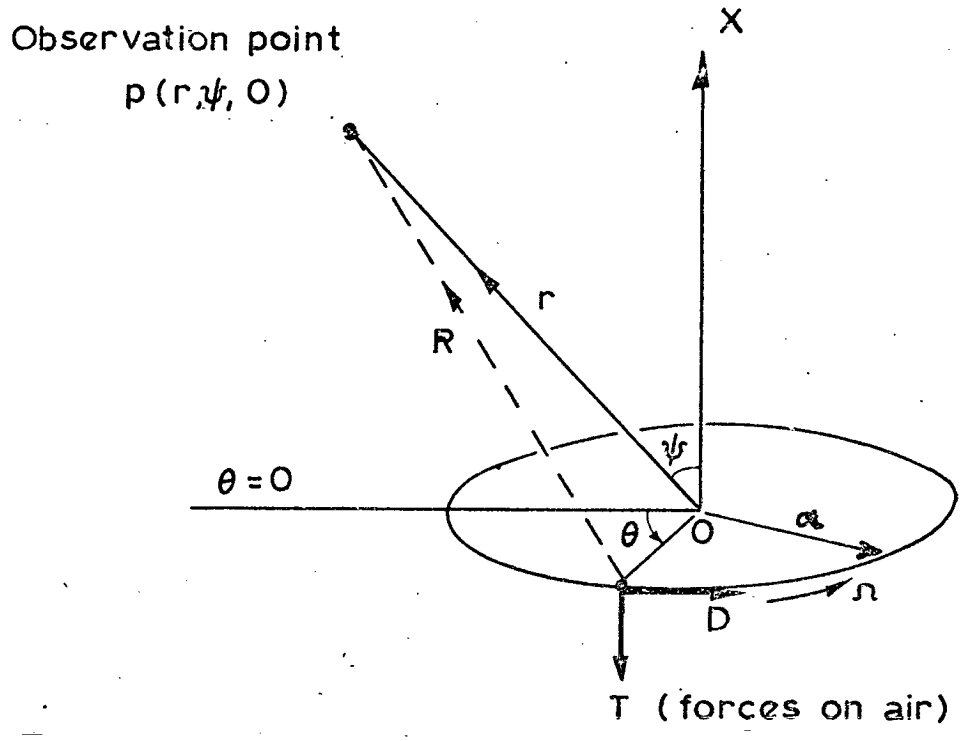

Fig. 5.5 Point force in uniform circular motion.

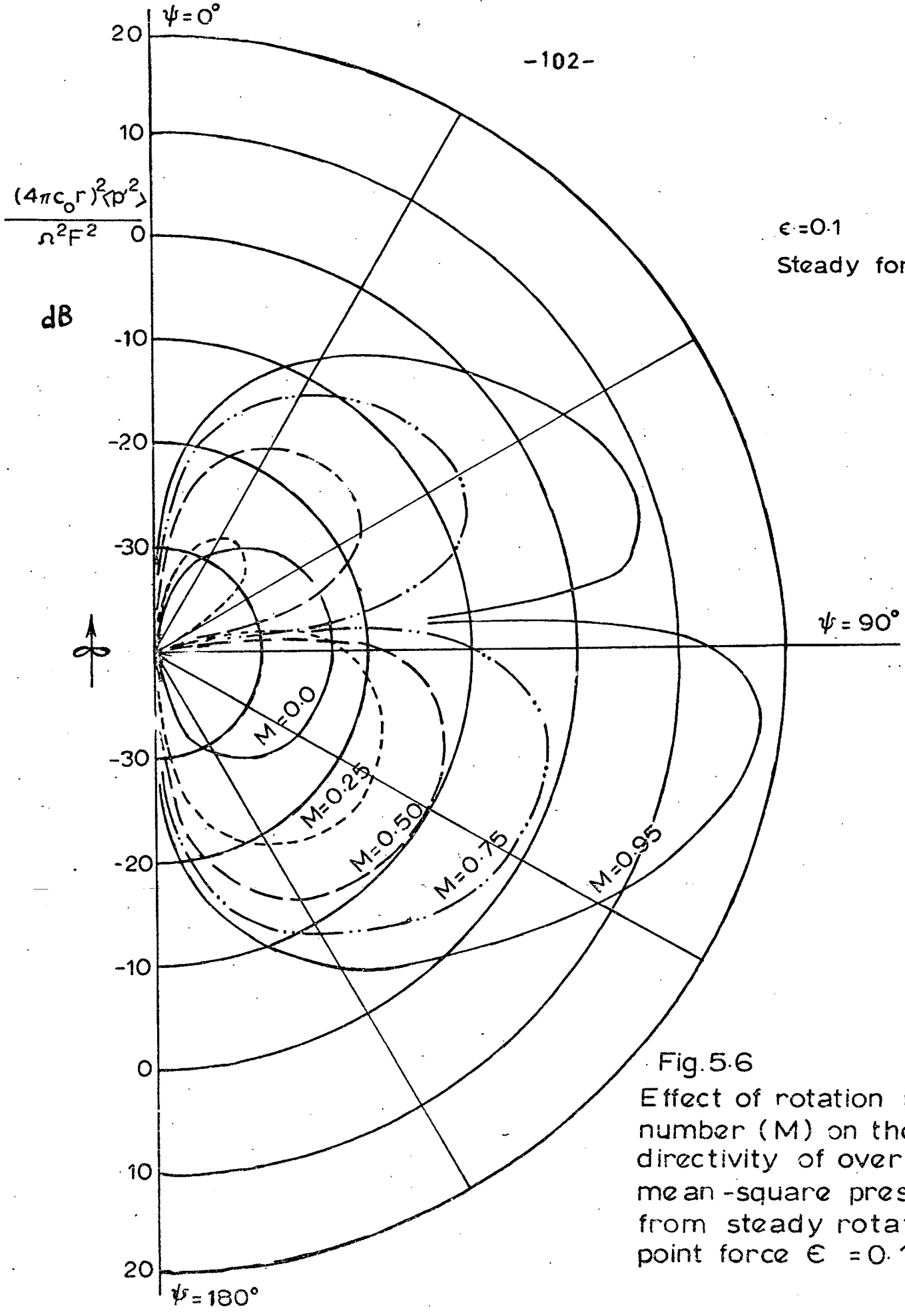

Fig. 5.6
Effect of rotation Mach number (M) on the directivity of overall mean-square pressure from steady rotating point force $\epsilon = 0.1$

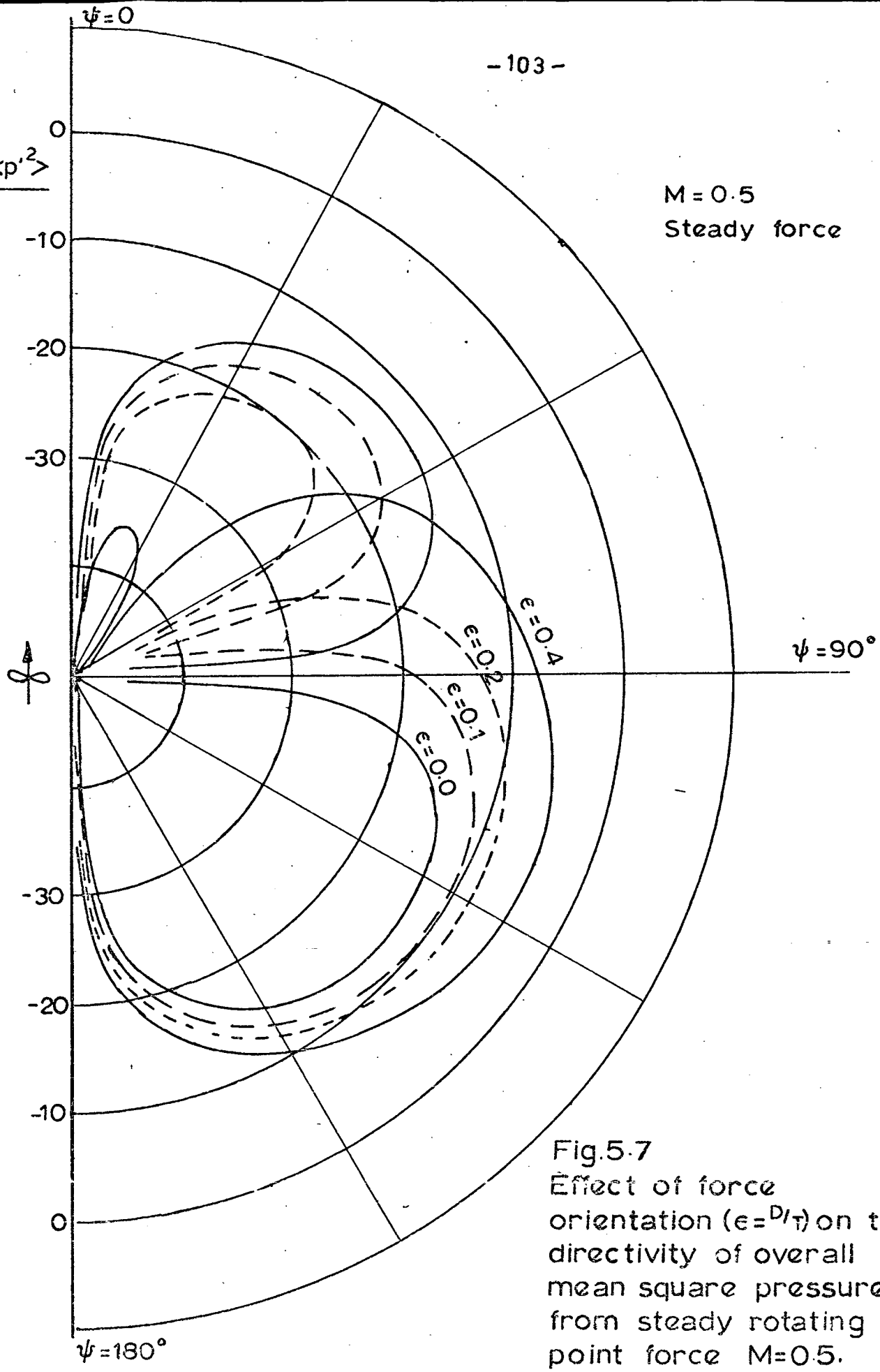

Fig.5.7
Effect of force orientation ($\epsilon = D/\tau$) on the directivity of overall mean square pressure from steady rotating point force M=0.5.

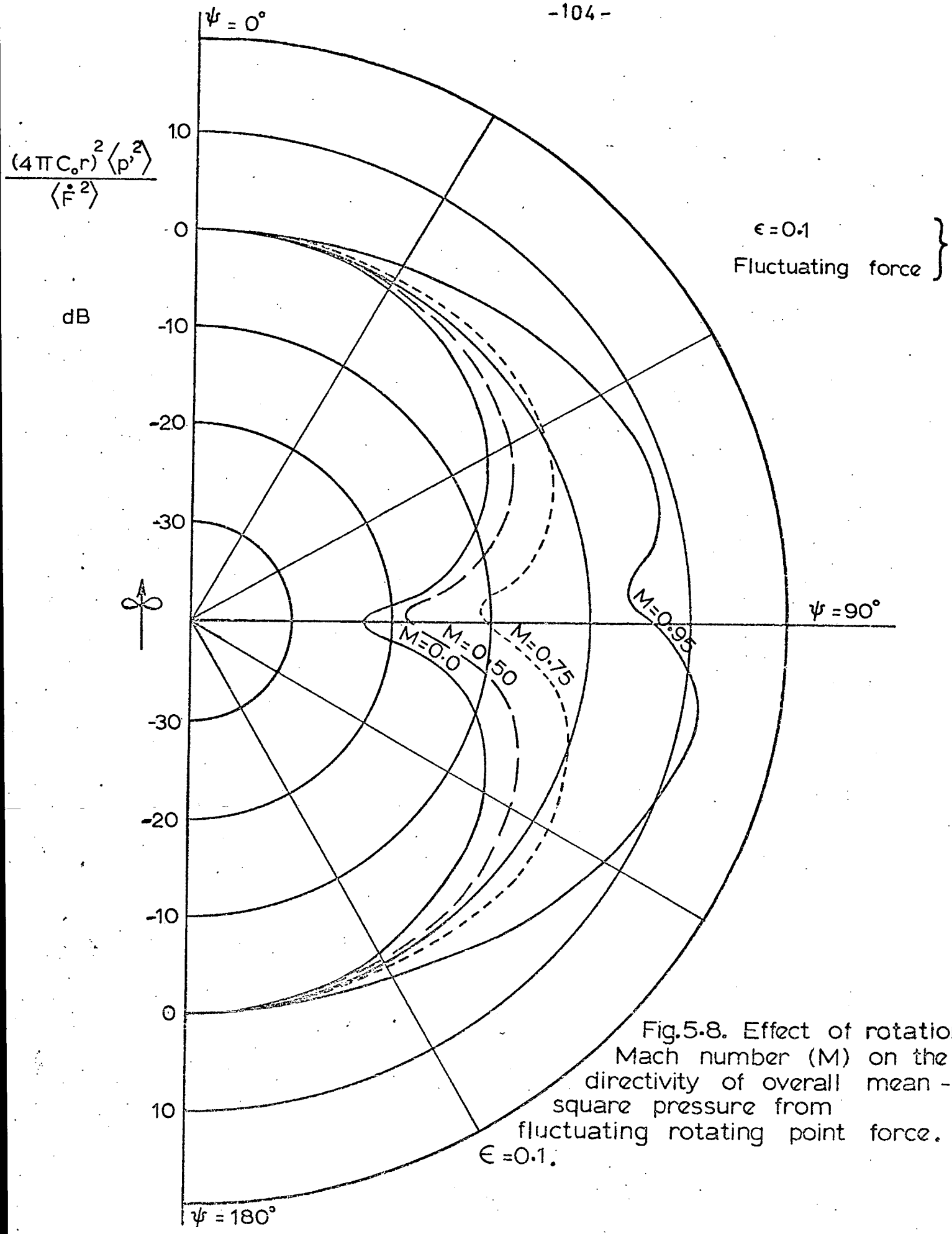

Fig.5.8. Effect of rotation Mach number (M) on the directivity of overall mean-square pressure from fluctuating rotating point force. $\epsilon = 0.1$.

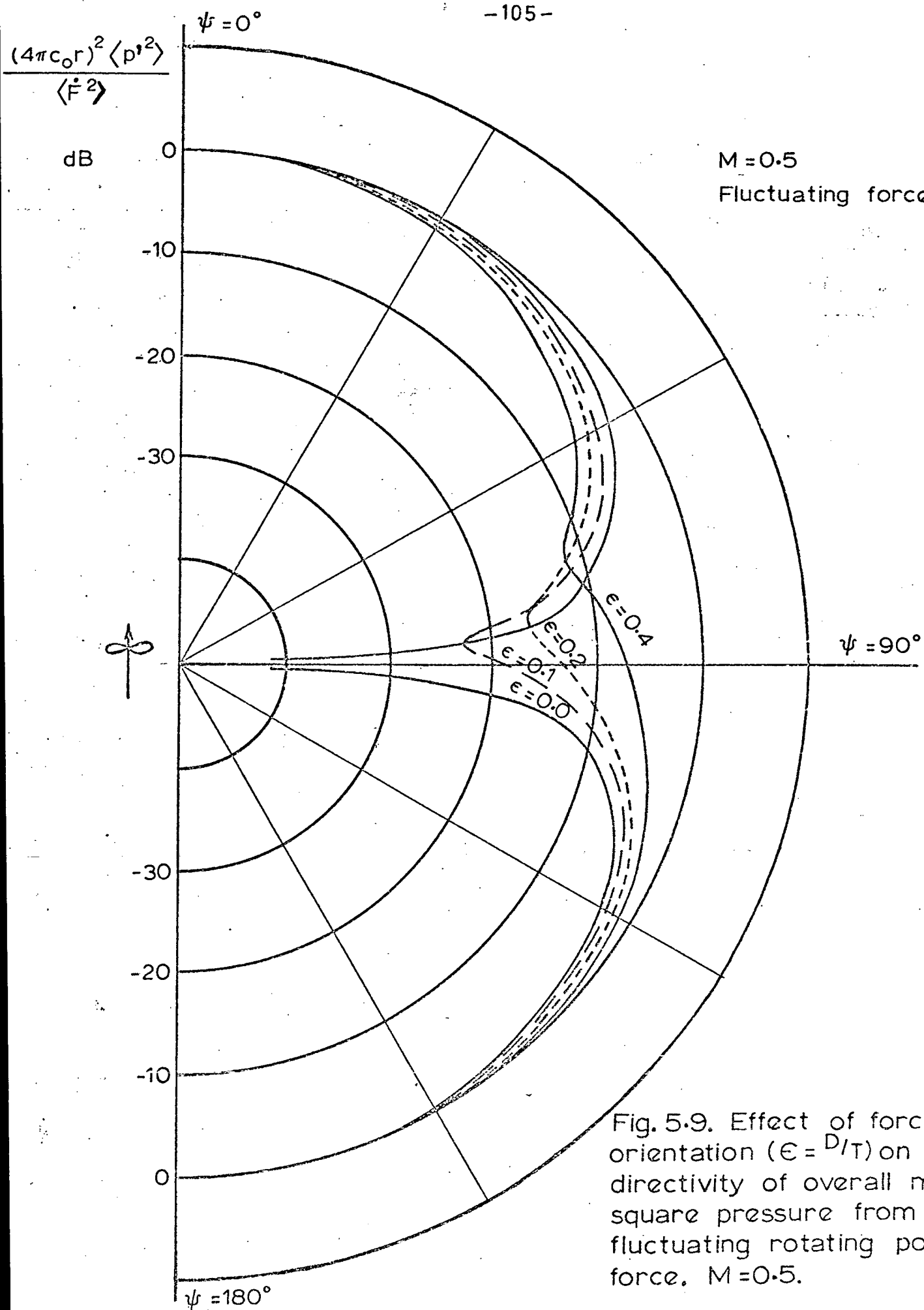

Fig. 5.9. Effect of force orientation ($\epsilon = D/T$) on the directivity of overall mean-square pressure from fluctuating rotating point force. M = 0·5.

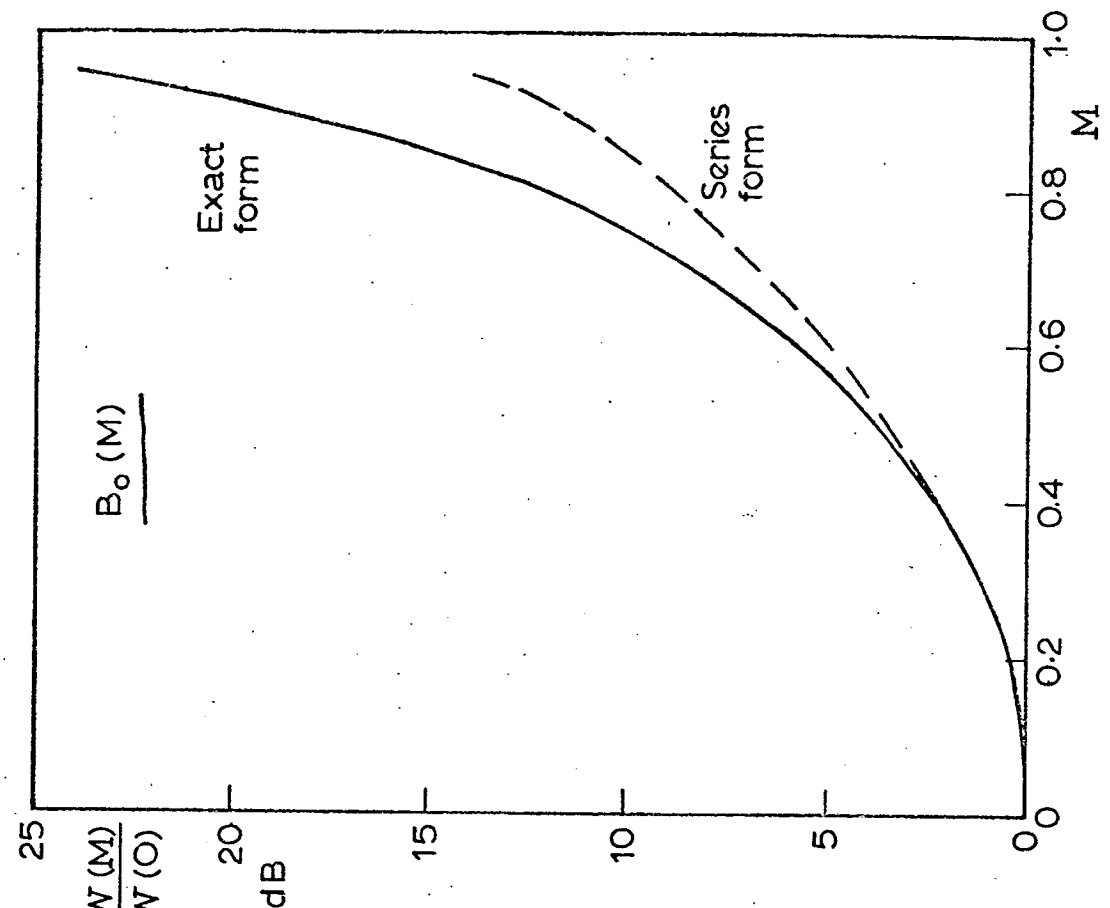

Fig. 5.10b

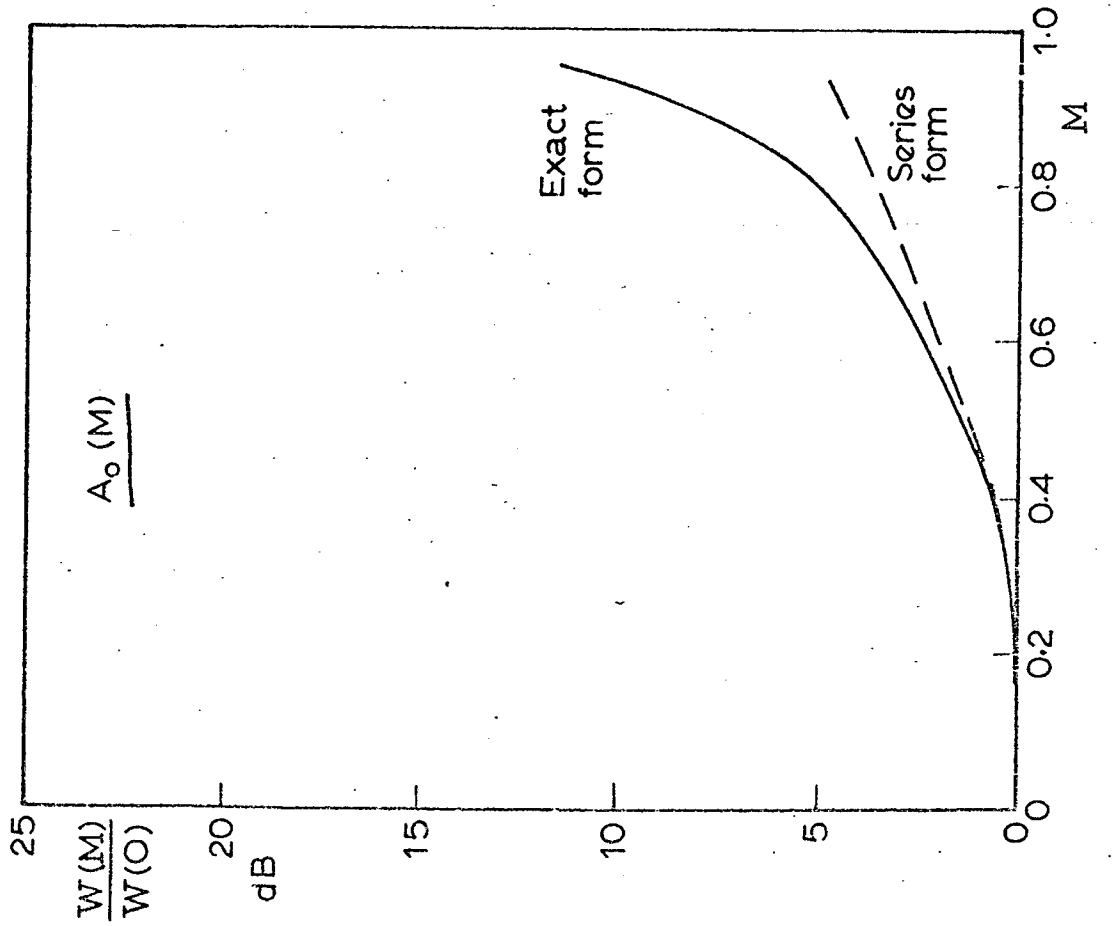

Fig. 5.10a

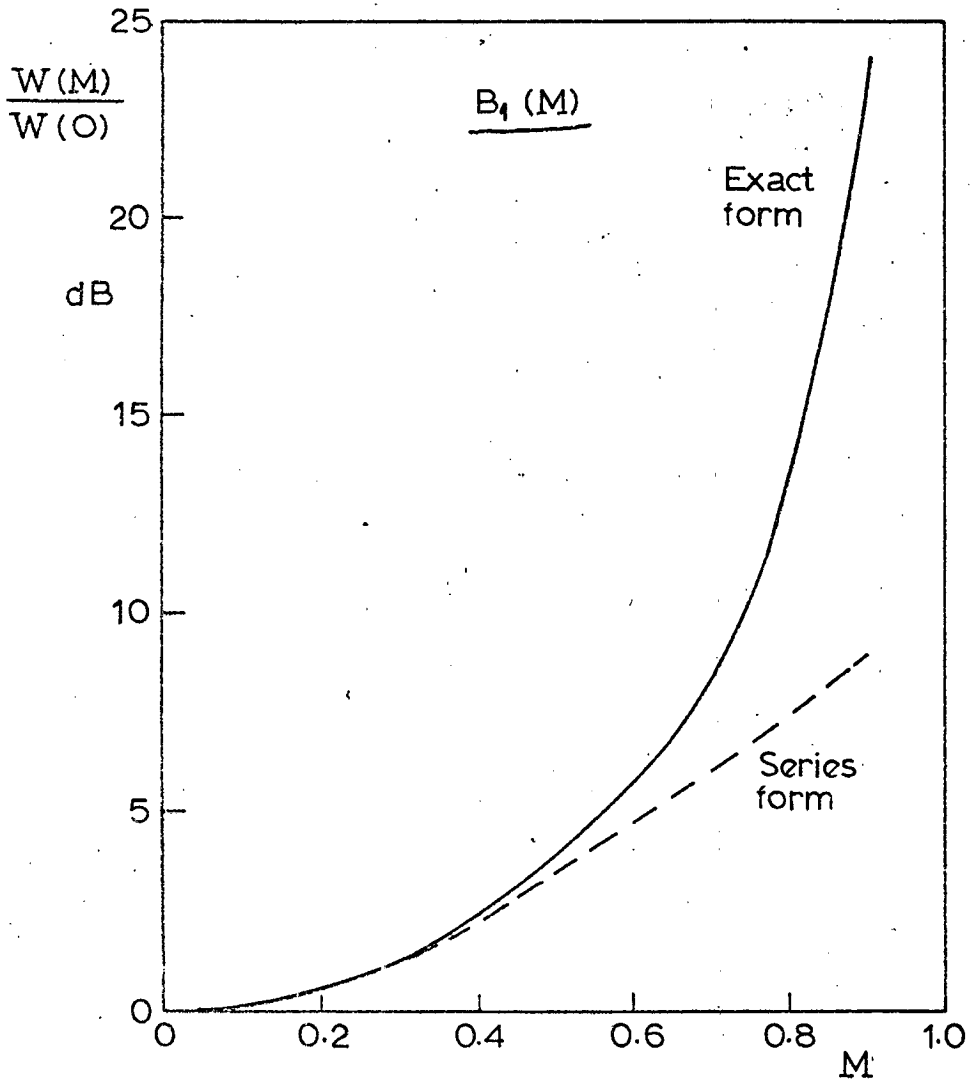

Fig.5.10 c

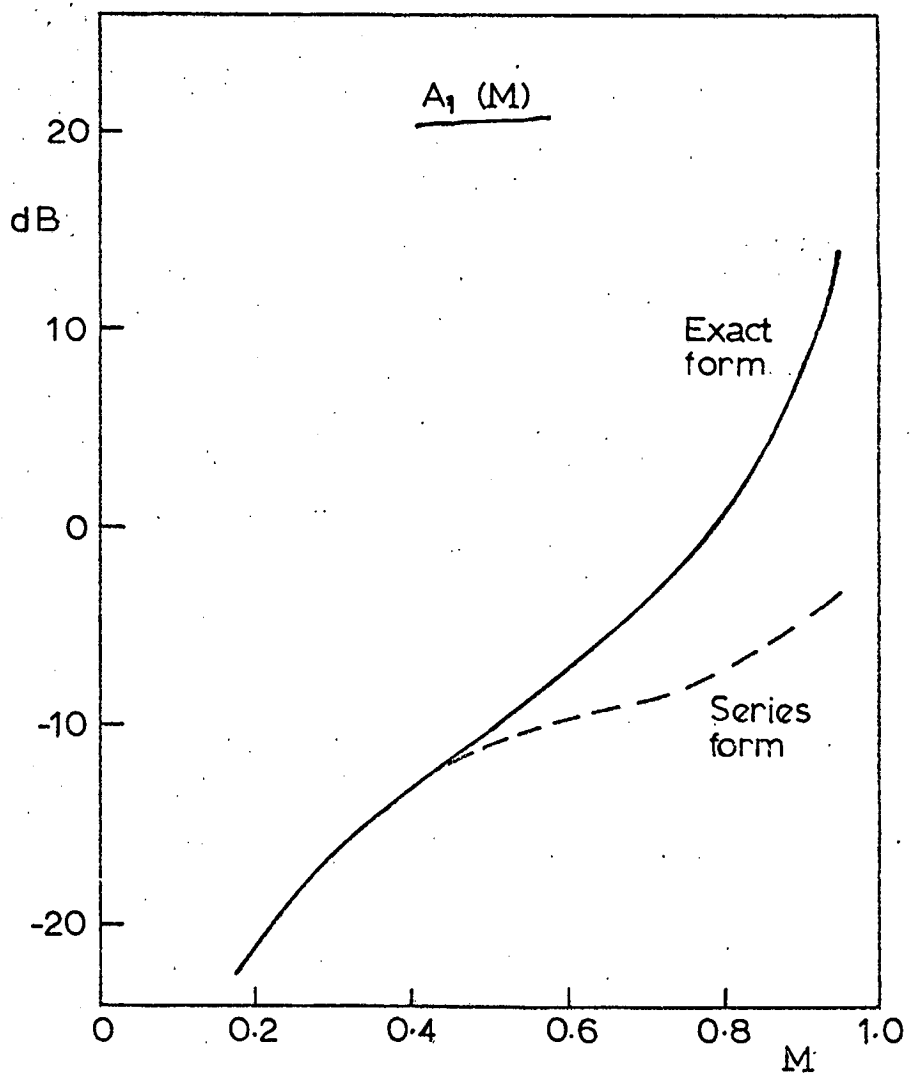

Fig.5.10 d

Fig.5.10. Comparison of series expansions of coefficients (a) $A_0(M)$, (b) $B_0(M)$, (c) $B_1(M)$ and (d) $A_1(M)$, terminated at M^4 terms, with their closed-form expressions.

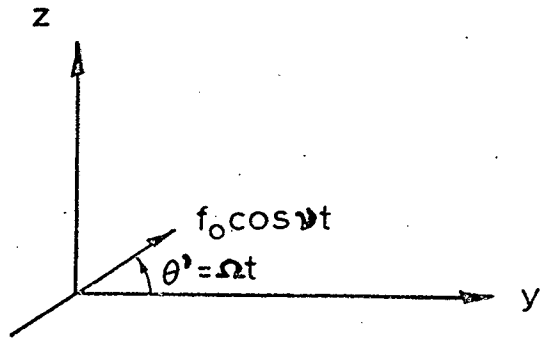

Fig. 5.11. Harmonic point force spinning in its own plane.

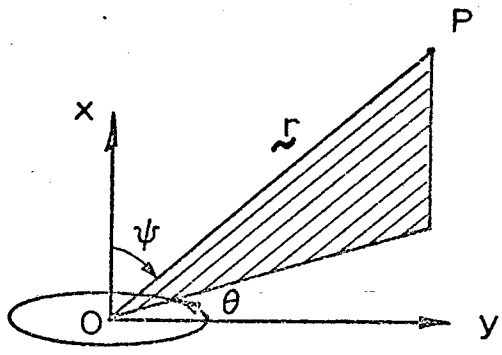

Fig. 5.12. Observation point geometry.

CHAPTER 6

SPECTRAL DENSITY OF SOUND RADIATION FROM BROADBAND ROTATING FORCES

Having obtained exact closed-form results for the overall radiation field of a rotating point force, we can now go on to derive expressions for the spectral density of the sound radiation in the far field of this rotating point force. Spectral results will be derived for a simplified case defined by the following two assumptions:

(a) The orientation of the rotating force remains constant relative to the radius vector, so that equation (5.27) applies.

(b) The rotational frequency $\Omega/2\pi$ is much less than the frequencies with which the force itself fluctuates. This means that correlation functions such as $R_{fg}(\tau)$ may be approximated by appropriate asymptotic expressions for $\tau = 0$. Terms up to and including Ω^2 will be retained in the analysis which follows.

Owing to the large amount of algebra involved in the analysis, only the outline of the method is presented in the following sections.

The spectral results will then be used to derive the properties of the radiation spectrum; in particular, the effects of finite rotational frequency Ω on the linear-motion results will be established. Finally, the theoretical results will be compared with some experimental data.

6.1 Spectral density of sound pressure

The time-averaged spectral density of the sound pressure is obtained from the pressure auto-correlation, given by equation (5.22), in three stages.

6.1.1 Ensemble-averaged pressure auto-correlation

The ensemble average of the sound pressure product in equation (5.22)

is first evaluated, for times t_1 at intervals $2\pi/\Omega$. In other words the sound pressure $p'(t_1)$ is sampled each time the rotating force passes a particular point in its revolution, and $p'(t_2)$ is sampled at time τ later. The average, over all samples, of $p'_1 p'_2$ is denoted by $\langle p'_1 p'_2 \rangle_\Omega$.

In order to evaluate expressions such as $\langle [X]_1 [Y]_2 \rangle_\Omega$ which appear in the average, $[Y]_2$ is expanded about $[t]_1 + \sigma$, where

$$\sigma = \frac{\tau}{[1 - M_r]_1} \quad . \tag{6.1}$$

Thus $[Y]_2$ is written as

$$[Y]_2 = Y\left\{ [t]_1 + [\tau] \right\} = Y\left\{ ([t]_1 + \sigma) + ([\tau] - \sigma) \right\} ,$$

which leads to the Taylor series

$$[Y]_2 = Y([t]_1 + \sigma) + ([\tau] - \sigma) \cdot \frac{dY}{dt} ([t]_1 + \sigma) + \tfrac{1}{2}([\tau] - \sigma)^2 \cdot \frac{d^2Y}{dt^2} ([t]_1 + \sigma) + \ldots \quad . \tag{6.2}$$

The series can be terminated after three terms because the variable $([\tau] - \sigma)$ is proportional to Ω (plus higher powers), as will be shown below.

In order to express $([\tau] - \sigma)$ in terms of σ, let $[t] = x(t)$. Then the source time delay $[\tau]$, corresponding to observer time delay $\tau = t_2 - t_1$, is

$$[\tau] = x(t_1 + \tau) - x(t_1) ,$$

which when expanded in series form becomes

$$[\tau] = \tau \cdot x'(t_1) + \tfrac{1}{2}\tau^2 \cdot x''(t_1) + \frac{1}{6}\tau^3 \cdot x'''(t_1) + \ldots \quad . \tag{6.3}$$

Now the source time and observer time are related by

$$\left[1 - M_r\right] d\left[t\right] = dt \tag{6.4}$$

(section 5.1); hence

$$\left.\begin{aligned} x'(t) &= \frac{1}{\left[1 - M_r\right]_1} \quad , \\ x''(t) &= \left[\frac{dM_r/dt}{(1 - M_r)^3}\right] \quad , \\ \text{and} \quad x'''(t) &= \left[\frac{d^2M_r/dt^2}{(1 - M_r)^4} + \frac{3(dM_r/dt)^2}{(1 - M_r)^5}\right] . \end{aligned}\right\} \tag{6.5}$$

From (6.3) and (6.5), writing $\tau = \sigma\left[1 - M_r\right]_1$, it follows that

$$\left[\tau\right] - \sigma = \tfrac{1}{2}\left[\frac{dM_r/dt}{1 - M_r}\right]_1 \sigma^2 + \frac{1}{6}\left[\frac{d^2M_r/dt^2}{1 - M_r} + 3\left(\frac{dM_r/dt}{1 - M_r}\right)^2\right]_1 \sigma^3 + \text{higher powers.} \tag{6.6}$$

From section 5.2 (Chapter 5), in terms of source and observer co-ordinates,

$$M_r = -\alpha\sin\theta \ , \quad \frac{dM_r}{dt} = -\Omega\alpha\cos\theta \ , \text{ and } \frac{d^2M_r}{dt^2} = \Omega^2\alpha\sin\theta \ .$$

Thus the coefficient of σ^2 in (6.6) is of order Ω, and the coefficient of σ^3 is of the order Ω^2. Only terms of order Ω^2 or less will be retained, to give a first approximation to the effects of source rotation. Thus in equation (6.2), the series for $\left[Y\right]_2$ will be terminated at the $(\left[\tau\right] - \sigma)^2$ term since this is of order Ω^2. Equations (6.2) and (6.6) together give $\left[Y\right]_2$ in terms of $Y(\left[t\right]_1 + \sigma)$ and its derivatives, all the coefficients being constant under the ensemble averaging process. The result is an

expression for $\langle [X]_1 [Y]_2 \rangle_\Omega$ in terms of $R_{XY}(\sigma)$, $R_{X\dot{Y}}(\sigma)$, and $R_{X\ddot{Y}}(\sigma)$, where these correlation functions can be evaluated as time averages rather than ensemble averages since X(t), Y(t) are assumed to be stationary random functions.

$$\langle [X]_1 [Y]_2 \rangle_\Omega = R_{XY}(\sigma) + R_{X\dot{Y}}(\sigma)\left\{ - \tfrac{1}{2}\Omega \left[\frac{\alpha\cos\theta}{1+\alpha\sin\theta}\right] \sigma^2 + \frac{1}{6}\Omega^2 \left[\frac{\alpha\sin\theta}{1+\alpha\sin\theta} + \frac{3\alpha^2\cos^2\theta}{(1+\alpha\sin\theta)^2}\right] \sigma^3 \right\} + R_{X\ddot{Y}}(\sigma)\left\{ \tfrac{1}{8}\Omega^2 \left[\frac{\alpha^2\cos^2\theta}{(1+\alpha\sin\theta)^2}\right] \sigma^4 \right\} + \ldots \quad . \tag{6.7}$$

Finally, the other factors involved in the ensemble-averaged pressure autocorrelation are of the type $\langle f_1 g_2 \rangle_\Omega$. Quantities such as $g_2 = g(t_2)$ can be expanded in a Taylor series about t_1 to give

$$g_2 = g_1 + \tau \cdot \left(\frac{dg}{dt}\right)_1 + \tfrac{1}{2}\tau^2 \cdot \left(\frac{d^2 g}{dt^2}\right)_1 + \ldots \quad , \tag{6.8}$$

where successive terms will automatically involve successive powers of Ω. It is never necessary to go beyond τ^2; sometimes even the first term is enough to give Ω^2 accuracy in the pressure autocorrelation. The functions g_1, $\left(\frac{dg}{dt}\right)_1$, $\left(\frac{d^2 g}{dt^2}\right)_1$ are easily evaluated in terms of Ω, α and $[\theta]$, starting from the definitions in equation (5.21).

The resulting ensemble average $\langle p_1' p_2' \rangle_\Omega$ is most conveniently expressed in terms of the variable σ;

$$\sigma = \frac{\tau}{[1 + \alpha\sin\theta]_1} \quad . \tag{6.9}$$

All terms in odd powers of Ω are found to contain a $\cos\theta$ factor in the final expression, and so may conveniently be deleted at this stage because

they will not contribute to the pressure field when the time average is taken.

6.1.2 Transformation to instantaneous spectral density

Once the pressure auto-correlation as an ensemble average is known, the spectral density follows by transformation. Since $R_p(\tau)$ is given in terms of $R_{XY}(\sigma)$, etc., it is convenient to carry out the transformation as follows.

Each side is multiplied by $e^{-i\omega\tau} = e^{-i\nu\sigma}$, where

$$\nu = \left[1 + \alpha\sin\theta\right]_1 \omega \tag{6.10}$$

is the source frequency which instantaneously corresponds to the observed frequency ω at time t_1. Integration over

$$d\tau = \left[1 + \alpha\sin\theta\right]_1 d\sigma \tag{6.11}$$

then gives the sound pressure spectrum $G_p(\omega)$ on the left, in terms of the force spectrum $G_T(\nu)$ and its derivatives in series form on the right. The formulae needed in the transformation are derived in Appendix VIII.

The above process gives an instantaneous sound pressure spectral density $G_p(\omega)$, for each observation time t_1 corresponding to a given source position, as an ensemble average over successive revolutions.

$$\begin{aligned}(4\pi c_o r)^2 G_p(\omega) = {} & \left(\frac{\Omega}{\nu}\right)^0 \nu^2 G_T(\nu) \cdot \left[(1+\alpha\sin\theta)^{-3}\right]\left\{\cos^2\psi\left[1\right]+\varepsilon\sin\psi\cos\psi\left[2\sin\theta\right]\right. \\ & \left. + \varepsilon^2\sin^2\psi\left[\sin^2\theta\right]\right\} \\ & + \left(\frac{\Omega}{\nu}\right)^2 \nu^2 G_T(\nu)\left\{\cos^2\psi\left[0\right]+\varepsilon\sin\psi\cos\psi\left[0\right]+\varepsilon^2\sin^2\psi\left[0\right]\right\} \\ & + \left(\frac{\Omega}{\nu}\right)^2 \nu^3 G_T'(\nu) \cdot \left[(1+\alpha\sin\theta)^{-5}\right]\left\{\cos^2\psi\left[0\right]\right. \\ & + \varepsilon\sin\psi\cos\psi\left[\sin\theta+\alpha\cos^2\theta+2\alpha\sin^2\theta+\alpha^2\cos^2\theta\sin\theta+\alpha^2\sin^3\theta\right] \\ & \left. + \varepsilon^2\sin^2\psi\left[\sin^2\theta-\cos^2\theta-\alpha\cos^2\theta\sin\theta+2\alpha\sin^3\theta+\alpha^2\sin^4\theta\right]\right\}\end{aligned}$$

$$+ \left(\frac{\Omega}{\nu}\right)^2 \nu^4 G''_T(\nu) \cdot \left[(1+\alpha\sin\theta)^{-5}\right]\Big\{\cos^2\psi\left[\tfrac{1}{2}\alpha\sin\theta+\tfrac{1}{2}\alpha^2\right]$$

$$+ \varepsilon\sin\psi\cos\psi\left[\tfrac{1}{2}\sin\theta+2\alpha\sin^2\theta-2\alpha\cos^2\theta-\alpha^2\cos^2\theta\sin\theta+\frac{3}{2}\alpha^2\sin^3\theta\right]$$

$$+ \varepsilon^3\sin^2\psi\left[\tfrac{1}{2}\sin^2\theta-2\alpha\cos^2\theta\sin\theta+\frac{3}{2}\alpha\sin^3\theta+\alpha^2\sin^4\theta-\frac{3}{2}\alpha^2\cos^2\theta\sin^2\theta\right]\Big\}$$

$$+ \left(\frac{\Omega}{\nu}\right)^2 \nu^5 G'''_T(\nu) \cdot \left[(1+\alpha\sin\theta)^{-5}\right]\Big\{\cos^2\psi\left[\frac{1}{6}\alpha\sin\theta+\frac{1}{6}\alpha^2\sin^2\theta-\tfrac{1}{2}\alpha^2\cos^2\theta\right]$$

$$+ \varepsilon\sin\psi\cos\psi\left[\tfrac{1}{3}\alpha\sin^2\theta-\tfrac{1}{2}\alpha\cos^2\theta+\tfrac{1}{3}\alpha^2\sin^3\theta-\frac{3}{2}\alpha^2\cos^2\theta\sin\theta\right]$$

$$+ \varepsilon^2\sin^2\psi\left[\frac{1}{6}\alpha\sin^3\theta-\tfrac{1}{2}\alpha\cos^2\theta\sin\theta+\frac{1}{6}\alpha^2\sin^4\theta-\alpha^2\cos^2\theta\sin^2\theta\right]\Big\}$$

$$+ \left(\frac{\Omega}{\nu}\right)^2 \nu^6 G^{iv}_T(\nu) \cdot \left[(1+\alpha\sin\theta)^{-5}\right]\Big\{\cos^2\psi\left[-\tfrac{1}{8}\alpha^2\cos^2\theta\right]+$$

$$+ \varepsilon\sin\psi\cos\psi\left[-\tfrac{1}{4}\alpha^2\cos^2\theta\sin\theta\right] + \varepsilon^2\sin^2\psi\left[-\tfrac{1}{8}\alpha^2\cos^2\theta\sin^2\theta\right]\Big\}$$

$$+ \text{terms of order } \left(\frac{\Omega}{\nu}\right)^4 \text{ and higher,} \qquad (6.12)$$

where the prime denotes differentiation with respect to ν . The variation of the spectrum $G_p(\omega)$ with time t_1 corresponds to the variation in sound heard as the force moves round, for slow enough rotation.

6.1.3 Time-averaged spectrum

The time-averaged sound pressure spectral density $\overline{G}_p(\omega)$ can be obtained simply by averaging the result of equation (6.12) over t_1, in this case over one revolution of the source. Although the time-average could have been performed before the transformation was carried out, it was found easier to do it at this later stage. The method for time-averaging functions of $[\theta]$ is indicated in Appendix VII; but before this is done, it should be noted that the source frequency ν corresponding to a fixed value of ω is not constant but varies with t_1. Therefore ν , and the force spectrum $G_T(\nu)$, need to be rewritten in terms of ω and $G_T(\omega)$ before

the time-average is taken. This is done by expanding $G_T(\nu)$ as a series in $G_T(\omega)$;

$$G_T(\nu) = G_T(\omega) + (\nu-\omega)G'_T(\omega) + \tfrac{1}{2}(\nu-\omega)^2 G''_T(\omega) + \frac{1}{6}(\nu-\omega)^3 G'''_T(\omega) + \frac{1}{24}(\nu-\omega)^4 G^{iv}_T(\omega) + \ldots \quad . \tag{6.13}$$

Since the source frequency is related to the observer frequency by $\nu = \omega\left[1 + \alpha\sin\theta\right]_1$, the above series can be expressed as

$$G_T(\nu) = G_T(\omega) + \omega\left[\alpha\sin\theta\right] G'_T(\omega) + \tfrac{1}{2}\omega^2\left[\alpha^2\sin^2\theta\right] G''_T(\omega) + \frac{1}{6}\omega^3\left[\alpha^3\sin^3\theta\right] G'''_T(\omega) + \frac{1}{24}\omega^4\left[\alpha^4\sin^4\theta\right] G^{iv}_T(\omega) + \ldots \quad . \tag{6.14}$$

Four terms are sufficient to give accuracy up to α^4 terms. The time-averaged sound pressure spectral density, accurate up to α^4 terms, is then obtained as

$$\begin{aligned}(4\pi c_o r)^2\, \overline{G}_p(\omega) \doteq (\tfrac{\Omega}{\omega})^0 \Big\{ & \omega^2 G_T(\omega)\left(\cos^2\psi(1) + \varepsilon^2\sin^2\psi(\tfrac{1}{2})\right) + \omega^3 G'_T(\omega)\left(\varepsilon\sin\psi\cos\psi(\alpha)\right) \\ & + \omega^4 G''_T(\omega)\left(\cos^2\psi(\tfrac{1}{4}\alpha^2) + \varepsilon^2\sin^2\psi(\tfrac{3}{16}\alpha^2)\right) + \omega^5 G'''_T(\omega)\left(\varepsilon\sin\psi\cos\psi(\tfrac{1}{8}\alpha^3)\right) \\ & + \omega^6 G^{iv}_T(\omega)\left(\cos^2\psi(\tfrac{1}{64}\alpha^4) + \varepsilon^2\sin^2\psi(\tfrac{5}{384}\alpha^4)\right)\Big\} \\ & + (\tfrac{\Omega}{\omega})^2\Big\{\omega^4 G''_T(\omega)\left(\varepsilon^2\sin^2\psi(\tfrac{1}{4})\right) + \omega^5 G'''_T(\omega)\left(\varepsilon\sin\psi\cos\psi(\tfrac{1}{6}\alpha)\right) \\ & + \omega^6 G^{iv}_T(\omega)\left(\cos^2\psi(\tfrac{1}{48}\alpha^2) + \varepsilon\sin\psi\cos\psi(\tfrac{1}{16}\alpha^3) + \varepsilon^2\sin^2\psi(\tfrac{5}{64}\alpha^2)\right)\Big\} \\ & + \ldots\ldots \text{ terms of order } (\tfrac{\Omega}{\omega})^4 \text{ and higher.}\end{aligned} \tag{6.15}$$

Several interesting features of the radiation spectrum can now be obtained from the above result.

6.1.4 Radiation spectrum in particular cases

(1) Equation (6.15) gives the radiation spectrum on the axis of rotation as

$$(4\pi c_o r)^2 \, \overline{G}_p(\omega) = \omega^2 G_T(\omega) \quad , \tag{6.16}$$

in agreement with [7] . The on-axis radiation is independent of source motion (M and Ω) and is controlled by the thrust component of the rotating force, whereas the radiation in the plane of rotation is controlled by the drag component.

(2) For a pure thrust force, the radiation at any angle is given by

$$(4\pi c_o r)^2 \, \overline{G}_p(\omega) \doteq (\tfrac{\Omega}{\omega})^0 \cos^2\psi \left\{ \omega^2 G_T(\omega) + \tfrac{1}{4}\alpha^2.\omega^4 G_T''(\omega) + \frac{1}{64}\alpha^4.\omega^6 G_T^{iv}(\omega) \right\}$$
$$+ (\tfrac{\Omega}{\omega})^2 \cos^2\psi \left\{ \frac{1}{48}\alpha^2.\omega^6 G_T^{iv}(\omega) \right\} + \ldots \quad . \tag{6.17}$$

Thus if the thrust spectrum is linear in ω , circular motion has no effect on the radiation spectrum because the derivative terms G_T'' , etc. in (6.17) all vanish. This agrees with the results of Ffowcs Williams and Hawkings [7] and Morse and Ingard [6].

(3) For a pure drag force of spectral density $G_D(\omega)$, equation (6.15) gives

$$(4\pi c_o r)^2 \, \overline{G}_p(\omega) \doteq (\tfrac{\Omega}{\omega})^0 \sin^2\psi \left\{ \tfrac{1}{2}\omega^2 G_D(\omega) + \frac{3}{16}\alpha^2.\omega^4 G_D''(\omega) + \frac{5}{384}\alpha^4.\omega^6 G_D^{iv}(\omega) \right\}$$
$$+ (\tfrac{\Omega}{\omega})^2 \sin^2\psi \left\{ \tfrac{1}{4}\omega^4 G_D''(\omega) + \frac{5}{64}\alpha^2.\omega^6 G_D^{iv}(\omega) \right\} + \ldots \quad . \tag{6.18}$$

Thus if $G_D(\omega)$ is linear in ω (which includes the flat spectrum and a spectrum rising at 3 dB/octave as special cases), circular motion again has no effect on the radiation spectrum. This does not mean that the overall radiation is unaffected - compare section 5.2 (Chapter 5).

The special case of this result for M = 0 can in fact be derived at an earlier stage in the analysis without any approximation, as shown in Appendix IX. It can also be obtained from equation (41) of [7], if the fixed-axis force spectrum used by Ffowcs Williams and Hawkings is converted to the rotating frame of reference.

(4) In the case of a helicopter rotor, the typical blade force spectrum is proportional to ω^{-2} (6 dB/octave fall-off) over part of the frequency range. The corresponding radiation spectrum follows from (6.15); in normalized form, it is

$$\frac{(4\pi c_o r)^2\, \bar{G}_p(\omega)}{\omega^2 G_F(\omega)} \doteq \frac{1}{1+\varepsilon^2}\left\{\cos^2\psi\left(1+\tfrac{3}{2}\alpha^2+\tfrac{15}{8}\alpha^4\right)+\varepsilon\sin\psi\cos\psi\left(-2\alpha-3\alpha^3\right)+\varepsilon^2\sin^2\psi\left(\tfrac{1}{2}+\tfrac{9}{8}\alpha^2+\tfrac{25}{16}\alpha^4\right)\right\}$$
$$+\left(\frac{\Omega}{\omega}\right)^2\frac{1}{1+\varepsilon^2}\left\{\cos^2\psi\left(\tfrac{5}{2}\alpha^2\right)+\varepsilon\sin\psi\cos\psi\left(-4\alpha+\tfrac{15}{2}\alpha^3\right)+\varepsilon^2\sin^2\psi\left(\tfrac{3}{2}+\tfrac{75}{8}\alpha^2\right)\right\}, \qquad (6.19)$$

where the resultant force spectral density $G_F (= G_T + G_D)$ has been used for normalization.

Figures 6.1 to 6.6 show various calculations based on equation (6.19). The in-plane radiation from a pure drag force is plotted in Fig. 6.1, showing the increase in spectrum level as either M or (Ω/ω) is increased. The effects of varying (Ω/ω), ε and M are illustrated in the polar diagrams of Figs. 6.2, 6.3 and 6.4, with the values $(\Omega/\omega) = 0$, $\varepsilon = 0.1$ and $M = 0.5$ used to form a standard case. Finally, the polar diagrams for pure thrust and drag forces are plotted in Figs. 6.5 and 6.6, for various values of M in the limit $(\Omega/\omega) = 0$.

(5) The validity of assuming a power-law approximation to the force

spectrum, as in (4) above, depends on the fact that for small (Ω/ω) values, the radiation spectrum at frequency ω comes almost entirely from a limited band of the force spectrum between $\omega(1-M)$ and $\omega(1+M)$. Any approximation to the shape of the force spectrum therefore applies to this band of frequencies only.

(6) For a narrow-band force spectrum with centre-frequency ν, the radiation spectrum becomes progressively broader as the observation point moves from the axis to the plane of rotation: (a) for $M = 0$ (pure rotation), the in-plane radiation spectrum is the sum of contributions from force spectra with centre-frequencies $(\nu-\Omega)$ and $(\nu+\Omega)$, as shown in Appendix IX; and (b) for finite M and $\Omega \to 0$, the instantaneous radiation spectrum has a centre-frequency which varies between the limits $\frac{\nu}{1+M}$ and $\frac{\nu}{1-M}$, giving a broader time-averaged radiation spectrum in the plane of rotation than on the axis.

6.1.5 Comparison with previous work

The exact result obtained by Ffowcs Williams and Hawkings [7, eqn. (39)] from their analysis of the same problem is, in the present notation,

$$(4\pi c_o r)^2 \, \bar{G}_p(\omega) = \omega^2 \sum_{n=-\infty}^{\infty} G_{F_r}(\omega - n\Omega) \, J_n^2\left(\frac{\omega}{\Omega}\alpha\right). \qquad (6.20)$$

Here G_{F_r} is the power spectral density of the force component $F_r(t)$ in the direction of the observer.

When (Ω/ω) is small, results (6.15) and (6.20) must give identical numerical answers for identical force inputs. On the other hand, when (Ω/ω) is large, equation (6.20) must be used to calculate the combined effects of M and Ω on the spectrum of the radiated sound, and no analytical simplification appears possible.

An attempt was made to derive equation (6.19) from (6.20) by series expansion for small arguments of the Bessel functions; the correct result was obtained for the special case of a pure thrust force ($\varepsilon = 0$), but not otherwise. In general, any approximation based on (6.20) which involves series expansion of the Bessel functions about zero argument is suspect. The reason is simply that the argument $(\frac{\omega}{\Omega}\alpha)$ becomes large when α is finite and (Ω/ω) is small - the situation assumed in the present analysis.

6.2 Spectral density of total sound power

The sound power output per unit frequency bandwidth follows from equation (6.15) by integrating over a spherical surface r = constant:

$$\frac{dW}{d\omega} = \frac{2\pi r^2}{\rho_o c_o} \int_o^\pi \overline{G}_p(\omega) \sin\psi . \, d\psi \quad . \tag{6.21}$$

Noting that $\alpha = M \sin\psi$ in (6.15), we get the general result accurate to M^4 as

$$12\pi\rho_o c_o^3 \cdot \frac{dW}{d\omega} = (\frac{\Omega}{\omega})^o \left\{ \omega^2 G_T(\omega).(1 + \varepsilon^2) + \omega^4 G_T''(\omega).(\frac{1}{10} + \frac{3}{10}\varepsilon^2)M^2 + \omega^6 G_T^{iv}(\omega).(\frac{1}{280} + \frac{1}{56}\varepsilon^2)M^4 \right\}$$

$$+ (\frac{\Omega}{\omega})^2 \left\{ \omega^4 G_T''(\omega).\tfrac{1}{2}\varepsilon^2 + \omega^6 G_T^{iv}(\omega).(\frac{1}{120} + \tfrac{1}{8}\varepsilon^2)M^2 \right\}$$

$$+ \ldots \quad ; \tag{6.22}$$

the thrust and drag contributions are additive.

For a force spectrum $G_F(\omega)$ which falls at 6 dB/octave, the normalized sound power spectrum is

$$\frac{12\pi\rho_o c_o^3}{\omega^2 G_F(\omega)} \frac{dW}{d\omega} = \frac{1}{1+\varepsilon^2} \left\{ (1 + \tfrac{3}{5}M^2 + \tfrac{3}{7}M^4) + \varepsilon^2 (1 + \tfrac{9}{5}M^2 + \tfrac{15}{7}M^4) \right\}$$

$$+ \left(\frac{\Omega}{\omega}\right)^2 \frac{1}{1+\varepsilon^2} \left\{ M^2 + \varepsilon^2 (3 + 15M^2) \right\} + \ldots \quad , \qquad (6.23)$$

accurate up to and including M^4 terms. The leading term in (6.23) can in fact be obtained in exact closed-form, by noting that it represents the limiting case of uniform straight-line motion ($\Omega = 0$), for which Morse and Ingard's analysis [6] gives

$$\frac{12\pi\rho_o c_o^3}{\omega^2 G_F(\omega)} \frac{dW}{d\omega} = \frac{1}{1+\varepsilon^2} A_2(M) + \frac{\varepsilon^2}{1+\varepsilon^2} B_2(M) \quad , \left(\frac{\Omega}{\omega} = 0,\ M < 1\right); \qquad (6.24)$$

$$A_2(M) = \frac{3}{M^3} \left\{ \tfrac{1}{2} \ln\left(\frac{1+M}{1-M}\right) - M \right\} = 1 + \tfrac{3}{5}M^2 + \tfrac{3}{7}M^4 + \ldots \quad , \qquad (6.25)$$

$$B_2(M) = \frac{3}{M^3} \left\{ \frac{M(2-M^2)}{1-M^2} - \ln\left(\frac{1+M}{1-M}\right) \right\} = 1 + \tfrac{9}{5}M^2 + \tfrac{15}{7}M^4 + \ldots \quad . \qquad (6.26)$$

(see Appendix X for details).

Numerical results for the 6 dB/octave fall-off force spectrum are shown in Figs. 6.7 and 6.8, based on equation (6.23). Also included is the exact result (6.24) for $(\Omega/\omega) = 0$, in order to show the effect of neglecting M^6 and higher-order terms in the series approximation. The main conclusions are that the series approximation is within ½ dB of the exact value for Mach numbers below 0.8; and the effect of finite Ω on the sound power spectrum becomes more pronounced as ε and M are increased.

6.3 Comparison with experimental results

Measured directivities of discrete tone sound pressure from three different rotor geometries are compared with predicted directivities and the results are presented in Fig. 6.9, 6.10 and 6.11.

The theoretical directivities for all cases are predicted by assuming that the equivalent point force spectrum falls off at 6 dB per octave over the appropriate frequency range - equation (6.19). This means that the theory predicts the envelope of the discrete tone spectrum at any observer angle for randomly phased blade loading harmonics, falling in amplitude at 6 dB per octave with frequency. Since the radiation spectrum on the rotor axis is proportional to the force spectrum, the on-axis levels of the theoretical directivities are adjusted to coincide with those of the measured directivities; the level at any other observer angle (ψ) is then plotted relative to the level at $\psi = 0^{o}$. Bearing these in mind, we can now discuss the comparison for each rotor in detail.

(a) Rolls-Royce (Old Hall, Derby) fan [30], 3000 r.p.m. (Fig. 6.9)

The correlation is within $\pm$ 2 dB. The theoretical directivity assumes random blade loading harmonic phase and so it does not contain the details of the measured directivity. The measured directivity is that of a discrete tone at mB = 28 and the detailed structure is because it contains the actual blade loading harmonic phase information.

The above comment will apply to (b) and (c) below as well.

(b) I.S.V.R. fan [31], 3600 r.p.m. (Fig. 6.10)

The comparisons between theoretical and measured directivities of discrete tones at the blade-passing frequencies of 5, 8 and 10 bladed rotors operating in free field are shown here.

The correlation for the 5 and 8 bladed rotors is not as good as that for the 10 bladed rotors. This is because of the fact that for rotors with small number of blades (up to 5 in this case), the discrete tone radiation at the blade-passing frequency is usually dominated by the steady loading. The comparison therefore is not really valid here because the ratio (Ω/ω) would be infinite when $\omega = 0$, and the theory is valid only when the frequency (ω) with which the force fluctuates is larger than the rotational frequency (Ω).

The lower and upper limits of the bands of frequencies (ω) of the force spectrum which contribute towards the observed blade-passing frequencies $(B\Omega)$ are:

	ω	(Ω/ω)
5-bladed rotor	$5\Omega(1 - M) < \omega < 5\Omega(1 + M)$	$0.167 < (\frac{\Omega}{\omega}) < 0.25$
8-bladed rotor	$8\Omega(1 - M) < \omega < 8\Omega(1 + M)$	$0.104 < (\frac{\Omega}{\omega}) < 0.156$
10-bladed rotor	$10\Omega(1 - M) < \omega < 10\Omega(1 + M)$	$0.083 < (\frac{\Omega}{\omega}) < 0.125$.

The correlation between theory and experiment should improve as the upper limit of the frequency ratio (Ω/ω) decreases, and therefore as the rotor blade number increases. This is in fact true as Fig. 6.10 shows. For the 10-bladed case, the theory predicts the directivity within $\pm$ 2 dB of the measured directivity.

(c) I.S.V.R. model rotor [32], 1800 r.p.m. (Fig. 6.11)

The figures show the comparison between theoretical and measured directivities of sound pressure level for various frequency ratios (Ω/ω) between the limits 0.111 and 0.017. The measured directivities are those of rotational noise harmonics m = 3, 5, 7, 11, 15 and 20 from

the 3-bladed I.S.V.R. helicopter rotor rig operating in the anechoic room [32]. Looking at the measured directivity plots, it appears that they contain sharp fluctuations in level, superimposed on the general shape. These fluctuations are time fluctuations and not angular fluctuations, as shown experimentally by Stainer [32]. This was also demonstrated computationally in Chapter 3, where the time-averaged directivity plots did not show any sharp angular fluctuations. Thus it is reasonable to plot the theoretical directivities on top of the measured directivities as shown in Fig. 6.11.

The correlation between theoretical and experimental directivities is excellent at all frequencies considered, and therefore it suggests that a fall-off of 6 dB per octave for the point force spectrum is a good assumption for the low solidity rotor considered here.

In comparing the theoretical and measured directivities above, the theory assumes that the distributed blade force can be represented by its resultant acting at a point on the blade. A few comments about the validity of this point force representation are therefore appropriate here.

Point force representation

In Chapter 3, it was shown that (a) the chordwise load distribution effects become important when predicting the actual levels of various harmonics, especially when $ka > 1$, and (b) the envelope of the spectrum functions for fluctuating chordwise loading distribution affects the radiation at all observer angles equally. Thus in the present comparison, since the theoretical directivities are plotted relative to the measured

level at $\psi = 0^{o}$ (rotor axis), the effects of chordwise distribution are eliminated automatically. This leaves only the spanwise loading distribution effects to be explained.

The effects of spanwise load distributions on the directivity plots are not as straightforward as those for the chordwise load distributions. In Chapter 3, although it was shown that the directivity of sound pressure is sensitive to the spanwise loading profile and its variation with azimuth, the limited amount of computation did not provide enough information on the magnitude of the length scale one should use to compare with the radiated sound wavelength λ. This is because of the fact that since the levels of the radiation spectra from the point span loading models (Fig. 3.9) could be varied by varying the position of the effective loading point r_e, these levels cannot be compared directly with the spectrum level from the distributed span loading model (Fig. 3.10). The result is that we cannot determine the exact value of the ratio (span/wavelength) above which the point loading representation predicts results that are in error.

On the other hand, we can perhaps extract some useful information by comparing the computed directivity plots for the two models discussed above - see Figs. 3.11 and 3.14. Here, the directivities of the 4^{th} rotational noise harmonic from the point span and distributed span loading models are similar, but as the harmonic number m increases, the directivities from the two models begin to deviate from each other.† It appears that the point span loading model becomes inadequate at about $m = 8$. The ratio of the blade span to the radiated sound wavelength at $m = 8$ in this case is $(r_T/\lambda) \doteq 3$.

† The directivities of the first rotational noise harmonic are not similar because they are dominated by the steady loading.

If we apply the above deductions to evaluate the validity of point force representation used in comparing the theoretical directivities with the measured directivities from the I.S.V.R. model rotor (r_T = 20 in.), the point force model should be adequate for acoustic frequencies whose wavelengths are larger than approximately ($r_T/3$) = 6.7 in. The rotor has 3 blades and is operating at 1800 r.p.m; the point force representation assumed in the theory is therefore valid for harmonic numbers up to about 22.

It remains to be seen whether the length scale of one-third span can be used to compare with λ in justifying the point force representation for other rotor configurations.

6.4 Conclusions

The main conclusions are as follows.

(1) Asymptotic expressions have been derived for the far-field spectral density of sound radiation (directivity and sound power) from a broadband point force moving uniformly in a circular path. A series approximation has been developed to show how the spectrum of far-field radiation is influenced by rotation.

(2) The main effect at Mach numbers up to 0.8 is on the radiation spectrum from the drag force component; the magnitude of the effect depends on the rate of change of slope of the force spectrum, but is typically less than 3 dB for values of (Ω/ω) less than 0.5.

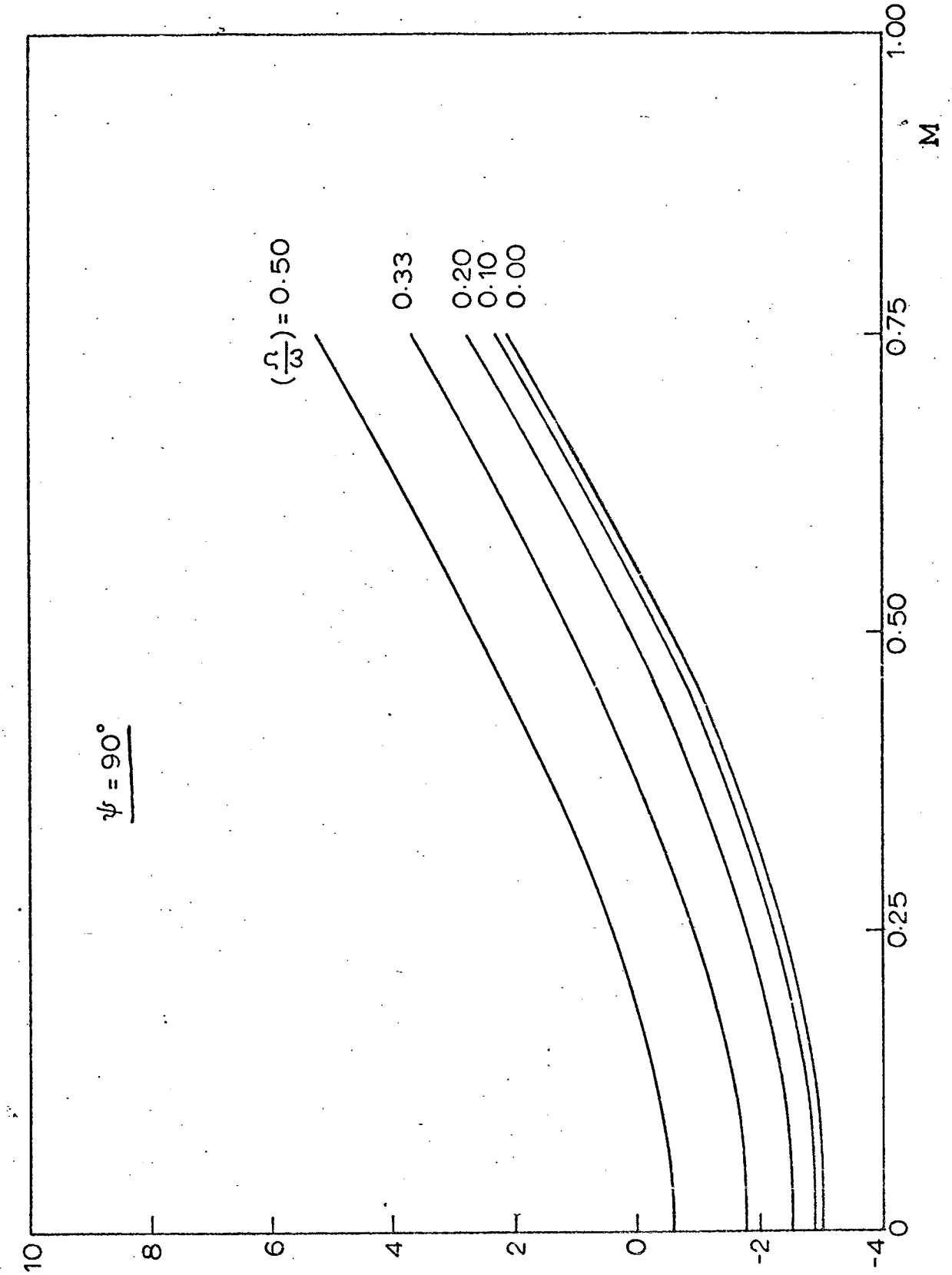

Fig. 6.1. Effect of rotation Mach number (M) on the spectral density of sound pressure in the rotor plane. $G_D(\omega) \propto \omega^{-2}$ (6 dB per octave fall-off).

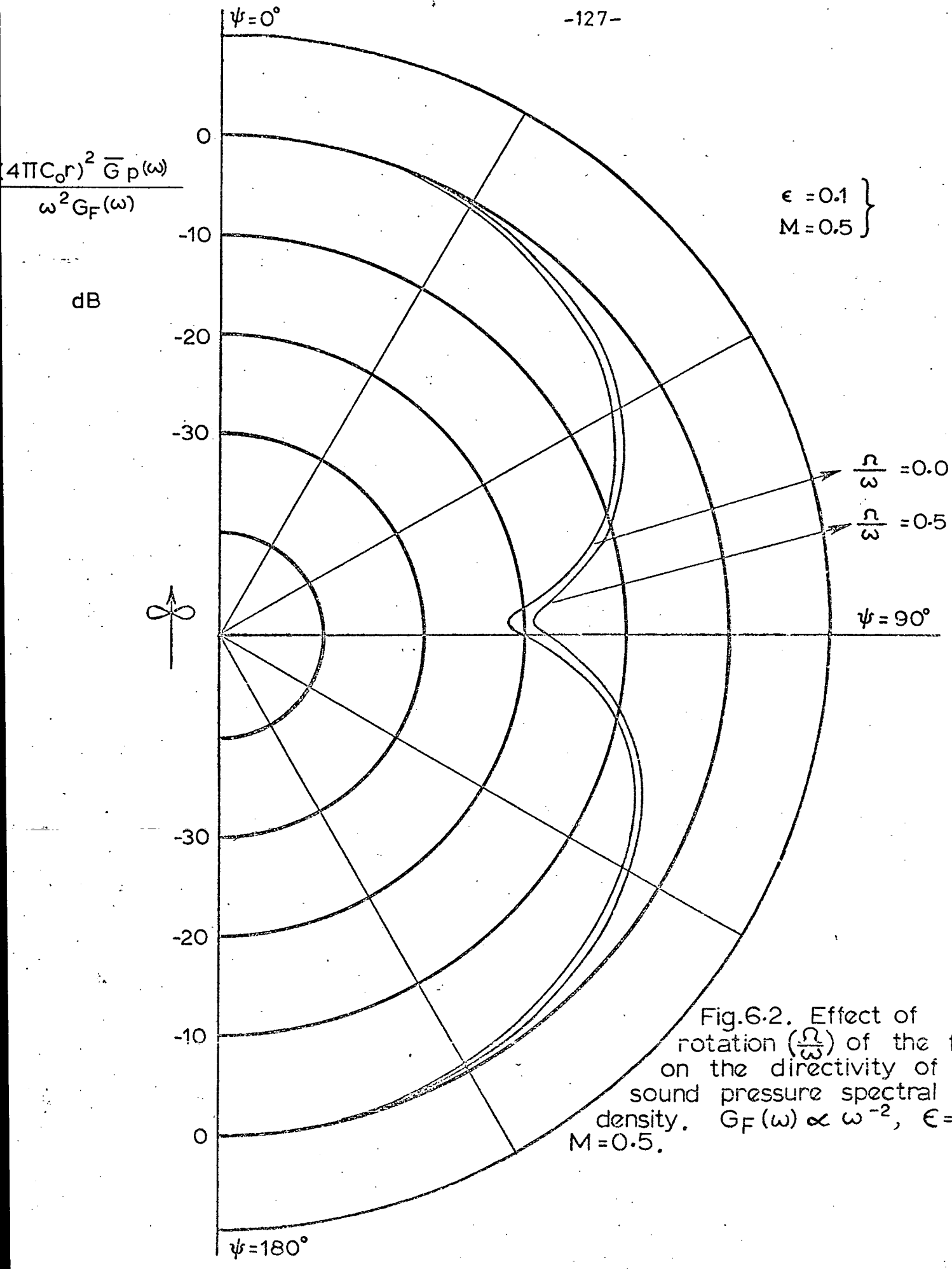

Fig.6.2. Effect of rotation $(\frac{\Omega}{\omega})$ of the force on the directivity of the sound pressure spectral density. $G_F(\omega) \propto \omega^{-2}$, $\epsilon = 0.1$, $M = 0.5$.

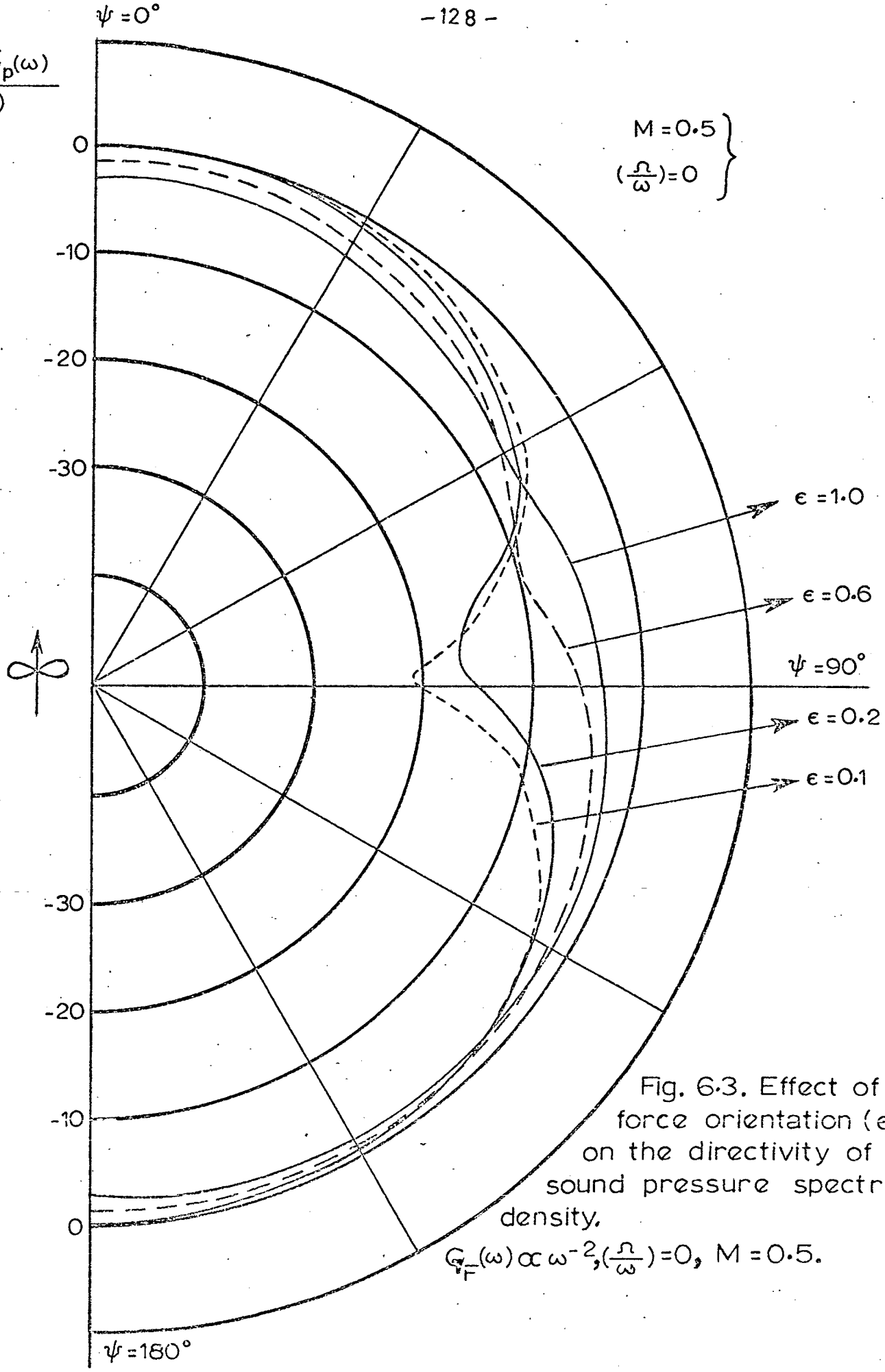

Fig. 6.3. Effect of force orientation (ϵ) on the directivity of the sound pressure spectral density.
$G_F(\omega) \propto \omega^{-2}, (\frac{\Omega}{\omega}) = 0$, M = 0.5.

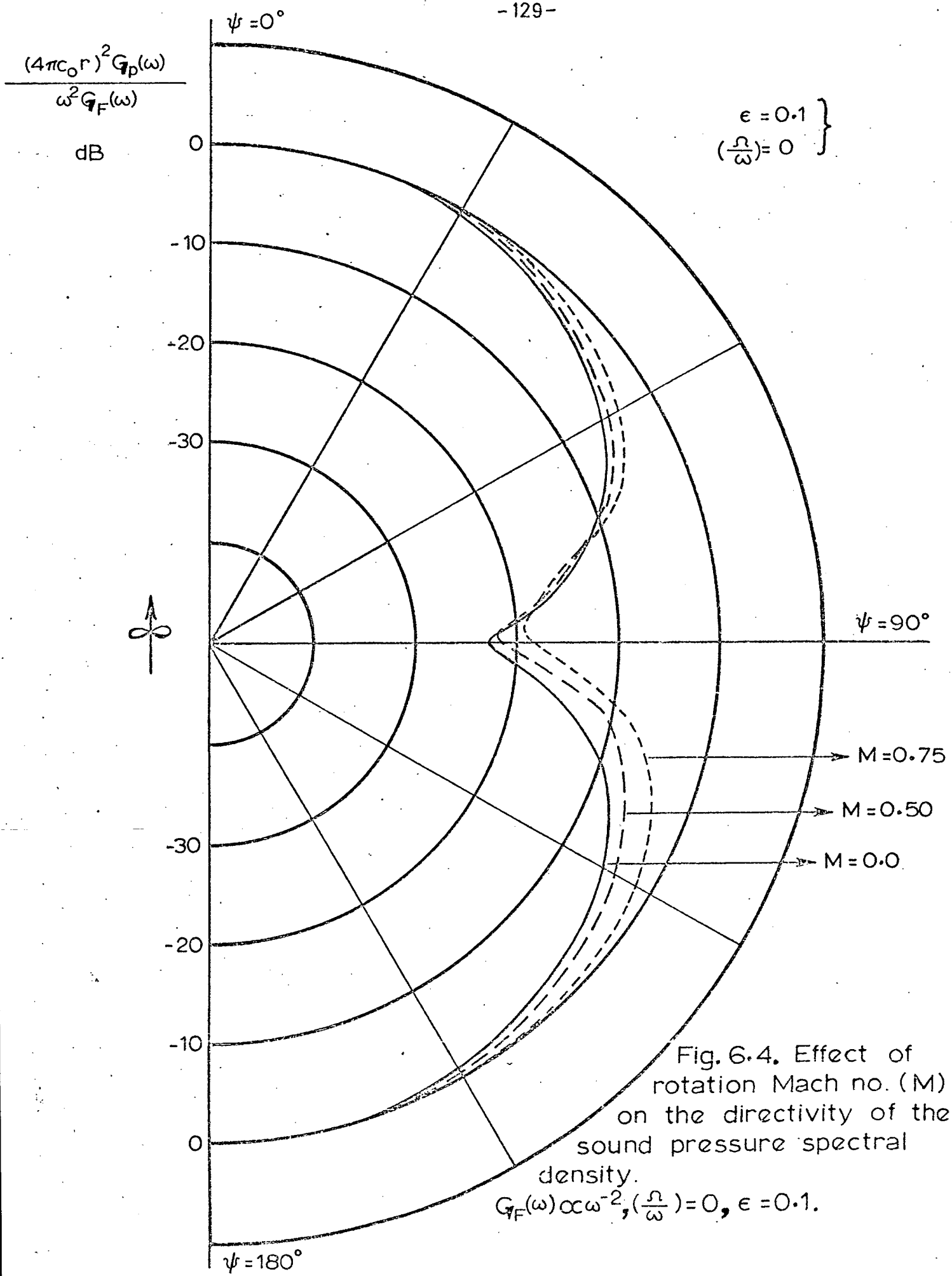

Fig. 6.4. Effect of rotation Mach no. (M) on the directivity of the sound pressure spectral density.
$G_F(\omega) \propto \omega^{-2}, (\frac{\Omega}{\omega}) = 0, \epsilon = 0.1.$

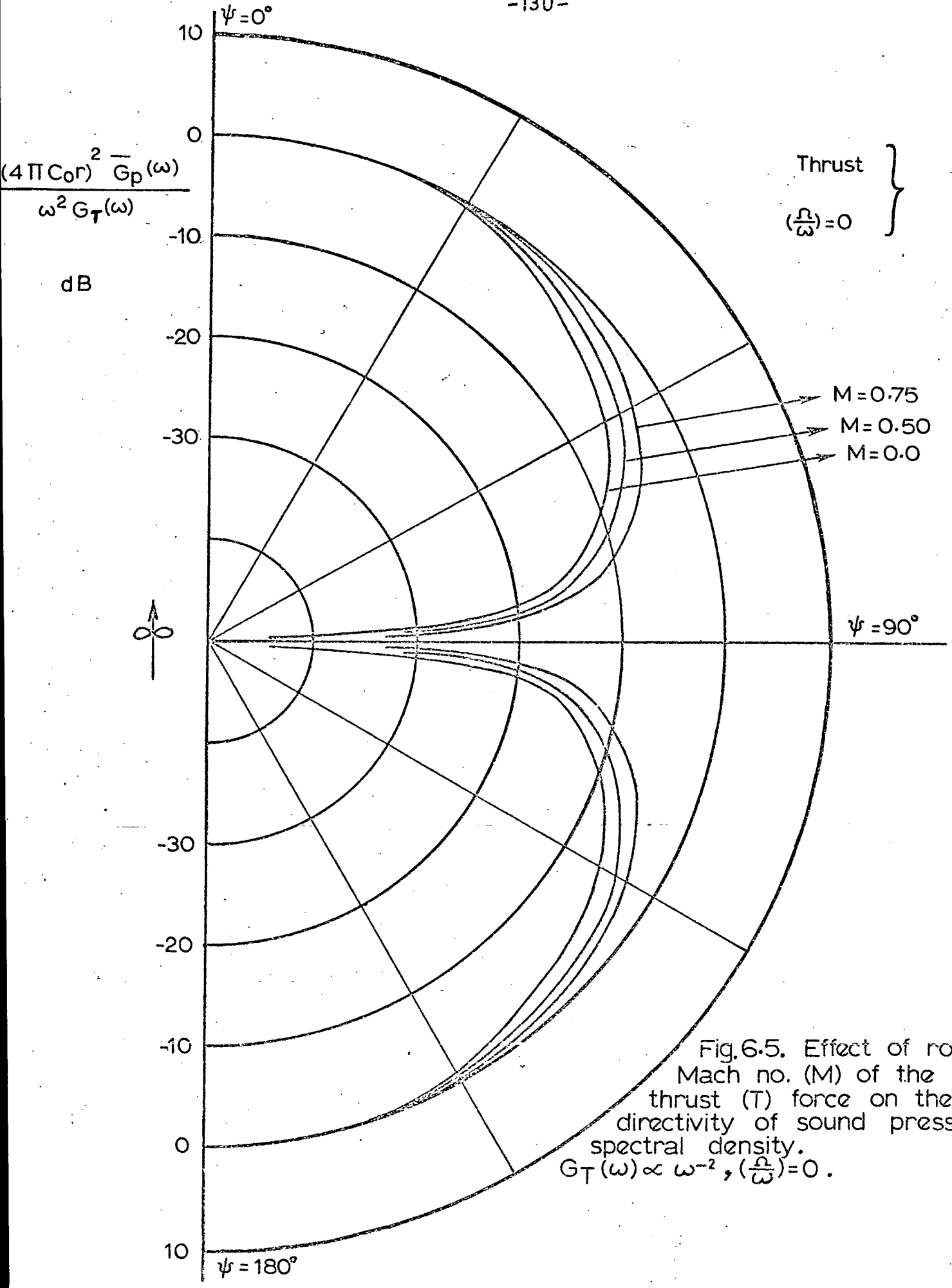

Fig. 6.5. Effect of rotation Mach no. (M) of the pure thrust (T) force on the directivity of sound pressure spectral density.
$G_T(\omega) \propto \omega^{-2}$, $(\frac{\Omega}{\omega}) = 0$.

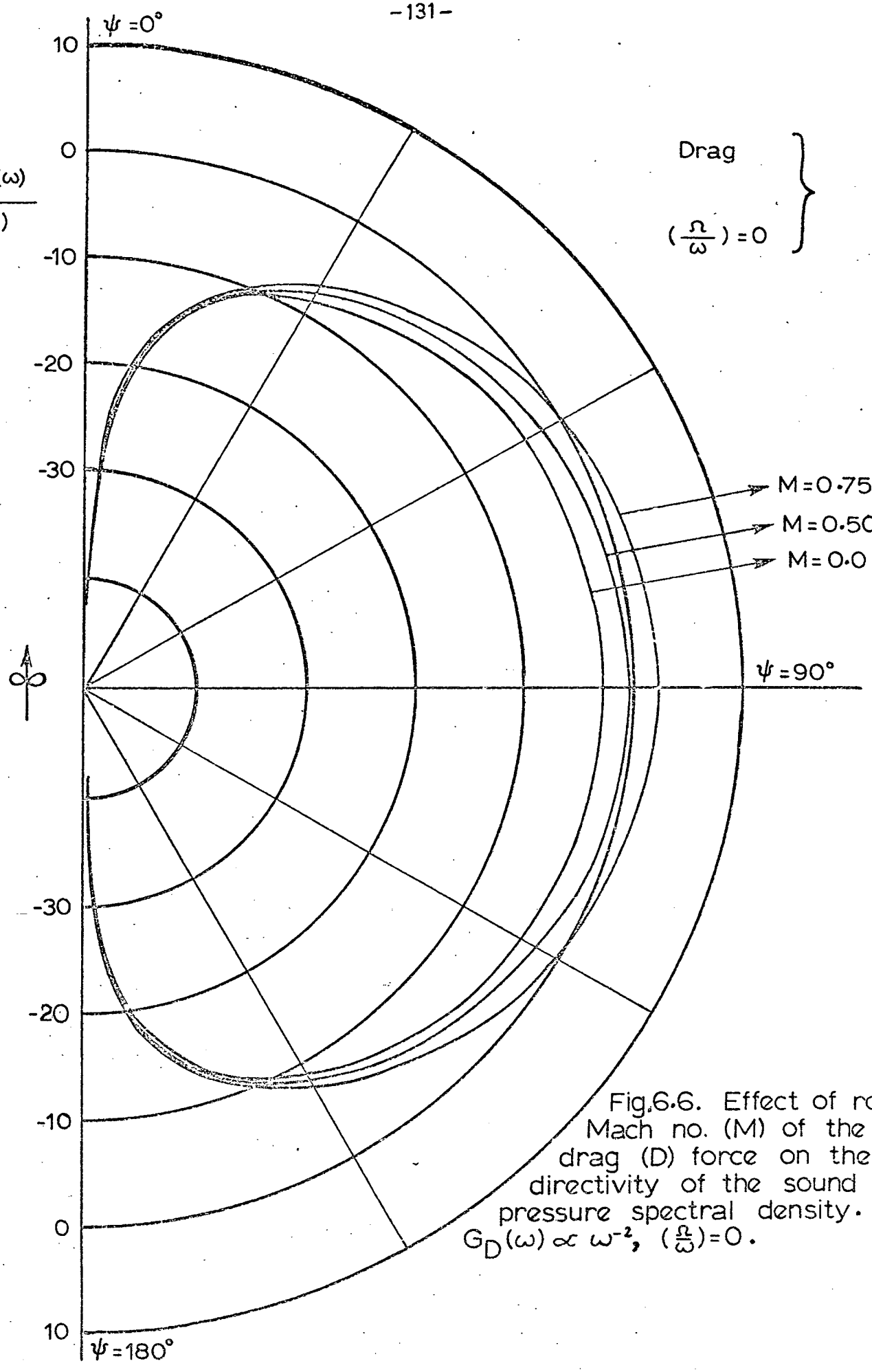

Fig.6.6. Effect of rotation Mach no. (M) of the pure drag (D) force on the directivity of the sound pressure spectral density. $G_D(\omega) \propto \omega^{-2}$, $(\frac{\Omega}{\omega})=0$.

Fig. 6.7. Effect of rotation (Ω/ω) and force orientation (ϵ) on the sound power spectral density. Force spectrum falling at 6dB per octave, $G_F(\omega) \propto \omega^{-2}$. M = 0.5.

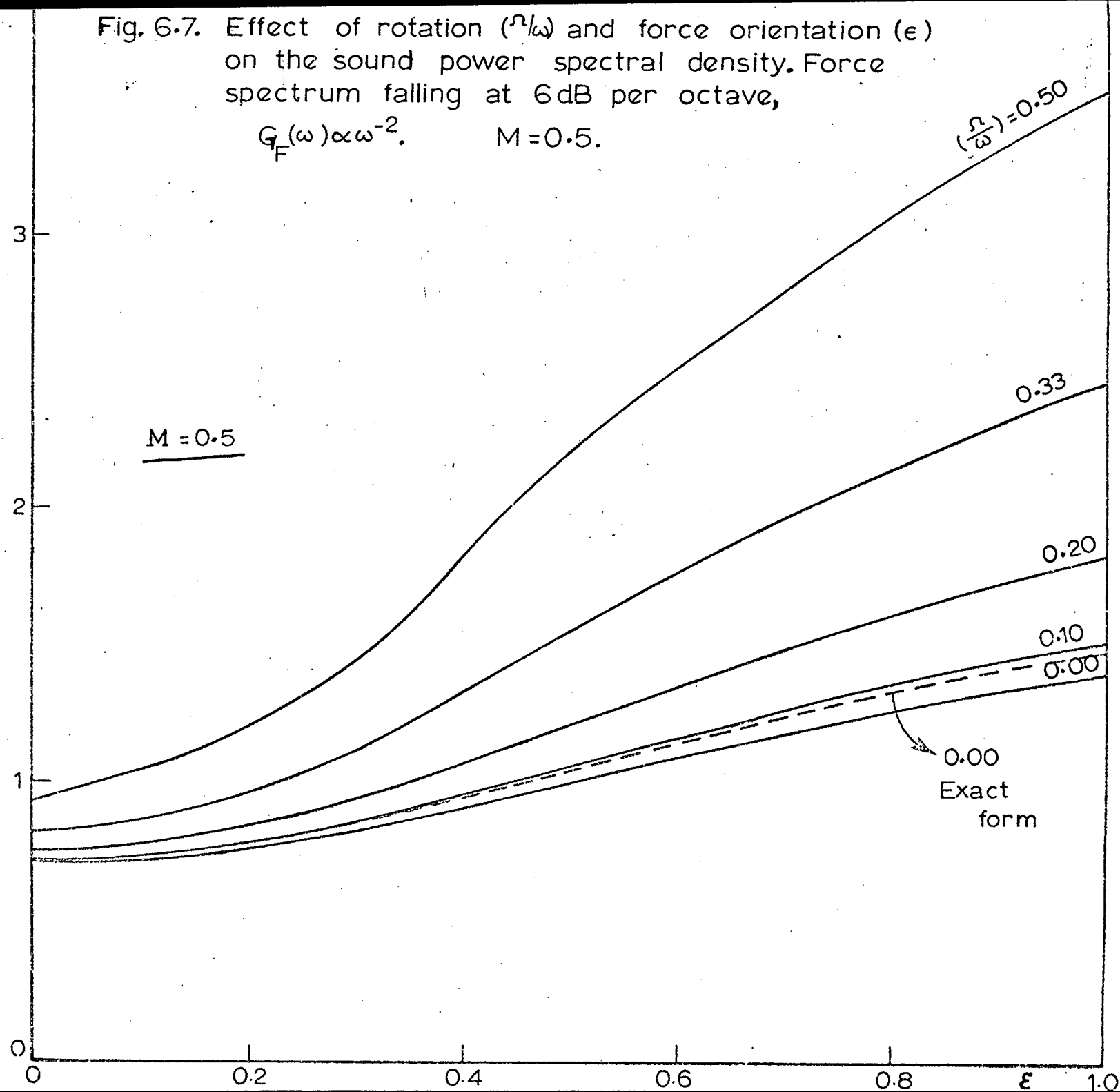

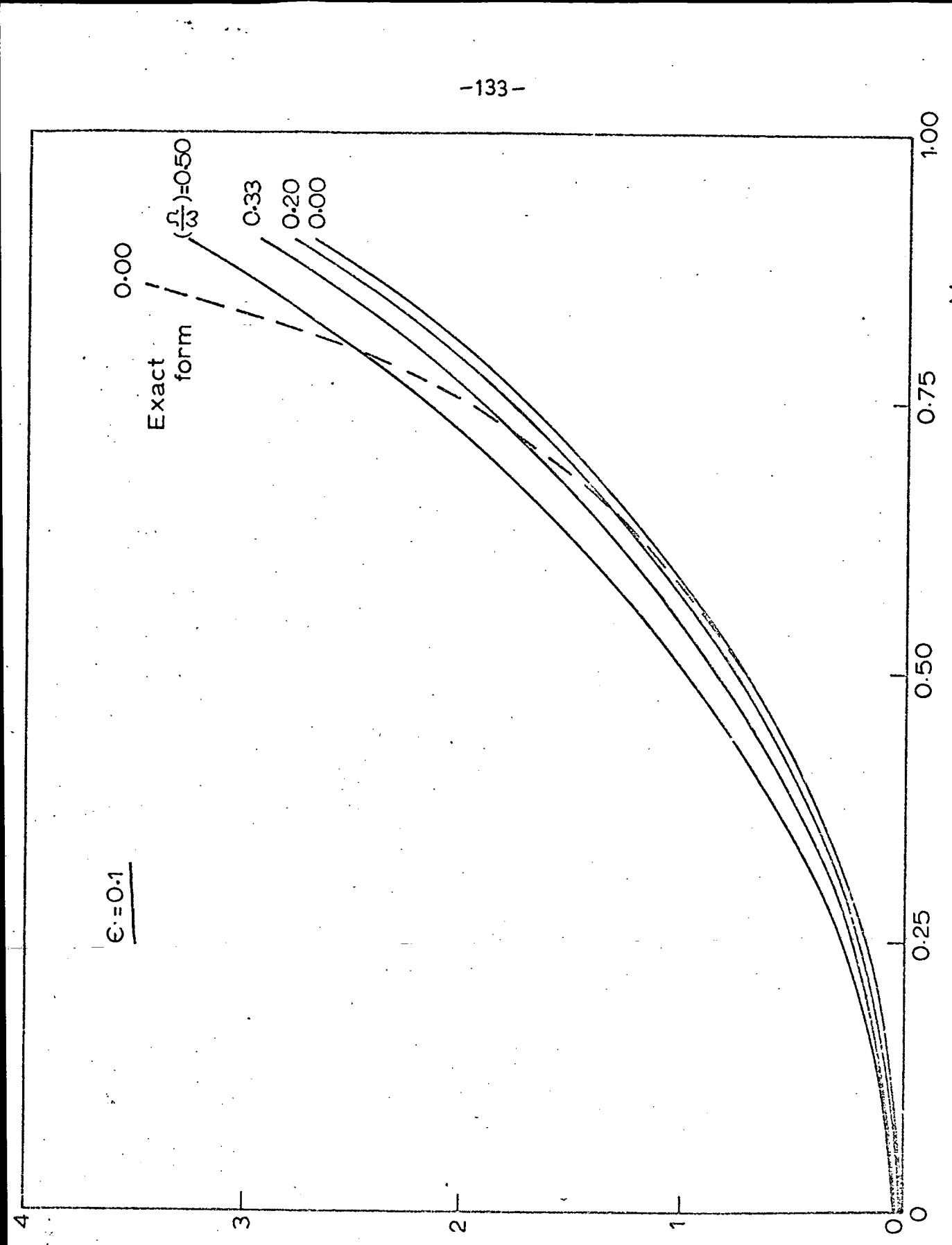

Fig. 6.8. Effect of rotation (Ω/ω) and Mach number (M) on the sound power spectral density. Force spectrum falling at 6dB per octave, $G_F(\omega) \propto \omega^{-2}$. $\epsilon = 0.1$.

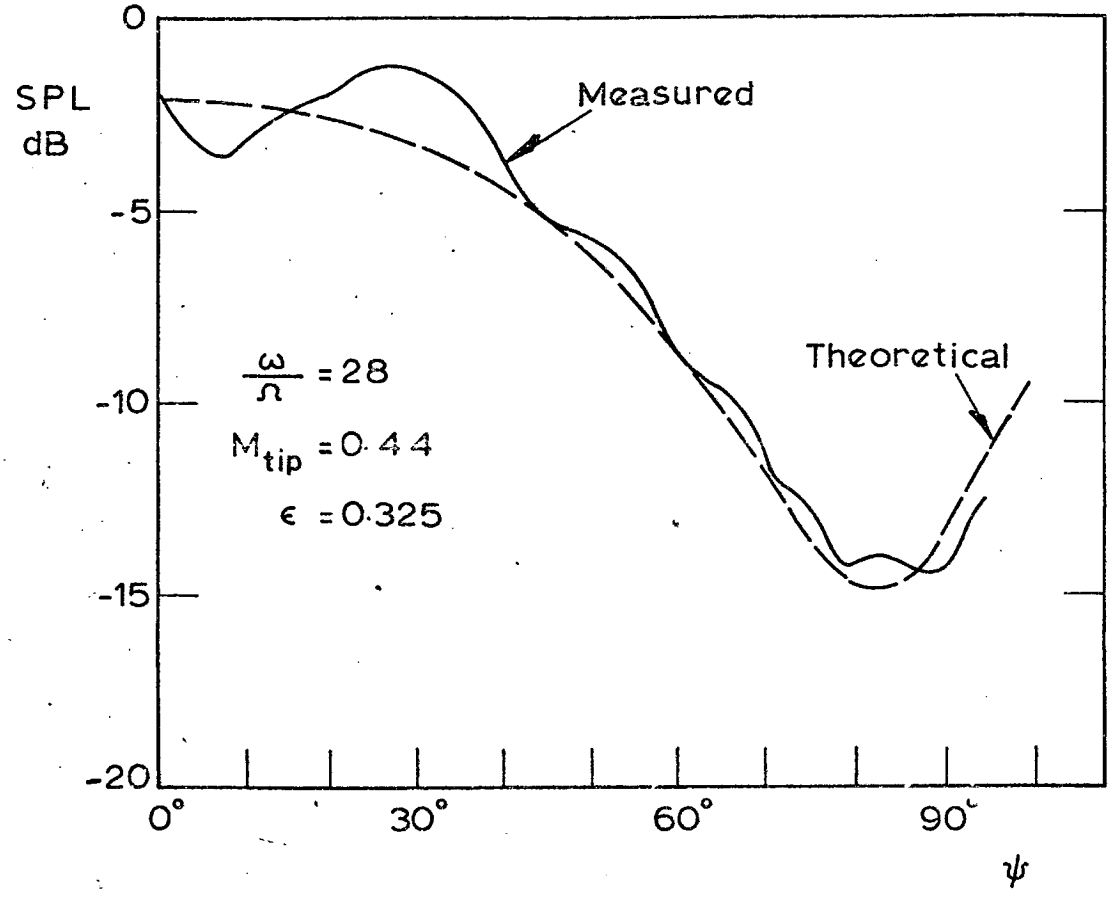

Fig. 6.9. Comparison between theoretical and measured (reference [30]) directivities. m = 7, B = 4, 3000 r.p.m. Force spectrum $\propto \omega^{-2}$ ($\frac{\omega}{\Omega}$ = 4 to 30).

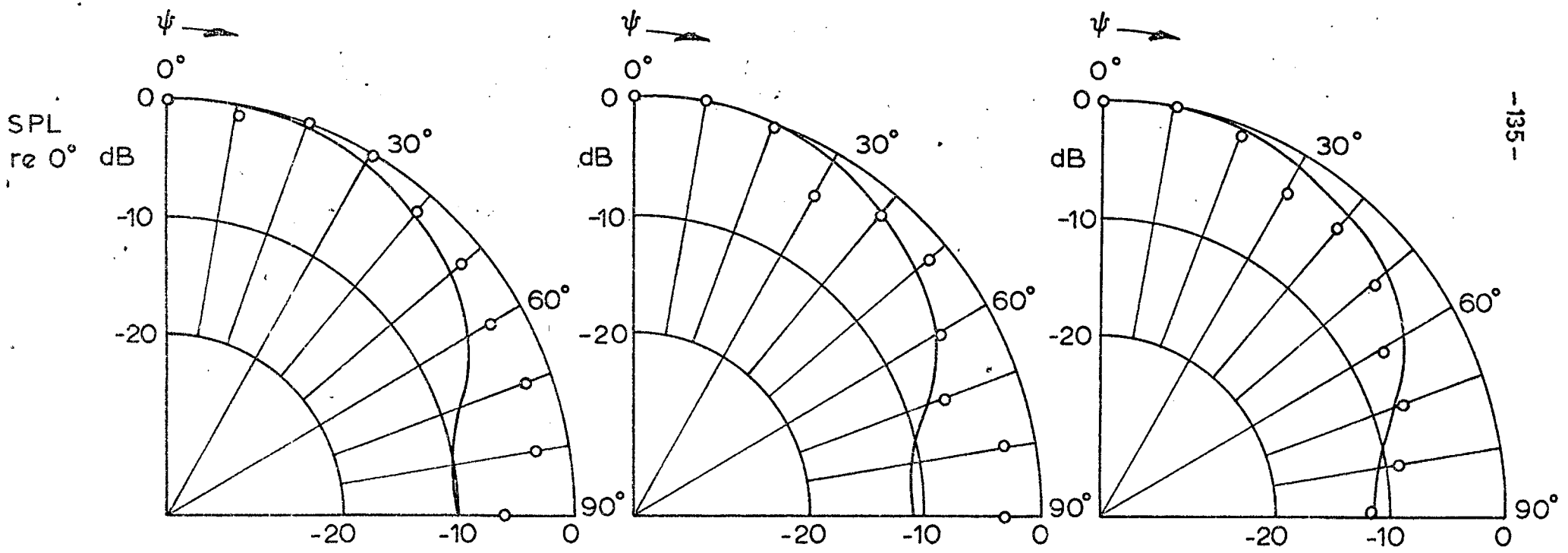

Fig. 6.10. Comparison between theoretical and measured (reference [31]) directivities. m=1; (a) B=5, (b) B=8, (c) B=10; 3600 r.p.m. Force spectrum $\propto \omega^{-2}$ ($\frac{\omega}{\Omega}$ = 3 to 12)

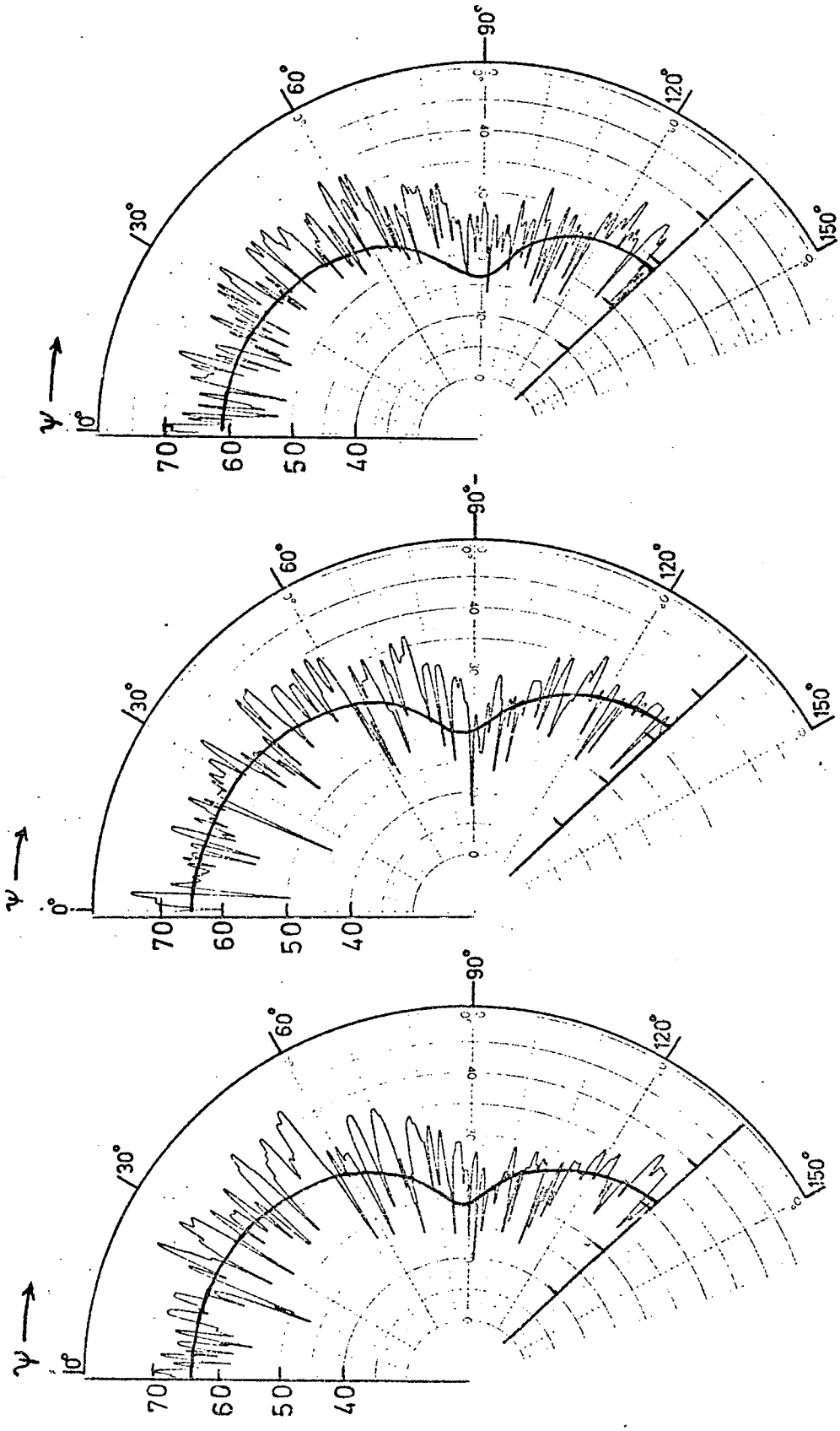

(a) $\frac{\Omega}{\omega} = 0{\cdot}111$

(b) $\frac{\Omega}{\omega} = 0{\cdot}067$

(c) $\frac{\Omega}{\omega} = 0{\cdot}048$

——— THEORETICAL RE $\psi = 0°$

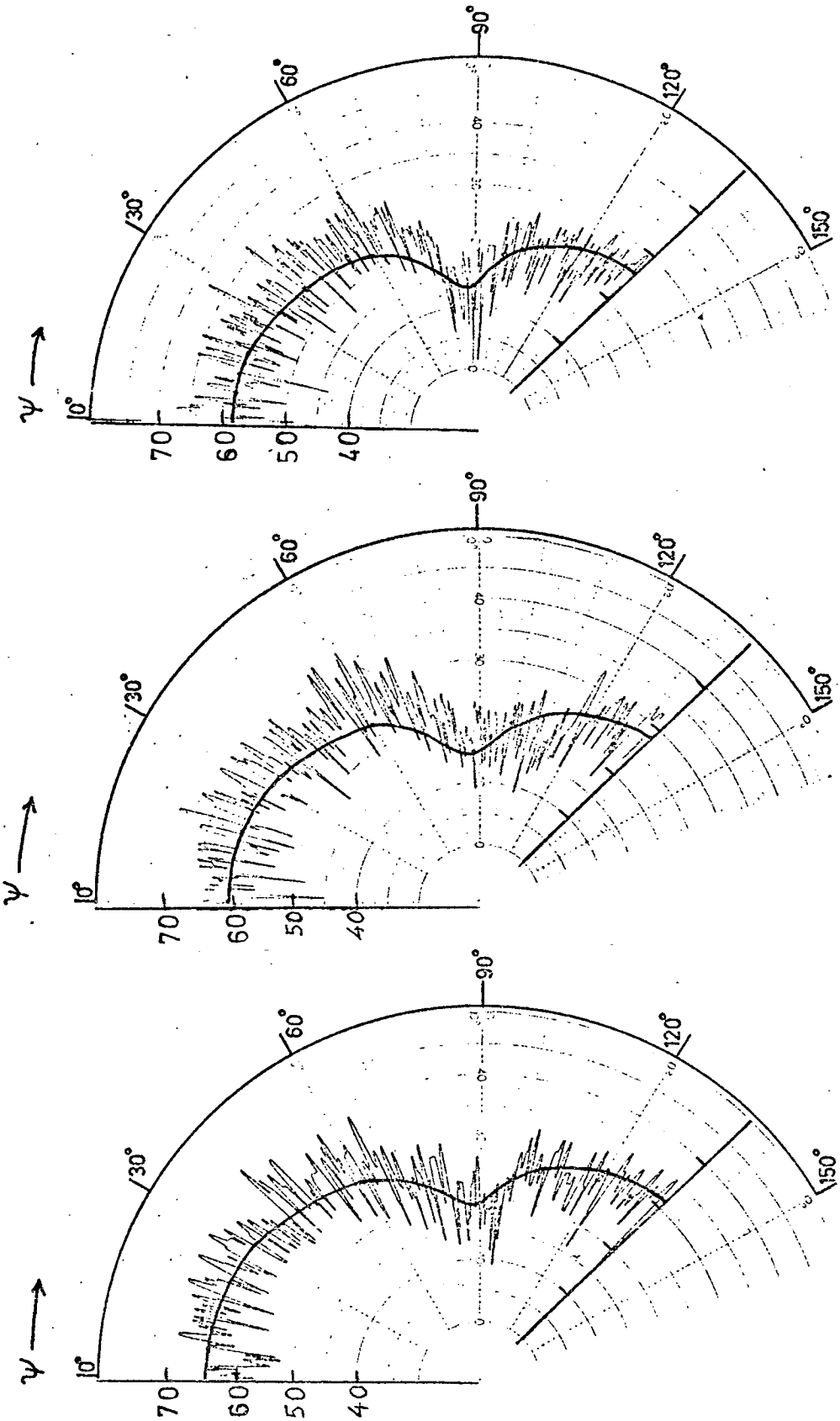

(d) $\frac{\Omega}{3} = 0.030$ (e) $\frac{\Omega}{3} = 0.022$ (f) $\frac{\Omega}{3} = 0.017$

$M = 0.357$, $\varepsilon = 0.213$

FIG. 6.11. Comparison between theoretical and measured directivities. B = 3 , 1800 R.P.M. [32]
(a) m = 3, (b) m = 5, (c) m = 7, (d) m = 11, (e) m = 15, (f) m = 20. Force spectrum $\propto \omega^{-2}$.

CHAPTER 7

SOUND RADIATION FROM POINT VOLUME-VELOCITY SOURCES IN CIRCULAR MOTION

In the previous chapters, we have basically considered the radiation from fluctuating forces, both periodic (at multiples of the rotational frequency) and random, acting on rotating blades. These fluctuating forces dominate the sound radiation from helicopter rotors operating at subsonic tip speeds. In the remaining chapters, we will go on to derive expressions for sound radiation from monopoles and quadrupoles in circular motion. Taken together with the dipole sources, we will then be in a position to describe the basic radiation properties of most of the rotating machinery used for developing thrust in the V/STOL aircraft technology, provided a point source model is appropriate.

The total noise from a rotating jet, as used for example in tip jet rotors is dominated by two mechanisms (see Chapter 1). First, any irregular combustion will result into fluctuating rate of mass introduction into the surrounding medium (air) as the tip jet rotates. This will give rise to rotating volume-velocity sources whose strength could fluctuate in harmonic or random manner. Secondly, sound is radiated from the turbulence in the jet and this results into what is commonly known as "jet noise". This jet noise is a subject on its own and is not tackled in the present investigation; but the effects of circular motion on the radiation from acoustic stresses will be established in Chapter 9.

In the present chapter, we will consider the volume-velocity sources mentioned above. Expressions for the overall and spectral radiation (directivity and sound power) from volume-velocity sources in uniform circular motion at subsonic speeds will be derived, by using the moving-

source approach adopted for the rotating point force study. Once again, it is assumed that the extent of the source distribution at any azimuth is small compared to the radiated sound wavelength; this allows us to use the point source model.

All the concepts used in this chapter are identical to those used in the previous two chapters, and so repetition is kept to a minimum. In particular, the sound pressure results for the volume velocity source required here are obtained from the corresponding results for rotating point force. The rest of the introductory comments made at the beginning of Chapter 5 apply here also.

7.1 Overall sound radiation

The far field sound pressure from a point volume velocity source $Q(\underset{\sim}{x},t)$ in arbitrary motion is given by Lowson [9] as

$$p'(\underset{\sim}{r},t) = \left[\frac{1}{4\pi R(1-M_R)^2} \left\{ \frac{\partial Q}{\partial t} + \frac{Q}{1-M_R} \frac{\partial M_R}{\partial t} \right\} \right] \tag{7.1}$$

where $\underset{\sim}{r}$, $\underset{\sim}{x}$ are the vector positions of observer and source respectively, and M_R is the component of convection Mach number in the direction $\underset{\sim}{R}$ of the observer;

$$M_R = \frac{\underset{\sim}{M} \cdot \underset{\sim}{R}}{R} = \frac{M_j(r_j - x_j)}{R} \quad . \tag{7.2}$$

The square brackets imply evaluation at retarded time

$$[t] = t - \frac{[R]}{c_o} \quad , \tag{7.3}$$

where t is the time of observation and $R = |\underset{\sim}{r} - \underset{\sim}{x}|$ is the observer-source separation.

A point volume velocity source of strength Q(t) (mass per unit time) may be represented physically by $Q(t) = \rho_o \dot{d}(t)$, where $\dot{d}(t)$ represents a time-varying fluid volume velocity as in an arbitrarily moving jet of air. The point volume velocity source should not be confused with the point acoustic source (the volume acceleration source) of specified volume acceleration $\ddot{d}(t)$, or the point volume displacement source of specified volume displacement d(t), which is treated separately in Chapter 8.

For the point source rotating in a circle about a fixed point, it is convenient to take the centre of the circle as origin; then $M_j x_j = 0$. Equation (7.1) thus reduces, at distances large compared with the radius of the circle ($r \gg a$), to

$$p'(\underset{\sim}{r},t) = \frac{1}{4\pi r}\left[\frac{\partial Q}{\partial t}(1 - M_r)^{-2} + Q\frac{\partial M_r}{\partial t}(1 - M_r)^{-3}\right] . \qquad (7.4)$$

In the above equation, it should be noted that $M_r = \frac{M_i r_i}{r}$ is the Mach number component parallel to the line from the origin to the observation point. In terms of the rotating source geometry defined in Fig. 7.1,

$$M_r = - M \sin\psi \sin\theta \qquad (7.5)$$

is the Mach number component parallel to $\underset{\sim}{r} = \overrightarrow{OP}$.

Since ψ and M are constant,

$$\frac{dM_r}{dt} = - \Omega M \sin\psi \cos\theta \ . \qquad (7.6)$$

Equation (7.4) then gives, writing $M \sin\psi = \alpha$,

$$4\pi r\, p' = \left[\dot{Q}(1 + \alpha\sin\theta)^{-2} - Q\Omega\alpha \cos\theta(1 + \alpha\sin\theta)^{-3}\right] . \qquad (7.7)$$

This general result can be used to find the mean square radiated

pressure for a rotating random source by repeating the procedure used for a rotating random source (see section 5.2 of Chapter 5), but this is not necessary as shown below. It should be noted that a random source here implies a source with no periodic components at multiples of the rotational frequency.

7.1.1 Mean square far-field sound pressure

For a pure thrust force, the general result (5.19) of Chapter 5 for a rotating force becomes

$$4\pi c_o r\, p' = -\cos\psi \left[\dot{T}(1+\alpha\sin\theta)^{-2} - T\Omega\alpha\cos\theta(1+\alpha\sin\theta)^{-3}\right], \qquad (7.8)$$

which is identical to the general result (7.7) above for a rotating source except for the $\cos\psi$ factor. Thus the mean square pressure for a rotating source follows from equations (5.23) and (5.24) of Chapter 5 as

$$(4\pi r)^2 \langle p'^2\rangle = \langle \dot{Q}^2\rangle \left\{\frac{1+\frac{1}{2}\alpha^2}{(1-\alpha^2)^{5/2}}\right\} + \Omega^2 \langle Q^2\rangle \alpha^2 \left\{\frac{\frac{1}{2}+\frac{1}{8}\alpha^2}{(1-\alpha^2)^{7/2}}\right\} . \qquad (7.9)$$

This is the main result of this section. It gives an exact expression for the mean square far-field sound pressure at the observation point (r,ψ), due to a point volume velocity source with random time variation rotating uniformly in a circle. The effect of source acceleration is clearly displayed in the Ω^2 term, which also contains the contribution of steady volume velocity sources to the overall radiation.

A particular case is that of a harmonically varying source strength, with radian frequency ν; then $\langle \dot{Q}^2\rangle = \nu^2 \langle Q^2\rangle$ and the resulting mean square pressure is obtained from (7.9) as

$$\langle p'^2 \rangle = \frac{Q^2}{16\pi^2 r^2} \left\{ \nu^2 \frac{2+\alpha^2}{2(1-\alpha^2)^{5/2}} + \Omega^2 \frac{\alpha^2(4+\alpha^2)}{8(1-\alpha^2)^{7/2}} \right\} , \qquad (7.10)$$

which is in agreement with Dokuchaev's result [33] derived by direct calculation.

Figures 7.2 and 7.3 show the effect of Mach number M on the overall radiated sound field, for both steady and fluctuating source strengths. For this purpose the mean square pressures are normalized by Q^2 and $\langle \dot{Q}^2 \rangle$ respectively.

7.1.2 Overall sound power output

The overall radiated power corresponding to (7.9) follows by integrating the intensity over a spherical surface r = constant;

$$W = \int_S I(r,\Psi)\, dS . \qquad (7.11)$$

When the integral above is evaluated using (7.9) for the intensity, the power output from a rotating point volume velocity source is obtained in the form

$$4\pi\rho_o c_o \cdot W = \langle \dot{Q}^2 \rangle A(M) + \Omega^2 \langle Q^2 \rangle B(M) . \qquad (7.12)$$

In equation (7.12), the A term is independent of the rotational frequency Ω; it gives the sound power radiated from a point volume velocity source in uniform linear motion, which was calculated directly in section 5.1 of Chapter 5. Thus A(M) is given by

$$A(M) = (1 - M^2)^{-2} . \qquad (7.13)$$

The effects of finite rotational frequency are contained in the B term in (7.12); this is the only term which remains when the source strength is constant. B(M) is given by

$$B(M) = \tfrac{1}{3} M^2 (1 - M^2)^{-3} \quad . \tag{7.14}$$

This last result was also obtained by Dokuchaev [33], by considering the special case of a harmonic monopole in circular motion.

For low Mach number applications, it may be useful to approximate A, B by the first few terms of a series. Expansion in powers of M gives

$$A(M) = 1 + 2M^2 + 3M^4 + \ldots \quad , \tag{7.15}$$

$$B(M) = \tfrac{1}{3}M^2 + M^4 + \ldots \quad . \tag{7.16}$$

Figure 7.4 shows the effect of terminating the series expansions at the M^4 term.

7.2 Spectral density of sound radiation from broadband rotating volume-velocity sources

7.2.1 Spectral density of sound pressure

The spectral density of far-field sound radiation from a rotating point source can be derived in a manner identical to that used for a rotating point force (Chapter 6), but here again, examination of the equations involved shows that the required result can be extracted directly from the rotating thrust force result:

Noting that the sound pressure equations (7.7) and (7.8) for the two cases differ only by the $\cos\psi$ factor, the time-averaged sound pressure spectral density from a rotating volume velocity source, accurate up to α^4 terms, follows from the general result (6.15) of Chapter 6 as

$$\begin{aligned}(4\pi r)^2\, \overline{G}_p(\omega) \doteq\ & (\tfrac{\Omega}{\omega})^0 \left\{ \omega^2 G_Q(\omega) + \tfrac{1}{4}\alpha^2 \cdot \omega^4 G_Q''(\omega) + \frac{1}{64}\alpha^4 \cdot \omega^6 G_Q^{iv}(\omega) \right\} \\ & + (\tfrac{\Omega}{\omega})^2 \left\{ \frac{1}{48}\alpha^2 \cdot \omega^6 G_Q^{iv}(\omega) \right\} + \ldots \text{ terms of order} \\ & (\tfrac{\Omega}{\omega})^4 \quad \text{and higher.}\end{aligned} \tag{7.17}$$

In the above equation, $G_Q(\omega)$ is the spectral density of the source and the prime denotes differentiation with respect to ω. The result is valid when the rotational frequency $\Omega/2\pi$ is much less than the frequencies with which the source strength (volume velocity) itself fluctuates.

The properties of the radiation spectrum are obviously similar to those displayed by the pressure spectrum from a pure thrust force in circular motion:

(1) If the source spectrum is linear in ω (which includes the flat spectrum and a spectrum rising at 3 dB/octave as special cases), circular motion has no effect on the radiation spectrum because the derivative terms G_Q'', etc. in (7.17) all vanish. This agrees with the results of Morse and Ingard [6] and Ffowcs Williams and Hawkings [7].

(2) Equation (7.17) gives the radiation spectrum on the axis of rotation as

$$(4\pi r)^2 \, \overline{G}_p(\omega) = \omega^2 \, G_Q(\omega) \, , \qquad (7.18)$$

in agreement with [7]. The on-axis radiation is independent of source motion (M and Ω).

(3) As an example, let us assume that the source spectrum is proportional to ω^{-2} (6 dB/octave fall-off) over part of the frequency range. The corresponding radiation spectrum, in normalized form, follows from (7.17) as

$$\frac{(4\pi r)^2 \, \overline{G}_p(\omega)}{\omega^2 G_Q(\omega)} \doteq \left(\frac{\Omega}{\omega}\right)^0 \left\{ 1 + \frac{3}{2}\alpha^2 + \frac{15}{8}\alpha^4 \right\} + \left(\frac{\Omega}{\omega}\right)^2 \left\{ \frac{5}{2}\alpha^2 \right\} . \qquad (7.19)$$

The effects of varying (Ω/ω) and M are illustrated in the polar diagrams of Figs. 7.5 and 7.6, with the values $(\Omega/\omega) = 0$ and $M = 0.5$ used to form a standard case.

(4) The validity of assuming a power-law approximation to the source

spectrum, as in (3) above, depends on the fact that for small (Ω/ω) values, the radiation spectrum at frequency ω comes almost entirely from a limited band of the source spectrum between $\omega(1-M)$ and $\omega(1+M)$. Any approximation to the shape of the source spectrum therefore applies to this band of frequencies only.

(5) The exact result obtained by Ffowcs Williams and Hawkings [7] from their analysis of the same problem is, in the present notation,

$$(4\pi r)^2 \, \overline{G}_p(\omega) = \sum_{n=-\infty}^{\infty} G_Q(\omega - n\Omega) \, J_n^2 \left(\frac{\omega}{\Omega} \alpha\right) . \qquad (7.20)$$

The same remarks apply here as in Chapter 6; in particular, the exact form above must be used when (Ω/ω) is large.

7.2.2 Spectral density of total sound power

The sound power output per unit frequency bandwidth follows from equation (7.17) by integrating over a spherical surface r = constant:

$$\frac{dW}{d\omega} = \frac{2\pi r^2}{\rho_o c_o} \int_o^{\pi} \overline{G}_p(\omega) \sin\psi \, . \, d\psi \quad . \qquad (7.21)$$

Noting that $\alpha = M \sin\psi$ in (7.17), we get the general result accurate to M^4 as

$$4\pi\rho_o c_o \frac{dW}{d\omega} = \left(\frac{\Omega}{\omega}\right)^o \left\{ \omega^2 G_Q(\omega) + \omega^4 G_Q''(\omega) \, . \, \left(\tfrac{1}{6}M^2\right) + \omega^6 G_Q^{iv}(\omega) \, . \, \left(\tfrac{1}{120}M^4\right) \right\}$$

$$+ \left(\frac{\Omega}{\omega}\right)^2 \left\{ \omega^6 G_Q^{iv}(\omega) \, . \, \left(\tfrac{1}{72}M^2\right) \right\} + \ldots \qquad (7.22)$$

For a source spectrum $G_Q(\omega)$ which falls at 6 dB/octave, the normalized sound power spectrum is

$$\frac{4\pi\rho_o c_o}{\omega^2 G_Q(\omega)} \frac{dW}{d\omega} = \left(\frac{\Omega}{\omega}\right)^0 (1 + M^2 + M^4) + \left(\frac{\Omega}{\omega}\right)^2 \left(\frac{5}{3}M^2\right) \quad , \tag{7.23}$$

accurate up to and including M^4 terms. The leading term in (7.23) can in fact be obtained in exact closed-form by noting that it represents the limiting case of uniform straight-line motion ($\Omega = 0$), for which Morse and Ingard's analysis [6] gives

$$\frac{4\pi\rho_o c_o}{\omega^2 G_Q(\omega)} \frac{dW}{d\omega} = \frac{1}{1 - M^2} \quad , \quad \left(\frac{\Omega}{\omega} = 0,\ M < 1\right). \tag{7.24}$$

(see Appendix XI for details).

Numerical results for the 6 dB/octave fall-off spectrum are shown in Fig. 7.7, based on equation (7.23). Also included is the exact result (7.24) for $(\Omega/\omega) = 0$, in order to show the effect of neglecting M^6 and higher-order terms in the series approximation. The main conclusions are that the series approximation is within ½ dB of the exact value for Mach numbers below 0.7, and the effect of finite Ω on the sound power spectrum becomes more pronounced as M is increased.

7.3 Conclusions

(1) Exact expressions have been obtained in closed form for the overall far-field radiation (directivity and total sound power) from a point volume-velocity source moving uniformly in a circle. The only restriction on the source spectrum is that it contain no discrete components at multiples of the rotation rate.

(2) The contributions from steady and fluctuating source strengths to the overall radiation are additive.

(3) Asymptotic expressions have been derived for the far-field spectral density of sound radiation (directivity and sound power) from a broad-

band point volume-velocity source moving uniformly in a circular path. A series approximation has been developed to show how the spectrum of far-field radiation is influenced by rotation.

(4) The biggest effect is on the radiation spectrum in the plane of rotation; the magnitude of the effect depends on the rate of change of slope of the source spectrum, but is typically less than 1 dB for values of (Ω/ω) less than 0.5.

The effect of finite Ω on the sound power spectrum becomes more pronounced as M increases.

(5) The properties of the radiation spectrum are similar to those displayed by the pressure spectrum from a pure thrust force in circular motion.

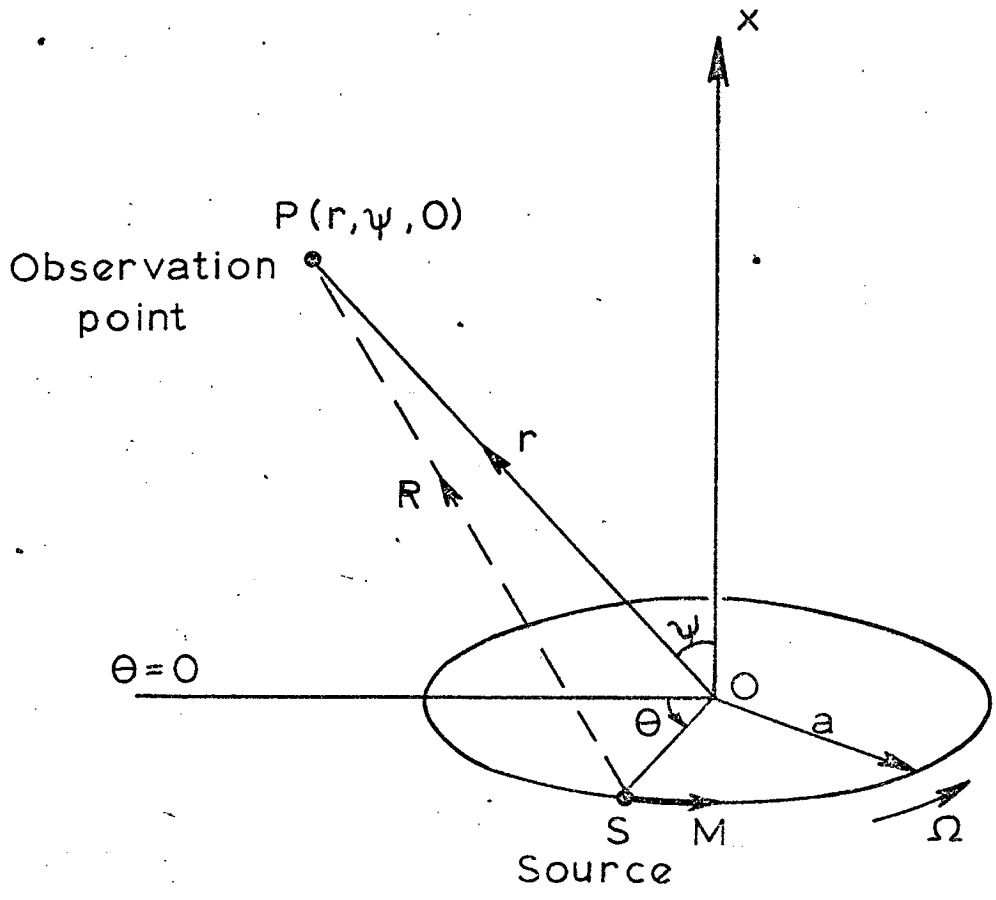

Fig. 7.1. Point source in uniform circular motion.

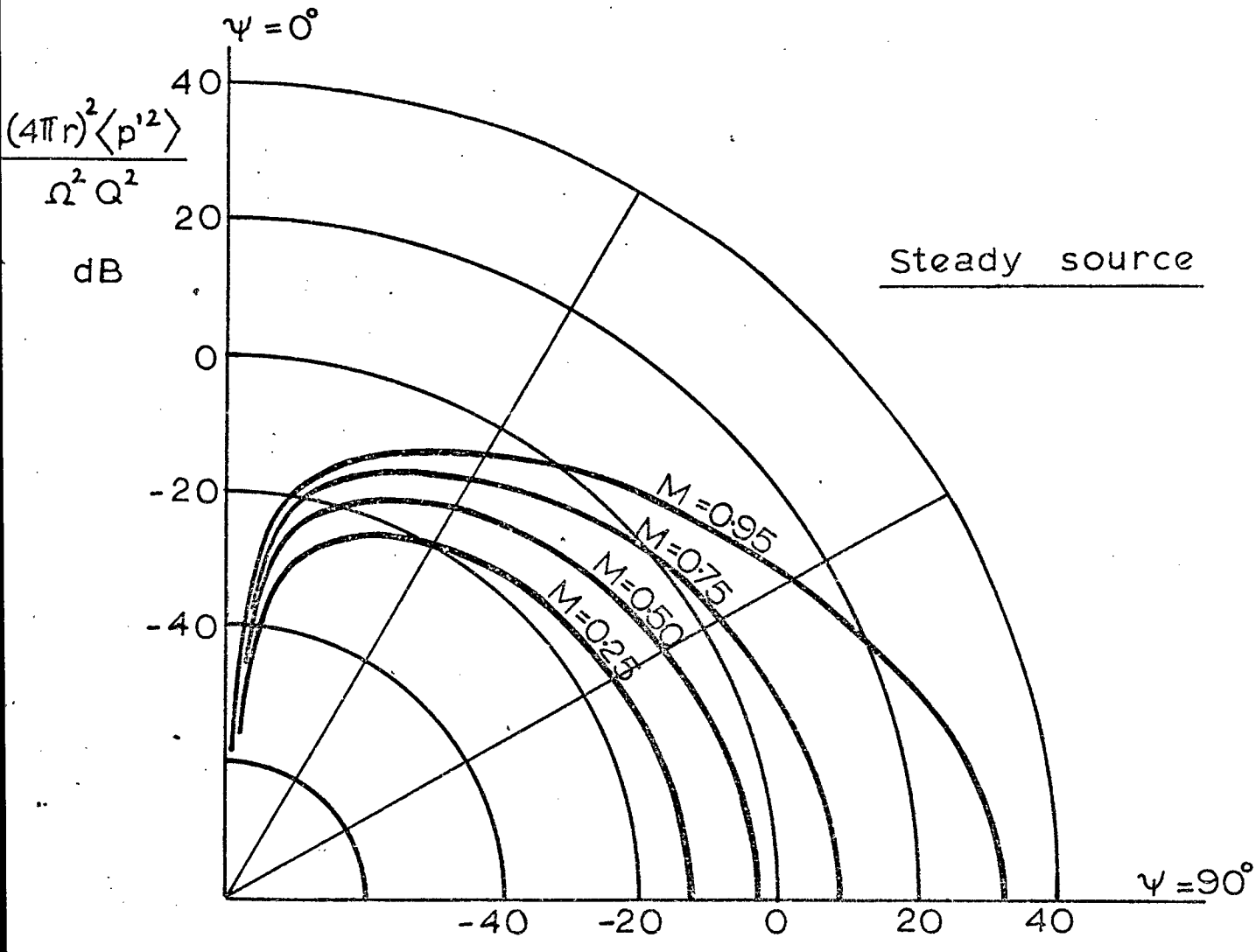

Fig. 7.2. Effect of rotation Mach number (M) on the directivity of overall mean square pressure from steady rotating volume velocity source.

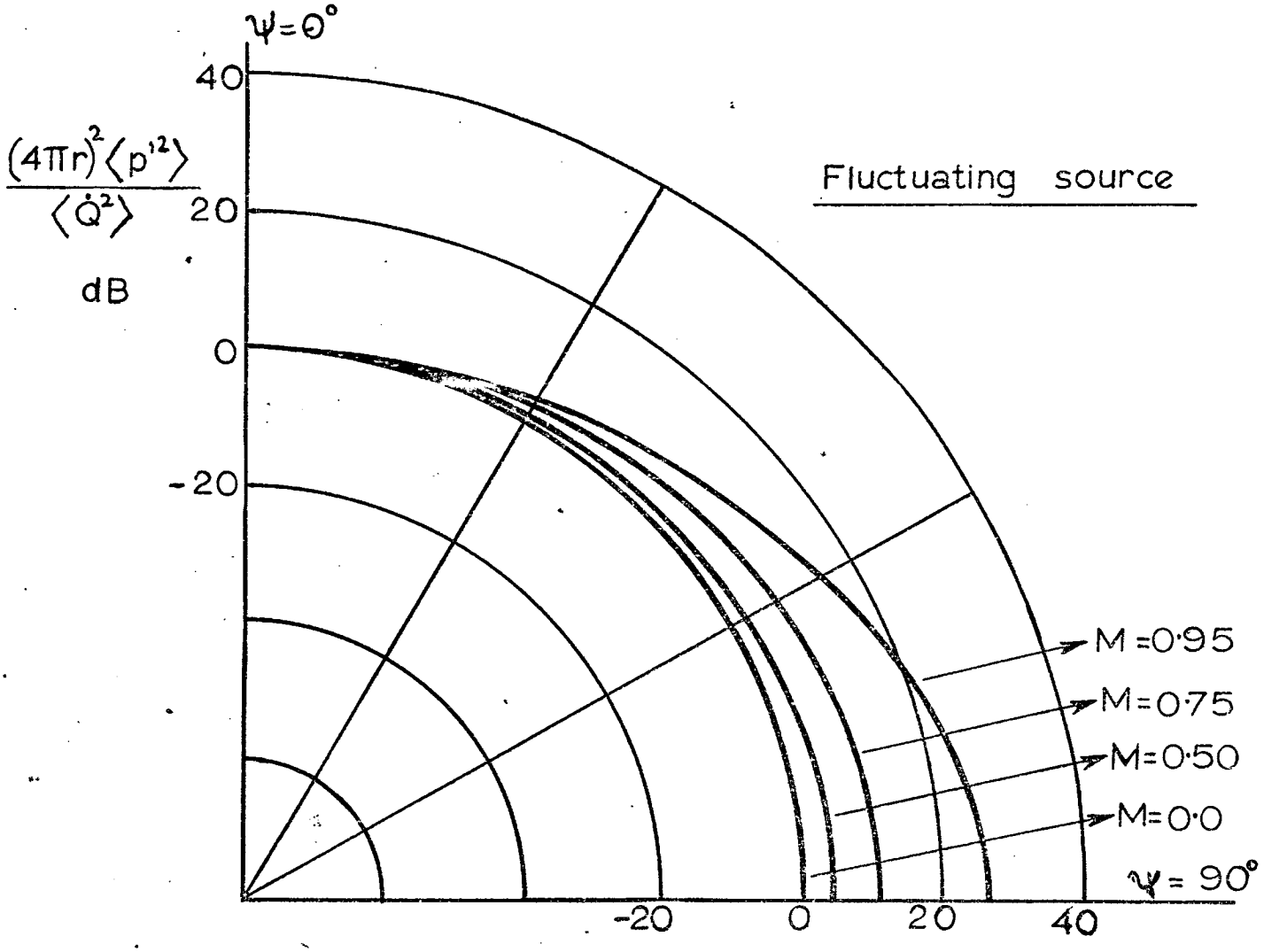

Fig. 7.3. Effect of rotation Mach number (M) on the directivity of overall mean square pressure from fluctuating rotating volume velocity source.

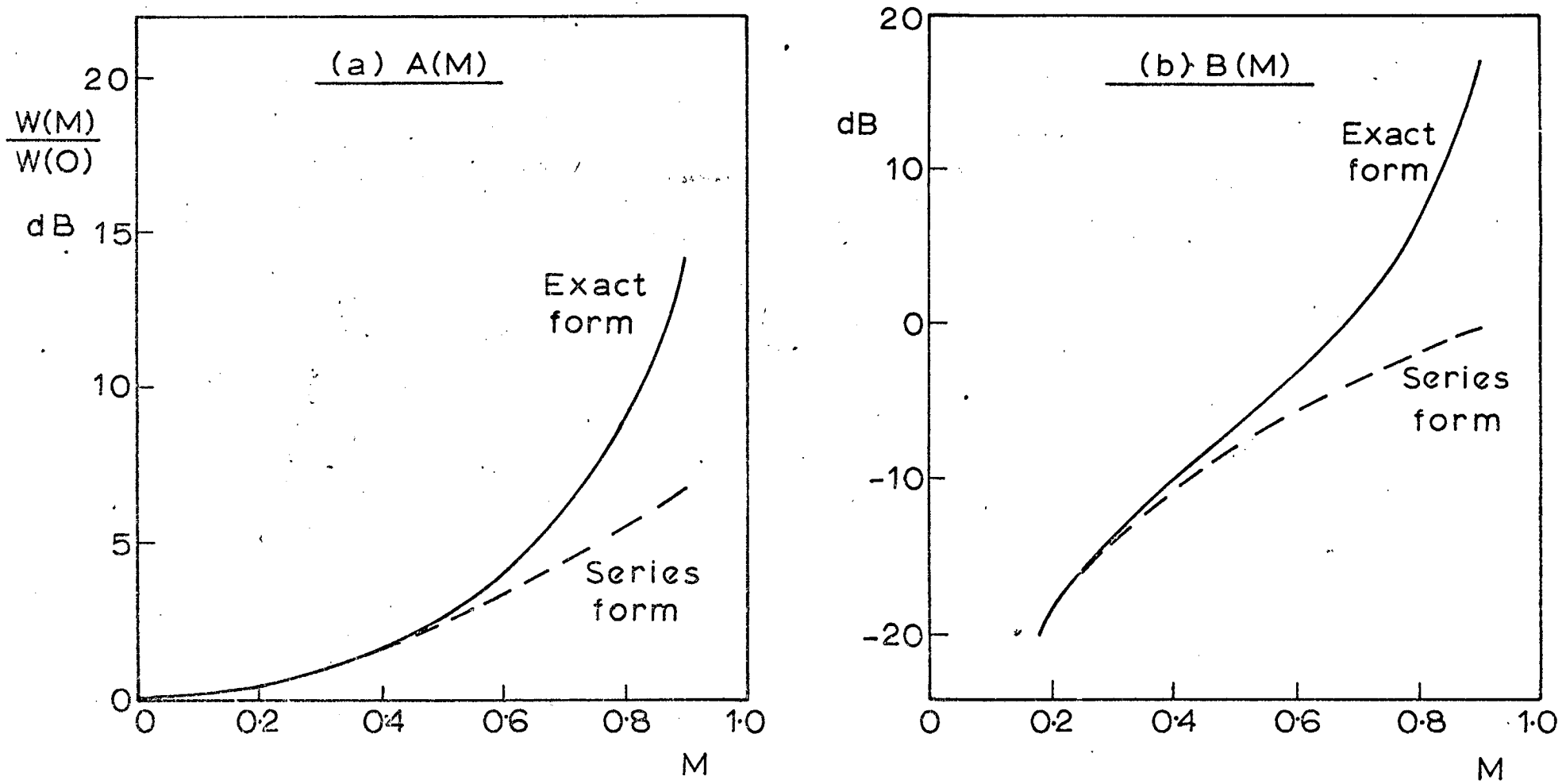

Fig. 7.4. Comparison of series expansions of coefficients (a) A(M) and (b) B(M), terminated at M^4 terms, with their closed form expressions.

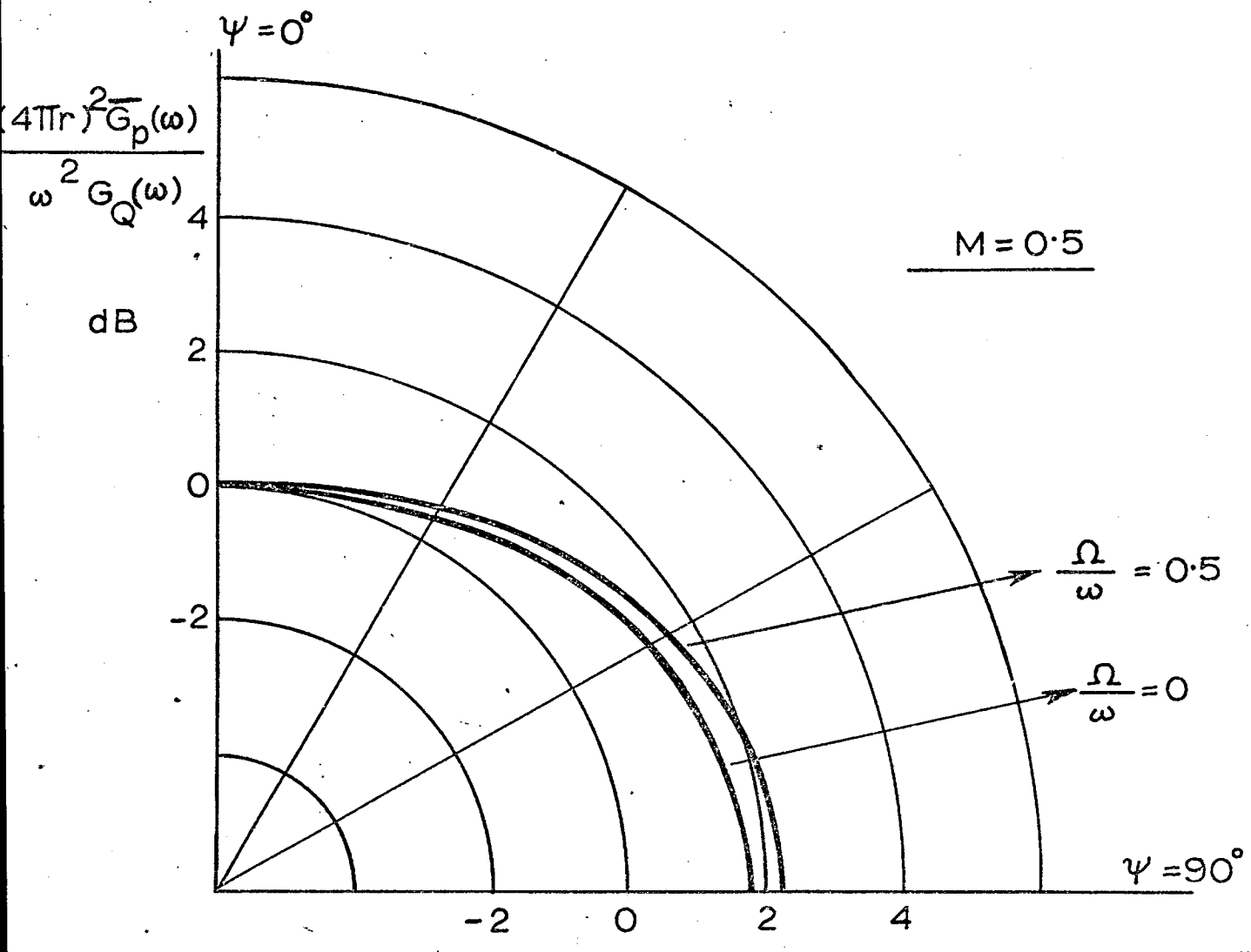

Fig. 7.5. Effect of rotation (Ω/ω) of the source on the directivity of the sound pressure spectral density. $G_Q(\omega) \propto \omega^{-2}$, M=0·5.

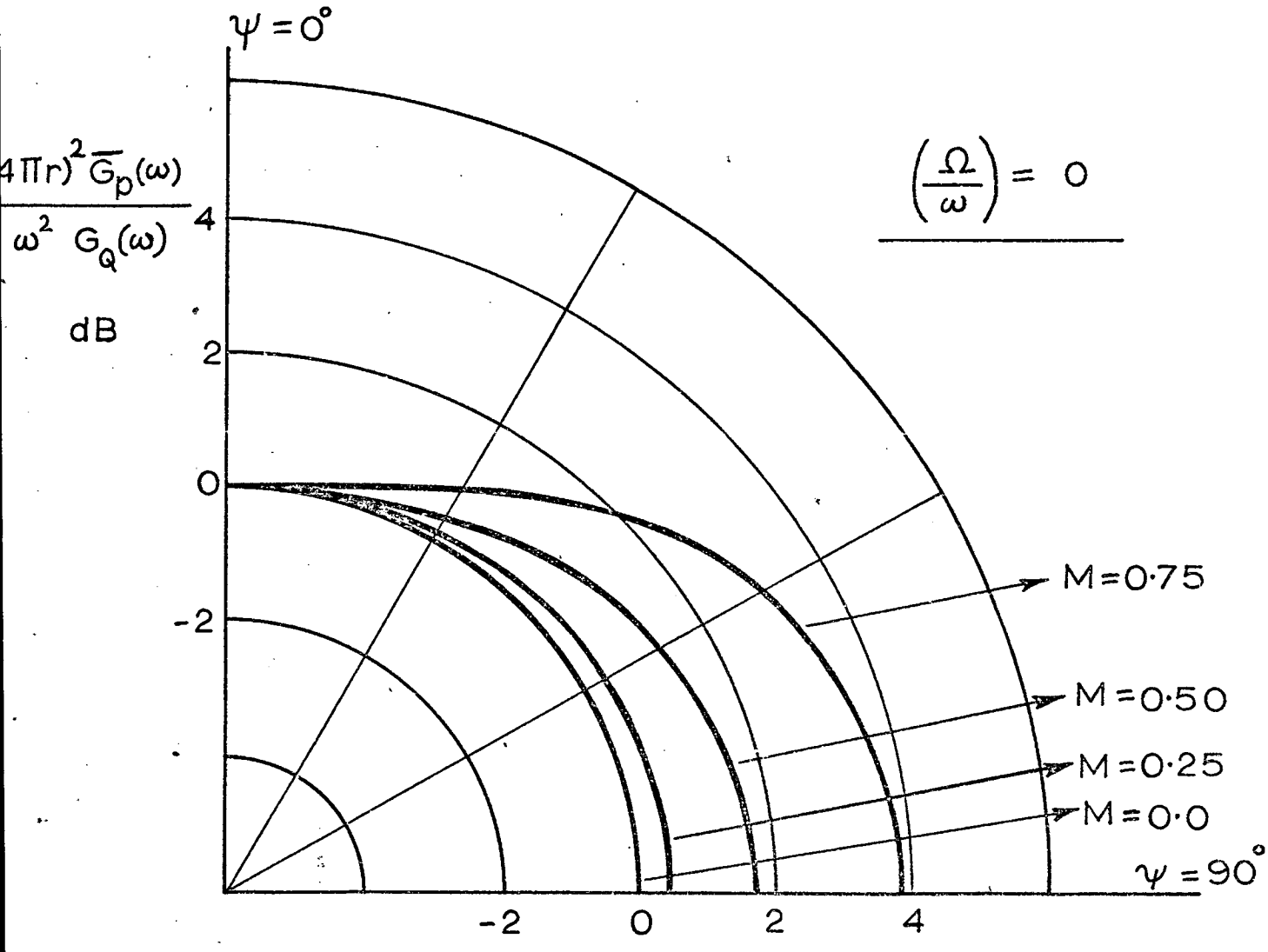

Fig. 7.6. Effect of rotation Mach number (M) on the directivity of the sound pressure spectral density. $G_Q(\omega) \propto \omega^{-2}, (\Omega/\omega) = 0$.

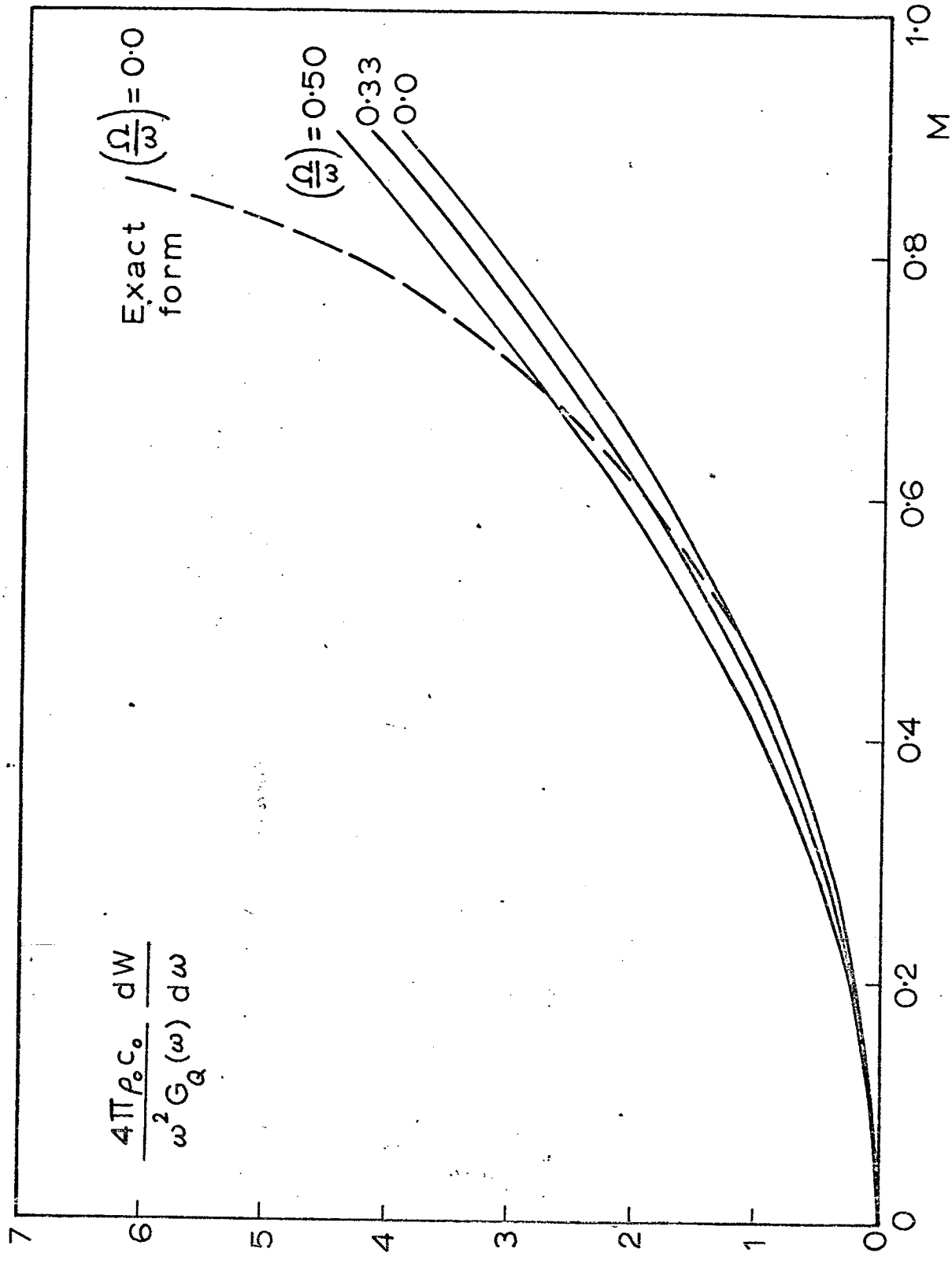

Fig. 7.7. Effect of rotation (Ω/ω) and Mach number (M) on the sound power spectral density. $G_Q(\omega) \propto \omega^{-2}$.

CHAPTER 8

SOUND RADIATION FROM POINT VOLUME-DISPLACEMENT SOURCES IN CIRCULAR MOTION

In the case of noise radiation from fans, propellers and rotors, part of the sound field arises from mass displacements due to finite effective thickness of the rotating blades, which give rise to rotating volume displacement sources. Here, unlike the rotating jet, no extra mass is introduced into the system but the passage of blades through the fluid results into volume displacement at every point in the path of the blade. The source strength S(t) (mass) in this situation can be represented physically by $S(t) = \rho_o \, d(t)$, where d(t) is a time-varying fluid volume displacement.

So far we have neglected the contribution from these sources in analyzing the sound field of rotating blades. This is valid at low and moderate tip Mach numbers, but as the tip speed approaches transonic values, the contribution from the parting of air due to the passage of blades can be important [41]. The object of this chapter is to derive radiation results for point volume-displacement sources of arbitrarily varying strength, rotating uniformly in a circle at subsonic speeds.

The analysis is restricted to overall results only; for this, the moving-source approach used before is most suitable. The spectral results can be obtained, if desired, by adopting the procedure described for the rotating point force (Chapter 6).

The sound field of a point volume-displacement source in arbitrary motion is derived first and this is then applied to the special case of

uniform circular motion in order to establish the effects of source acceleration on the radiated sound.

Once again, repetition is kept to a minimum since many of the comments are already given in the previous three chapters.

8.1 Sound field of a point volume displacement source in arbitrary motion

In the general case of a three-dimensional volume-displacement distribution $d(\underset{\sim}{x},t)$ per unit volume, the wave equation for an otherwise undisturbed ideal fluid is

$$\frac{1}{c_o^2}\frac{\partial^2 p}{\partial t^2} - \nabla^2 p = \rho_o \frac{\partial^2 d}{\partial t^2} \quad . \tag{8.1}$$

A point volume displacement $d(t)$ situated at position $\underset{\sim}{y}(t)$ is represented by

$$d(\underset{\sim}{x},t) = d(t)\ \delta(\underset{\sim}{x} - \underset{\sim}{y}) \quad , \tag{8.2}$$

where δ is the three-dimensional Dirac δ function. Writing $S(t) = \rho_o\, d(t)$ as the time-varying mass displacement, the solution to (8.1), for an unbounded fluid, is then

$$p' = p - p_o = \frac{1}{4\pi}\int_V \left[\frac{1}{r}\frac{\partial^2 (S\delta)}{\partial t^2}\right] dv \quad . \tag{8.3}$$

The square brackets imply evaluation at the retarded time $\left[t\right] = t - \left[r\right]/c_o$, where t is the time of observation and r is the distance from source to observer.

The integral in equation (8.3) can be evaluated by using Lowson's method [9]; that is, by using Green's identity the appropriate number of times and retaining the radiative terms. This involves a large amount of algebra and is in fact not necessary as shown below.

Examination of equation (8.3) reveals that the source term $\frac{\partial^2(S\delta)}{\partial t^2}$ is a second-order function as opposed to the source term $\frac{\partial(Q\delta)}{\partial t}$ for the point volume velocity source [Lowson, 9], which is a first order function. Once this is noticed, the sound pressure result for the point volume displacement source can be obtained by differentiating the result for the point volume velocity source. That is, since

$$\frac{\partial}{\partial t} = \frac{1}{[1-M_R]} \frac{\partial}{\partial [t]} \qquad \text{(from equation 5.2, Chapter 5)},$$

the required result follows from equation (7.1) as

$$p' = \left[\frac{1}{(1-M_R)} \frac{\partial}{\partial t} \left\{ \frac{1}{4\pi R(1-M_R)^2} \left(\frac{\partial S}{\partial t} + \frac{S}{1-M_R} \frac{\partial M_R}{\partial t}\right)\right\}\right]. \qquad (8.4)$$

The far-field sound pressure from a point volume displacement source $S(\underset{\sim}{x},t)$ in arbitrary motion is thus obtained from (8.4) as

$$p'(\underset{\sim}{r},t) = \left[\frac{1}{4\pi R(1-M_R)^3} \left\{ \frac{\partial^2 S}{\partial t^2} + \frac{\partial S}{\partial t} \frac{3(\partial M_R/\partial t)}{1 - M_R} + \frac{S}{1-M_R} \frac{\partial^2 M_R}{\partial t^2} + \frac{3S}{(1-M_R)^2} \left(\frac{\partial M_R}{\partial t}\right)^2 \right\}\right]$$

where $\underset{\sim}{r}$, $\underset{\sim}{x}$ are the vector positions of observer and source respectively, and M_R is the component of convection Mach number in the direction $\underset{\sim}{R}$ of the observer;

$$M_R = \frac{\underset{\sim}{M} \cdot \underset{\sim}{R}}{R} = \frac{M_j(r_j - x_j)}{R}. \qquad (8.6)$$

The square brackets again imply evaluation at retarded time.

8.2 Overall sound radiation from uniform circular motion

For the special case of uniform circular motion defined in Fig. 7.1,

result (8.5) reduces to

$$p'(\underset{\sim}{r},t) = \frac{1}{4\pi r}\left[\frac{\partial^2 S}{\partial t^2}(1-M_r)^{-3} + 3\,\frac{\partial S}{\partial t}\,\frac{\partial M_r}{\partial t}\,(1-M_r)^{-4} + S\,\frac{\partial^2 M_r}{\partial t^2}\,(1-M_r)^{-4}\right.$$

$$\left. + 3S\left(\frac{\partial M_r}{\partial t}\right)^2 (1-M_r)^{-5}\right] , \qquad (8.7)$$

where

$$M_r = -\,M \sin\psi \sin\theta \quad . \qquad (8.8)$$

(For details, see Section 7.1).

Since ψ and M are constant,

$$\frac{dM_r}{dt} = -\,\Omega M \sin\psi\cos\theta \qquad (8.9)$$

and

$$\frac{d^2M_r}{dt^2} = \Omega^2 M \sin\psi \sin\theta \quad . \qquad (8.10)$$

Equation (8.7) then gives, writing $M \sin\psi = \alpha$,

$$4\pi r\, p' = \left[\ddot{S}\,(1+\alpha\sin\theta)^{-3} - 3\dot{S}\Omega\alpha\cos\theta(1+\alpha\sin\theta)^{-4} + S\Omega^2\,\alpha\sin\theta(1+\alpha\sin\theta)^{-4}\right.$$

$$\left. + 3S\Omega^2\alpha^2\cos^2\theta(1+\alpha\sin\theta)^{-5}\right] . \qquad (8.11)$$

This general result is used below to find the mean square radiated pressure and sound power for a rotating random volume displacement source. Once again, it should be noted that a <u>random</u> source here implies a source which contains no periodic components at multiples of the rotational frequency.

8.2.1 <u>Mean square far-field sound pressure</u>

Equation (8.11) may be written as

$$4\pi r\, p' = e_1\left[\ddot{S}\right] - 3\Omega\alpha e_2\left[\dot{S}\right] + \Omega^2\alpha e_3\left[S\right] + 3\Omega^2\alpha^2 e_4\left[S\right] \qquad (8.12)$$

where

$$\left.\begin{aligned} e_1 &= \left[(1+\alpha\sin\theta)^{-3}\right], \\ e_2 &= \left[\cos\theta(1+\alpha\sin\theta)^{-4}\right], \\ e_3 &= \left[\sin\theta(1+\alpha\sin\theta)^{-4}\right], \\ \text{and}\quad e_4 &= \left[\cos^2\theta(1+\alpha\sin\theta)^{-5}\right]. \end{aligned}\right\} \tag{8.13}$$

If $\dot{S}$, $\ddot{S}$ are stationary random functions of time, they will contribute a continuous spectrum of radiated sound pressure which can be calculated by forming the pressure covariance from (8.12). The required procedure is described in Chapter 5, and the mean square far-field pressure is obtained as

$$(4\pi r)^2 R_p(0) = R_{\ddot{S}}(0)\left\{R_{e_1}(0)\right\} + \Omega^2 R_{\dot{S}}(0)\left\{-2\alpha R_{e_1e_3}(0) - 6\alpha^2 R_{e_1e_4}(0) + 9\alpha^2 R_{e_2}(0)\right\} + \Omega^4 R_S(0)\left\{\alpha^2 R_{e_3}(0) + 6\alpha^3 R_{e_3e_4}(0) + 9\alpha^4 R_{e_4}(0)\right\}. \tag{8.14}$$

In arriving at equation (8.14), terms in Ω, Ω^3 disappear since $R_{e_2e_1}(0) = R_{e_2e_3}(0) = R_{e_2e_4}(0) = 0$; also the correlation functions $R_{S\ddot{S}}(\tau)$ for $\tau = 0$ can be expressed in terms of $R_{\dot{S}}(0)$ by the relation

$$R_{S\ddot{S}}(0) = R_{\ddot{S}S}(0) = -R_{\dot{S}}(0), \tag{8.15}$$

which is derived in Appendix XII.

The correlation functions for $\tau = 0$ of the periodic functions e_1, e_2, e_3, e_4 may be evaluated by changing the variable of integration from $[\theta]$ to ϕ as indicated in Appendix VII. It follows from (8.13) that provided $\alpha < 1$,

$$R_{e_1}(0) = \frac{1}{2\pi}\int_0^{2\pi}(1+\alpha\sin\phi)^{-5}\,d\phi = 1 + \frac{15}{2}\alpha^2 + \frac{105}{4}\alpha^4 + \ldots \quad ,$$

$$R_{e_1e_3}(0) = \frac{1}{2\pi}\int_0^{2\pi}\sin\phi(1+\alpha\sin\phi)^{-6}\,d\phi = -3\alpha - 21\alpha^3 - \ldots \quad ,$$

$$R_{e_1e_4}(0) = R_{e_2}(0) = \frac{1}{2\pi}\int_0^{2\pi}\cos^2\phi(1+\alpha\sin\phi)^{-7}\,d\phi = \tfrac{1}{2} + \frac{7}{2}\alpha^2 + \ldots \quad ,$$

$$R_{e_3}(0) = \frac{1}{2\pi}\int_0^{2\pi}\sin^2\phi(1+\alpha\sin\phi)^{-7}\,d\phi = \tfrac{1}{2} + \frac{21}{2}\alpha^2 + \ldots \quad ,$$

$$R_{e_3e_4}(0) = \frac{1}{2\pi}\int_0^{2\pi}\cos^2\phi\sin\phi(1+\alpha\sin\phi)^{-8}\,d\phi = -\alpha - \ldots \quad ,$$

and

$$R_{e_4}(0) = \frac{1}{2\pi}\int_0^{2\pi}\cos^4\phi(1+\alpha\sin\phi)^{-9}\,d\phi = \tfrac{3}{8} + \ldots \quad . \qquad (8.16)$$

If exact forms are required, the integrals in (8.16) above can be evaluated by contour integration in the complex plane $z = e^{i\phi}$.

Taken together, equations (8.14) and (8.16) give an expression, accurate up to and including α^4 terms, for the mean square far-field sound pressure at the observation point (r,ψ), due to a point volume displacement source with random time variation rotating uniformly in a circle as

$$(4\pi r)^2 \langle p'^2\rangle = \langle \ddot{S}^2\rangle \left(1 + \frac{15}{2}\alpha^2 + \frac{105}{4}\alpha^4\right) + \Omega^2\langle \dot{S}^2\rangle \left(\frac{15}{2}\alpha^2 + \frac{105}{4}\alpha^4\right)$$

$$+ \Omega^4\langle S^2\rangle \left(\tfrac{1}{2}\alpha^2 + \frac{63}{8}\alpha^4\right) ; \qquad (\alpha = M\sin\psi). \qquad (8.17)$$

The effect of source acceleration is clearly displayed in the Ω^2 and Ω^4 terms, of which the Ω^4 term also contains the contribution of steady volume displacement to the overall radiation.

In the special case when the source strength is constant with time (steady thickness noise),

$$\langle p'^2 \rangle = \frac{\Omega^4 \langle S^2 \rangle}{(4\pi r)^2} \cdot \left(\tfrac{1}{2}\alpha^2 + \frac{63}{8}\alpha^4 + \ldots\right)$$

(steady thickness, $\alpha < 1$). (8.18)

This result can be compared with Gutin's propeller thickness noise calculation [3] by putting the number of blades equal to 1. Gutin gives the n^{th} harmonic amplitude of the radiated pressure as

$$p' = \frac{\Omega^2 S}{2\pi r} \; n^2 \; J_n(n\alpha) \; ; \qquad (8.19)$$

so adding the mean square contributions from all harmonics ($n = 1$ to ∞) gives

$$\langle p'^2 \rangle = \frac{\Omega^4 \langle S^2 \rangle}{(4\pi r)^2} \; 2 \sum_{n=1}^{\infty} n^4 \, J_n^2(n\alpha) \; . \qquad (8.20)$$

series expansion of Bessel functions shows that equations (8.18) and (8.20) are identical.

8.2.2 Overall sound power output

The overall radiated power corresponding to (8.17) follows by integrating the intensity over a spherical surface r = constant. Using (8.17) for the intensity, the power output from a rotating point volume displacement source, accurate up to and including M^4 terms, is obtained as

$$4\pi\rho_o c_o \cdot W = \langle \ddot{S}^2 \rangle \; (1 + 5M^2 + 14M^4) + \Omega^2 \langle \dot{S}^2 \rangle \; (5M^2 + 28M^4)$$

$$+ \Omega^4 \langle S^2 \rangle \; (\tfrac{1}{3}M^2 + \frac{21}{5}M^4) \; ; \qquad (M < 1) \; . \qquad (8.21)$$

The first term in the above equation is independent of the rotational frequency Ω; it gives the sound power radiated from a point volume dis-

placement source in uniform linear motion, which was calculated directly in section 5.1 of Chapter 5. The coefficient C(M) of $<\ddot{S}^2>$ is thus given by

$$C(M) = \frac{1 + M^2}{(1-M^2)^4} \quad . \tag{8.22}$$

8.3 Conclusions

(1) The sound field of a point volume displacement source in arbitrary motion has been derived and the result has been applied to the special case of uniform circular motion in order to establish the effects of source acceleration on the overall radiated sound field. The only restriction on the source spectrum is that it contain no periodic components at multiples of the rotational frequency.

(2) The effect of finite rotational frequency Ω on the overall radiation is maximum in the plane of rotation and its magnitude increases as M increases.

CHAPTER 9

SOUND RADIATION FROM POINT ACOUSTIC STRESSES IN CIRCULAR MOTION

Having established the radiation properties of point sources and point forces which execute circular motion, we now consider the radiation from the most complex sound source of practical significance, namely the acoustic stress tensor T_{ij}. Lowson's general result [9] for the sound field of a point acoustic stress in arbitrary motion is applied in this chapter to study the effects of (a) subsonic uniform straight-line motion, (b) subsonic uniform circular motion and (c) pure rotation on the overall sound radiation from random point acoustic stresses.

The effects of acceleration of the stresses due to steady rotation in a circle are established, using the moving-source approach adopted in previous chapters for the far-field sound radiation from rotating point forces and point sources. For the special case of linear motion, closed form solutions for the overall radiation are derived in section 9.1. The effects of acceleration perpendicular to the source path on these linear motion results are established in section 9.2.

To refresh our memories, it is worthwhile to mention that the moving-source approach is used because it gives simple results for the overall radiation directly, without involving the radiation spectrum. Although the spectral results are not derived here, they can be obtained by using the procedure adopted for the rotating point force theory (chapter 6). In fact, since the structure of the present analysis is identical to that used in the previous two studies, repetition is kept to a minimum, and the reader is

advised to become familiar with those chapters (5,6,7,8) before reading the present one.

Applications include the turbulent sound generation from tip jet rotors and noise from rotating blades with distributed forces, as described later on.

9.1 Power output from point acoustic stresses in uniform straight-line motion

The overall sound power output is studied as a function of convection Mach number M for three different orientations of acoustic stresses, relative to the direction of motion: (a) longitudinal stress T_{xx} with both axes normal to the direction of motion, (b) lateral stress $T_{x\theta}$ with one axis in the direction of motion and (c) longitudinal stress $T_{\theta\theta}$ with both axes in the direction of motion; see Fig. 9.1.

The far-field sound pressure from a point acoustic stress in uniform straight-line motion is given by Lighthill [1] as

$$p' = \frac{1}{4\pi c_o^2 R} \left[\frac{\partial^2 T_{RR}}{\partial t^2} (1 - M_R)^{-3} \right] , \qquad (9.1)$$

where the square brackets imply evaluation at retarded time

$$[t] = t - [R]/c_o \qquad (9.2)$$

and M_R is the approach Mach number of the source towards the observer,

$$M_R = M \cos \psi \quad . \qquad (9.3)$$

In terms of the observation point geometry defined in Fig. 9.1, the values of T_{RR} for the three stress orientations are

(a) T_{xx} : $T_{RR} = T_{xx} \sin^2\psi \cos^2\phi$, (9.4)

(b) $T_{x\theta}$: $T_{RR} = T_{x\theta} \sin\psi \cos\psi \cos\phi$, (9.5)

and

(c) $T_{\theta\theta}$: $T_{RR} = T_{\theta\theta} \cos^2\psi$. (9.6)

The mean square sound pressures for the three cases are then obtained from (9.1) as

(a) T_{xx} : $(4\pi c_o^2 R)^2 \langle p'^2 \rangle = \langle \ddot{T}_{xx}^2 \rangle \dfrac{\sin^4\psi \cos^4\phi}{(1 - M\cos\psi)^6}$, (9.7)

(b) $T_{x\theta}$: $(4\pi c_o^2 R)^2 \langle p'^2 \rangle = \langle \ddot{T}_{x\theta}^2 \rangle \dfrac{\sin^2\psi \cos^2\psi \cos^2\phi}{(1 - M\cos\psi)^6}$, (9.8)

(c) $T_{\theta\theta}$: $(4\pi c_o^2 R)^2 \langle p'^2 \rangle = \langle \ddot{T}_{\theta\theta}^2 \rangle \dfrac{\cos^4\psi}{(1 - M\cos\psi)^6}$. (9.9)

The overall sound power output from the moving singularity is obtained by integrating the acoustic intensity,

$$I = \langle p'^2 / \rho_o c_o \rangle \quad , \tag{9.10}$$

over a large spherical surface; for a uniformly convected source in rectilinear motion, the result was derived in section 5.1 of chapter 5 and is given by

$$W = \int_S I(1 - M\cos\psi)\, dS \ . \tag{9.11}$$

Using equations (9.7), (9.8) and (9.9), the overall sound power output results for the point acoustic stresses considered are given by

$$\text{(a)}\quad T_{xx}: \quad 16\pi^2\rho_o c_o^5 . W(M) = \langle \ddot{T}_{xx}^2 \rangle \int_0^{2\pi} \cos^4\phi \, d\phi \int_0^{\pi} \frac{\sin^5\psi \, . \, d\psi}{(1 - M\cos\psi)^5} \quad , \quad (9.12)$$

$$\text{(b)}\quad T_{x\theta}: \quad 16\pi^2\rho_o c_o^5 . W(M) = \langle \ddot{T}_{x\theta}^2 \rangle \int_0^{2\pi} \cos^2\phi \, d\phi \int_0^{\pi} \frac{\sin^3\psi \cos^2\psi . \, d\psi}{(1 - M\cos\psi)^5} \quad , \quad (9.13)$$

$$\text{(c)}\quad T_{\theta\theta}: \quad 16\pi^2\rho_o c_o^5 . W(M) = \langle \ddot{T}_{\theta\theta}^2 \rangle \int_0^{2\pi} d\phi \int_0^{\pi} \frac{\cos^4\psi \sin\psi \, . \, d\psi}{(1 - M\cos\psi)^5} \quad . \quad (9.14)$$

The required results then follow by straightforward integrations and the ratios of sound power output with uniform straight-line convection to the sound power output without convection, for the three cases, are obtained as

$$\text{(a)}\quad T_{xx}: \quad \frac{W(M)}{W(O)} = \frac{5}{16M^5}\left\{ 3 \ln\left(\frac{1+M}{1-M}\right) - \frac{2M(3-5M^2)}{(1-M^2)^2} \right\} , \quad (9.15)$$

$$\text{(b)}\quad T_{x\theta}: \quad \frac{W(M)}{W(O)} = \frac{15}{2M^5}\left\{ \frac{M(3-8M^2+7M^4)}{3(1-M^2)^3} - \tfrac{1}{2} \ln\left(\frac{1+M}{1-M}\right) \right\} , \quad (9.16)$$

$$\text{(c)}\quad T_{\theta\theta}: \quad \frac{W(M)}{W(O)} = \frac{5}{M^5}\left\{ \tfrac{1}{2} \ln\left(\frac{1+M}{1-M}\right) - \frac{M(3-11M^2+14M^4-12M^6)}{3(1-M^2)^4} \right\} . \quad (9.17)$$

Values of the sound power ratio in dB are plotted in Fig. 9.7.

9.2. Overall sound radiation from point acoustic stresses in uniform circular motion

The far-field sound pressure from a point acoustic stress $T_{ij}(\underset{\sim}{x},t)$ in arbitrary motion is given by Lowson [9] as

$$p'(\underset{\sim}{r},t) = \left[\frac{(r_i - x_i)(r_j - x_j)}{4\pi c_o^2 R^3 (1-M_R)^3} \left\{ \frac{\partial^2 T_{ij}}{\partial t^2} + \frac{\partial T_{ij}}{\partial t} \frac{3(\partial M_R/\partial t)}{(1-M_R)} + \frac{T_{ij}}{(1-M_R)} \frac{\partial^2 M_R}{\partial t^2} + \frac{3T_{ij}}{(1-M_R)^2} \left(\frac{\partial M_R}{\partial t}\right)^2 \right\} \right] \quad (9.18)$$

where M_R is the component of convection Mach number in the direction $\underset{\sim}{R}$ of the observer,

$$M_R = \frac{\underset{\sim}{M} \cdot \underset{\sim}{R}}{R} \quad . \tag{9.19}$$

The square brackets again imply evaluation at retarded time

$$\left[t \right] = t - \left[R \right] / c_o \quad , \tag{9.20}$$

where t is the time of observation and $R = \left| \underset{\sim}{r} - \underset{\sim}{x} \right|$ is the observer-source separation.

For a point acoustic stress rotating in a circle about a fixed point, it is convenient to take the centre of the circle as origin, see Fig. 9.2. Then at distances large compared with the radius of the circle ($r \gg a$), $R \doteq r$ and so

$$T_{ij} \frac{r_i r_j}{r^2} = T_{rr} \quad ; \quad M_R = M_r \quad . \tag{9.21}$$

Thus equation (9.18) reduces to

$$p'(\underset{\sim}{r},t) = \frac{1}{4\pi c_o^2 r} \left[\frac{\partial^2 T_{rr}}{\partial t^2} (1-M_r)^{-3} + \frac{\partial T_{rr}}{\partial t} \; 3\left(\frac{\partial M_r}{\partial t}\right)(1-M_r)^{-4} \right.$$

$$\left. + T_{rr}\left(\frac{\partial^2 M_r}{\partial t^2}\right)(1-M_r)^{-4} + 3T_{rr}\left(\frac{\partial M_r}{\partial t}\right)^2 (1-M_r)^{-5} \right] \quad . \tag{9.22}$$

In terms of the rotating acoustic stress geometry defined in Fig. 9.2,

$$M_r = - M \sin\psi \sin\theta \tag{9.23}$$

and

$$T_{rr} = T_{xx} \cos^2\psi + T_{\theta\theta} \sin^2\psi \sin^2\theta + T_{\sigma\sigma} \sin^2\psi \cos^2\theta + T_{x\theta} \sin\psi \cos\psi \sin\theta$$

$$- T_{x\sigma} \sin\psi \cos\psi \cos\theta - T_{\theta\sigma} \sin^2\psi \sin\theta \cos\theta \tag{9.24}$$

are the Mach number and acoustic stress components parallel to $\underset{\sim}{r} = \overrightarrow{OP}$. The pairs of axes for each of the six stress components are chosen to be combinations of axial (x), circumferential (θ) and radial (σ) directions.

The terminology used above is convenient for the use of this model for helicopter rotor noise calculations. Since the rotating blade has finite dimensions, the distributed force on it acts over a bounded region and vanishes with all its space derivatives on the surface of this bounded region. The concept of multipole analysis (see chapter 1 of [34]) can thus be applied here to represent the distribution of first-order sources (dipoles) by second-order point sources (quadrupoles) - see also § 325 of Lord Rayleigh's book [35]. That is, the moments of the axial and circumferential force components for (a) the point span, distributed chord loading model, and (b) the point chord, distributed span loading model are then represented by (a) $T_{x\theta}$ and $T_{\theta\theta}$, and (b) $T_{x\sigma}$ and $T_{\theta\sigma}$, respectively.

Expressions for the overall sound radiation (directivity and total power) will now be derived for two separate cases:

(1) zero rotation ($\Omega = 0$, M finite) with all six stress components, and

(2) Finite rotation with a restricted number of stress components.

9.2.1 Zero rotation, finite M

Since ψ does not vary with time, differentiation of equation (9.24) gives

$$\left(\frac{\partial^2 T_{rr}}{\partial t^2}\right)_{\Omega=0} = (\ddot{T}_{xx}\cos^2\psi + \ddot{T}_{\theta\theta}\sin^2\psi\sin^2\theta + \ddot{T}_{\sigma\sigma}\sin^2\psi\cos^2\theta + \ddot{T}_{x\theta}\sin\psi\cos\psi\sin\theta - \ddot{T}_{x\sigma}\sin\psi\cos\psi\cos\theta - \ddot{T}_{\theta\sigma}\sin^2\psi\sin\theta\cos\theta) \quad . \tag{9.25}$$

Equation (9.22) then gives, writing $M \sin\psi = \alpha$,

$$(4\pi c_o^2 r)\, p' = e_1 \left[\ddot{T}_{xx}\right] \cos^2\psi + e_2 \left[\ddot{T}_{\theta\theta}\right] \sin^2\psi + e_3 \left[\ddot{T}_{\sigma\sigma}\right] \sin^2\psi + e_4 \left[\ddot{T}_{x\theta}\right] \sin\psi \cos\psi - e_5 \left[\ddot{T}_{x\sigma}\right] \sin\psi \cos\psi - e_6 \left[\ddot{T}_{\theta\sigma}\right] \sin^2\psi \tag{9.26}$$

where

$$\left.\begin{aligned} e_1 &= \left[(1 + \alpha\sin\theta)^{-3} \right], \\ e_2 &= \left[\sin^2\theta\, (1 + \alpha\sin\theta)^{-3}\right], \\ e_3 &= \left[\cos^2\theta\, (1 + \alpha\sin\theta)^{-3}\right], \\ e_4 &= \left[\sin\theta\, (1 + \alpha\sin\theta)^{-3} \right], \\ e_5 &= \left[\cos\theta\, (1 + \alpha\sin\theta)^{-3} \right], \\ \text{and} \quad e_6 &= \left[\sin\theta\cos\theta\, (1 + \alpha\sin\theta)^{-3}\right] \end{aligned}\right\} \tag{9.27}$$

are all periodic functions of time, with period $2\pi/\Omega$. Results (9.26) and (9.27) are used below to find the mean square radiated pressure and sound power for a random acoustic stress.

9.2.1.1 Mean square far-field sound pressure

If $\ddot{T}_{rr}$ is a stationary random function of time, it will contribute a continuous spectrum of radiated sound pressure which can be calculated by forming the pressure covariance from (9.26). The procedure is explained in section 5.2 of Chapter 5 and after much algebra, the mean square far-field pressure is given in terms of the six acoustic stress components as

$$(4\pi c_o^2 r)^2 \langle p'^2 \rangle = \langle \ddot{T}_{xx}^2 \rangle (1 + \frac{15}{2}\alpha^2 + \frac{105}{4}\alpha^4)\cos^4\psi + \langle \ddot{T}_{\theta\theta}^2 \rangle (\tfrac{3}{8} + \frac{75}{16}\alpha^2 + \frac{1225}{64}\alpha^4)\sin^4\psi$$

$$+ \langle \ddot{T}_{\sigma\sigma}^2 \rangle (\tfrac{3}{8} + \frac{15}{16}\alpha^2 + \frac{105}{64}\alpha^4)\sin^4\psi + \langle \ddot{T}_{x\theta}^2 \rangle (\tfrac{1}{2} + \frac{45}{8}\alpha^2 + \frac{175}{8}\alpha^4)\sin^2\psi \cos^2\psi$$

$$+ \langle \ddot{T}_{x\sigma}^2 \rangle (\tfrac{1}{2} + \frac{15}{8}\alpha^2 + \frac{35}{8}\alpha^4)\sin^2\psi \cos^2\psi + \langle \ddot{T}_{\theta\sigma}^2 \rangle (\tfrac{1}{8} + \frac{15}{16}\alpha^2 + \frac{175}{64}\alpha^4)\sin^4\psi$$

$$+ \langle \ddot{T}_{xx}\ddot{T}_{\theta\theta} \rangle (1 + \frac{45}{4}\alpha^2 + \frac{175}{4}\alpha^4)\sin^2\psi \cos^2\psi + \langle \ddot{T}_{xx}\ddot{T}_{\sigma\sigma} \rangle (1 + \frac{15}{4}\alpha^2 + \frac{35}{4}\alpha^4)\sin^2\psi \cos^2\psi$$

$$+ \langle \ddot{T}_{\theta\theta}\ddot{T}_{\sigma\sigma} \rangle (\tfrac{1}{4} + \frac{15}{8}\alpha^2 + \frac{175}{32}\alpha^4)\sin^4\psi + \langle \ddot{T}_{xx}\ddot{T}_{x\theta} \rangle (-5\alpha - \frac{105}{4}\alpha^3)\sin\psi \cos^3\psi$$

$$+ \langle \ddot{T}_{\theta\theta}\ddot{T}_{x\theta} \rangle (-\frac{15}{4}\alpha - \frac{175}{8}\alpha^3)\sin^3\psi \cos\psi + \langle \ddot{T}_{\sigma\sigma}\ddot{T}_{x\theta} \rangle (-\frac{5}{4}\alpha - \frac{35}{8}\alpha^3)\sin^3\psi \cos\psi$$

$$+ \langle \ddot{T}_{x\sigma}\ddot{T}_{\theta\sigma} \rangle (-\frac{5}{4}\alpha - \frac{35}{8}\alpha^3)\sin^3\psi \cos\psi \quad , \qquad (\alpha < 1) \; . \qquad (9.28)$$

This is the main result of this section. In arriving at equation (9.28), the correlation functions for $\tau = 0$ of the periodic functions e_1 to e_6 were evaluated by change of variable from $[\theta]$ to ϕ as indicated in Appendix VII. Equation (9.28) gives an asymptotic expression, accurate up to α^4 terms, for the mean square far-field sound pressure at observation point (r,ψ) due to a point acoustic stress with random time variation when the effects of rotation are neglected. If an exact closed-form result is required, the integrals for the correlation functions should be evaluated by contour integration in the complex plane. Two special cases of the above result are now considered as a model for sound radiated from distributed forces on rotating blades.

(a) Point span, distributed chord loading

Only two components of the acoustic stress need to be considered here, $T_{x\theta}$ and $T_{\theta\theta}$. The resulting mean square pressure can be written more simply

using the further assumption that these are related by

$$\ddot{T}_{\theta\theta} = \varepsilon \ddot{T}_{x\theta} \quad , \qquad (\varepsilon = \text{constant}) . \tag{9.29}$$

Equation (9.29) applies, for example, if the local fluctuating forces on the blade have a fixed orientation in the rotating frame of reference. With equation (9.28) it gives

$$\frac{(4\pi c_o^2 r)^2 \langle p'^2 \rangle}{\langle \ddot{T}_{x\theta}^2 \rangle} = \left\{ (\tfrac{1}{2} + \frac{45}{8}\alpha^2 + \frac{175}{8}\alpha^4)\sin^2\psi \cos^2\psi - \varepsilon(\frac{15}{4}\alpha + \frac{175}{8}\alpha^3)\sin^3\psi\cos\psi \right.$$
$$\left. + \varepsilon^2(\tfrac{3}{8} + \frac{75}{16}\alpha^2 + \frac{1225}{64}\alpha^4)\sin^4\psi \right\}, \quad (\alpha < 1) . \tag{9.30}$$

(b) Point chord, distributed span loading

Here only $T_{x\sigma}$ and $T_{\theta\sigma}$ components are present and if they are also related by

$$\ddot{T}_{\theta\sigma} = \varepsilon \ddot{T}_{x\sigma} \quad , \tag{9.31}$$

the mean square pressure is obtained from (9.28) as

$$\frac{(4\pi c_o^2 r)^2 \langle p'^2 \rangle}{\langle \ddot{T}_{x\sigma}^2 \rangle} = \left\{ (\tfrac{1}{2} + \frac{15}{8}\alpha^2 + \frac{35}{8}\alpha^4)\sin^2\psi \cos^2\psi - \varepsilon(\frac{5}{4}\alpha + \frac{35}{8}\alpha^3)\sin^3\psi \cos\psi \right.$$
$$\left. + \varepsilon^2(\tfrac{1}{8} + \frac{15}{16}\alpha^2 + \frac{175}{64}\alpha^4)\sin^4\psi \right\}, \quad (\alpha < 1) . \tag{9.32}$$

Figures 9.3 to 9.6 show the effects of Mach number M and drag-thrust ratio ε on the overall radiated sound field, for both point span and point chord loading models. For this purpose the mean square sound pressures are normalized by the resultant stresses

$(1 + \varepsilon^2) \langle \ddot{T}^2_{x\theta} \rangle$ and $(1 + \varepsilon^2) \langle \ddot{T}^2_{x\sigma} \rangle$ respectively. The standard values of $\varepsilon = 0.1$ and $M = 0.5$ are chosen to be characteristic of helicopter rotors.

It should be noted that when the forces on the blade are distributed both along the chord and along the span, the resulting overall mean square pressure can be obtained by adding the results (9.30) and (9.32) in appropriate proportions. This result follows from equation (9.28).

9.2.1.2 Overall sound power output

The overall radiated power corresponding to (9.28) follows by integrating the intensity over a spherical surface r = constant;

$$W = \int_S I(r,\psi)\, dS \,. \tag{9.33}$$

When the integral above is evaluated using (9.28) for the intensity, the power output from a random point acoustic stress, neglecting the effects of rotation, is obtained in the form

$$\begin{aligned}(60\pi\rho_o c_o^5)\, W = {} & C_1(M)\left\{ 3 \langle \ddot{T}^2_{xx} \rangle + 3 \langle \ddot{T}^2_{\sigma\sigma} \rangle + \langle \ddot{T}^2_{x\sigma} \rangle + 2 \langle \ddot{T}_{xx} \ddot{T}_{\sigma\sigma} \rangle \right\} \\ & + C_2(M)\left\{ \langle \ddot{T}^2_{x\theta} \rangle + \langle \ddot{T}^2_{\theta\sigma} \rangle + 2 \langle \ddot{T}_{xx} \ddot{T}_{\theta\theta} \rangle + 2 \langle \ddot{T}_{\theta\theta} \ddot{T}_{\sigma\sigma} \rangle \right\} \\ & + C_3(M)\left\{ 3 \langle \ddot{T}^2_{\theta\theta} \rangle \right\} . \end{aligned} \tag{9.34}$$

Since $\Omega = 0$, equation (9.34) in fact gives the sound power radiated from a point acoustic stress in uniform linear motion. The results for various components of the acoustic stress were calculated directly in section 9.1. Thus $C_1(M)$ is given by equation (9.15), $C_2(M)$ by equation (9.16), and $C_3(M)$ by equation (9.17).

For low Mach number applications, it may be useful to approximate

C_1, C_2, C_3 by the first few terms of a series. Expansion in powers of M gives

$$C_1(M) = 1 + \frac{15}{7} M^2 + \frac{10}{3} M^4 + \ldots \quad , \tag{9.35}$$

$$C_2(M) = 1 + \frac{45}{7} M^2 + \frac{50}{3} M^4 + \ldots \quad , \tag{9.36}$$

$$C_3(M) = 1 + \frac{75}{7} M^2 + \frac{350}{9} M^4 + \ldots \quad . \tag{9.37}$$

Figure 9.7 shows the effect of terminating the series expansions at the M^4 term.

9.2.2 Effect of rotation

In order to reduce the amount of algebra involved, the effects of finite rotational frequency Ω on the overall radiation are established in this section for the special case where only three acoustic stress components T_{xx}, $T_{x\theta}$ and $T_{\theta\theta}$ are present.

Writing $M \sin\psi = \alpha$, $T_{xx} \cos^2\psi = X$, $T_{x\theta} \sin\psi \cos\psi = Y$, and $T_{\theta\theta} \sin^2\psi = Z$, equations (9.23) and (9.24) become

$$M_r = \alpha \sin\theta \tag{9.38}$$

and

$$T_{rr} = X + Y \sin\theta + Z \sin^2\theta \quad . \tag{9.39}$$

Since α is constant,

$$\frac{dM_r}{dt} = - \Omega\alpha\cos\theta \quad , \qquad \frac{d^2M_r}{dt^2} = \Omega^2 \alpha\sin\theta \quad , \tag{9.40}$$

$$\frac{dT_{rr}}{dt} = \dot{X} + \dot{Y} \sin\theta + \dot{Z} \sin^2\theta + \Omega Y\cos\theta + \Omega Z \sin 2\theta \ , \tag{9.41}$$

and

$$\frac{d^2T_{rr}}{dt^2} = \ddot{X} + \ddot{Y} \sin\theta + \ddot{Z} \sin^2\theta + 2\Omega\dot{Y} \cos\theta + 2\Omega\dot{Z} \sin 2\theta$$
$$- \Omega^2 Y \sin\theta + 2\Omega^2 Z \cos 2\theta \quad . \tag{9.42}$$

Equation (9.22) then gives

$$(4\pi c_o r)\, p' = f_1\left[\ddot{X}\right] + f_2\left[\ddot{Y}\right] + f_3\left[\ddot{Z}\right] + 2\Omega f_4\left[\dot{Y}\right] + 2\Omega f_5\left[\dot{Z}\right]$$
$$- \Omega^2 f_2\left[Y\right] + 2\Omega^2 f_6\left[Z\right] - 3\Omega\alpha g_1\left[\dot{X}\right] - 3\Omega\alpha g_2\left[\dot{Y}\right]$$
$$- 3\Omega\alpha g_3\left[\dot{Z}\right] - 3\Omega\bar{\alpha}^2 g_4\left[Y\right] - 3\Omega^2\alpha g_5\left[Z\right] + \Omega^2\alpha g_6\left[X\right]$$
$$+ \Omega^2\alpha g_7\left[Y\right] + \Omega^2\alpha g_8\left[Z\right] + 3\Omega^2\alpha^2 h_1\left[X\right]$$
$$+ 3\Omega^2\alpha^2 h_2\left[Y\right] + 3\Omega^2\alpha^2 h_3\left[Z\right] \qquad (9.43)$$

where

$$\begin{cases} f_1 = \left[(1+\alpha\sin\theta)^{-3}\right], & f_2 = \left[\sin\theta(1+\alpha\sin\theta)^{-3}\right], \\ f_3 = \left[\sin^2\theta(1+\alpha\sin\theta)^{-3}\right], & f_4 = \left[\cos\theta(1+\alpha\sin\theta)^{-3}\right], \\ f_5 = \left[\sin 2\theta(1+\alpha\sin\theta)^{-3}\right], & f_6 = \left[\cos 2\theta(1+\alpha\sin\theta)^{-3}\right]; \end{cases} \qquad (9.44)$$

$$\begin{cases} g_1 = \left[\cos\theta(1+\alpha\sin\theta)^{-4}\right], & g_2 = \left[\sin\theta\cos\theta(1+\alpha\sin\theta)^{-4}\right], \\ g_3 = \left[\sin^2\theta\cos\theta(1+\alpha\sin\theta)^{-4}\right], & g_4 = \left[\cos^2\theta(1+\alpha\sin\theta)^{-4}\right], \\ g_5 = \left[\sin 2\theta\cos\theta(1+\alpha\sin\theta)^{-4}\right], & g_6 = \left[\sin\theta(1+\alpha\sin\theta)^{-4}\right], \\ g_7 = \left[\sin^2\theta(1+\alpha\sin\theta)^{-4}\right], & g_8 = \left[\sin^3\theta(1+\alpha\sin\theta)^{-4}\right]; \end{cases} \qquad (9.45)$$

$$\begin{cases} h_1 = \left[\cos^2\theta(1+\alpha\sin\theta)^{-5}\right], & h_2 = \left[\sin\theta\cos^2\theta(1+\alpha\sin\theta)^{-5}\right], \\ h_3 = \left[\sin^2\theta\cos^2\theta(1+\alpha\sin\theta)^{-5}\right] \end{cases} \qquad (9.46)$$

are all periodic functions of time, with period $2\pi/\Omega$.

9.2.2.1 Mean square far-field sound pressure

If the rotating point acoustic stress is a stationary random function of time, it will contribute a continuous spectrum of radiated sound pressure. The mean square pressure can be calculated by forming the pressure covariance from (9.43); the method is described in chapter 5. After a tremendous

amount of algebra, the overall mean square far-field pressure is obtained in terms of the three acoustic stress components as

$$(4\pi c_o^2 r)^2 \langle p'^2 \rangle \doteq \Big\{ \langle \ddot{T}_{xx}^2 \rangle \left(1+\tfrac{15}{2}\alpha^2+\tfrac{105}{4}\alpha^4\right)\cos^4\psi + \langle \ddot{T}_{x\theta}^2 \rangle \left(\tfrac{1}{2}+\tfrac{45}{8}\alpha^2+\tfrac{175}{8}\alpha^4\right)\sin^2\psi\cos^2\psi$$

$$+ \langle \ddot{T}_{\theta\theta}^2 \rangle \left(\tfrac{3}{8}+\tfrac{75}{16}\alpha^2+\tfrac{1225}{64}\alpha^4\right)\sin^4\psi + \langle \ddot{T}_{xx}\ddot{T}_{x\theta} \rangle \left(-5\alpha-\tfrac{105}{4}\alpha^3\right)\sin\psi\cos^3\psi$$

$$+ \langle \ddot{T}_{xx}\ddot{T}_{\theta\theta} \rangle \left(1+\tfrac{45}{4}\alpha^2+\tfrac{175}{4}\alpha^4\right)\sin^2\psi\cos^2\psi + \langle \ddot{T}_{x\theta}\ddot{T}_{\theta\theta} \rangle \left(-\tfrac{15}{4}\alpha-\tfrac{175}{8}\alpha^3\right)\sin^3\psi\cos\psi \Big\}$$

$$+\Omega^2\Big\{ \langle \dot{T}_{xx}^2 \rangle \left(\tfrac{15}{2}\alpha^2+\tfrac{105}{2}\alpha^4\right)\cos^4\psi + \langle \dot{T}_{x\theta}^2 \rangle \left(3+\tfrac{225}{8}\alpha^2+\tfrac{245}{2}\alpha^4\right)\sin^2\psi\cos^2\psi$$

$$+ \langle \dot{T}_{\theta\theta}^2 \rangle \left(3+\tfrac{651}{16}\alpha^2+\tfrac{5845}{32}\alpha^4\right)\sin^4\psi + \langle \dot{T}_{xx}\dot{T}_{x\theta} \rangle \left(-10\alpha-\tfrac{315}{4}\alpha^3\right)\sin\psi\cos^3\psi$$

$$+ \langle \dot{T}_{xx}\dot{T}_{\theta\theta} \rangle \left(\tfrac{153}{4}\alpha^2+\tfrac{427}{2}\alpha^4\right)\sin^2\psi\cos^2\psi + \langle \dot{T}_{x\theta}\dot{T}_{\theta\theta} \rangle \left(-\tfrac{45}{2}\alpha-\tfrac{1155}{8}\alpha^3\right)\sin^3\psi\cos\psi \Big\}$$

$$+\Omega^4\Big\{ \langle T_{xx}^2 \rangle \left(\tfrac{1}{2}\alpha^2+\tfrac{63}{8}\alpha^4\right)\cos^4\psi + \langle T_{x\theta}^2 \rangle \left(\tfrac{1}{2}+\tfrac{63}{8}\alpha^2+\tfrac{735}{16}\alpha^4\right)\sin^2\psi\cos^2\psi$$

$$+ \langle T_{\theta\theta}^2 \rangle \left(2+\tfrac{365}{16}\alpha^2+\tfrac{14151}{128}\alpha^4\right)\sin^4\psi + \langle T_{xx}T_{x\theta} \rangle \left(-\alpha-\tfrac{63}{4}\alpha^3\right)\sin\psi\cos^3\psi$$

$$+ \langle T_{xx}T_{\theta\theta} \rangle \left(\tfrac{33}{4}\alpha^2+\tfrac{525}{8}\alpha^4\right)\sin^2\psi\cos^2\psi$$

$$+ \langle T_{x\theta}T_{\theta\theta} \rangle \left(-\tfrac{33}{4}\alpha-\tfrac{525}{8}\alpha^3\right)\sin^3\psi\cos\psi \Big\}, \qquad (\alpha < 1). \qquad (9.47)$$

Once again, in arriving at the above result, the correlation functions for $\tau = 0$ of the periodic functions f, g, h were evaluated by changing the variable of integration from $[\theta]$ to ϕ, as shown in Appendix VII. Also correlation functions of the form $R_{\ddot{x}\ddot{y}}(\tau)$ for $\tau = 0$ were expressed in terms of $R_{\dot{x}\dot{y}}(0)$ by the relation

$$R_{\ddot{x}\ddot{y}}(0) = R_{\dot{x}\dot{y}}(0) = -R_{\dot{x}\dot{y}}(0), \qquad (9.48)$$

which is derived in Appendix XII.

Equation (9.47) is the main result of this section. It gives an asymptotic expression, accurate up to α^4 terms, for the mean square far-field sound pressure at observation point (r,ψ) due to a point acoustic stress with random time variation rotating uniformly in a circle. As before, it should be remembered that the source spectrum should contain no discrete components at multiples of the rotational frequency. Exact expressions in closed form can be obtained by evaluating the correlation function integrals by contour integration in the complex plane. The effect of source acceleration is clearly displayed in the Ω^2 and Ω^4 terms, of which the Ω^4 term also contains the contribution of steady acoustic stress components to the overall radiation.

Close examination of equation (9.47) reveals that the numerical coefficients of the α terms in the Ω^o, Ω^2 and Ω^4 terms are approximately similar in order of magnitude; this observation also applies to the α^2, α^3 and α^4 terms. Thus at least at low Mach numbers ($M < 0.5$), the effects of rotation would be roughly similar to those for the pure rotation ($M = 0$, Ω finite) case, which are established in section 9.3.

Two special cases of the general result are now considered below.

(a) Radiation in the plane of rotation

The overall mean square pressure in the plane of rotation is obtained from (9.47) as

$$(4\pi c_o^2 r)^2 \langle p'^2 \rangle = \langle \ddot{T}_{\theta\theta}^2 \rangle \left(\tfrac{3}{8} + \frac{75}{16}M^2 + \frac{1225}{64}M^4\right) + \Omega^2 \langle \dot{T}_{\theta\theta}^2 \rangle \left(3 + \frac{651}{16}M^2 + \frac{5845}{32}M^4\right)$$

$$+ \Omega^4 \langle T_{\theta\theta}^2 \rangle \left(2 + \frac{365}{16}M^2 + \frac{14151}{128}M^4\right) . \qquad (9.49)$$

For a single-frequency acoustic stress of radian frequency ν ,

$$\langle \dot{T}_{\theta\theta}^2 \rangle = \nu^2 \langle T_{\theta\theta}^2 \rangle \quad \text{and} \quad \langle \ddot{T}_{\theta\theta}^2 \rangle = \nu^4 \langle T_{\theta\theta}^2 \rangle \ . \tag{9.50}$$

The corresponding radiation can be written in normalized form as

$$\frac{(4\pi c_o^2 r)^2 \langle p'^2 \rangle}{\nu^4 \langle T_{\theta\theta}^2 \rangle} = (\tfrac{3}{8} + \frac{75}{16}M^2 + \frac{1225}{64}M^4) + (\frac{\Omega}{\nu})^2(3 + \frac{651}{16}M^2 + \frac{5845}{32}M^4)$$
$$+ (\frac{\Omega}{\nu})^4(2 + \frac{365}{16}M^2 + \frac{14151}{128}M^4) \ . \tag{9.51}$$

The in-plane radiation is plotted in Fig. 9.8, showing the increase in level as either M or (Ω/ν) is increased.

(b) Point span, distributed chord loading

As in section 9.2.1.1, the mean square pressure result can be simplified by assuming that the local fluctuating forces on the blade have a fixed orientation in the rotating frame of reference. For a single-frequency (ν) acoustic stress, the overall radiation is then obtained from (9.47) in the form

$$\frac{(4\pi c_o^2 r)^2 \langle p'^2 \rangle}{\nu^4 \langle T_{x\theta}^2 \rangle} = \Big\{(\tfrac{1}{2} + \frac{45}{8}\alpha^2 + \frac{175}{8}\alpha^4)\sin^2\psi\cos^2\psi - \varepsilon(\frac{15}{4}\alpha + \frac{175}{8}\alpha^3)\sin^3\psi\cos\psi$$
$$+ \varepsilon^2(\tfrac{3}{8} + \frac{75}{16}\alpha^2 + \frac{1225}{64}\alpha^4)\sin^4\psi \Big\} + (\frac{\Omega}{\nu})^2\Big\{(3 + \frac{225}{8}\alpha^2 + \frac{245}{2}\alpha^4)\sin^2\psi\cos^2\psi$$
$$- \varepsilon(\frac{45}{2}\alpha + \frac{1155}{8}\alpha^3)\sin^3\psi\cos\psi + \varepsilon^2(3 + \frac{651}{16}\alpha^2 + \frac{5845}{32}\alpha^4)\sin^4\psi \Big\}$$
$$+ (\frac{\Omega}{\nu})^4\Big\{(\tfrac{1}{2} + \frac{63}{8}\alpha^2 + \frac{735}{16}\alpha^4)\sin^2\psi\cos^2\psi - \varepsilon(\frac{33}{4}\alpha + \frac{525}{8}\alpha^3)\sin^3\psi\cos\psi$$
$$+ \varepsilon^2(2 + \frac{365}{16}\alpha^2 + \frac{14151}{128}\alpha^4)\sin^4\psi \Big\} \ . \tag{9.52}$$

The effect of varying (Ω/ν) is illustrated in the polar diagram of Fig. 9.9, where the sound pressure is normalized by the resultant stress $(1 + \varepsilon^2) \langle T_{x\theta}^2 \rangle$, and the values $M = 0.5$, $\varepsilon = 0.1$ used to form a standard case.

9.2.2.2 Overall sound power output

Using (9.47) for the intensity, the overall radiated power follows by integration over the spherical surface r = constant. The power output from a rotating point acoustic stress, accurate up to M^4 terms, is then given by

$$
\begin{aligned}
(60\pi\rho_o c_o^5)W = &\Big\{ \langle \ddot{T}_{xx}^2 \rangle \left(3 + \tfrac{45}{7}M^2 + 10M^4\right) + \langle \ddot{T}_{x\theta}^2 \rangle \left(1 + \tfrac{45}{7}M^2 + \tfrac{50}{3}M^4\right) \\
&+ \langle \ddot{T}_{\theta\theta}^2 \rangle \left(3 + \tfrac{225}{7}M^2 + \tfrac{350}{3}M^4\right) + \langle \ddot{T}_{xx}\ddot{T}_{\theta\theta} \rangle \left(2 + \tfrac{90}{7}M^2 + \tfrac{100}{3}M^4\right) \Big\} \\
&+ \Omega^2 \Big\{ \langle \dot{T}_{xx}^2 \rangle \left(\tfrac{45}{7}M^2 + 20M^4\right) + \langle \dot{T}_{x\theta}^2 \rangle \left(6 + \tfrac{225}{7}M^2 + \tfrac{280}{3}M^4\right) \\
&+ \langle \dot{T}_{\theta\theta}^2 \rangle \left(24 + 279M^2 + \tfrac{3340}{3}M^4\right) + \langle \dot{T}_{xx}\dot{T}_{\theta\theta} \rangle \left(\tfrac{306}{7}M^2 + \tfrac{488}{3}M^4\right) \Big\} \\
&+ \Omega^4 \Big\{ \langle T_{xx}^2 \rangle \left(\tfrac{3}{7}M^2 + 3M^4\right) + \langle T_{x\theta}^2 \rangle \left(1 + 9M^2 + 35M^4\right) \\
&+ \langle T_{\theta\theta}^2 \rangle \left(16 + \tfrac{1095}{7}M^2 + \tfrac{4717}{7}M^4\right) + \langle T_{xx}T_{\theta\theta} \rangle \left(\tfrac{66}{7}M^2 + 50M^4\right) \Big\} .
\end{aligned}
\tag{9.53}
$$

The first term in the above equation is independent of the rotational frequency Ω. It gives the sound power radiated from a point acoustic stress in uniform linear motion, for which closed-form expressions were discussed in section 9.2.1.2.

9.3 Spinning point acoustic stresses

If the radius of the circular path is now reduced to zero, then $M = 0$ although Ω remains finite. The resulting overall mean square pressure due to pure rotation of the point acoustic stress with components T_{xx}, $T_{x\theta}$ and

$T_{\theta\theta}$ is given by the general equation (9.47) as

$$(4\pi c_o^2 r)^2 \langle p'^2 \rangle = \langle \ddot{T}_{xx}^2 \rangle \cos^4\psi + \langle \ddot{T}_{xx} \ddot{T}_{\theta\theta} \rangle \sin^2\psi \cos^2\psi$$
$$+ (\tfrac{1}{2} \langle \ddot{T}_{x\theta}^2 \rangle + \Omega^2 3 \langle \dot{T}_{x\theta}^2 \rangle + \Omega^4 \tfrac{1}{2} \langle T_{x\theta}^2 \rangle) \sin^2\psi \cos^2\psi$$
$$+ (\tfrac{3}{8} \langle \ddot{T}_{\theta\theta}^2 \rangle + \Omega^2 3 \langle \dot{T}_{\theta\theta}^2 \rangle + \Omega^4 2 \langle T_{\theta\theta}^2 \rangle) \sin^4\psi \; . \qquad (9.54)$$

Integration over a spherical surface gives the corresponding sound power output as

$$(60\pi\rho_o c_o^5).W(\Omega) = 3 \langle \ddot{T}_{xx}^2 \rangle + 2 \langle \ddot{T}_{xx} \ddot{T}_{\theta\theta} \rangle + \langle \ddot{T}_{x\theta}^2 \rangle + 3 \langle \ddot{T}_{\theta\theta}^2 \rangle$$
$$+ 6\Omega^2 \langle \dot{T}_{x\theta}^2 \rangle + 24\Omega^2 \langle \dot{T}_{\theta\theta}^2 \rangle$$
$$+ \Omega^4 \langle T_{x\theta}^2 \rangle + 16\Omega^4 \langle T_{\theta\theta}^2 \rangle \; . \qquad (9.55)$$

9.3.1 Single frequency spinning acoustic stresses

Two particular cases are the harmonically varying stress components $T_{x\theta}$ and $T_{\theta\theta}$, with radian frequency ν; then

$$\left.\begin{aligned} &\langle \dot{T}_{x\theta}^2 \rangle = \nu^2 \langle T_{x\theta}^2 \rangle \; , \quad \langle \ddot{T}_{x\theta}^2 \rangle = \nu^4 \langle T_{x\theta}^2 \rangle \; ; \\ \text{and} \quad &\langle \dot{T}_{\theta\theta}^2 \rangle = \nu^2 \langle T_{\theta\theta}^2 \rangle \; , \quad \langle \ddot{T}_{\theta\theta}^2 \rangle = \nu^4 \langle T_{\theta\theta}^2 \rangle \; . \end{aligned}\right\} \qquad (9.56)$$

The ratio of the sound power output due to pure rotation to the power output without rotation, for the two cases, is then given by

$$\text{(a)} \quad T_{x\theta} : \frac{W(\Omega)}{W(0)} = 1 + 6\left(\frac{\Omega}{\nu}\right)^2 + \left(\frac{\Omega}{\nu}\right)^4 \; , \qquad (9.57)$$

$$\text{(b)} \quad T_{\theta\theta} : \frac{W(\Omega)}{W(0)} = 1 + 8\left(\frac{\Omega}{\nu}\right)^2 + \frac{16}{3}\left(\frac{\Omega}{\nu}\right)^4 \; . \qquad (9.58)$$

The above results, obtained as special cases of (9.55), can alternatively be derived by direct calculation as shown below.

If the acoustic stresses (a) $T_{x\theta} = \hat{T}_{x\theta} \cos\nu t$, (b) $T_{\theta\theta} = \hat{T}_{\theta\theta} \cos\nu t$ rotate in the θ plane at Ω radians/second, then in terms of the observation point geometry defined in Fig. 9.10, the stress components parallel to $\underset{\sim}{r} = \vec{OP}$ can be obtained from (9.24) as

$$\text{(a) } T_{x\theta} : T_{rr} = \hat{T}_{x\theta} \sin\psi\cos\psi \sin(\Omega t - \phi) \cos\nu t, \tag{9.59}$$

$$\text{(b) } T_{\theta\theta} : T_{rr} = \hat{T}_{\theta\theta} \sin^2\psi \sin^2(\Omega t - \phi) \cos\nu t . \tag{9.60}$$

The resultant sound pressure at a point $\underset{\sim}{r}$ in the far field is given by

$$p' = \frac{1}{4\pi c_o^2 r} \left[\frac{\partial^2 T_{rr}}{\partial t^2} \right] . \tag{9.61}$$

Differentiating (9.59) and (9.60) twice, the corresponding mean square pressures follow from (9.61) as

$$\begin{aligned}\text{(a) } (4\pi c_o^2 r)^2 \langle p'^2 \rangle &= \hat{T}_{x\theta}^2 \sin^2\psi\cos^2\psi \langle \Omega^4 \sin^2(\Omega t-\phi)\cos^2\nu t + \Omega^3 \nu \sin 2(\Omega t-\phi)\sin 2\nu t \\ &+ 4\Omega^2\nu^2\cos^2(\Omega t-\phi)\sin^2\nu t + 2\Omega^2\nu^2\sin^2(\Omega t-\phi)\cos^2\nu t \\ &+ \Omega\nu^3 \sin 2(\Omega t-\phi)\sin 2\nu t + \nu^4 \sin^2(\Omega t-\phi)\cos^2\nu t \rangle ,\end{aligned} \tag{9.62}$$

$$\begin{aligned}\text{(b) } (4\pi c_o^2 r)^2 \langle p'^2 \rangle &= \hat{T}_{\theta\theta}^2 \sin^4\psi \langle 4\Omega^4 \cos^2 2(\Omega t-\phi)\cos^2\nu t - 2\Omega^3 \nu \sin 4(\Omega t-\phi)\sin 2\nu t \\ &+ 4\Omega^2\nu^2 \sin^2 2(\Omega t-\phi)\sin^2\nu t - 4\Omega^2\nu^2\sin^2(\Omega t-\phi)\cos 2(\Omega t-\phi)\cos^2\nu t \\ &+ 2\Omega\nu^3 \sin^2(\Omega t-\phi)\sin 2(\Omega t-\phi)\sin 2\nu t + \nu^4 \sin^4(\Omega t-\phi)\cos^2\nu t \rangle .\end{aligned} \tag{9.63}$$

Provided Ω and ν are not integrally related, these reduce to

$$\text{(a) } T_{x\theta} : (4\pi c_o^2 r)^2 \langle p'^2 \rangle = \tfrac{1}{4}(\Omega^4 + 6\Omega^2\nu^2 + \nu^4)\hat{T}_{x\theta}^2 \sin^2\psi \cos^2\psi , \tag{9.64}$$

$$\text{(b)}\quad T_{\theta\theta} : (4\pi c_o^2 r)^2 \langle p'^2 \rangle = \frac{3}{16}\left(\frac{16}{3}\Omega^4 + 8\Omega^2\nu^2 + \nu^4\right)\hat{T}_{\theta\theta}^2 \sin^4\psi \quad . \qquad (9.65)$$

It is clear from the above equations that spinning the point acoustic stresses $T_{x\theta}$, $T_{\theta\theta}$ at angular speed Ω in the θ plane, increases the sound power output by the factors

$$\text{(a)}\quad T_{x\theta} : \frac{W(\Omega)}{W(0)} = 1 + 6\left(\frac{\Omega}{\nu}\right)^2 + \left(\frac{\Omega}{\nu}\right)^4 \quad , \qquad (9.66)$$

and

$$\text{(b)}\quad T_{\theta\theta} : \frac{W(\Omega)}{W(0)} = 1 + 8\left(\frac{\Omega}{\nu}\right)^2 + \frac{16}{3}\left(\frac{\Omega}{\nu}\right)^4 \quad . \qquad (9.67)$$

9.4 Conclusions

(1) The effects of (a) subsonic uniform straight-line motion, (b) subsonic uniform circular motion and (c) pure rotation on the overall sound radiation from point acoustic stresses have been studied in this chapter. It has been suggested that the analysis can be used for studying the sound radiated from distributed forces on rotating blades.

(2) At low Mach numbers ($M < 0.5$), the effects of circular motion on the overall radiation are roughly similar to those for the pure rotation ($M = 0$, Ω finite) case.

(3) The biggest effect of rotation is on the overall radiation from longitudinal stresses with both axes in the circumferential ($T_{\theta\theta}$) or radial ($T_{\sigma\sigma}$) directions. The magnitude of the effect is maximum in the plane of rotation, but is typically less than 6 dB for values of (Ω/ν) less than 0.5.

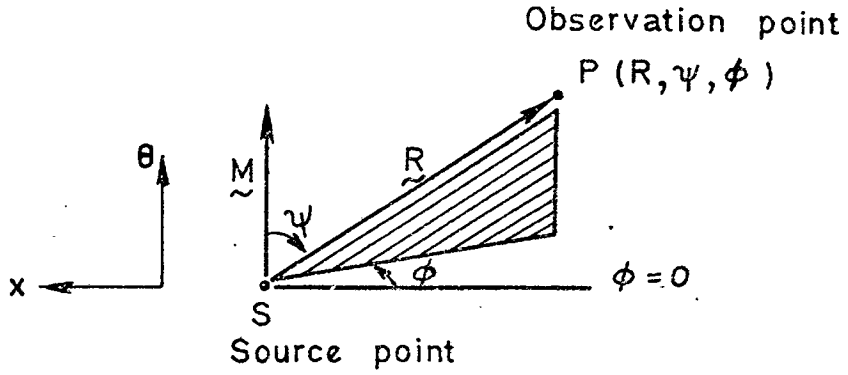

Fig. 9.1. Point acoustic stress in uniform straight-line motion.

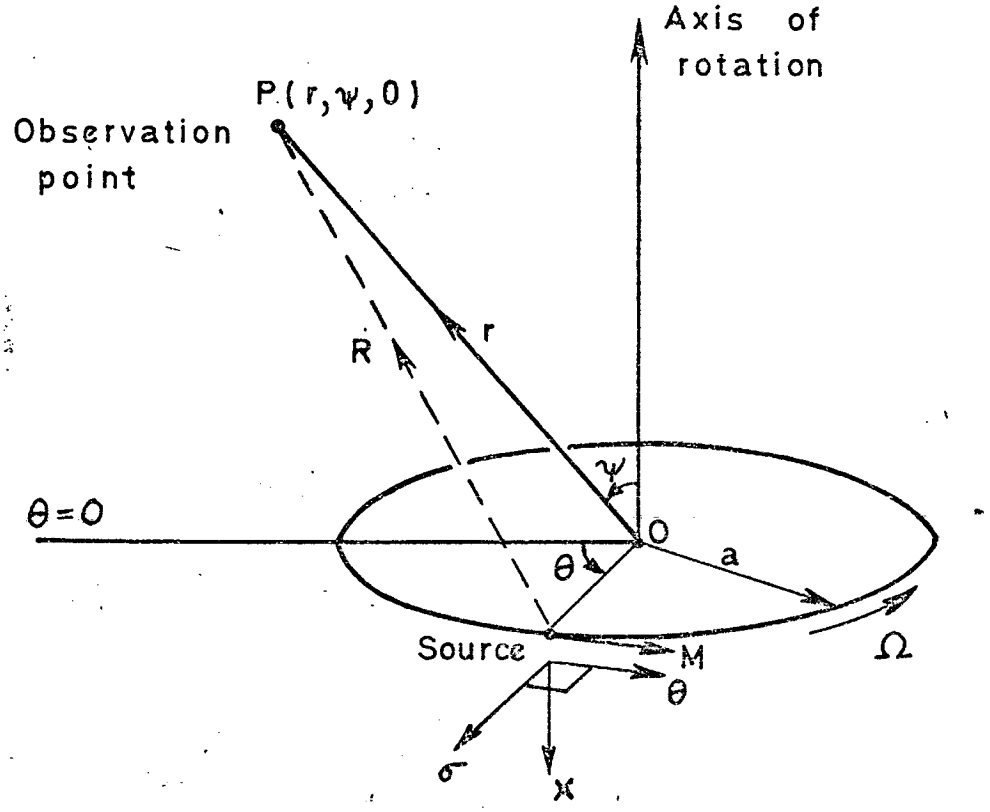

Fig. 9.2. Point acoustic stress in uniform circular motion.

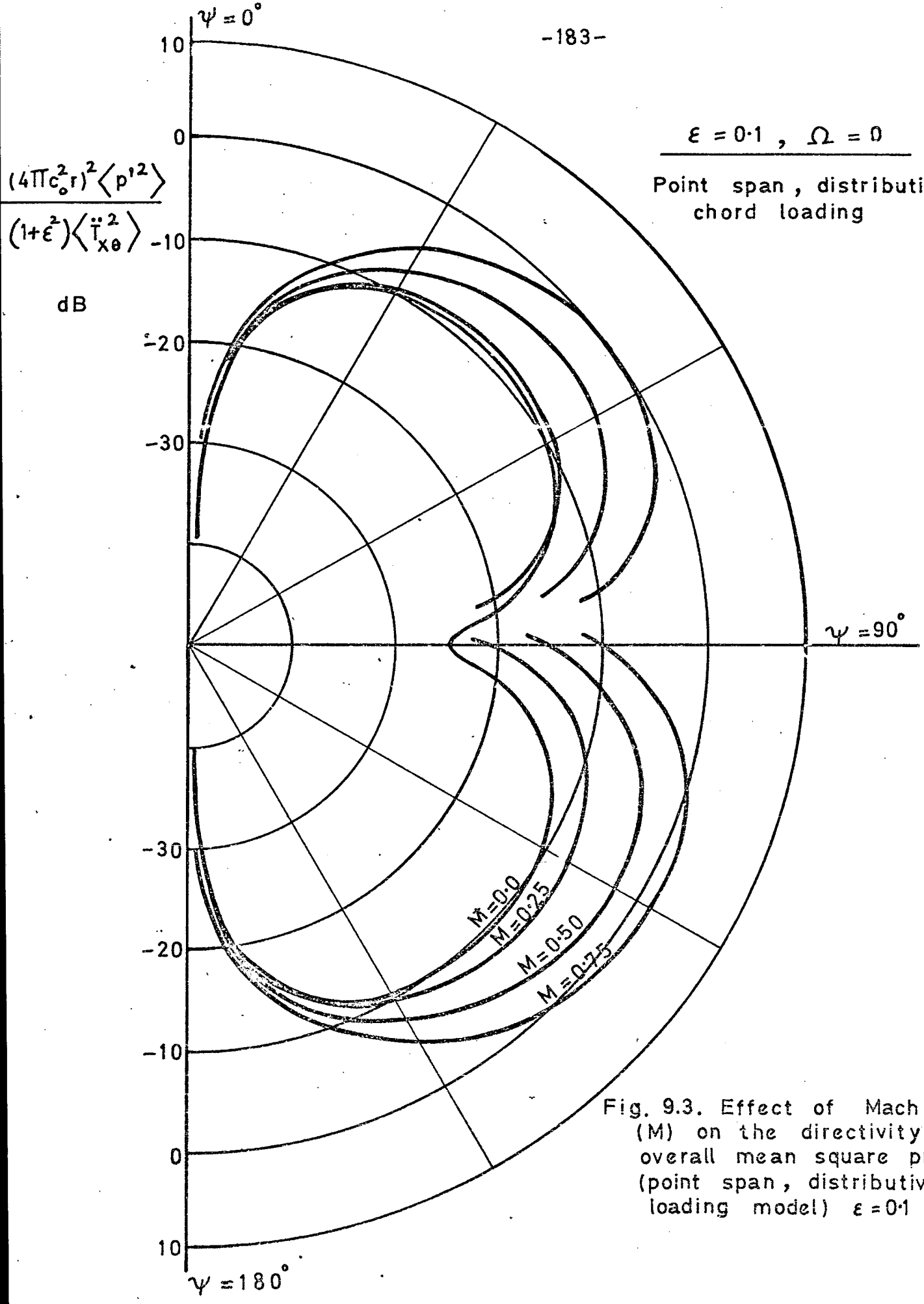

Fig. 9.3. Effect of Mach number (M) on the directivity of overall mean square pressure (point span, distributive chord loading model) $\varepsilon = 0{\cdot}1$, $\Omega = 0$.

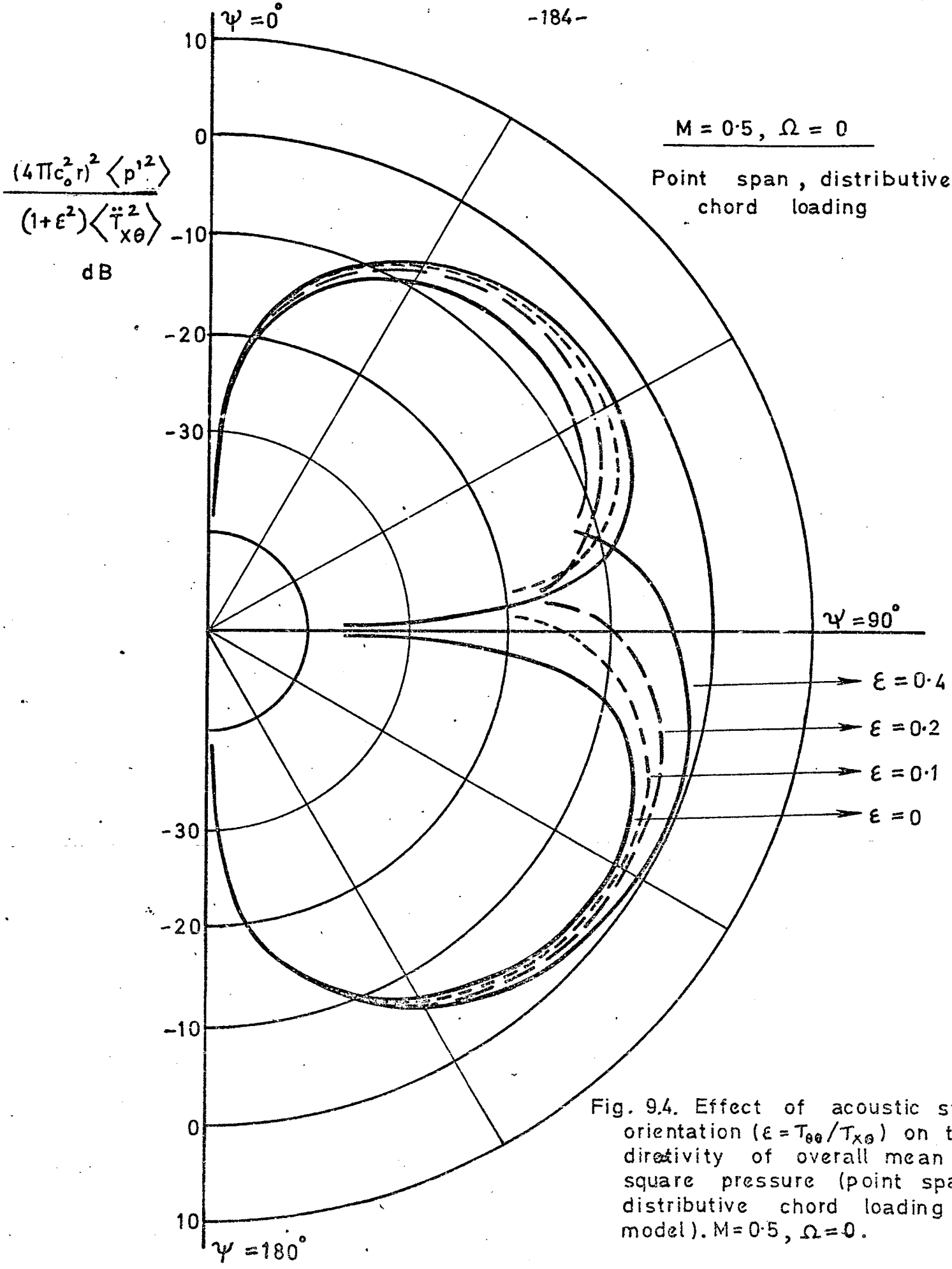

Fig. 9.4. Effect of acoustic stress orientation ($\epsilon = T_{\theta\theta}/T_{x\theta}$) on the directivity of overall mean square pressure (point span, distributive chord loading model). M = 0·5, Ω = 0.

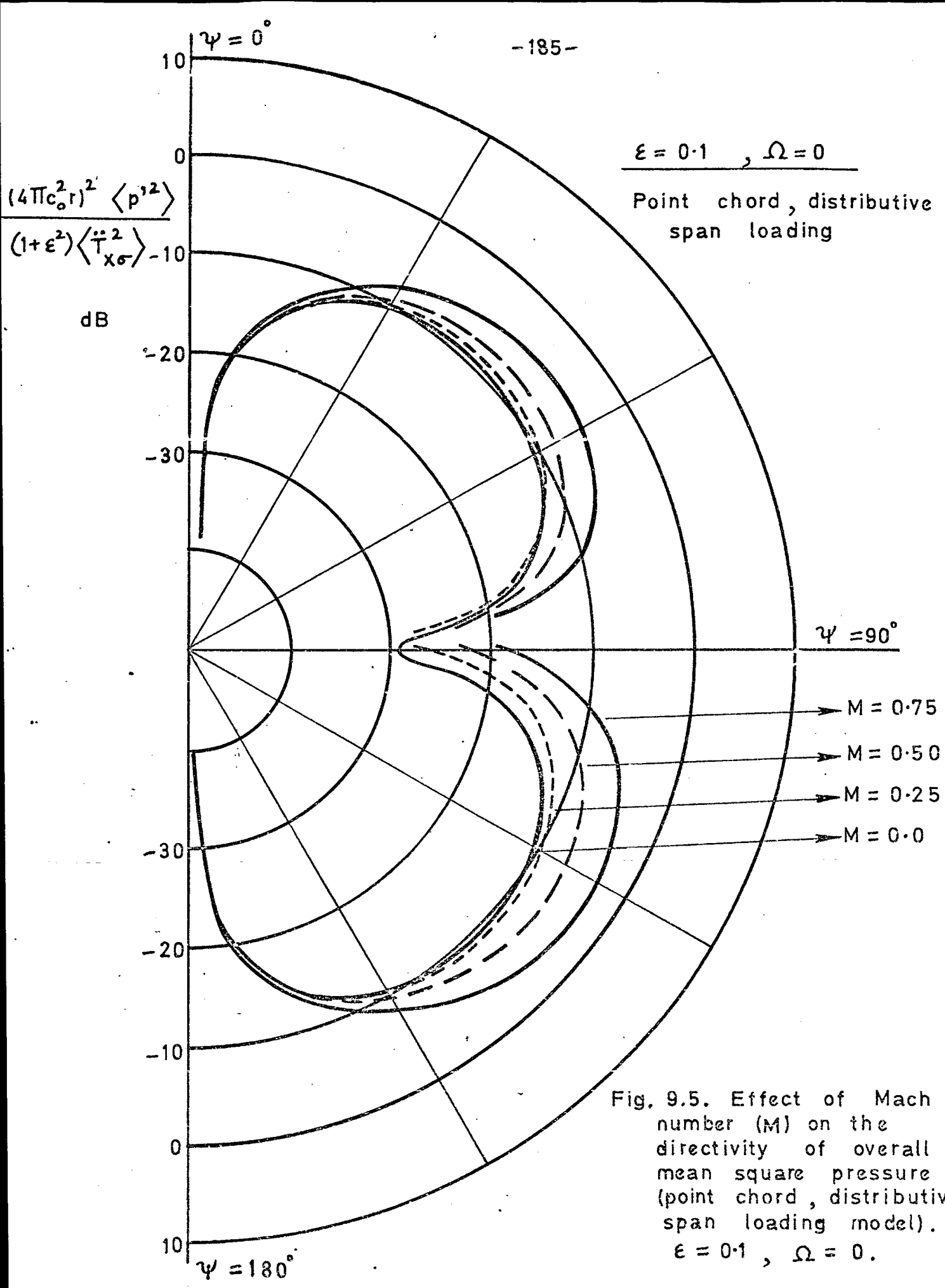

Fig. 9.5. Effect of Mach number (M) on the directivity of overall mean square pressure (point chord, distributive span loading model). $\epsilon = 0.1$, $\Omega = 0$.

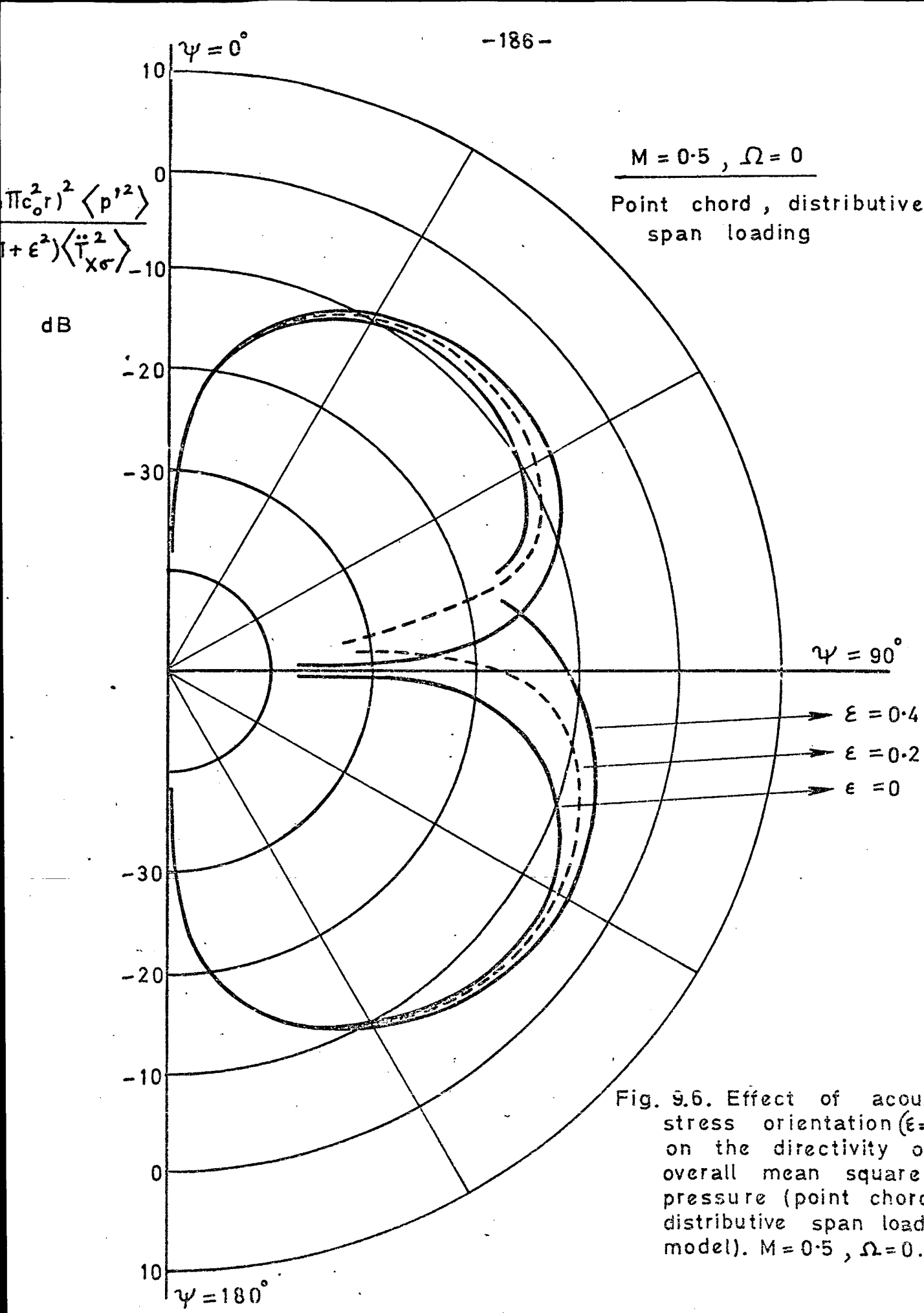

Fig. 9.6. Effect of acoustic stress orientation ($\epsilon = T_{o\sigma}/T_{x\sigma}$) on the directivity of overall mean square pressure (point chord, distributive span loading model). M = 0·5 , Ω = 0.

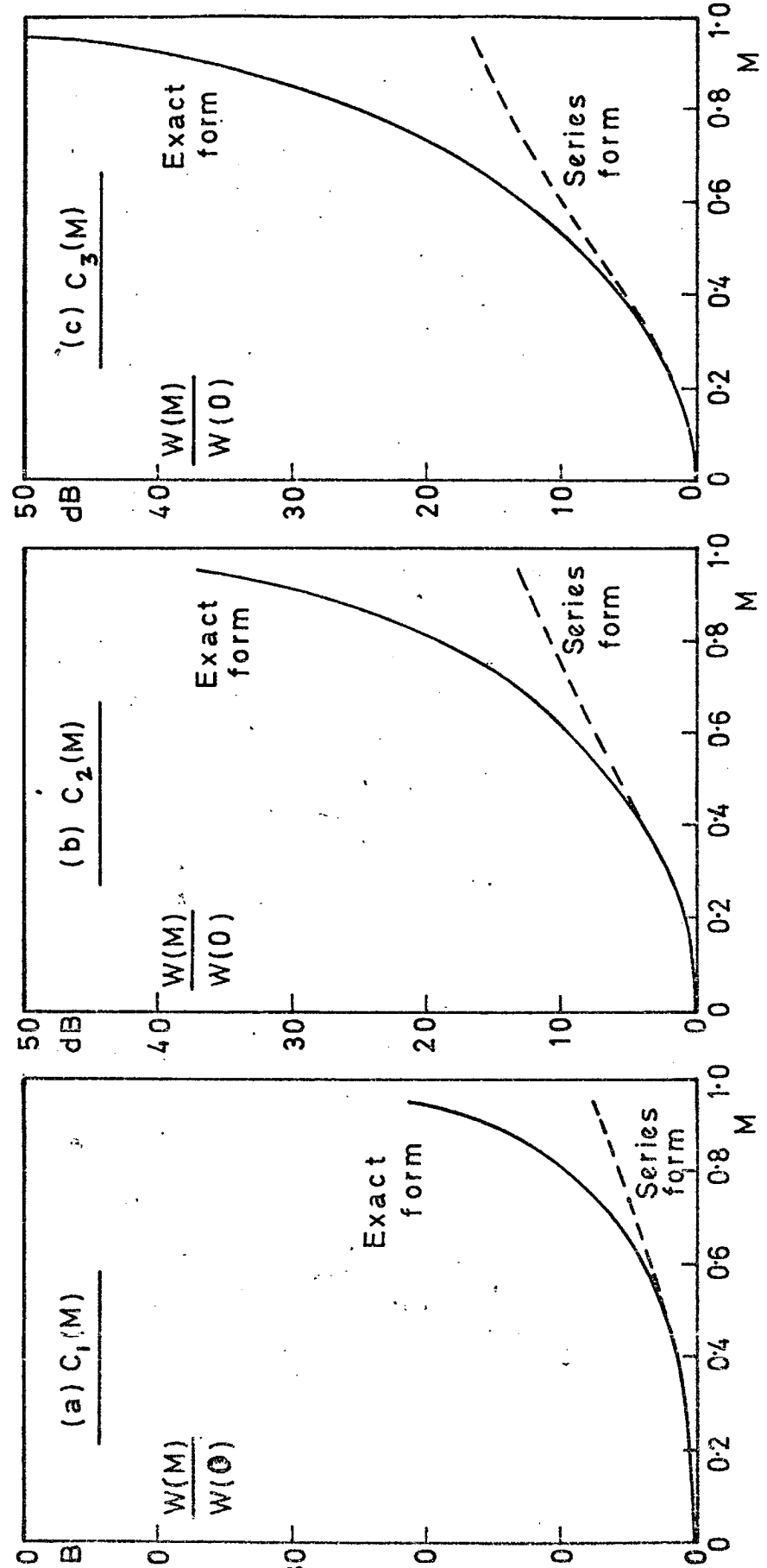

Fig. 9.7. Comparison of series expansions of coefficients (a) $C_1(M)$, (b) $C_2(M)$ and (c) $C_3(M)$, terminated at M^4 terms, with their closed form expressions.

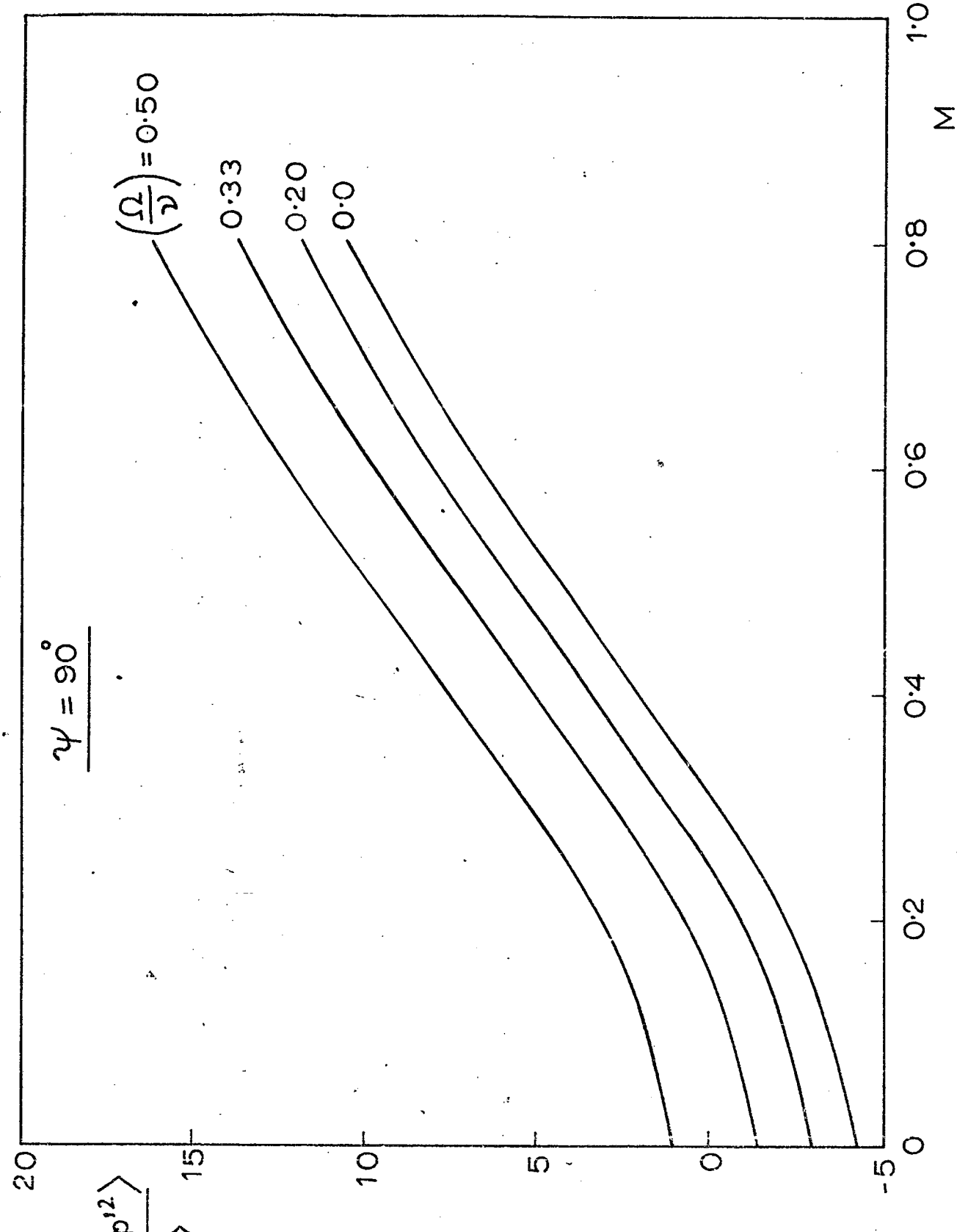

Fig. 9.8. Effect of rotation (Ω/ν) and Mach number (M) on the mean square sound pressure in the plane of rotation.

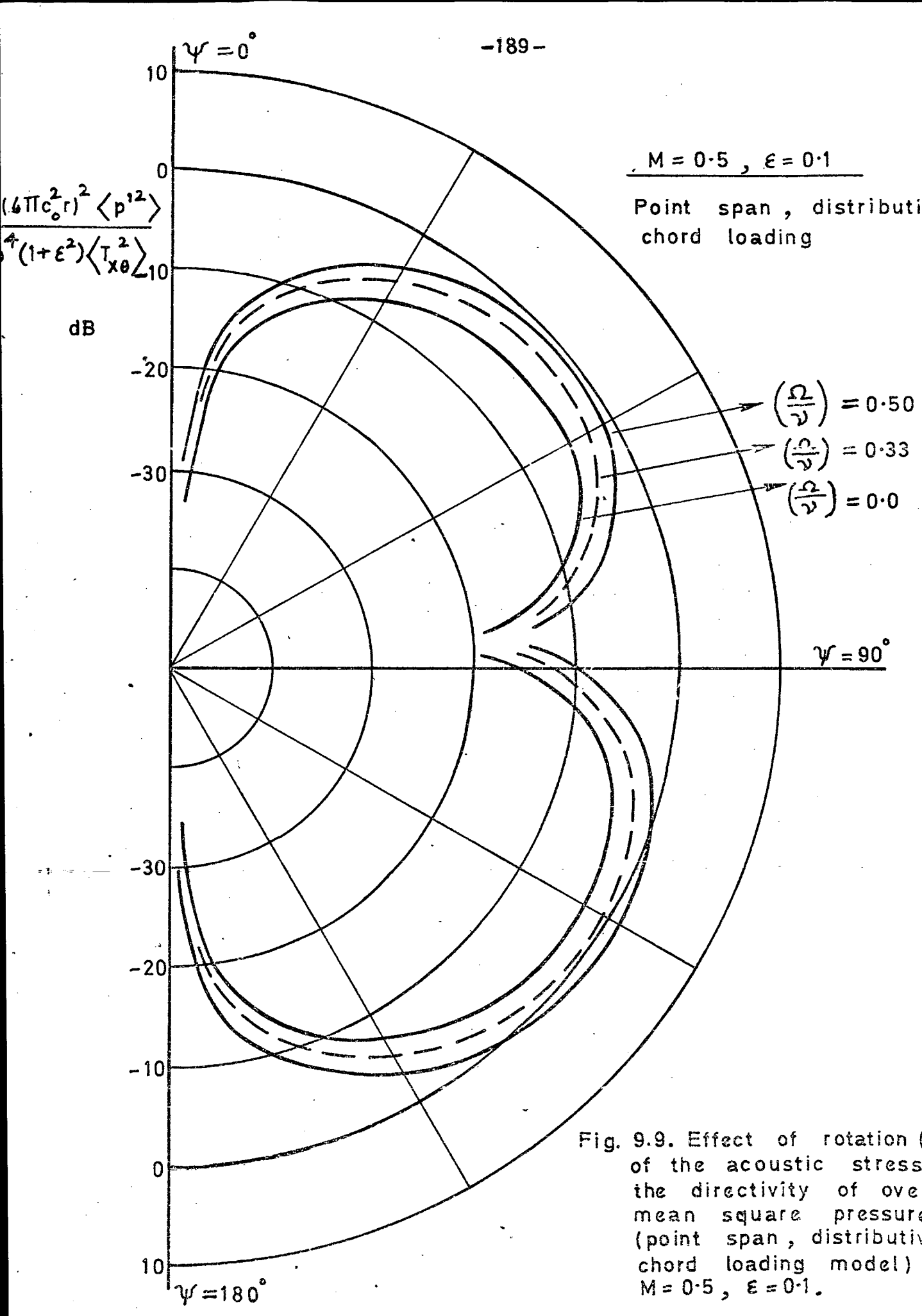

Fig. 9.9. Effect of rotation (Ω/ν) of the acoustic stress on the directivity of overall mean square pressure (point span, distributive chord loading model). $M = 0{\cdot}5$, $\varepsilon = 0{\cdot}1$.

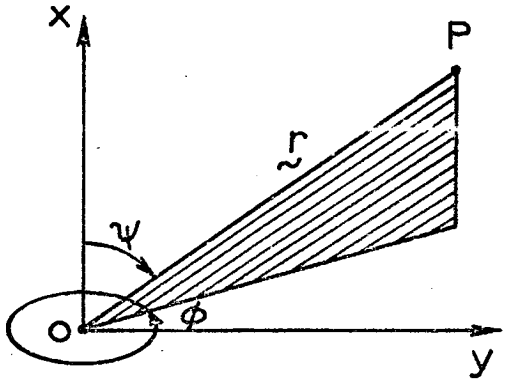

Fig. 9.10. Observation point geometry for spinning point acoustic stresses.

CHAPTER 10

CONCLUSIONS

The purpose of the investigation was to study the radiation properties of various noise generating mechanisms inherent in the thrust producing devices associated with helicopters, V/STOL aircraft and ground effect machines.

Sound radiation from both steady and fluctuating sound sources executing circular motion has been considered, and particular attention has been focussed on noise from helicopter rotors.

The use of two alternative approaches in the analysis of acoustic radiation from moving sources has been illustrated. It is shown that the moving-source approach (where the moving-frame source description is retained in the acoustic analysis) is more appropriate for deriving the sound radiation from rotating sources, especially for sources of arbitrary time dependent source strength, for the following two reasons:

(a) Simple results for the overall radiation can be obtained directly, without involving the radiation spectrum, and

(b) Since the spectrum result takes the form of a series expansion about the linear-motion case, it enables us to establish the effects of source acceleration due to circular motion on the linear-motion results conveniently.

The main conclusions are summarized in the following sections, and these are followed by recommendations for future work in this particular field of acoustics.

10.1 Main conclusions

10.1.1 Rotational noise from helicopter rotors

The main interest here was to establish the effects of chordwise and spanwise differential-pressure profiles and their variations with azimuth on the higher harmonic rotational noise, especially at high tip Mach numbers and high forward speeds. Previous point loading theories were modified to include these profiles and according to the available measured blade airloads, the following conclusions were reached computationally:

(1) Different blade loading models give different radiation results.

(2) The spanwise loading profile and its variation with azimuth produces the biggest effect over the point loading assumption.

10.1.2 Rotor aerodynamics

Detailed study of the available measured blade loading data reveals the following:

(1) Each flight regime has characteristic low-frequency blade loading fluctuations which can be explained qualitatively by combining the factors (like blade-tip vortex intersection, blade stall, effect of fuselage, vortex pattern shed by the blades, and so on) which produce the asymmetry. Such low-frequency force fluctuations will give rise to the lower harmonics of rotational noise.

(2) Study of blade loading harmonics amplitude fall-off at various positions on the rotor blade gives lower fall-offs near the trailing edge than at the leading edge, at most span stations. In addition, the general level of the loading spectrum appears to be higher at the

trailing edge than at the leading edge. These suggest that the higher frequency force fluctuations are dominant near the trailing edge of the blade at all points along the span.

(3) The loading spectra near the blade tip, which cause the dominant sound radiation, fall off at approximately 6 dB per octave near the trailing edge of S-61F rotor blades. This implies that

$$\hat{A}_{pg} = \hat{A}_{p1}\, g^{-1}$$

may be taken as the standard power law for loading harmonics amplitude fall-off over all flight regimes of S-61F compound helicopter.

(4) Statements (2) and (3) above are strictly valid for the S-61F helicopter rotor only, and it remains to be seen whether they can be applied to other similar rotor configurations.

10.1.3 Radiation from random rotating forces (broadband noise)

(a) Overall radiation

(1) Exact expressions have been obtained in closed form for the overall far-field radiation (directivity and total sound power) from a point force moving uniformly in a circle. The only restriction on the force spectrum is that it contain no discrete components at multiples of the rotational frequency.

(2) The contributions from steady and fluctuating components of the force to the overall radiation are additive.

(3) The effects of source acceleration due to circular motion (finite rotational frequency) are displayed in a separate term which also contains the contribution of steady thrust and drag forces to the overall radiation.

(4) A quadrupole model has been developed to represent distributed forces on rotating blades.

(b) Radiation spectrum

(1) Asymptotic expressions have been derived for the far-field spectral density of sound radiation (directivity and sound power) from a broadband point force moving uniformly in a circular path. A series approximation has been developed to show how the spectrum of far-field radiation is influenced by rotation.

(2) The on-axis radiation is independent of source motion (M and Ω) and is controlled by the thrust component of the rotating force, whereas the radiation in the plane of rotation is controlled by the drag component.

(3) If the pure thrust spectrum is linear with frequency, circular motion has no effect on the radiation spectrum.

(4) If the pure drag spectrum is linear with frequency (which includes the flat spectrum and a spectrum rising at 3 dB per octave), circular motion again has no effect on the radiation spectrum. This does not mean that the overall radiation is unaffected.

(5) For a narrow-band force spectrum, the radiation spectrum becomes progressively broader as the observation point moves from the axis to the plane of rotation.

(6) The main effect of rotation at Mach numbers up to 0.8 is on the radiation spectrum from the drag force component; the magnitude of the effect depends on the rate of change of slope of the force spectrum, but is typically less than 3 dB for ratios (Ω/ω) of rotational to force frequencies less than 0.5.

(7) The point force spectrum falling at 6 dB per octave over the appropriate frequency range gives correlation within $\pm$ 2 dB between predicted and experimental discrete tone directivities from (a) Rolls-Royce fan [30], (b) I.S.V.R. fan [31] and (c) I.S.V.R. model rotor [32].

In the case of the I.S.V.R. model rotor, the point force representation assumed in the theory appears to be adequate at least up to those frequencies, whose wavelengths are larger than approximately one-third of the blade span length.

It remains to be seen whether the length scale of one-third span can be used generally to compare with the radiated sound wavelength λ in justifying the point force representation for other rotor configurations.

10.1.4 Radiation from random rotating volume-velocity sources

Although the radiation properties here are similar to those displayed by a pure thrust force, the conclusions are given in full below for completeness.

(a) Overall radiation

(1) Exact closed-form expressions are obtained for the overall far-field radiation from a point volume-velocity source in uniform circular motion. The only restriction on the source spectrum is that it contain no discrete components at multiples of the rotational frequency.

(2) The contributions from steady and fluctuating source strengths (mass per unit time) to the overall radiation are additive.

(3) The effect of source acceleration due to circular motion is displayed in a separate term which also contains the contribution of steady volume-velocity sources (constant rate of introduction of mass) to the overall radiation.

(b) Radiation spectrum

(1) Asymptotic expressions are derived for the far-field spectral density of sound radiation from a broadband point volume velocity source

moving uniformly in a circular path. A series approximation is developed to show how the spectrum of far-field radiation is influenced by rotation.

(2) The on-axis radiation is independent of source motion (M and Ω).

(3) If the source spectrum varies linearly with frequency (which includes the flat spectrum and a spectrum rising at 3 dB per octave as special cases), circular motion has no effect on the radiation spectrum.

(4) The biggest effect is on the radiation spectrum in the plane of rotation; the magnitude of the effect depends on the rate of change of slope of the source spectrum, but is typically less than 1 dB for values of (Ω/ω) less than 0.5.

The effect of finite rotational frequency Ω on the sound power spectrum becomes more pronounced as M increases.

10.1.5 Overall radiation from random rotating volume-displacement sources

(1) The sound field of a point volume-displacement source in arbitrary motion has been derived, and the result has been applied to the special case of uniform circular motion in order to establish the effects of source acceleration on the overall radiated sound field. The only restriction on the source spectrum is that it contain no periodic components at multiples of the rotational frequency.

(2) The effect of finite rotational frequency Ω on the overall radiation is maximum in the plane of rotation and its magnitude increases as M increases.

10.1.6 Overall radiation from random rotating point acoustic stresses

(1) The effects of (a) subsonic uniform straight-line motion, (b) subsonic uniform circular motion and (c) pure rotation on the overall sound

radiation from point acoustic stresses have been studied. It has been suggested that the analysis can be used for studying the sound radiated from distributed forces on rotating blades.

(2) At low Mach numbers ($M < 0.5$), the effects of circular motion on the overall radiation are roughly similar to those for the pure rotation ($M = 0$, Ω finite) case.

(3) The biggest effect of rotation is on the overall radiation from longitudinal stresses with both axes in the circumferential ($T_{\theta\theta}$) or radial ($T_{\sigma\sigma}$) directions. The magnitude of the effect is maximum in the plane of rotation, but is typically less than 6 dB for ratios (Ω/ν) of rotational to acoustic stress frequencies less than 0.5.

10.2 Research recommendations

Although the basic acoustic properties of rotating sound sources are now understood, more work is required from the applications point of view. In order to develop accurate noise prediction techniques and reduce rotating machinery noise generally, the following areas of future research are recommended.

(1) Full application of the computer programmes developed for rotational noise is at present being limited by the lack of sufficiently detailed measurements on aerodynamic blade loadings. Statements (1) and (2) for rotational noise above (section 10.1.1) are based on only one set of loading data. They need to be verified for other rotor configurations when measured blade loading data become available. In addition, any future blade airloads measurement programme must include simultaneous noise measurements, so that the relative usefulness of various theoretical loading models for noise prediction can be established.

(2) According to available acoustic measurements, it appears that there is not much difference in rotor noise levels for different flight regimes including hover, providing blade slap is not present. Rotational noise is rich in higher harmonic content even when a helicopter is hovering; as many as 30 harmonics can be detected by narrow-band analysis in some cases. This suggests that in addition to the low-frequency harmonic force fluctuations described in Chapter 4, there are higher frequency harmonic force fluctuations present which can be detected only if differential-pressure measurements are recorded at smaller azimuthal intervals. Acoustic spectra suggest that these higher frequency fluctuating forces are inherent in all free field rotors irrespective of external conditions. Experimental studies to identify the mechanisms which give rise to these fluctuations will be useful here. For example, if it can be established that intersection of a blade with the tip vortices shed by previous blades is also responsible for higher-harmonic fluctuating forces, then the rotor geometry (in particular blade tip design) can perhaps be modified to achieve some noise reduction.

(3) In the present investigation, the point force theory developed in simplified analytical form for broadband noise, has been tested for the envelope of discrete tones. This is because no systematic measurements of broadband noise directivities from open rotors are available at the present time. It would be useful to confirm the validity of this theory when measurements of broadband noise become available. Since the prediction of overall radiation directivity requires no description of the force spectrum, a powerful check can be obtained initially by comparison with measured overall sound pressure directivity from a fan geometry whose spectrum is dominated by broadband noise.

(4) Extension of the point force theory to point quadrupoles in order to study the effects of distributed random blade forces has been rather preliminary so far. The rotating point acoustic stresses analysis developed in Chapter 9 should be extended to obtain the spectral results; this will provide a simplified analytical description of high-frequency rotational noise and also broadband noise, where the radiated sound wavelength is relatively small compared with the blade dimensions.

It is expected that a wave number representation of the fluctuating blade pressures might also prove suitable in this case.

(5) The theoretical models from (3) and (4) above can then be applied to interpret the transient stall data from the experimental study proposed at I.S.V.R. [36].

(6) Rolls-Royce Ltd. (Bristol Engines Division) is at the present time conducting an experimental programme on jet noise measurements, where a steady fly-over of the model jet is simulated by rotating the jet on a spinning rig. The rotating point volume velocity source and point acoustic stress theories together with the proposed extensions mentioned in (4) above can be used here to verify the conclusions listed in sections 10.1.4 and 10.1.6, as well as to interpret the measurements. The extra effects introduced by circular motion can then be filtered out conveniently to obtain valid linear-motion results.

(7) The results derived for rotating sound sources contain the usual transonic singularities, and are therefore valid at subsonic speeds only. In order to apply them to supersonic cases, further work is required.

(8) The analysis developed for the acoustic radiation from rotating sound sources should be applied to investigate noise from the circulation-controlled rotor, which is proposed as a possible thrust producing device in the future generation of VTOL aircraft - see references [42] and [43].

Although the preliminary noise measurements [44] on a circulation-controlled rotor at the National Gas Turbine Establishment suggest that the radiation spectrum is dominated by broadband noise, there is not enough evidence to establish whether it is the fluctuating blade forces, or the injection of air through the blowing slots (volume-velocity sources), that is the dominant noise source. The rotating point force theory (Chapters 5 and 6) and the rotating volume-velocity source theory (Chapter 7), combined with detailed noise measurements on different circulation-controlled rotor geometries, should be used here to develop accurate noise prediction methods for such rotors.

In addition, if the rotor is driven by jets at the blade tips, the acoustic stress analysis, developed in Chapter 9, should also be used in the investigation.

10.3 Final comment

The general conclusion on the subject of noise from rotating thrust producing devices is that the research carried out so far has provided us with the basic acoustic properties of the noise sources involved. In the case of helicopter rotor noise, before the prediction methods developed for rotational noise and broadband noise can be exploited fully for noise reduction at early design stages, it is vital to improve our present knowledge of (a) fluctuating blade forces, and (b) the mechanisms which induce them.

In most physical processes, the problems arise due to unsteadiness. For rotating blades, it is the unsteady flow through the rotor that causes the problem of noise. In order to reduce the noise levels generally, this unsteadiness in the flow must be reduced. It is felt therefore that the major effort should now be spent on studying the characteristics of the

flow through the rotating-blades systems. Once we identify the various factors which produce the unsteady flow, we can hopefully go on to look for means of controlling this unsteadiness.

REFERENCES

1. M. J. LIGHTHILL 1962 Proc. Roy. Soc. (London) A267, 147. Sound generated aerodynamically.

2. L. GUTIN 1936 Phys. Z. Sowj Un. 9, 57. Transl: NACA TM 1195 (1948). On the sound field of a rotating propeller.

3. L. GUTIN 1936 J. Applied Physics (Leningrad) 6, 5. Transl: A.R.C. Report 3115 (1946). The sound distribution around a rotating airscrew.

4. T.F.W. EMBLETON and G.J. THIESSEN 1962 J. Acoust. Soc. Am. 34, 6. Efficiency of circular sources and circular array of point sources with linear phase variation.

5. S. E. WRIGHT 1969 J. Sound Vib. 9, 223. Sound radiation from a lifting rotor generated by asymmetric disc loading.

6. P.M. MORSE and K.U. INGARD 1968 Theoretical Acoustics (McGraw-Hill Book Co., New York).

7. J.E. FFOWCS WILLIAMS and D.L. HAWKINGS 1969 J. Sound Vib. 10, 10. Theory relating to the noise of rotating machinery.

8. G.M. LILLEY 1961 Rolls-Royce Ltd. Noise Panel Report. On the vortex noise from airscrews, fans and compressors.

9. M.V. LOWSON 1965 Proc. Roy. Soc. (London) A286, 559. The sound field for singularities in motion.

10. M.V. LOWSON and J.B. OLLERHEAD 1969 J. Sound Vib. 9, 197. A theoretical study of helicopter rotor noise.

11. M.V. LOWSON and J.B. OLLERHEAD 1969 USAAVLABS Technical Report 68-60. Studies of helicopter rotor noise.

12. M.V. LOWSON 1970 J. Acoust. Soc. Am. 47, 371. Theoretical analysis of compressor noise.

13. M.V. LOWSON 1969 NASA CR 1287. Theoretical studies of compressor noise.

14. R.G. SCHLEGEL, R.J. KING and H.R. MULL 1966 USAAVLABS Technical Report 66-4. Helicopter rotor noise generation and propagation.

15. R.G. LOEWY and L.R. SUTTON 1966 J. Sound Vib. 4, 305. A theory for predicting the rotational noise of lifting rotors in forward flight including a comparison with experiment.

16. H.K. TANNA 1968 I.S.V.R. Technical Report No. 13. Computer program for the prediction of rotational noise due to fluctuating loading on rotor blades.

17. S.E. WRIGHT and H.K. TANNA 1969 I.S.V.R. Technical Report No. 15. A computational study of rotational noise. (Also NASA CR - 66869)

18. S.E. WRIGHT 1969 Ph.D. thesis, University of Southampton. Sound radiation from a lifting rotor.

19. R.P. WHITE 1966 J. Sound Vib. 4, 282. VTOL periodic aerodynamic loadings: the problems, what is being done and what needs to be done.

20. J.E. FFOWCS WILLIAMS and C.G. GORDON 1965 A.I.A.A. Journal 3, 791. Noise of highly turbulent jets at low exhaust speeds.

21. S.E. WRIGHT 1969 I.S.V.R. Technical Report No. 14. Theoretical study of rotational noise.

22. R.G. SCHLEGEL and W.E. BAUSCH USAAVLABS Technical Report (Preliminary copy). Helicopter rotor rotational noise prediction and correlation.

23. J. SCHEIMAN 1964 N.A.S.A. TM-X-952. A tabulation of helicopter rotor blade differential-pressures, stresses, and motions, as measured in flight.

24. A.F. LEHMAN 1968 USAAVLABS Technical Report 68-17. Model studies of helicopter rotor flow patterns.

25. C.R. .COX and R.R. LYNN 1962 TCREC Technical Report 62-73. A study of the origin and means of reducing helicopter noise.

26. H.L. OESTREICHER 1951 Centr. Air. Docum. Off (Washington), Tech. Data. Digest. 16, 9. The effect of motion on the acoustic radiation of a sound source.

27. G.N. WATSON 1966 Theory of Bessel Functions. (Cambridge University Press, second edition).

28. V.P. DOKUCHAEV 1966 Soviet Physics-Acoustics (Translation) 11, 275. Radiation of sound waves by a body moving in a circle and by a rotating vane of simple configuration.

29. L.N. SRETENSKII 1956 Soviet Physics-Acoustics (Translation) 2, 89. Sound radiation by a rotating dipole.

30. B. BARRY and C.J. MOORE 1970 Paper No. D4, presented at the Symposium on Aerodynamic Noise, Loughborough University of Technology. Subsonic fan noise.

31. N. CHANDRASHEKHARA 1970 Ph.D. thesis, University of Southampton.

32. N.J. STAINER 1969 M.Sc. thesis, University of Southampton. An experimental investigation into rotational noise for a low solidity rotor.

33. V.P. DOKUCHAEV 1970 Soviet Physics-Acoustics (Translation) 15, 316. Sound radiation by a harmonic monopole in circular motion.

34. E.J. RICHARDS and D.J. MEAD 1968 Noise and Acoustic Fatigue in Aeronautics (John Wiley and Sons Ltd.)

35. J.W.S. RAYLEIGH The Theory of Sound - Volume II (Dover Publications, New York. Second revised edition.)

36. J.W. LEVERTON 1969 Proposal for continuation of contract research work on helicopter noise (Mintech. Ref. AT/2040/039/SRA), submitted by I.S.V.R., University of Southampton.

37. S.E. WRIGHT and J.W. LEVERTON 1969 Paper presented at Third CAL/AVLABS Symposium on Aerodynamics of Rotary Wing and V/STOL Aircraft, Buffalo, New York. Helicopter rotor noise generation.

38. J.W. LEVERTON and F.W. TAYLOR 1966 J. Sound Vib. 4, 345. Helicopter blade slap.

39. A. GESSOW and G.C. MYERS 1952 Aerodynamics of the Helicopter (The Macmillan Co., New York).

40. G.K. TIMM 1966 J. Sound Vib. 4, 490. Obstacle-induced flow recirculation.

41. K.V. DIPROSE 1955 R.A.E. Technical Note No. M.S. 19. Some propeller noise calculations showing the effect of thickness and planform.

42. I.C. CHEESEMAN 1968 J. Roy. Aero. Soc. 72, 635. Circulation control and its application to stopped rotor aircraft.

43. I.C. CHEESEMAN 1969 (July) Aircraft Engineering. Circulation-controlled rotor aircraft.

44. C.B. PEASE 1969 N.G.T.E. Powered Lift and Noise Note No. 53. Preliminary noise measurements on a circulation controlled rotor.

APPENDIX I : COMPUTER PROGRAM FOR THE PREDICTION OF ROTATIONAL NOISE

This appendix describes in detail the computer program written to compute harmonics of rotational noise as predicted by Schlegel, King and Mull [14] of Sikorsky Aircraft for fluctuating blade loadings. Sufficient detail has been included that other investigators with very little previous knowledge of computer programming can make use of the program.

General comments:

The program can be used for predicting harmonics of rotational noise, at any point in the near-field or the far-field, due to asymmetric but stationary loading over the rotor disc.

Although the blade span loading distribution can be varied with azimuth, the chordwise differential-pressure distribution is assumed to be rectangular in shape at all azimuthal points.

The program is written in the HARTRAN version of 1900 FORTRAN to be used at the Atlas Computer Laboratory, Chilton.

It should be noted that no details about the theories involved are given here, and only the final formulae useful for computation are quoted. The appendix is written solely from the computational point of view. The program was used to carry out an extensive computational study of rotational noise, details of which are summarized in Appendix II.

1. Quoted formulae and simplification

With reference to the rotor and field point geometry shown in Fig. 2.1, the r.m.s. value of m^{th} harmonic of sound pressure, SP_{mB}, at observation point (R, θ, σ) due to a B-bladed rotor rotating at Ω

radians per second is given by

$$SP_{mB} = \frac{R}{2\sqrt{2}\pi^2 a} \left\{ (Re)^2 + (Im)^2 \right\}^{\frac{1}{2}} \quad (1)$$

where

$$Re = \int_0^{r_T} \int_0^{2\pi} \frac{L(r,\psi)}{mD^2} \sin\left(\frac{maB}{2r}\right) \cdot \left\{ \frac{mB\Omega}{c_o} \sin U + \frac{\cos U}{D} \right\} x$$

$$\left\{ \sin\beta \cos\sigma \sin(\psi - \theta) + \cos\beta \sin\sigma \right\} r \, dr \, d\psi \quad (2)$$

and

$$Im = \int_0^{r_T} \int_0^{2\pi} \frac{L(r,\psi)}{mD^2} \sin\left(\frac{maB}{2r}\right) \cdot \left\{ \frac{mB\Omega}{c_o} \cos U - \frac{\sin U}{D} \right\} x$$

$$\left\{ \sin\beta \cos\sigma \sin(\psi - \theta) + \cos\beta \sin\sigma \right\} r \, dr \, d\psi \quad (3)$$

for which

$$U = mB\left\{ \frac{\Omega D}{c_o} + \frac{a}{2r} + \psi \right\} , \quad (4)$$

$$D = \left\{ R^2 + r^2 - 2rR\cos\sigma \cos(\psi - \theta) \right\}^{\frac{1}{2}} \quad (5)$$

and $$\beta = \beta_o + \beta_1 \cos\psi + \bar{\beta}_1 \sin\psi - \gamma(r - r_o) . \quad (6)$$

$L(r,\psi)$ is the blade loading at point (r,ψ) on the rotor disc.

$$L(r,\psi) = L_o(r) + L_s \cos s\psi + M_s \cos s\psi . \quad (7)$$

Other symbols are explained in the list of symbols.

2. Computation procedure:

The method used repeatedly evaluates the basic sound pressure equations (1), (2) and (3). This includes a double integration. One integration is around the rotor disc with the sample points (azimuth

angles) chosen at constant intervals. The other integration is along the radius where sample radial stations are unevenly spaced.

A subroutine called SIMCOR is written to perform the integrations. It uses standard trapezoidal rule for integration; details of this method are described later on.

In the program, the quantities included in the integrands, namely $L(r,\psi)$, D, β and U are evaluated first and then the values of integrands are calculated at each source point (r,ψ). Azimuthal integration at each radial station is performed next and this is followed by radial integration to obtain Re, Im.

If $L(r,\psi)$ is in pounds per inch and R, r are in inches, then D is in inches and the two integrands are in pounds/in^3. The sound pressure, SP_{mB} is in pounds/in^2. The sound pressure level in decibels is then obtained by using

$$SPL = 20 \log_{10} \left| \frac{SP_{mB}}{2.9 \times 10^{-9}} \right| \qquad (8)$$

where the factor 2.9×10^{-9} arises by converting pounds/in^2 into dynes/cm^2 and referencing SP_{mB} to 0.0002 dynes/cm^2.

The flow diagram is shown in Fig. 1 and a copy of the printout is produced in Fig. 2. The program details are mentioned in the following sections.

3. Program nomenclature:

(In order of appearance)

Name of subroutine : SIMCOR

Name	Meaning
Q	blade loading L, pounds per inch
R	distance of radial station from centre of rotor disc, inches
V8	real part of the integrand under the radial integration, azimuthal integration completed
V8I	imaginary part of the integrand under the radial integration, azimuthal integration completed
TITLE	any desired title
V25	integrand for Re, pounds/in^3
V25I	integrand for Im, pounds/in^3
PSI	value of ψ in integration step, degrees
PRAD	value of ψ in radians
XLO	steady component L_o of blade loading, pounds/in
XLM	cosine component L_s of s^{th} harmonic of blade loading, pounds/in
XMM	sine component M_s of s^{th} harmonic of blade loading, pounds/in
RAD	converts degrees into radians
NEND	end code = 0 if last case = 1 if cases to follow
NFP	number of field points
RBN	rotor blade number, B
OMG	rotor rotational speed, r.p.m.
CH	blade chord width a, inches
SOS	speed of sound c_o, feet/second
RO	radial distance r_o at which blade twist begins, inches
BO1	steady pitch angle β_o, degrees
B1	cosine component of cyclic pitch β_1, degrees
B11	sine component of cyclic pitch $\bar{\beta}_1$, degrees

G	blade twist rate, degrees per inch
NHAR	number of harmonics of SPL required, m
NRAD	number of radial stations
ANG	integration interval $\Delta\psi$, degrees
NP,NT	number of azimuthal integration points
I	azimuth angle, radial station counter
J	azimuth station, blade loading harmonic counter
Q(J,I)	= $L(r,\psi)$, pounds/in
K	blade loading harmonic counter
X	blade loading harmonic, s
II	field point counter
CAPR	field point distance R, feet
THETA	field point azimuth angle θ, degrees
ALFA	field point elevation angle σ, degrees
M	harmonic counter
KK	radial station counter
JJ	azimuthal station counter
CAPS	observer-source separation D, inches
BETA	blade pitch angle β at source point (r,ψ)
SBTA	= sin β
CBTA	= cos β
V	= U
TEMP	harmonic number
AR	area under the curve in integration
PRTAR	Re, pounds/in^2
PRTAI	Im, pounds/in^2

PRTA r.m.s. sound pressure, pounds/in^2

SPL r.m.s. sound pressure level in decibels .

The following standard functions used in the program were available in the computer:

SINF sine of an angle

COSF cosine of an angle

ALOGF logarithm to the base e of a number

ABSF absolute value (modulus) of a number

SQRTF square root of a number

4. Input parameters:

The paremeters (and their units) which must be known to use the program are listed below:

B rotor blade number

N rotor rotational speed, r.p.m.

a blade chord, inches

c_o speed of sound, feet/second

r_o radius at start of blade twist, inches

β_o steady pitch angle, degrees

β_1 cosine component of cyclic pitch, degrees

$\overline{\beta}_1$ sine component of cyclic pitch, degrees

γ blade twist rate, degrees per inch

R Observation point distance from rotor centre, feet

θ Observation point azimuth angle (0^o at tail, positive in direction of rotation), degrees

σ Observation point elevation angle (0^o in rotor plane), degrees

The following loading data is required for every radial station:

L_o steady blade section loading, pounds/in

L_s cosine coefficient of s^{th} harmonic of blade section loading, pounds/in

M_s sine coefficient of s^{th} harmonic of blade section loading, pounds/in.

5. Input format for data cards:

The input format, which is to be used for every case is described below. The input format is shown on the coding form in Fig. 3, where the numbers written above each card refer to sample examples.

Card 1: Title card

Col. 1: 1

Col. 2-72: any desired title

Card 2: Basic constants

Col. 2: end code

= 0 if last case

= 1 if case(s) to follow

Col. 3-4: number of field points (right adjusted)

Col. 5-12*: B

Col. 13-20*: N

Col. 21-28*: a

Col. 29-36*: c_o

Col. 37-44*: r_c

Col. 45-52*: β_o

Col. 53-60*: β_1

Col. 61-68*: $\overline{\beta}_1$

Col. 69-76*: γ

Card 3: Control constants

Col. 1-2: number of harmonics of rotational noise desired; $1 \leq m \leq 50$ (right adjusted)

Col. 4 : number of radial stations; $4 \leq N \leq 8$

Col. 5-12*: angular increment of integration; $\Delta\psi \geq 0.5^{o}$

(Note $360/\Delta\psi$ = integer)

Card 4: Output controls

This facility enables one to obtain the intermediate output from the program, if desired, by introducing an extra card punched as follows, wherever the intermediate output is desired.

IF (KEY1.EQ.99) PRINT (Desired output)

Thus output controls (KEY1, KEY2, KEY3)

= 00 if intermediate output not desired

= 99 if intermediate output desired

For example,

Col. 1-2: may control printout of input and radial integration

Col. 3-4: may control printout of azimuthal integrations

Col. 5-6: may control printout of D, β , U.

Card 5: Radial stations

Radial blade stations in field of 9*, inches.

Card 6 onwards:

Loading data:

For each radial station,

L_o in Col. 1-8* on first card

L_1-L_{50} in fields of 8* on the next 5 cards

M_1-M_{50} in fields of 8* on the next 5 cards

Field point data:

For each field point, one card with three parameters as follows,

Col. 1-12*: R

Col. 13-24*: θ

Col. 25-36*: σ

*All fields specified must contain decimal points.

6. Notes regarding the input data format:

A case (card 2, col. 2) is a complete set of input data with a number of harmonics, field points, etc. A case may contain several field points but if any of the other input parameters is changed, a new case is required. A new case would require a new title, a new set of basic constants, etc.

The number of field points here (card 2, col. 3-4) must agree with the number of cards describing the individual field points which are the last set of input cards.

The number of rotational noise harmonics desired (card 3, col. 1-2) partially determines the program running time.

The number of radial stations (card 3, col. 4) is arbitrary and is dependent on the number of stations at which blade loading data is available. Evenly spaced stations over the span of the blade are desirable because the program interpolates between points. The last station is usually at the blade tip and the loading is zero at this position.

The number of radial blade stations (card 5) must correspond to that specified in card 3, col. 4.

The normal printout from the computer includes various rotor parameters and basic constants, field point co-ordinates, sound pressure and sound pressure level. Any intermediate values in the arithmetic could be included by using the control card (card 4) as mentioned in section 5. Such intermediate output adds a great deal of volume to the output and is not ordinarily required.

7. Control cards and card sequence:

Every computer has a set of control cards which must be used at particular stages of program and data cards, as specified by the manufacturer. Control cards and card sequence necessary to use the program on the Atlas computer are shown in coded form in Fig. 4.

The first six cards are control cards and they are described in detail below.

Card 1:

The programmer's job number and name, together with the title of the program are punched on this card.

Card 2:

A rough estimate of the expected number of lines of printout should be given on this card. 500 lines of printout are sufficient for the program printout and this number should be added to the expected number of lines of numerical printout in order to obtain a complete estimate.

Card 3:

An estimate of computing time in minutes or seconds should be given on this card.

Card 4:

The amount of core store necessary for the program should be specified here. A store of about 30 Blocks (where 1 Block = 512 words)

is quite adequate for this program.

Card 5:

The name of the compiler is specified on this card, a compiler being the unit which compiles (checks) the program. Since the program is written in HARTRAN, the name of the compiler is also HARTRAN.

Card 6:

This card suppresses the production of BAS DECK, which are a set of binary cards used when the program is to be used over and over again.

The six control cards are followed by the "master program" cards. A card identical to card 6 above is introduced next and it is followed by "subroutine" cards.

A card with *ENTER in columns 1-6 appears at the beginning of "data" cards.

The last card of the sequence, i.e. the card at the end of "data" cards, has a multi-punch 7/8 in column 1 and Z in column 80. This represents end of data.

8. Computation time on ICT Atlas computer:

The total computation time consists of program compilation (checking) time and data execution time.

Compilation time is about 6 seconds.

For any particular case, it is clear that the execution time is proportional to the number of field points and the number of harmonics of rotational noise desired.

For any field-point harmonic, the execution time increases as the number of radial stations increases and the execution time decreases as the azimuthal integration interval, $\Delta\psi$, increases. The relation is

approximately linear in both the cases. See section 9.3.

It was found that when $\Delta\psi = 2^{o}$, it takes 6 seconds per harmonic per field point when there are 8 radial stations.

The execution time for any other combination can then be easily calculated. For example, if $\Delta\psi = 0.5^{o}$ and there are 6 radial stations, then the execution time per harmonic per field point is

$$6 \times (\frac{6}{8}) \times (\frac{2}{0.5}) = 18 \text{ seconds.}$$

An increase in the number of blade loading harmonics (s) results in a slight increase in the execution time. The table below may serve as a useful guide in estimating the execution time.

s	number of radial stations	$\Delta\psi$	execution time per harmonic per field point
$0 \rightarrow 10$	8	2^{o}	5 sec.
$0 \rightarrow 10$	8	0.5^{o}	20 sec.
$0 \rightarrow 50$	6	2^{o}	5 sec.
$0 \rightarrow 50$	8	2^{o}	6 sec.
$0 \rightarrow 50$	6	0.5^{o}	20 sec.
$0 \rightarrow 100$	6	0.5^{o}	24 sec.
$0 \rightarrow 200$	6	0.5^{o}	28 sec.

9. Integration details:

9.1 Method of integration:

The integrand is evaluated at several points and the area under the integrand curve is determined by the "trapezoidal rule" approximation. That is, the area is divided into several strips and each of these strips is approximated by a trapezium, as shown in the figure below.

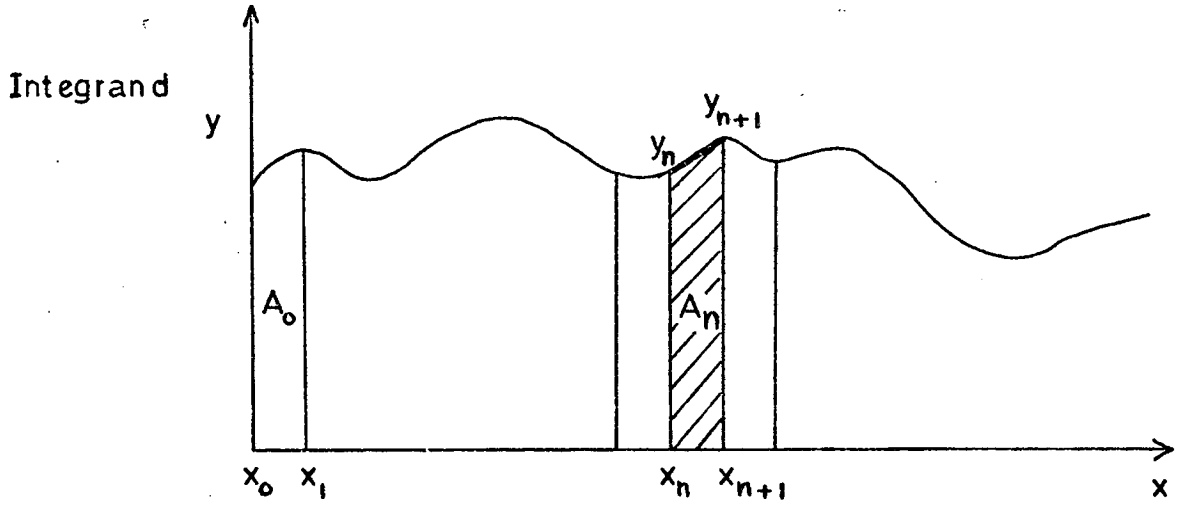

$$\text{Area} = \int_{o}^{x} y(x)\, dx.$$

Since $$A_n \doteq \left\{ \frac{y_n + y_{n+1}}{2} \right\} (x_{n+1} - x_n) \quad ,$$

the total area is

$$\sum A_n = \sum \left\{ \frac{y_n + y_{n+1}}{2} \right\} (x_{n+1} - x_n)$$

which is the integral of y(x) with respect to x.

9.2 Importance of integration interval:

It is obvious that the accuracy of the method depends on keeping the integration interval $(x_{n+1} - x_n)$ very small. Thus the angular increment of integration $(\Delta\psi)$ must be small enough to obtain a valid solution.

It should be noted that the integrand is a function of mB. Thus in order to define the integrand curve accurately for all values of m,

the integration interval must be reduced as the harmonic number m of sound pressure is increased.

The following figures may serve as a useful guide in choosing a value for $\Delta\psi$ when a spectrum is to be computed.

mB numbers of SPL required	maximum tolerable value of $\Delta\psi$
80	2^{o}
140	1^{o}
320	0.5^{o}

(refer Fig. 5)

For mB > 320 a smaller value of $\Delta\psi$ (e.g. 0.25^{o}) should be used.

It is advisable to leave a safety margin whenever possible in order to ensure a valid computation.

9.3 Relation between integration interval and computing time:

Considering the amount of arithmetic involved in different sections of the program, it can be seen that the majority of the arithmetic is involved in the azimuthal and radial integrations.

i.e. $\int_{0}^{r_T} \int_{0}^{2\pi} (\quad) \, dr \, d\psi$.

The computing time thus approximately depends upon the number of times the integrand is evaluated, which in turn depends directly upon the number of radial stations and inversely upon the integration interval $\Delta\psi$.

Thus the computing time approximately increases as the number of radial stations increases and it approximately decreases as the integration interval increases.

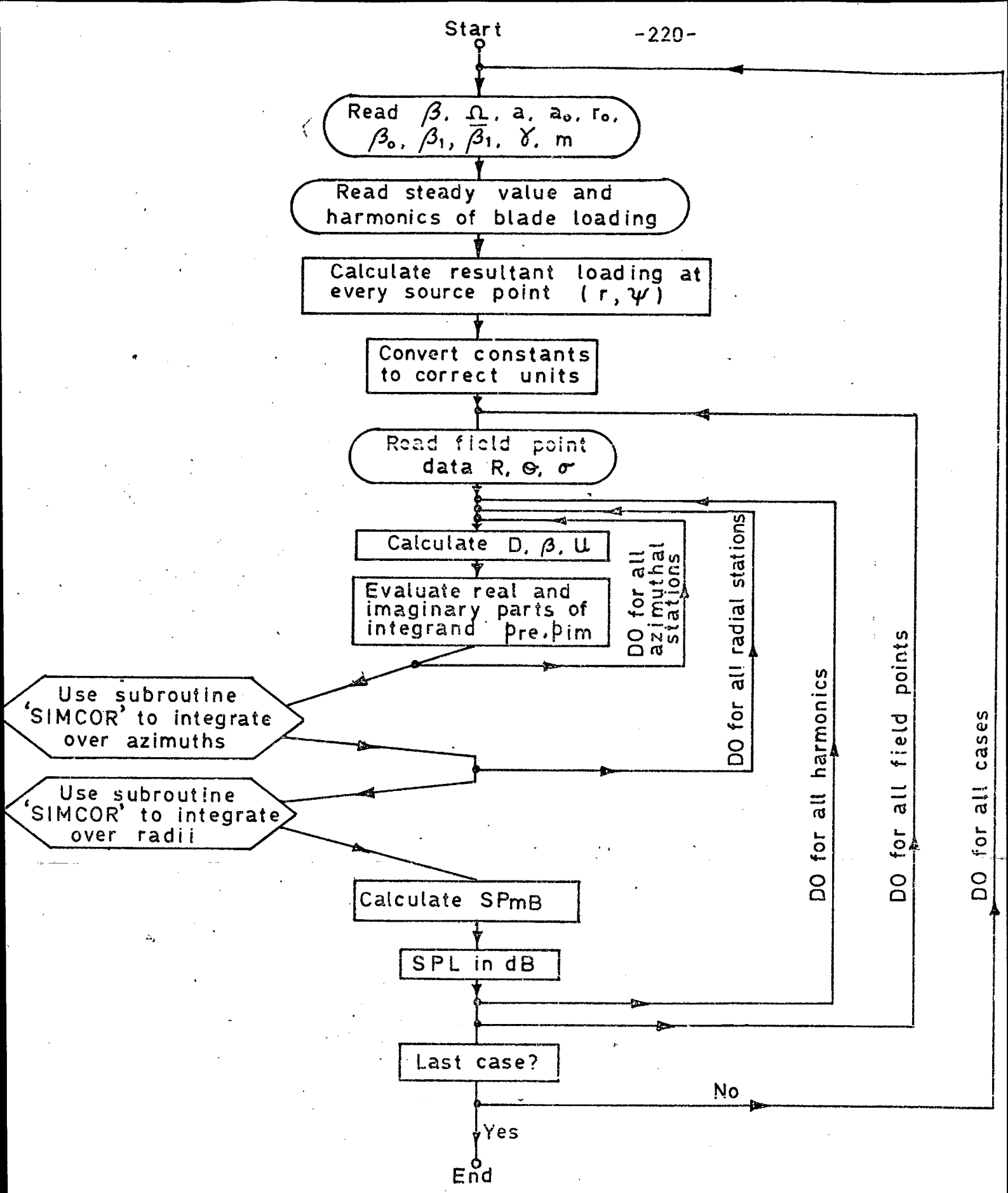

Fig. 1. Flow diagram for the program.

```
LINE                                ATLAS  FORTRAN                    06/05/68        VERSION 6
NUMBER                        SOURCE ROUTINE LISTING                   21.21.57    COUNTER=      11
                                                                                   LABEL FIELD
    1          DIMENSION P(50),S(50),Q(721,8),R(8),V8(5),V9I(8),TITLE(12),
              1 V25(721),V25I(721),PSI(721),PRAD(721),XL0(8),XLM(8,50),XMM(8,50)
        C     READ FLT. COND. PARAMETERS AND BLADE SECTION LOADING, PRINT SAME.
    2          RAD =1./57.2957795
    3        111 READ 2,TITLE
    4          2 FORMAT(12A6)
    5            READ 3,NEND,NFP,RBN,OMG,CH,SOS,R0,B01,B1,B11,G
    6            READ 3,NHAR,NRAD,ANG
    7            READ 33,KEY1,KEY2,KEY3
    8           33 FORMAT (3I2)
    9            3 FORMAT (2I2,9F8.2)
   10            NP=(360./ANG)+1.001
   11            NT=NP-1
   12            PSI(1)=0.
   13            PRAD(1)=0.
   14            DO 4 I=2,NP
   15            PSI(I)=PSI(I-1)+ANG
   16            4 PRAD(I)=PSI(I)*RAD
   17              READ 5,(R(I),I=1,NRAD)
   18            5 FORMAT (8F9.2)
   19              DO 6 I=1,NRAD
   20            6 READ 7,XL0(I),(XLM(I,J),J=1,50),(XMM(I,J),J=1,50)
   21            7 FORMAT (F8.2/,(10F8.2))
   22              DO 77 I=1,NRAD
   23              DO 77 J=1,NP
   24              Q(J,I)=XL0(I)
   25              DO 77 K=1,50
   26              X=K
   27           77 Q(J,I)=Q(J,I)+XLM(I,K)*COSF(X*PRAD(J))+XMM(I,K)*SINF(X*PRAD(J))
   28           88 PRINT 2,TITLE
   29              PRINT 8,B01,B1,B11,CH,OMG,RBN,R0,(R(I),I=1,NRAD)
   30            8 FORMAT (4HOB01,E15.6,4H  B1,E15.6,5H  B11,E15.6,7H  CHORD,E15.6,
                  1 7H  OMEGA,E15.6,8H  BLADES,F7.0,//25H RADIUS AT START OF TWIST,
                  2 E15.6,////30X,21HBLADE SECTION LOADING,////7H RADIUS,10X,1H1,14X,
                  3 1H2,14X,1H3,14X,1H4,14X,1H5,14X,1H6,14X,1H7,14X,1H8,/8H AZIMUTH,
                  4 2X,8E15.6,//)
   31              PRINT 2,TITLE
   32              OMG=3.14159265*OMG/30.
   33              SOS=12.*SOS
   34              B01=B01*RAD
   35              B1=B1*RAD
   36              B11=B11*RAD
   37              G=G*RAD
        C       BEGIN MAJOR LOOP ON FIELD POINTS
   38              DO 999 II=1,NFP
   39              READ 11,CAPR,THETA,ALFA
   40           11 FORMAT (3F12.4)
   41              PRINT 12, CAPR,THETA,ALFA
   42           12 FORMAT (12HOFIELD POINT,10X,9HRADIUS,E15.6,5X,7HAZIMUTH,E15.6,5X,
                  1 9HELEVATION,E15.6,/20X,8HHARMONIC,10X,14HSOUND PRESSURE,15X,
                  2 3HSPL)
   43              CAPR=12.*CAPR
   44              ALFA=RAD*ALFA
   45              THETA=RAD*THETA
   46              DO 999 M=1,NHAR
   47              DO 990 KK=1,NRAD
   48              DO 99  JJ=1,NT
   49              CAPS=SQRTF(CAPR*CAPR+R(KK)*R(KK)-2.*CAPR*R(KK)*COSF(ALFA)*
                  1 COSF(PRAD(JJ)-THETA))
   50              BETA=B01-G*(R(KK)-R0)+B1*COSF(PRAD(JJ))+B11*SINF(PRAD(JJ))
   51              SBTA=SINF(BETA)
   52              CBTA=COSF(BETA)
   53              V=M
   54              V=V*(RBN*OMG*CAPS/SOS+.5*CH*RBN/R(KK)+RBN*PRAD(JJ))
   55              TEMP=M
   56              V25(JJ)=Q(JJ,KK)*SINF(.5*TEMP*RBN*CH/R(KK))*(COSF(V)/CAPS+(TEMP*
                  1 RBN*OMG/SOS)*SINF(V))*(SBTA*COSF(ALFA)*SINF(PRAD(JJ)-THETA)+SINF
                  2 (ALFA)*CBTA)*R(KK))/(TEMP*CAPS*CAPS)
   57              V25I(JJ)=(Q(JJ,KK)*SINF(.5*TEMP*RBN*CH/R(KK))*(COSF(V)+TEMP*RBN*
                  1 OMG/SOS-SINF(V)/CAPS)*(SBTA*COSF(ALFA)*SINF(PRAD(JJ)-THETA)+
                  2 SINF(ALFA)*CBTA)*R(KK))/(TEMP*CAPS*CAPS)
   58           99 CONTINUE
   59              V25(NP)=V25(1)
   60              V25I(NP)=V25I(1)
   61              CALL SIMCOR (NP,PRAD,V25,AR)
   62              V8(KK)=AR
   63              CALL SIMCOR (NP,PRAD,V25I,AR)
   64              V8I(KK)=AR
   65          990 CONTINUE
   66              CALL SIMCOR (NRAD,R,V8,PRTAR)
   67              CALL SIMCOR (NRAD,R,V8I,PRTAI)
   68              PRTA=(.03582245*CAPR/CH)*SQRTF(PRTAR**2+PRTAI**2)
   69              SPL=20.*0.4343*ALOGF(ABSF(PRTA/2.9E-9))
   70              PRINT 997,M,PRTA,SPL
   71          997 FORMAT (25X,I2,5X,2E20.8)
   72          999 CONTINUE
   73              CALL OUTBRK(0)
   74              IF (NEND) 9999,9999,111
   75         9999 GO TO EXIT
   76              END

LINE                                ATLAS  FORTRAN                    06/05/68        VERSION 6
NUMBER                        SOURCE ROUTINE LISTING                   21.22.04    COUNTER=     574
                                                                                   LABEL FIELD
    1          SUBROUTINE SIMCOR (N,A,X,R)
    2          DIMENSION A(721),X(721)
    3          R=0.0
    4          DO 159 MM=2,N
    5        159 R=R+(X(MM-1)+X(MM))*(A(MM)-A(MM-1))/2
    6              RETURN
    7              END
```

FIG. 2. COMPUTER PROGRAM (HARTRAN)

UNIVERSITY of SOUTHAMPTON.
Computation Laboratory

~~Tape~~ / Card: (DELETE AS REQUIRED)
~~Algol~~ / Fortran Coding Form.

PROGRAMMER: H. K. TANNA.	DEPARTMENT: I.S.V. R.	CONTRACT: 9634/32	PROBLEM:
DATE:	PAGE: OF		

Statement number. | Identification

CARD 1:

1 ANY DESIRED TITLE INFORMATION

CARD 2:

19	4.0	210.0	16.00	1126.0	50.0	13.08	2.21	-5.28	0.024
	B	N	d	a_0	γ_0	B_0	B_1	β_1	β

No. of field points ≤ 99
End Code = 0 or 1

CARD 3:

58	2.00
	$\Delta\psi$

No. of radial stations ≤ 8
No. of harmonics ≤ 50

CARD 4:

000000
Output controls

CARD 5:

84.0	134.5	185.0	252.0	286.0	302.0	319.0	336.0

Radial Blade stations in inches

LOADING DATA (A SET FOR EACH RADIAL STATION):
↳ = 11 cards as follows

L_0
L_1 L_2 L_3
L_{11}
L_{21}
L_{31}
L_{41}
M_1 M_2 M_3
M_{11}
M_{21}
M_{31}
M_{41}

L_{48} L_{49} L_{50}
M_{48} M_{49} M_{50}

FIELD POINT DATA (A CARD FOR EACH FIELD POINT):

320.00	90.000	-30.000
$\tilde{R}$	θ	σ

(THE NUMBERS WRITTEN ABOVE EACH CARD REFER TO SAMPLE EXAMPLES)

FIG. 3. INPUT FORMAT FOR DATA CARDS

UNIVERSITY of SOUTHAMPTON.
Computation Laboratory

~~Tape~~/ Card. (DELETE AS REQUIRED)
~~Algol~~/ Fortran Coding Form.

PROGRAMMER: H. K. TANNA.	DEPARTMENT: I. S. V. R.	CONTRACT: 9634/32	PROBLEM:
DATE:	PAGE: OF		

Statement number. | Identification

```
JOB _____, H.K.TANNA. I.S.V.R. → Any desired title information
OUTPUT 0 LINEPRINTER ____ LINES
COMPUTING __ MINUTES
STORE __ BLOCKS
COMPILER HARTRAN
*FORTRAN NOCARDS
        Master Program Cards
*FORTRAN NOCARDS
        Subroutine Cards
*ENTER °
        Data Cards
7/8 9
```

FIG. 4. CONTROL CARDS AND CARD SEQUENCE FOR ICT ATLAS COMPUTER

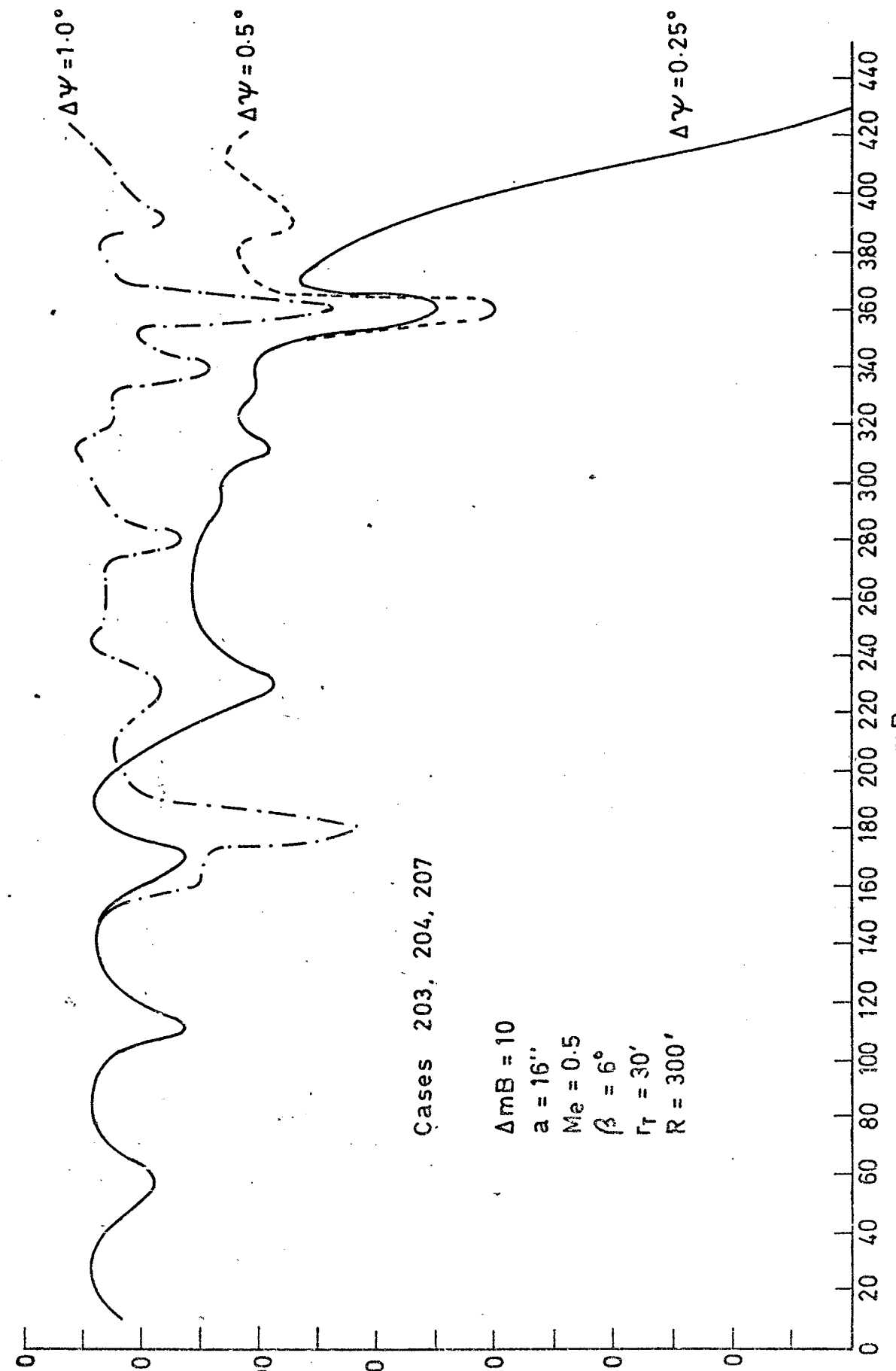

Fig. 5. Effect of integration interval $\Delta\psi$ on computed spectrum.

APPENDIX II : PRELIMINARY COMPUTATIONAL STUDY OF ROTATIONAL NOISE - SUMMARY

The computation covers the properties of blade loading harmonic radiation for a wide range of rotor parameters, including near field, distributed loading both chord and span, and for tip speed in excess of Mach one. The investigation then considers composite blade loading radiation, both simple and compound. Finally the radiation is computed for an ensemble of blade loading harmonics corresponding to well-defined blade loading azimuth functions, similar to those produced by blade-tip vortex and rotor-stator interactions. The study although designed for a particular rotor (helicopter), has sufficient scope to cover geometries of other rotor configurations.

The investigation has been designed to establish the properties of rotational noise over as wide a range of parameters as computing time would allow. Bearing in mind that the typical computing time on a fast computer is of the order of six seconds per harmonic per field point, then each computed case must be an attempt to achieve maximum information for minimum computing time.

Standard case:

As a consequence of the number of parameters involved, a standard case has been adopted such that the sound pressure is calculated for a standard set of parameter (those of a typical helicopter rotor) and then deviations in radiation computed for a range of parameter changes taken one at a time; it is of course computationally prohibitive to cover all combinations of rotor variables. However, some parameter

reduction is possible; for instance, the sound pressure harmonics (m) are plotted in terms of the mB parameter, as m and B (blade number) are indistinguishable mathematically, even for distributive loading - e.g. if B = 4 and m = 1 or B = 1 and m = 4 the S.P.L. is the same. The spectrum envelope, both in shape and level is independent of the number of blades providing the total arithmetic blade loading is the same. Only spectrum levels of mB numbers corresponding to multiples of B have physical significance. Similarly the rotor frequency (N) and the effective radius loading point (r_e) can be plotted in the form of an effective Mach number parameter (M_e). The values of various parameters for the standard case are given in Fig. 6.

Single blade loading harmonics:

For the study of blade loading harmonic properties, the total lift L_{OT} on the rotor is kept constant at 12,000 pounds irrespective of the number of blades, by adjusting the lift per blade accordingly. The total arithmetic blade loading harmonic amplitude L_{ST} is also maintained at 12,000 pounds, irrespective of the blade loading harmonic S or blade number B.

Four of the parameters listed in the standard case are linear parameters, i.e. the S.P.L. is directly related to their value. The first two, total lift L_{OT} and blade loading harmonic coefficient α_S, are directly proportional to the sound pressure and the remaining two, rotor radius r_T (providing the blade aspect ratio is constant) and far field observer distance R are inversely proportional to the sound pressure. Obviously there is no need to compute a range of these values. For example, to correct for a rotor having half the total thrust (- 6 dB), a blade loading harmonic coefficient of a tenth (- 20 dB),

a rotor radius of one-half having the same tip speed (+ 6 dB) and an observer a third of the distance (+ 10 dB), then a total of 10 dB will have to be subtracted from the general spectrum level. The remaining parameters are not simple multipliers, and they affect the spectrum shape as well as the general level; these are the blade force angle β , effective tip Mach number M_e, span distribution, and chord width a. Therefore the effects of the above parameters are computed over a limited range of practical interest.

Further, the sound pressure spectrum is a function of observer elevation angle for single blade loading harmonic radiations and depends on both elevation and azimuth angles for composite blade loading radiations. It was therefore decided to define all output at one fixed point for mB spectra; i.e., azimuth angle $\theta = 0^{\circ}$ (from tail) and elevation angle $\sigma = -30^{\circ}$ (below rotor plane). Polar plots corresponding to the polar elevation and polar plan were then positioned so as to contain the above co-ordinates. The observer distance R in each case is 300 feet from the centre of the rotor (see Fig. 7).

In the case of near field calculations, where the S.P.L. is not directly related to the observer distance, the additional effects of mB number, span distribution, rotor speed and rotor radius are also computed. The various span distributions used in the investigation are defined in Fig. 8, and are calculated for a total lift of 3000 pounds per blade.

Continuous blade loading spectra:

The additional parameters for the flat blade loading spectrum study are defined as a continuous spectrum of loading harmonics from $S = 1 \rightarrow 200$ with zero blade loading harmonic fall-off ($\alpha_S = 1$ for all S values) and zero blade loading harmonic phase $\phi_S = 0^{\circ}$. For compu-

tational convenience, the amplitude L_S of loading harmonics is kept constant at 3000 pounds per blade irrespective of the blade number used. This means that to correct for a standard total arithmetic blade loading amplitude L_{ST} of 12,000 pounds, 20 log (B/4) will have to be subtracted from the computed level; e.g. if the computational blade number B = 12 then the correction is - 10 dB.

The 6 dB per octave blade loading spectrum is defined as a continuous blade loading spectrum with $\alpha_S = 0.1$ for S = 1, and then progressive values of α_S reducing at the rate of 6 dB per octave in S.

Blade loading azimuth functions:

The blade loading azimuth functions used in the study are illustrated in Fig. 9. The standard blade loading function is a single rectangular excursion per blade revolution E = 1, having a load solidity $\rho = 1\%$, or an excursion width W of 1% of the effective disc solidity; i.e. $\rho = W/2\pi r_e$. The height of the function, or load change ΔL, is 50 pounds per inch or 1800 pounds per blade, which when expressed as a percentage of the standard steady load of 3000 pounds per blade, is 60%. A load change ΔL of 1800 pounds per blade corresponds to a maximum blade loading amplitude L_S max (at low S numbers for rectangular and half cosine functions and at medium S numbers for full sine function) of 1 pound per inch or 36 pounds per blade.

For computing purposes, this particular value of L_S max = 36 pounds per blade is kept constant throughout the azimuth blade loading study. Therefore if the number of function excursions E, or the load solidity ρ is for example doubled, then the load change is effectively halved, and 6 dB would have to be added to the computed spectrum level to correct for

a standard load change of 1800 pounds per blade.

As in the case for the flat blade loading spectrum study, the total blade loading is that of one blade times the blade number used in the computation. Therefore, if a radiation spectrum is required for a blade number other than that used in the computation, then a subtraction of 20 log (B/B_r) dB will have to be made from the general spectrum level, where B is the computational blade number and B_r is the required blade number.

Two further parameters which affect the accuracy of computed S.P.L. are the azimuth and span integration intervals. These parameters are discussed fully in Appendix I. It is sufficient to say here that the accuracy of the computation is a function of the integration intervals used, and for economic reasons, these intervals were adjusted to give a reasonable accuracy for a realistic computing time.

Detailed descriptions of the computed cases and the computed output (in graphical form) are given in I.S.V.R. Technical Report No. 15 [17].

B.L.H. PROPERTIES

total lift	L_{OT} =	12 000 lbs = B L_O
B.L.H. coefficient	α_S =	$1 = \frac{L_S}{L_O}$
S^{th} B.L.H. amplitude	L_S =	Variable (fn of B)
total arithmetic B.L.H. amplitude	L_{ST} =	12 000 lbs
blade force angle	β =	6°
effective tip Mach No.	M_e =	0·5
effective tip radius	r_e =	24 ft
tip radius	r_T =	30 ft
rotational frequency	N =	3·7 Hz
span distribution	Dist =	Rectangular 10 %
chord width	a =	16 in

FLAT BLADE LOADING SPECTRUM

as B.L.H. properties

B.L.H. spectrum range	S =	1 — 200
B.L.H. coefficient	α_S =	1
B.L.H. phase	ϕ_S =	0°
S^{th} B.L.H. amplitude	L_S =	3000 lbs/blade or 83·3 lbs/in
	L_{ST} =	Variable (fn of B)

B.L. AZIMUTH FUNCTIONS

as B.L.H. properties

Type of function	fn =	Rectangular
load solidity	ρ =	1 %
Number of excursions	E =	1
L_S Max	=	1 lb/in or 36 lbs/blade
load change $\frac{\Delta L}{L_O}$	=	60 % or ΔL = 50 lbs/in

Fig. 6. The standard cases

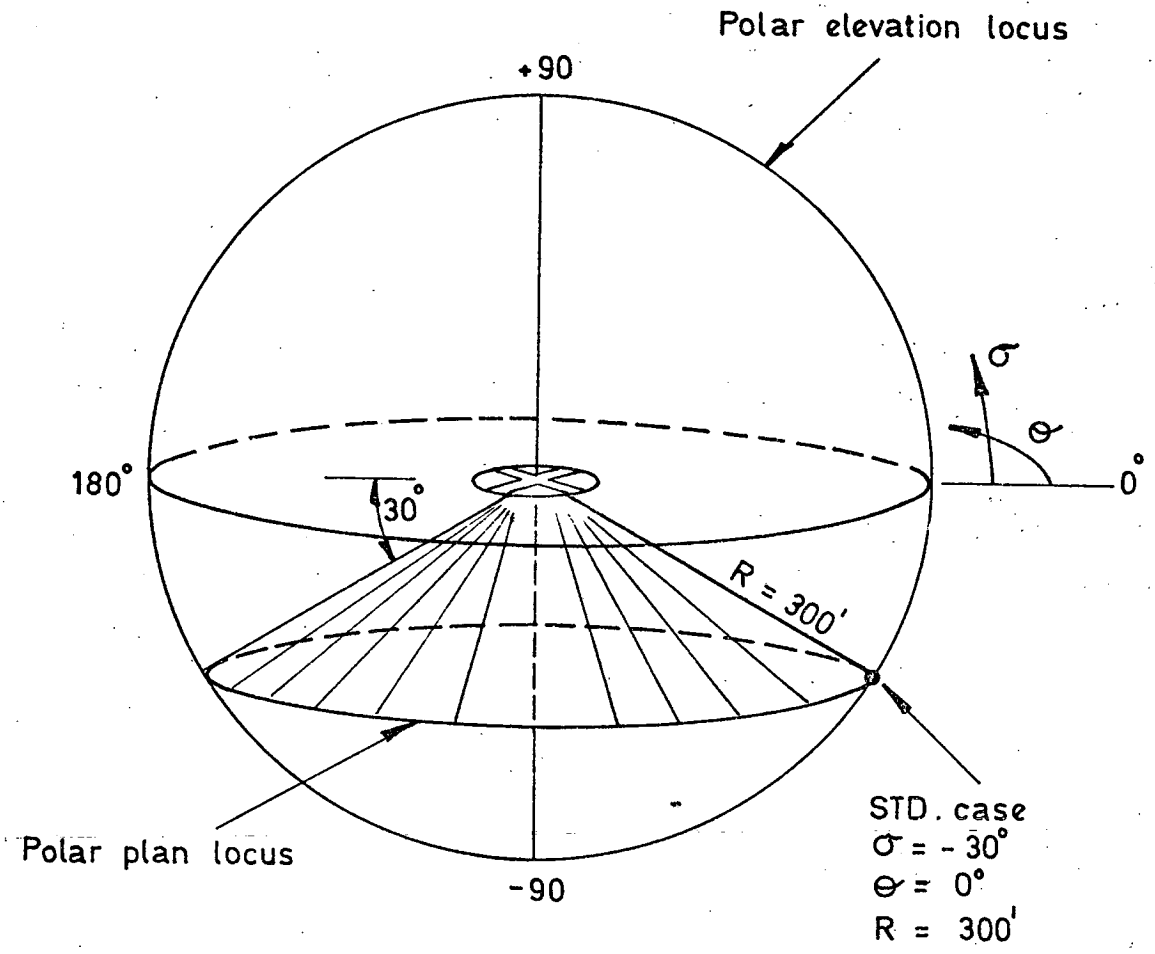

Fig. 7. Observer definition around rotor.

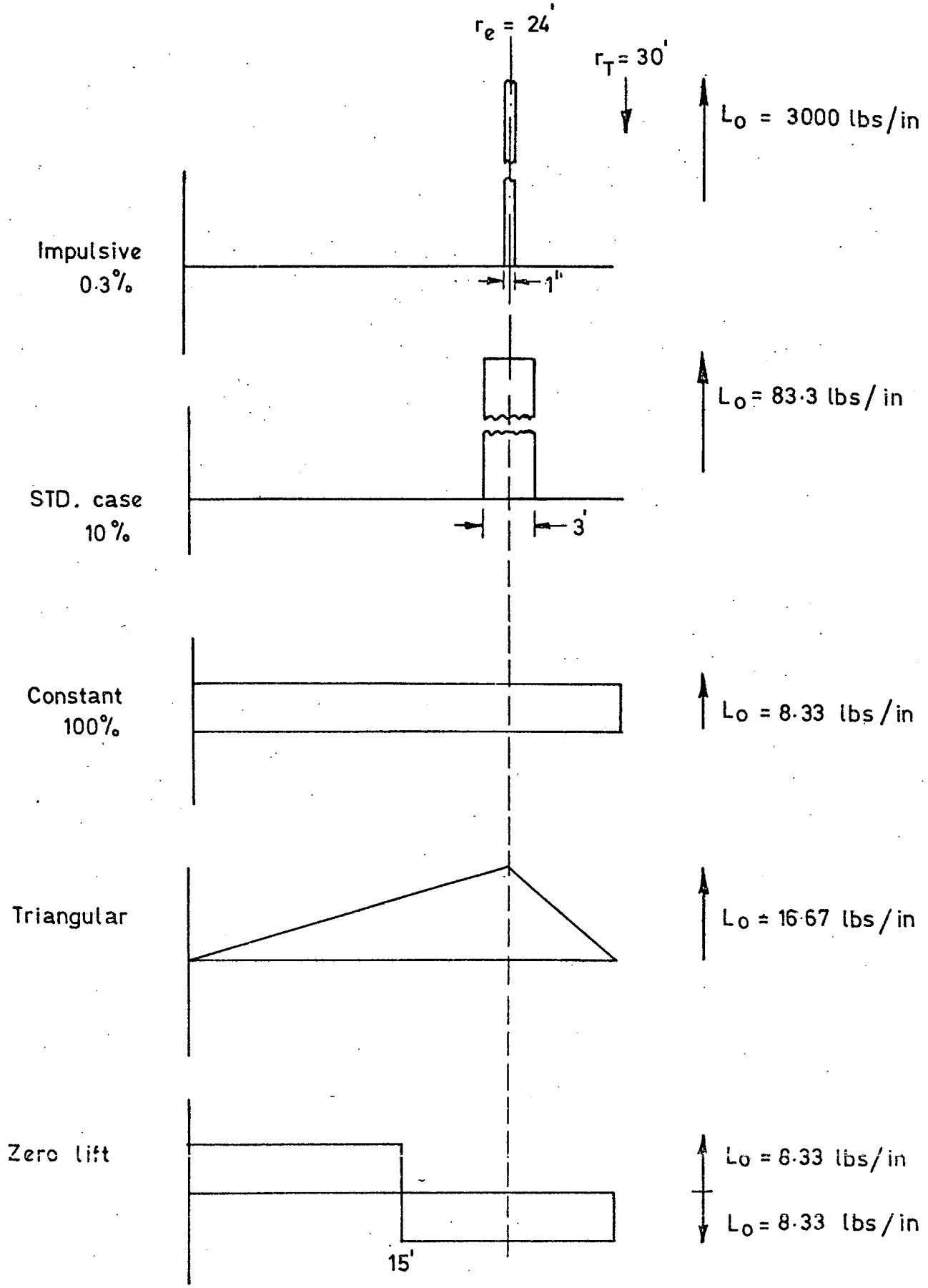

Fig. 8. Span distribution definitions .

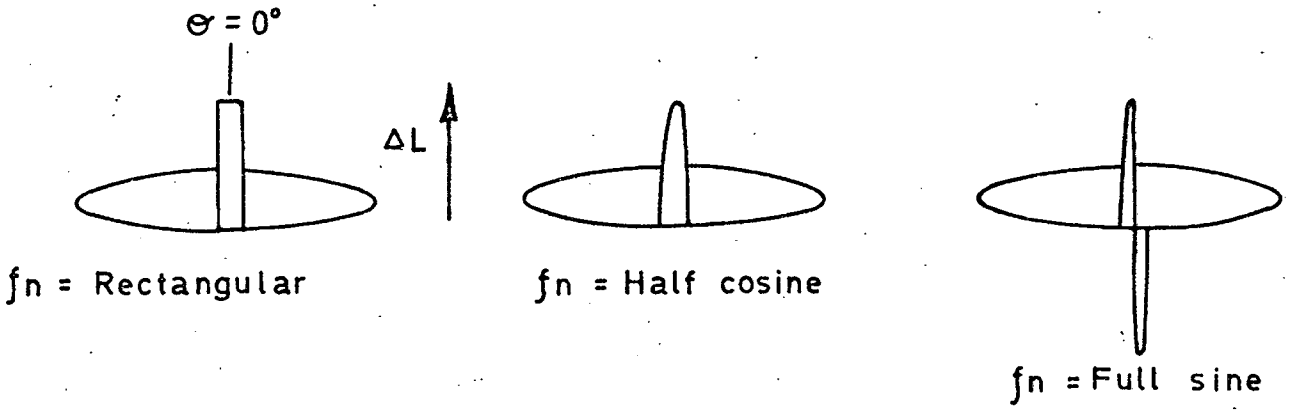

Type of function E=1, ρ =1%

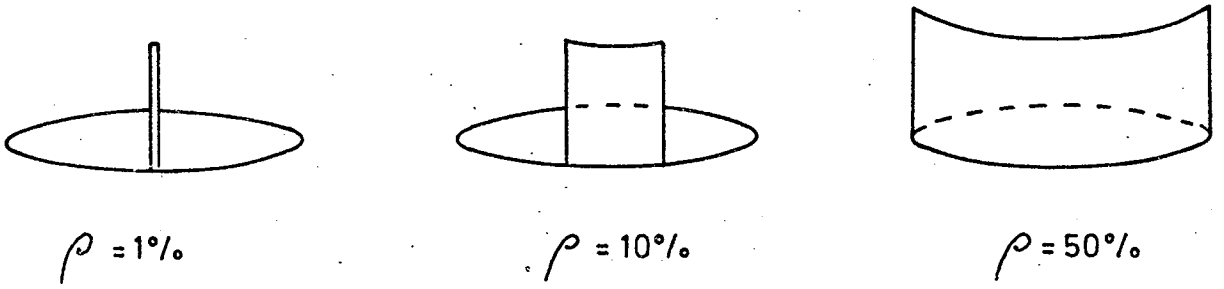

Load solidity fn = rect, E= 1

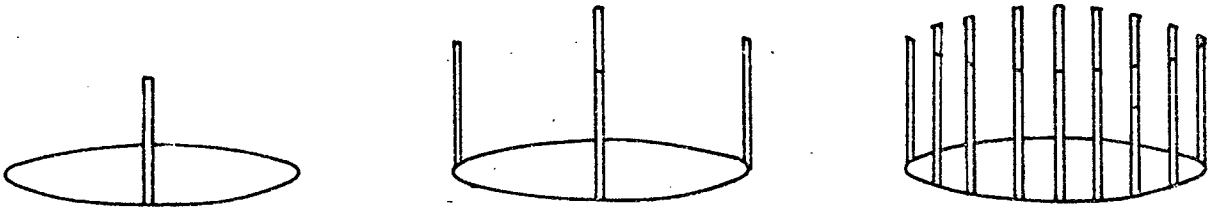

Number of excursions fn = rect, ρ =1%

Fig. 9. B.L. Azimuth functions

APPENDIX III : COMPUTER PROGRAM A

Radiation from a single blade loading harmonic with arbitrary chordwise loading profile (point span loading):

Equations to be computed:

The peak value of m^{th} harmonic of sound pressure in the far field is given by

$$\hat{SP}_{mBg} = \frac{N}{2Rc_o}\left\{\cos\beta\,\sin\sigma - \frac{\sin\beta}{M_e}\frac{\mu_-}{mB}\right\} mB\,J_{\mu_-}(mBM_e\cos\sigma)\,x$$

$$\frac{2r_e}{m}\left[\left(\sum_{p=1}^{n}\alpha_{pg}(r_e)\,.\,L'_{po}(r_e)\,.\,\sin\left(\frac{mw_pB}{2r_e}\right)\cos\left\{\frac{mB(a_p-a_1)}{r_e}\right\}\right)^2\right.$$

$$\left.+\left(\sum_{p=1}^{n}-\alpha_{pg}(r_e)\,.\,L'_{po}(r_e)\,.\,\sin\left(\frac{mw_pB}{2r_e}\right)\sin\left\{\frac{mB(a_p-a_1)}{r_e}\right\}\right)^2\right]^{\frac{1}{2}} \qquad (1)$$

where $$\mu_- = (mB - g)\ , \qquad (1a)$$

$$\alpha_{pg}(r_e) = \frac{L'_{pg}(r_e)}{L'_{po}(r_e)}\ , \qquad (1b)$$

and $$w_p \doteq \tfrac{1}{2}(a_{p+1} - a_{p-1})\ . \qquad (1c)$$

Method:

The sound pressure equation (1) can be written as

$$\hat{SP}_{mBg} = K\,.\,\gamma_{\mu_-}\,.\,\chi \qquad (2)$$

where $$K = \frac{N}{2Rc_o}\left\{\cos\beta\,\sin\sigma - \frac{\sin\beta}{M_e}\frac{\mu_-}{mB}\right\}\ , \qquad (3)$$

$$\gamma_{\mu_-} = mB\,J_{\mu_-}(mBM_e\cos\sigma)\ , \text{ (directivity term)} \qquad (4)$$

$$\text{and} \quad \chi = \frac{2r_e}{m} \left[\left(\sum_{p=1}^{n} \alpha_{pg}(r_e) \cdot L'_{po}(r_e) \cdot \sin\left(\frac{mw_p B}{2r_e}\right) \cos\left\{ \frac{mB(a_p - a_1)}{r_e} \right\} \right)^2 \right.$$

$$\left. + \left(\sum_{p=1}^{n} -\alpha_{pg}(r_e) \cdot L'_{po}(r_e) \cdot \sin\left(\frac{mw_p B}{2r_e}\right) \sin\left\{ \frac{mB(a_p - a_1)}{r_e} \right\} \right)^2 \right]^{\frac{1}{2}}$$

(spectrum function). (5)

The three terms are evaluated separately in decibels. In order to compute the Bessel functions, they are represented in the integral form

$$J_{\mu}(x) = \frac{1}{\pi} \int_0^{\pi} \cos(\mu\theta - x \sin\theta)\, d\theta \quad , \qquad (6)$$

and the integrals are evaluated in the subroutine which uses trapezoidal rule for integration; see Appendix I for details.

If R, r_T are in feet and the loading is in pounds/inch, then K term is in ft^{-2} and χ term is in pounds. The root-mean-square sound pressure level is then given by

$$\text{SPL (dB) r.m.s.} = 124.6 + K(dB) + \gamma_{\mu}(dB) + \chi(dB) \quad . \qquad (7)$$

The flow diagram is shown in Fig. 10.

Input parameters required:

The parameters (and their units) required to use the program are

n number of blade chord stations

a blade chord width, inches

g blade loading harmonic number

m number of harmonics of SPL required

B rotor blade number

r_T rotor tip radius, feet

N rotor frequency, Hz.

β blade force (pitch) angle, degrees

a_p distances of blade chord stations from the leading edge, inches

R field point distance from rotor centre, feet

α field point elevation angle, degrees

For each blade chord section p, the following loading data per blade is required:

L'_{pg} peak amplitude of g^{th} blade loading harmonic, pounds/inch

L'_{po} steady blade chord section loading, pounds/inch.

The format for input data is shown in Fig. 11 and the computer program is presented in Fig. 12.

Computer core store: 18 Blocks (approximately 9,000 words).

Computation time on ICT Atlas Computer:

Compilation time = 4 seconds.

Execution time = 0.5 second per harmonic per field-point when $\Delta\theta = 0.2^{o}$.

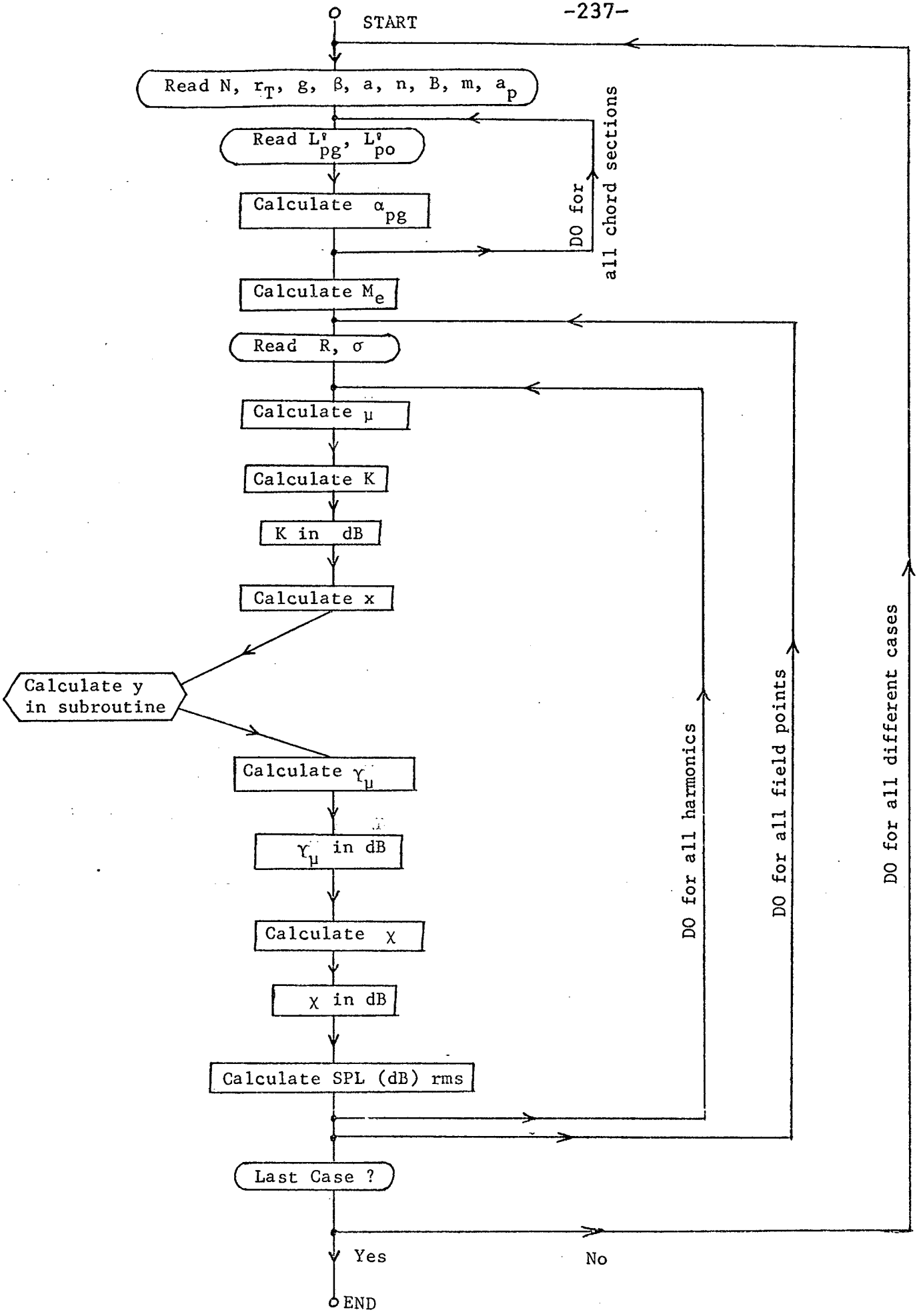

FIG. 10. Flow Diagram for Program A.

UNIVERSITY of SOUTHAMPTON
Computation Laboratory

Tape Card (DELETE AS REQUIRED)
Algol Fortran Coding Form

PROGRAMMER | DEPARTMENT | CONTRACT | PROBLEM

1	ANY DESIRED TITLE

I2	I2	I2	I2	F8.2	F8.2	F8.2	F8.2
	n	g	B	N Hz.	r_T ft.	a ins.	β deg.

End Code = 0 if last case
= 1 if cases to follow

$\left\{ \begin{array}{l} n \leqslant 50 \\ \Delta\theta \geqslant 0{\cdot}2^\circ \end{array} \right.$

I2	I2	F8.2
m		Δθ deg.

No. of field points

Blade chord stations in inches, first & last stations at leading and trailing edges respectively.

F8.3	F8.3	F8.3	F8.3	F8.3	F8.3	F8.3	F8.3	F8.3	F8.3
a_1 ins.	a_2 ins.	a_3 ins.					a_{n+2} ins.		

F12.4	F12.4	
L'_{pp} pounds/inch	L'_{pg} pounds/inch	one card for each chord station, excluding two stations at the edges.

F12.4	F12.4	
R ft.	σ deg.	one card for each field point.

FIG. 11. Input Format for Program A.

```
LINE NUMBER                    ATLAS  FORTRAN                    11/06/70        VERSION 7
                               SOURCE ROUTINE LISTING             14.43.06    COUNTER=        1?
                                                                  LABEL FIELD
      1          DIMENSION TITLE(12),ANDEG(901),ANRAD(901),FUNC(901),
                 1 DCLOD(50),GLOD(50),ALPHA(50),CH(3?)
      2          REAL MACH
      3          INTEGER Q,RBR,HARM
      4          RAD=1.0/57.2957795
      5       11 READ 2,TITLE
      6          2 FORMAT(12A6)
      7            PRINT 2,TITLE
      8            READ 3,LRBR,NCHSEC,HARM,CPS,RADIUS,CHORD,BETA
      9          3 FORMAT(412,4F8.2)
     10            PRINT 4,NCHSEC,HARM,CPS,RADIUS,CHORD,BETA
     11          4 FORMAT(21HNUMBER OF CHORD SECTIONS,F7.0,4X,1HS,F7.0,4X,5HBLADES,F7.0,
                 1 4X,7HROTOR CPS,E15.6,//6HRADIUS,E13.6,4X,5HCHORD,E15.6,4X,
                 2 4HBETA,E15.6)
     12            READ 5,NBLAD,NFR,DELTA
     13          5 FORMAT(212,F8.2)
     14            NP=180.0/DELTA+1.00
     15            NT=NP+1
     16            ANDEG(1)=0
     17            ANRAD(1)=0
     18            DO 6 I=2,NP
     19            ANDEG(I)=ANDEG(I-1)+DELTA
     20            ANRAD(I)=ANDEG(I)*RAD
     21          6 CONTINUE
     22            READ 25,(CH(JJ), JJ=1,NCHSEC+2)
     23         25 FORMAT(10F8.3)
     24            DO 10 J=1,NCHSEC
     25            READ 7,DCLOD(J),GLOD(J)
     26          7 FORMAT(2F12.4)
     27            ALPHA(J)=(GLOD(J)/DCLOD(J))
     28         10 CONTINUE
     29            MACH=((CPS*RADIUS)/222.0)
     30            PRINT 8,MACH
     31          8 FORMAT(22HEFFECTIVE MACH NUMBER,E15.6)
     32            BETA=BETA*RAD
     33            DO 999 II=1,NFR
     34            READ 12,R,SIGMA
     35         12 FORMAT(2F12.4)
     36            PRINT 13,R,SIGMA
     37         13 FORMAT(12HFIELD POINT,10X,6HDISTANCE,E15.5,4X,13HELEVATION ANGLE,
                 1 E15.6,//6X,6HM (DB),8X,5HHARMONIC,11X,16HGAMMA (DB),12X,
                 2 7HXI (DB),11X,11HSPL (DB)//)
     38            SIGMA=SIGMA*RAD
     39            DO 999 M=1,NHAR
     40            MANE=M
     41            MODE=(HARM*RBR)-6
           C       EVALUATION OF K TERM
     42            CON=(CPS/(2240.0*P))*(((COSF(BETA)*SINF(SIGMA))-((SINF(BETA)*MODE)
                 1 /(MACH*RADIUS)))
     43            IF (6) 77,77,88
     44         77 CONDB=6.00+(20.0*0.4343*ALOGF(ABSF(CON)))
     45            GO TO 66
     46         88 CONDB=(20.0*0.4343*ALOGF(ABSF(CON)))
           C       EVALUATION OF GAMMA TERM
     47         66 X=HARM*RBR*MACH*COSF(SIGMA)
     48            DO 99 JJ=1,NT
     49            FUNC(JJ)=COSF((MODE*ANRAD(JJ))-(X*SINF(ANRAD(JJ))))
     50         99 CONTINUE
     51            FUNC(NP)=FUNC(1)
     52            CALL BESSEL(NP,ANRAD,FUNC,Y)
     53            GAMA=HARM*RBR*Y/3.142
     54            GAMADB=20.0*0.4343*ALOGF(ABSF(GAMA))
           C       EVALUATION OF XI TERM
     55            XIRE=DCLOD(1)*ALPHA(1)*SINF((HARM*RBR*(CH(3)-CH(1)))/
                 1 (36.40*RADIUS))
     56            XIIM=0.0
     57            DO 18 J=2,NCHSEC
     58            XIRE=XIRE+DCLOD(J)*ALPHA(J)*SINF((HARM*RBR*(CH(J+2)-CH(J)))/
                 1 (36.40*RADIUS))*COSF((HARM*RBR*(CH(J+1)-CH(2)))/(9.6*RADIUS))
     59            XIIM=XIIM+DCLOD(J)*ALPHA(J)*SINF((HARM*RBR*(CH(J+2)-CH(J)))/
                 1 (36.40*RADIUS))*SINF((HARM*RBR*(CH(J+1)-CH(2)))/(9.6*RADIUS))
     60         18 CONTINUE
     61            XI=((12.2*RADIUS)/HARM)*SQRTF(XIRE**2+XIIM**2)
     62            XIDB=20.0*0.4343*ALOGF(ABSF(XI))
     63            SPL=124.6+CONDB+GAMADB+XIDB
     64            PRINT 20,CONDB,GAMADB,XIDB,SPL
     65         20 FORMAT(E20.8,6X,I2,6X,3E20.8)
     66        999 CONTINUE
     67            IF (NEXT) 9999,9999,111
     68       9999 GO TO EXIT
     69            END

LINE NUMBER                    ATLAS  FORTRAN                    11/06/70        VERSION 7
                               SOURCE ROUTINE LISTING             14.44.07    COUNTER=        4?
                                                                  LABEL FIELD
      1          SUBROUTINE BESSEL(N,A,Z,AREA)
      2          DIMENSION A(901),Z(901)
      3          AREA=0.0
      4          DO 100 M=2,N
      5          AREA=AREA+(Z(M-1)+Z(M))*(A(M)-A(M-1))/2
      6       100 CONTINUE
      7          RETURN
      8          END
```

FIG. 12. COMPUTER PROGRAM A.

APPENDIX IV : COMPUTER PROGRAM B

Radiation from the point span loading model with fluctuating actual chordwise loading profile:

Equations to be computed:

The r.m.s. value of m^{th} harmonic of sound pressure in the far field is given by

$$SP_{mB} = \frac{BNr_e}{\sqrt{2}\,\pi Rc_o} \left\{ Re^2 + Im^2 \right\}^{\frac{1}{2}} \tag{1}$$

where $$Re = \int_o^{2\pi} \left\{ \sin\beta \cos\sigma \sin(\psi - \theta) + \sin\sigma \cos\beta \right\} x$$

$$\left[\sum_{p=1}^{n} L'_p(r_e,\psi) \cdot \sin\left(\frac{mw_p B}{2r_e}\right) \cdot \sin V_p(\psi) \right] d\psi \tag{1a}$$

and $$Im = \int_o^{2\pi} \left\{ \sin\beta \cos\sigma \sin(\psi - \theta) + \sin\sigma \cos\beta \right\} x$$

$$\left[\sum_{p=1}^{n} L'_p(r_e,\psi) \cdot \sin\left(\frac{mw_p B}{2r_e}\right) \cdot \cos V_p(\psi) \right] d\psi \quad , \tag{1b}$$

and where

$$V_p(\psi) = mB\left\{ M_e \cos\sigma \cos(\theta - \psi) - \psi - \frac{(a_p - a_1)}{r_e} \right\} \quad , \tag{1c}$$

$$L'_p(r_e,\psi) = L'_{po}(r_e) + \sum_{g=1}^{\infty} \left\{ L'_{pg}(r_e) \cos g\psi + \bar{L}'_{pg}(r_e) \sin g\psi \right\}, \tag{1d}$$

$$w_p \doteq \tfrac{1}{2}(a_{p+1} - a_{p-1}) \, . \tag{1e}$$

If the loading data (L'_{po}, L'_{pg}, $\bar{L}'_{pg}$) is in pounds/inch and R is in feet, then Re, Im are given in pounds/inch and SP_{mB} is obtained in pounds/ft^2.

The root-mean-square SPL is then given by

$$\text{SPL (dB) r.m.s.} = 127.6 + 20 \log_{10} (SP_{mB}). \qquad (2)$$

The flow diagram is shown in Fig. 13.

Input parameters required:

The parameters (and their units) required to use the program are

n number of blade chord sections

a blade chord width, inches

m number of harmonics of SPL required

B rotor blade number

r_T rotor tip radius, feet

β blade force (pitch) angle, degrees

a_p distances of blade chord stations from the leading edge, inches

R field point distance from rotor centre, feet

θ field point azimuth angle, degrees

σ field point elevation angle, degrees

For each blade chord section p, the following loading data per blade is required:

L'_{po} steady blade chord section loading, pounds/inch

L'_{pg} cosine component (peak) of g^{th} harmonic of blade chord section loading, pounds/inch

$\bar{L}'_{pg}$ sine component (peak) of g^{th} harmonic of blade chord section loading, pounds/inch.

The format for input data is shown in Fig. 14 and the computer program is presented in Fig. 15.

Computer core store: 50 Blocks (approximately 26,000 words).

Computation time on ICT Atlas Computer:

Compilation time = 5 seconds.

Execution time = 8 seconds per harmonic per field-point when

$n = 5, \quad \Delta\psi = 0.5 , \quad g = 0 \rightarrow 50.$

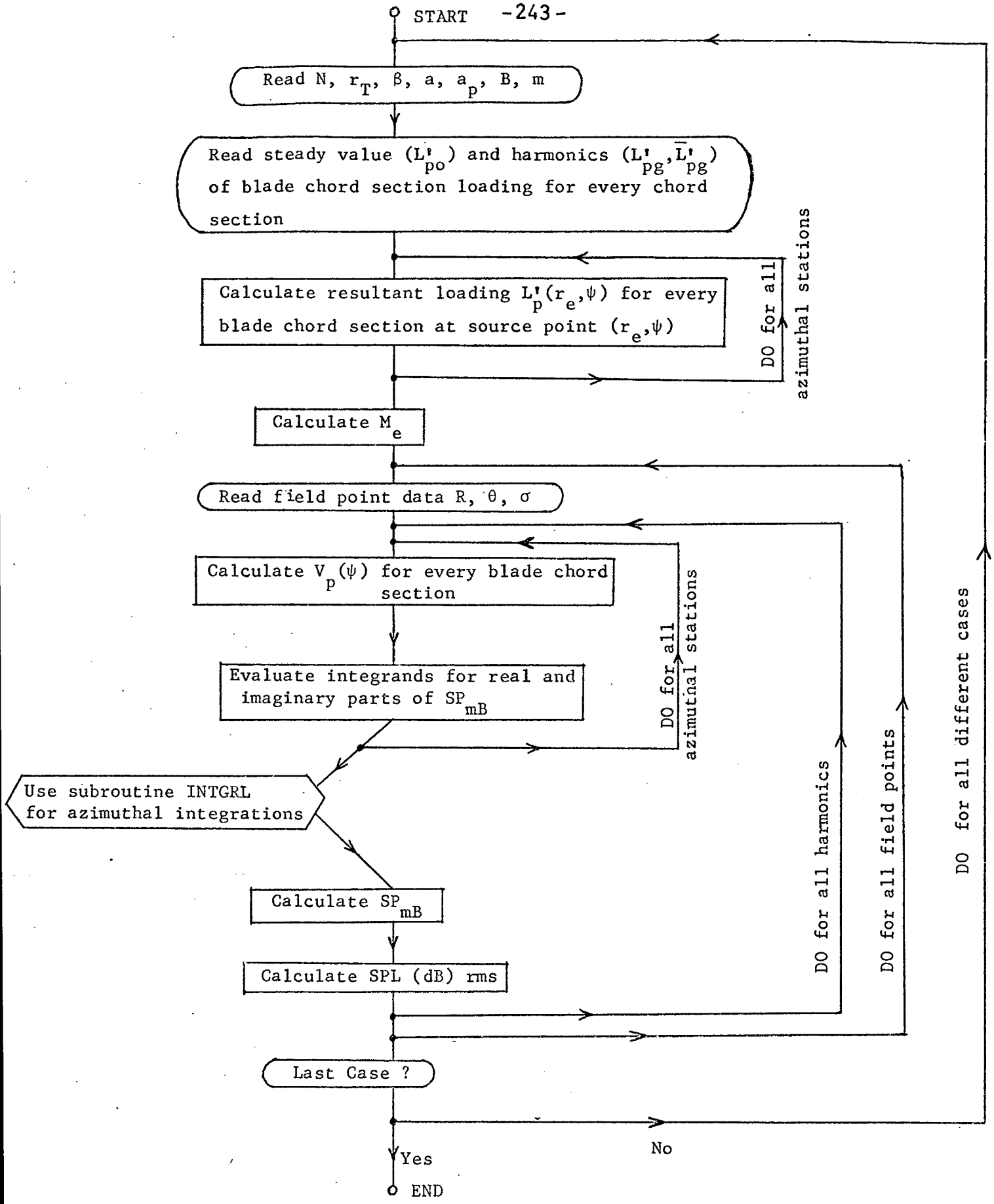

FIG. 13. Flow Diagram for Program B.

UNIVERSITY of SOUTHAMPTON
Computation Laboratory

Table Card (DELETE AS REQUIRED)
Algol Fortran Coding Form

1	ANY DESIRED TITLE

I2	I2	I2	F8.2	F8.2	F8.2	F8.2
	n	B	N Hz.	r_T ft.	a ins.	β deg.

End Code = 0 if last case
= 1 if cases to follow

$\left\{ \begin{array}{l} n \leq 10 \\ \Delta\psi \geqslant 0{\cdot}5^\circ \end{array} \right.$

I2	I2	F8.2
m		$\Delta\psi$ deg.

m = No. of field points

Blade chord stations in inches, first and last stations at leading and trailing edges respectively.

F6.2	F6.2	F6.2	F6.2	F6.2	F6.2	F6.2	F6.2	F6.2	F6.2	F6.2	F6.2
a_1 in.	a_2 in.	a_3 in.	a_4 in.	a_5 in.	a_6 in.	a_7 in.	a_8 in.	a_9 in.	a_{10} in.	a_{11} in.	a_{12} in.

F8.2 L'_{p0}

Loading in pounds per inch (11 cards for each chord section).

F8.2	F8.2	F8.2	F8.2	F8.2	F8.2	F8.2	F8.2	F8.2	F8.2
L'_{p1}	L'_{p2}							L'_{p49}	L'_{p50}
$\bar{L}'_{p1}$	$\bar{L}'_{p2}$							$\bar{L}'_{p49}$	$\bar{L}'_{p50}$

F12.4	F12.4	F12.4	
R ft.	θ deg.	σ deg.	one card for each field point.

FIG. 14. Input Format for Programs B and D.

```
LINE NUMBER                    ATLAS  FORTRAN                    11/06/70        VERSION 7
                          SOURCE ROUTINE LISTING                  14.48.53    COUNTER=      18
                                                                  LABEL FIELD
      1          DIMENSION TITLE(12),ANDEG(721),ANRAD(721),DCLOD(10),CLOD(10,50),
                1 SLOD(10,50),RLOD(10,721),PHASE(10,721),SUMRE(721),SUMIM(721),
                2 FUNCRE(721),FUNCIM(721),CH(12)
      2          REAL MACH
      3          INTEGER G,RBN,HARM,O
      4          RAD=1.0/57.2957795
      5        111 READ 2,TITLE
      6          2 FORMAT(12A6)
      7            PRINT 2,TITLE
      8            READ 3,NEND,NCHSEC,RBN,CPS,RADIUS,CHORD,BETA
      9          3 FORMAT(3I2,4F8.2)
     10            PRINT 4,NCHSEC,RBN,CPS,RADIUS,CHORD,BETA
     11          4 FORMAT(21H0NO OF CHORD SECTIONS,F7.0,4X,6HBLADES,F7.0,4X,
                1 9HROTOR CPS,E15.6,//6HRADIUS,E15.6,4X,5HCHORD,E15.6,4X,4HBETA,
                2 E15.6)
     12            READ 5,NHAR,NFP,DELTA
     13          5 FORMAT(2I2,F8.2)
     14            NP=360.0/DELTA+1.00
     15            NT=NP-1
     16            ANDEG(1)=0
     17            ANRAD(1)=0
     18            DO 6 I=2,NP
     19            ANDEG(I)=ANDEG(I-1)+DELTA
     20            ANRAD(I)=ANDEG(I)*RAD
     21          6 CONTINUE
     22            READ 18,(CH(NN),NN=1,NCHSEC*2)
     23         18 FORMAT(12F6.2)
     24            DO 10 J=1,NCHSEC
     25         10 READ 7,DCLOD(J),(CLOD(J,L),L=1,30),(SLOD(J,L),L=1,30)
     26          7 FORMAT(F8.2/,(10F8.2))
           C        CALCULATION OF RESULTANT LOADING AT EVERY SOURCE POINT
     27            DO 12 I=1,NP
     28            DO 12 J=1,NCHSEC
     29            RLOD(J,I)=DCLOD(J)
     30            DO 12 K=1,30
     31            G=K
     32            RLOD(J,I)=RLOD(J,I)+CLOD(J,K)*COSF(G*ANRAD(I))+SLOD(J,K)*
                1 SINF(G*ANRAD(I))
     33         12 CONTINUE
     34            MACH=((CPS*RADIUS)/222.0)
     35            PRINT 13,MACH
     36         13 FORMAT(22H0EFFECTIVE MACH NUMBER,E13.6)
     37            BETA=BETA*RAD
           C        BEGIN MAJOR LOOP ON FIELD POINTS
     38            DO 999 II=1,NFP
     39            READ 14,R,THETA,SIGMA
     40         14 FORMAT(3F12.4)
     41            PRINT 15,R,THETA,SIGMA
     42         15 FORMAT(12H0FIELD POINT,10X,8HDISTANCE,E15.6,5X,7HAZIMUTH,E15.6,
                1 5X,9HELEVATION,E15.6,//20X,8HHARMONIC,10X,14HSOUND PRESSURE,11X,
                2 11HSPL (DB)RMS)
     43            THETA=THETA*RAD
     44            SIGMA=SIGMA*RAD
     45            DO 999 M=1,NHAR
     46            DO 20 KK=1,NT
     47            DO 25 JJ=1,NCHSEC
     48            HARM=M
     49            O=JJ
     50            PHASE(JJ,KK)=HARM*RBN*(MACH*COSF(SIGMA)*COSF(ANRAD(KK))*ANRAD(KK)+
                1 ((CH(JJ+1)-CH(2))/(9.5*RADIUS)))
     51         25 CONTINUE
     52            SUMRE(KK)=RLOD(1,KK)*COSF(PHASE(1,KK))
                1 *SINF((HARM*RBN*(CH(3)-CH(1)))/(39.40*RADIUS))
     53            SUMIM(KK)=RLOD(1,KK)*SINF(PHASE(1,KK))
                1 *SINF((HARM*RBN*(CH(3)-CH(1)))/(39.40*RADIUS))
     54            DO 30 N=2,NCHSEC
     55            SUMRE(KK)=SUMRE(KK)+RLOD(N,KK)*COSF(PHASE(N,KK))
                1 *SINF((HARM*RBN*(CH(N+2)-CH(N)))/(39.40*RADIUS))
     56            SUMIM(KK)=SUMIM(KK)+RLOD(N,KK)*SINF(PHASE(N,KK))
                1 *SINF((HARM*RBN*(CH(N+2)-CH(N)))/(39.40*RADIUS))
     57         30 CONTINUE
     58            FUNCRE(KK)=SUMRE(KK)*(COSF(SIGMA)*SINF(BETA)*SINF(ANRAD(KK)-THETA)
                1 +COSF(BETA)*SINF(SIGMA))
     59            FUNCIM(KK)=SUMIM(KK)*(COSF(SIGMA)*SINF(BETA)*SINF(ANRAD(KK)-THETA)
                1 +COSF(BETA)*SINF(SIGMA))
     60         20 CONTINUE
     61            FUNCRE(NP)=FUNCRE(1)
     62            FUNCIM(NP)=FUNCIM(1)
     63            CALL INTGRL(NP,ANRAD,FUNCRE,SPRE)
     64            CALL INTGRL(NP,ANRAD,FUNCIM,SPIM)
     65            SP=((CPS*RBN*RADIUS)/(518.0*2))*SQRTF(SPRE**2+SPIM**2)
     66            SPL=127.6+20.0*0.4343*ALOGF(ABSF(SP))
     67            PRINT 40,M,SP,SPL
     68         40 FORMAT(25X,I2,5X,2E20.8)
     69        999 CONTINUE
     70            IF (NEND) 9999,9999,111
     71       9999 GO TO EXIT
     72            END

LINE NUMBER                    ATLAS  FORTRAN                    11/06/70        VERSION 7
                          SOURCE ROUTINE LISTING                  14.49.07    COUNTER=     939
                                                                  LABEL FIELD
      1            SUBROUTINE INTGRL(N,A,Z,AREA)
      2            DIMENSION A(721),Z(721)
      3            AREA=0.0
      4            DO 100 MM=2,N
      5            AREA=AREA+(Z(MM-1)+Z(MM))*(A(MM)-A(MM-1))/2
      6         100 CONTINUE
      7            RETURN
      8            END
```

FIG. 15. COMPUTER PROGRAM B.

APPENDIX V : COMPUTER PROGRAM C

Radiation from the general distributive loading model with fluctuating chordwise and spanwise loading profiles:

Equations to be computed:

The r.m.s. value of m^{th} harmonic of sound pressure is given by

$$SP_{mB} = \frac{R}{2\sqrt{2}\,\pi^2 m} \left\{ Re^2 + Im^2 \right\}^{\frac{1}{2}} \tag{1}$$

where

$$Re = \int_0^{r_T} \int_0^{2\pi} \frac{1}{D^2} \left\{ \sin\beta\cos\sigma \sin(\psi - \theta) + \sin\sigma \cos\beta \right\} x$$

$$\left[\sum_{p=1}^{n} \left\{ A_p(r,\psi) \cdot \sin\left(\frac{mw_p B}{2r}\right) \cdot \left(\frac{\cos U_p}{D} + \frac{mB\Omega}{c_o} \sin U_p\right) \right\} \right] r\,d\psi\,dr \tag{1a}$$

and

$$Im = \int_0^{r_T} \int_0^{2\pi} \frac{1}{D^2} \left\{ \sin\beta \cos\sigma \sin(\psi - \theta) + \sin\sigma \cos\beta \right\} x$$

$$\left[\sum_{p=1}^{n} \left\{ A_p(r,\psi) \cdot \sin\left(\frac{mw_p B}{2r}\right) \cdot \left(\frac{mB\Omega}{c_o} \cos U_p - \frac{\sin U_p}{D}\right) \right\} \right] r\,d\psi\,dr \tag{1b}$$

and where

$$U_p(r,\psi) = mB\left\{ \frac{\Omega D}{c_o} + \psi + \frac{(a_p - a_1)}{r} \right\} , \tag{1c}$$

$$A_p(r,\psi) = A_{po}(r) + \sum_{g=1}^{\infty} \left\{ A_{pg}(r) \cos g\psi + \bar{A}_{pg}(r) \sin g\psi \right\} , \tag{1d}$$

$$\beta(r,\psi) = \beta_o + \beta_1 \cos\psi + \bar{\beta}_1 \sin\psi - \gamma(r - r_o) , \tag{1e}$$

$$D = \left\{ R^2 + r^2 - 2rR \cos\sigma \cos(\theta - \psi) \right\}^{\frac{1}{2}} , \tag{1f}$$

$$w_p \triangleq \tfrac{1}{2}(a_{p+1} - a_{p-1}) . \tag{1g}$$

If the differential-pressure data (A_{po} , A_{pg} , $\bar{A}_{pg}$) is in pounds/inch^2 and R,r are in inches, then A_p is in pounds/inch^2, D is in inches and the two integrands are given in pounds/inch^3. The root-mean-square sound pressure is then obtained in pounds/inch^2 and this is expressed in decibels by

$$\text{SPL (dB) r.m.s.} = 20 \log_{10} \left| \frac{SP_{mB}}{2.9 \times 10^{-9}} \right| , \qquad (2)$$

where the factor 2.9×10^{-9} arises from converting pounds/inch^2 into dynes/cm^2. and referencing SP_{mB} to 0.0002 dynes/cm^2.

The flow diagram is shown in Fig. 16.

Input parameters required:

The parameters (and their units) required to use the program are

n number of blade chord sections

a blade chord width, inches

m number of harmonics of SPL required

B rotor blade number

N rotor frequency, Hz.

a_p distances of blade chord stations from the leading edge, inches

r_o radius at start of blade twist, inches

β_o steady pitch angle, degrees

β_1 cosine coefficient of cyclic pitch, degrees

$\bar{\beta}_1$ sine coefficient of cyclic pitch, degrees

γ blade twist rate, degrees per inch

r distances of span stations from rotor centre, inches

R field point distance from rotor centre, feet

θ field point azimuth angle, degrees

σ field point elevation angle, degrees

For each spanwise (r) and chordwise (p) station, the following differential-pressure data per blade is required:

$A_{po}(r)$ steady blade chord section pressure, pounds/in^2.

$A_{pg}(r)$ cosine component (peak) of g^{th} harmonic of blade chord section pressure, pounds/in^2.

$\bar{A}_{pg}(r)$ sine component (peak) of g^{th} harmonic of blade chord section pressure, pounds/in^2.

The format for input data is shown in Fig. 17 and the computer program is presented in Fig. 18.

Computer core store: 180 Blocks (approximately 92,000 words).

Computation time on ICT Atlas Computer:

Compilation time = 6 seconds.

Execution time = 15 seconds per harmonic per field point when

$n = 5$, $\Delta\psi = 0.5^o$, $g = 0 \rightarrow 50$ and four radial stations.

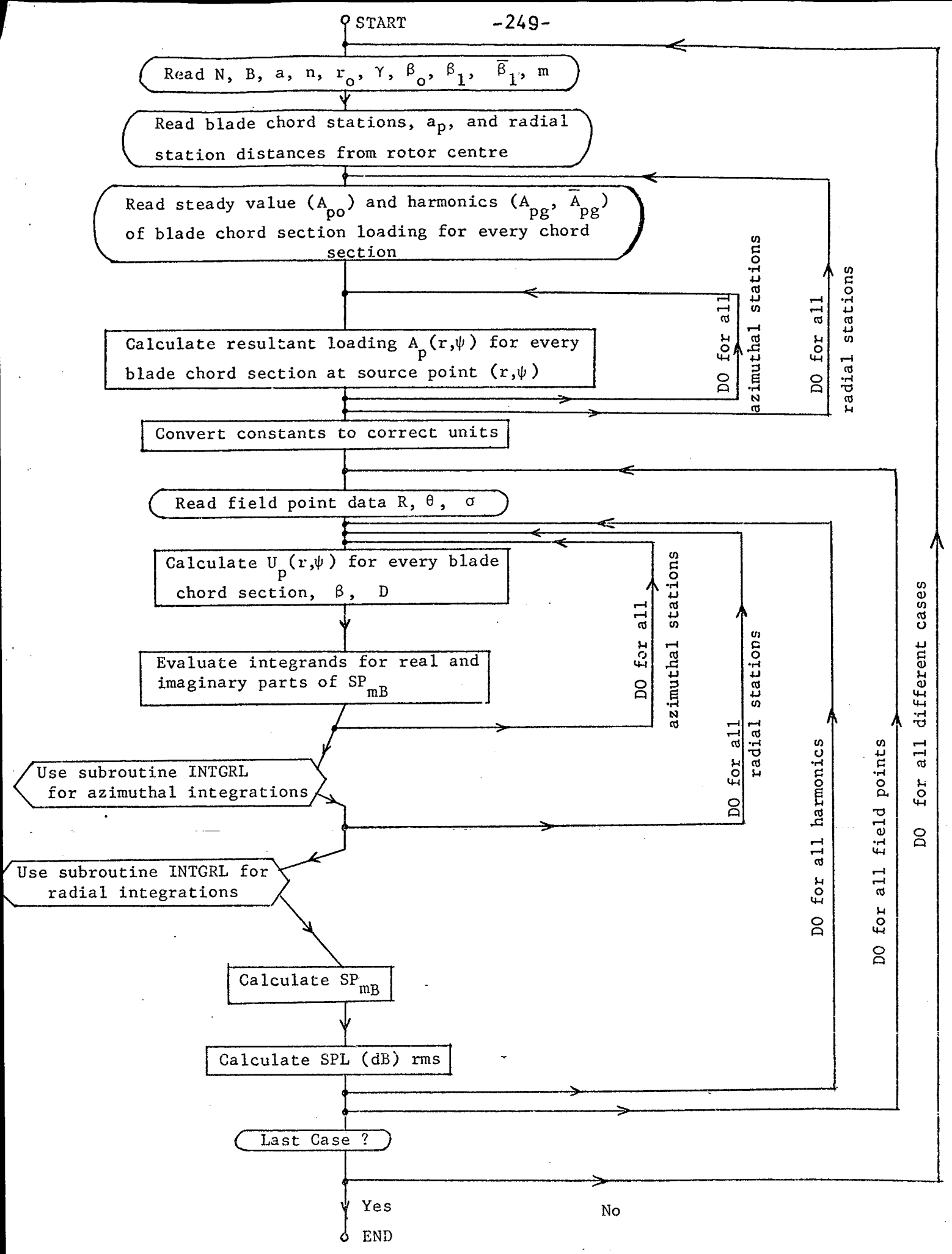

FIG. 16. Flow Diagram for Program C.

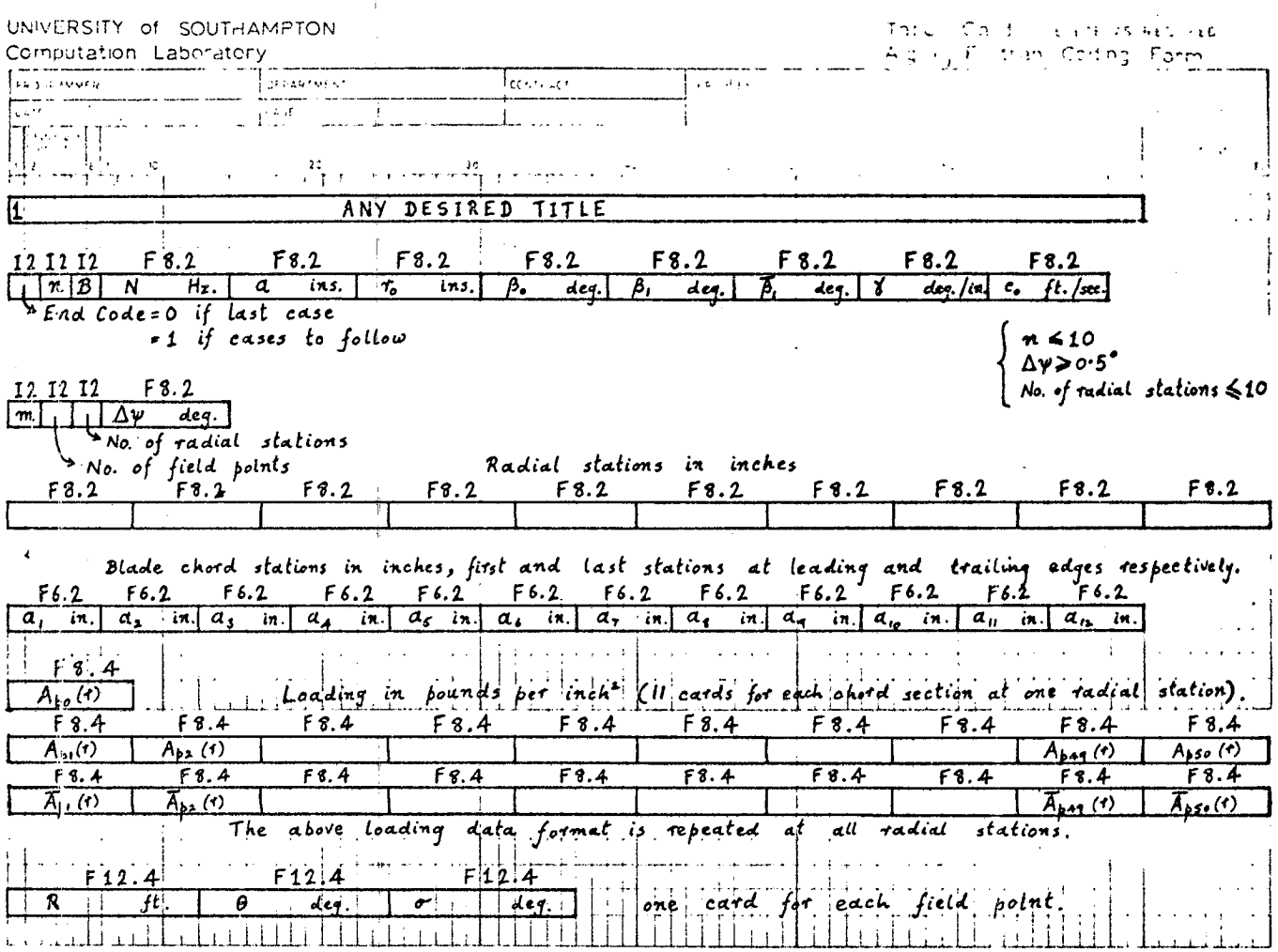

FIG. 17. Input Format for Program C.

```
LINE                    ATLAS  FORTRAN                    12/06/78      VERSION 7
NUMBER          SOURCE ROUTINE LISTING                   21.23.23    COUNTER=     9
                                                                    LABEL FIELD
    1          DIMENSION TITLE(12),ANDEG(721),ANRAD(721),RADIUS(10),DCLOD(10,10),
              1 CLOD(10,10,58),SLOD(10,10,58),RLOD(18,721,10),PHASE(10),
              2 SUMRE(721),SUMIM(721),AZMRE(721),AZMIM(721),RADRE(10),RADIM(10),
              3 CH(12)
    2          INTEGER Q,RBN,HARM,Q
    3          RAD=1.0/57.2957795
    4      111 READ 2,TITLE
    5        2 FORMAT(12A6)
    6          PRINT 2,TITLE
    7          READ 3,NEND,NCHSEC,RBN,CPS,CHORD,R0,DCBETA,CRETA,SBETA,TWIST,SOS
    8        3 FORMAT(312,8F8.2)
    9          PRINT 4,NCHSEC,RBN,CPS,CHORD,R0,DCBETA,CRETA,SBETA,TWIST
   10        4 FORMAT(21HNO OF  CHORD SECTIONS,F7.0,4X,6HBLADES,F7.0,4X,
              1 9HROTOR CPS,E15.6,//5HCHORD,E15.8,4X,24HRADIUS AT START OF TWIST,
              2 E15.6,4X,//6HDCBETA,E15.6,4X,5HCBETA,E15.6,4X,5HSBETA,E15.6,4X,
              3 19HTWIST RATE,E15.6)
   11          READ 5,NHAR,NFP,NRAD,DELTA
   12        5 FORMAT(312,F8.2)
   13          NP=360.0/DELTA+1.00
   14          NT=NP-1
   15          ANDEG(1)=0
   16          ANRAD(1)=0
   17          DO 6 I=2,NP
   18          ANDEG(I)=ANDEG(I-1)+DELTA
   19          ANRAD(I)=ANDEG(I)*RAD
   20        6 CONTINUE
   21          READ 7,(RADIUS(I),I=1,NRAD)
   22        7 FORMAT(10F8.2)
   23          READ 18,(CH(NN),NN=1,NCHSEC+2)
   24       18 FORMAT(12F6.2)
   25          DO 10 I=1,NRAD
   26          DO 10 J=1,NCHSEC
   27       10 READ 8,DCLOD(J,I),(CLOD(J,I,L),L=1,58),(SLOD(J,I,L),L=1,58)
   28        8 FORMAT(F8.4/,(10F8.4))
   29          DO 12 I=1,NRAD
   30          DO 12 K=1,NP
   31          DO 12 J=1,NCHSEC
   32          RLOD(J,K,I)=DCLOD(J,I)
   33          DO 12 L=1,58
   34          G=L
   35          RLOD(J,K,I)=RLOD(J,K,I)+CLOD(J,I,L)*COSF(G*ANRAD(K))+
              1 SLOD(J,I,L)*SINF(G*ANRAD(K))
   36       12 CONTINUE
   37          OMG=6.2831853*CPS
   38          DCBETA=DCBETA*RAD
   39          CBETA=CBETA*RAD
   40          SBETA=SBETA*RAD
   41          TWIST=TWIST*RAD
   42          SOS=12.0*SOS
   43          DO 999 II=1,NFP
   44          READ 14,R,THETA,SIGMA
   45       14 FORMAT(3F12.4)
   46          PRINT 15,R,THETA,SIGMA
   47       15 FORMAT(12HOFIELD POINT,10X,8HDISTANCE,E15.6,5X,7HAZIMUTH,E15.6,5X,
              1 9HELEVATION,E15.6,//20X,8HHARMONIC,10X,14HSOUND PRESSURE,11X,
              2 11HSPL (DB)RMS)
   48          R=12.0*R
   49          THETA=THETA*RAD
   50          SIGMA=SIGMA*RAD
   51          DO 999 H=1,NHAR
   52          DO 50 KK=1,NRAD
   53          DO 99 JJ=1,NT
   54          DIST=SQRTF(R**2-RADIUS(KK)**2-2.0*R*RADIUS(KK)*COSF(SIGMA)*
              1 COSF(THETA-ANRAD(JJ)))
   55          BETA=DCBETA+CBETA*COSF(ANRAD(JJ))+SBETA*SINF(ANRAD(JJ))-
              1 TWIST*(RADIUS(KK)-R0)
   56          DO 29 LL=1,NCHSEC
   57          HARM=H
   58          Q=LL
   59          PHASE(LL)=HARM*RBN*(OMG*DIST/SOS*ANRAD(JJ)+(CH(LL+1)-CH(2))/
              1 RADIUS(KK))
   60       29 CONTINUE
   61          SUMRE(JJ)=RLOD(1,JJ,KK)*(COSF(PHASE(1))/DIST*HARM*RBN*OMG*
              1 SINF(PHASE(1))/SOS)*SINF((HARM*RBN*(CH(3)-CH(1)))/
              2 (4.0*RADIUS(KK)))
   62          SUMIM(JJ)=RLOD(1,JJ,KK)*(HARM*RBN*0.42*COSF(PHASE(1))/SOS-
              1 SINF(PHASE(1))/DIST)*SINF((HARM*RBN*(CH(3)-CH(1)))/
              2 (4.0*RADIUS(KK)))
   63          DO 30 N=2,NCHSEC
   64          SUMRE(JJ)=SUMRE(JJ)+RLOD(N,JJ,KK)*(COSF(PHASE(N))/DIST+
              1 HARM*RBN*OMG*SINF(PHASE(N))/SOS)*SINF((HARM*RBN*(CH(N+2)-CH(N)))/
              2 (4.0*RADIUS(KK)))
   65          SUMIM(JJ)=SUMIM(JJ)+RLOD(N,JJ,KK)*(HARM*RBN*OMG*COSF(PHASE(N))/
              1 SOS-SINF(PHASE(N))/DIST)*SINF((HARM*RBN*(CH(N+2)-CH(N)))/
              2 (4.0*RADIUS(KK)))
   66       30 CONTINUE
   67          AZMRE(JJ)=SUMRE(JJ)+
              1 (COSF(SIGMA)*SINF(BETA)+SINF(ANRAD(JJ)+THETA)*COSF(BETA)*
              2 SINF(SIGMA))*RADIUS(KK)/(DIST**2)
   68          AZMIM(JJ)=SUMIM(JJ)+
              1 (COSF(SIGMA)*SINF(BETA)+SINF(ANRAD(JJ)+THETA)*COSF(BETA)*
              2 SINF(SIGMA))*RADIUS(KK)/(DIST**2)
   69       99 CONTINUE
   70          AZMRE(NP)=AZMRE(1)
   71          AZMIM(NP)=AZMIM(1)
   72          CALL INTGRL(NP,ANRAD,AZMRE,AR)
   73          RADRE(KK)=AR
   74          CALL INTGRL(NP,ANRAD,AZMIM,AR)
   75          RADIM(KK)=AR
   76       50 CONTINUE
   77          CALL INTGRL(NRAD,RADIUS,RADRE,SPRE)
   78          CALL INTGRL(NRAD,RADIUS,RADIM,SPIM)
   79          SP=SQRTF(SPRE**2+SPIM**2)*(R/(27.9*HARM))
   80          SPL=20.0*0.4343*ALOGF(ABSF(SP/2.9E-9))
   81          PRINT 40,M,SP,SPL
   82       40 FORMAT(29X,I2,5X,2E20.8)
   83      999 CONTINUE
   84          IF (NEND) 9999,9999,111
   85     9999 GO TO EXIT
   86          END

LINE                    ATLAS  FORTRAN                    12/06/78      VERSION 7
NUMBER          SOURCE ROUTINE LISTING                   21.23.36    COUNTER=   698
                                                                    LABEL FIELD
    1          SUBROUTINE INTGRL(N,A,Z,AREA)
    2          DIMENSION A(721),Z(721)
    3          AREA=0.0
    4          DO 100 MM=2,N
    5          AREA=AREA+(Z(MM-1)+Z(MM))*(A(MM)-A(MM-1))/2
    6      100 CONTINUE
    7          RETURN
    8          END
```

FIG. 18. COMPUTER PROGRAM C.

APPENDIX VI : COMPUTER PROGRAM D

Radiation from the point span loading model with fluctuating equivalent rectangular chordwise loading profile:

Equations to be computed:

The r.m.s. value of m^{th} harmonic of sound pressure in the far field is given by

$$SP_{mB} = \frac{BNr_e}{\sqrt{2}\ \pi Rc_o} \sin\left(\frac{maB}{2r_e}\right) \left\{ Re^2 + Im^2 \right\}^{\frac{1}{2}} \qquad (1)$$

where

$$Re = \int_0^{2\pi} \left\{ \sin\beta \cos\sigma \sin(\psi - \theta) + \sin\sigma \cos\beta \right\} L'(r_e,\psi) \cdot \sin V(\psi)\, d\psi \qquad (1a)$$

and

$$Im = \int_0^{2\pi} \left\{ \sin\beta \cos\sigma \sin(\psi - \theta) + \sin\sigma \cos\beta \right\} L'(r_e,\psi) \cdot \cos V(\psi)\, d\psi \qquad (1b)$$

and where

$$V(\psi) = mB\left\{ M_e \cos\sigma \cos(\theta - \psi) - \psi \right\}, \qquad (1c)$$

$$L'(r_e,\psi) = \frac{1}{a} \sum_{p=1}^{n} L'_p(r_e,\psi) \cdot w_p \quad , \qquad (1d)$$

$$L'_p(r_e,\psi) = L'_{po}(r_e) + \sum_{g=1}^{\infty} \left\{ L'_{pg}(r_e)\cos g\psi + \bar{L}'_{pg}(r_e)\sin g\psi \right\}, \qquad (1e)$$

$$w_p \doteq \tfrac{1}{2}(a_{p+1} - a_{p-1}) \quad . \qquad (1f)$$

If the loading data (L'_{po} , L'_{pg} , $\bar{L}'_{pg}$) is in pounds/inch, then $L'(r_e,\psi)$ is in pounds/inch giving Re and Im in pounds/inch. If R is now given in feet, SP_{mB} is obtained in pounds/ft^2. The root-mean-square SPL is then given by

$$\text{SPL (dB) r.m.s.} = 127.6 + 20 \log_{10} (SP_{mB}) \quad . \qquad (2)$$

The flow diagram is shown in Fig. 19.

Input parameters required:

The parameters (and their units) required to use the program are identical to those listed for program B, and the format for input data is also the same as that used for program B (Fig. 14, Appendix IV). The computer program is presented in Fig. 20.

Computer core store: 40 Blocks (approximately 20,000 words).

Computation time on ICT Atlas Computer:

Compilation time = 5 seconds.

Execution time = 5 seconds per harmonic per field point when n = 5,

$\Delta\psi = 0.5^{\circ}$, $g = 0 \rightarrow 50$.

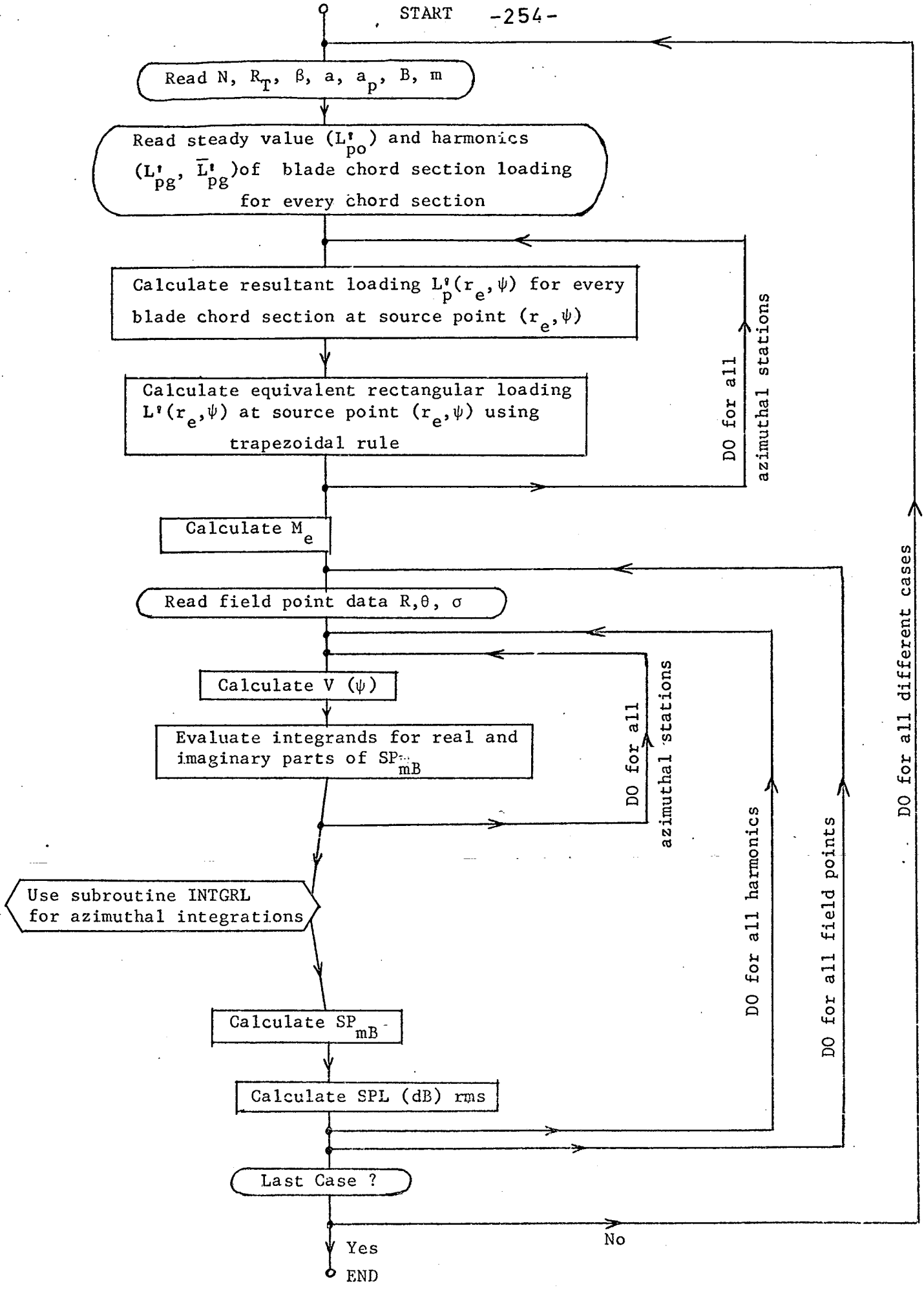

FIG. 19. Flow Diagram for Program D.

```
LINE                                ATLAS  FORTRAN                    11/06/70        VERSION 7
NUMBER                          SOURCE ROUTINE LISTING                 10.53.02    COUNTER=      10
                                                                                  LABEL FIELD
    1          DIMENSION TITLE(12),ANDEG(721),ANRAD(721),DCLOD(12),CLOD(12,50),
              1 SLOD(12,50),RLOD(12,721),EQLOD(721),PHASE(721),FUNCRE(721),
              2 FUNCIM(721),CH(12)
    2          REAL MACH
    3          INTEGER G,RBN,HARM
    4          RAD=1.0/57.2957795
    5      111 READ 2,TITLE
    6        2 FORMAT(12A6)
    7          PRINT 2,TITLE
    8          READ 3,NEND,MCH,RBN,CPS,RADIUS,CHORD,BETA
    9        3 FORMAT(3I2,4F8.2)
   10          PRINT 4,NCH,RBN,CPS,RADIUS,CHORD,BETA
   11        4 FORMAT(21H NO OF CHORD STATIONS,F7.0,4X,6HBLADES,F7.0,4X,
              1 9HROTOR CPS,E15.6,/,6HRADIUS,E15.6,4X,5HCHORD,E15.6,4X,4HBETA,
              2 E15.6)
   12          READ 5,NHAR,NFP,DELTA
   13        5 FORMAT(2I2,F8.2)
   14          NP=360. /DELTA+1.00
   15          NT=NP-1
   16          ANDEG(1)=0
   17          ANRAD(1)=0
   18          DO 6 I=2,NP
   19          ANDEG(I)=ANDEG(I-1)+DELTA
   20          ANRAD(I)=ANDEG(I)*RAD
   21        6 CONTINUE
   22          READ 18,(CH(NN),NN=1,NCH)
   23       18 FORMAT(12F6.2)
   24          DO 19 J=1,NCH
   25       19 READ 7,DCLOD(J),(CLOD(J,L),L=1,30),(SLOD(J,L),L=1,30)
   26        7 FORMAT(F8.2/,(10F8.2))
         C      CALCULATION OF EQUIVALENT RECTANGULAR LOADING AT EVERY SOURCEPOINT
   27          DO 12 I=1,NP
   28          DO 71 J=1,NCH
   29          RLOD(J,I)=DCLOD(J)
   30          DO 71 K=1,30
   31          G=K
   32          RLOD(J,I)=RLOD(J,I)+CLOD(J,K)*COSF(G*ANRAD(I))
              1 +SLOD(J,K)*SINF(G*ANRAD(I))
   33       71 CONTINUE
   34          EQLOD(I)=0.0
   35          DO 59 LL=2,NCH
   36       59 EQLOD(I)=EQLOD(I)+(((RLOD(LL-1,I)+RLOD(LL,I))*
              1 (CH(LL)-CH(LL-1)))/(2.*CHORD))
   37       12 CONTINUE
   38          MACH=((CPS*RADIUS)/222.1)
   39          PRINT 13,MACH
   40       13 FORMAT(22H EFFECTIVE MACH NUMBER,E15.6)
   41          BETA=BETA*RAD
         C      BEGIN MAJOR LOOP ON FIELD POINTS
   42          DO 999 II=1,NFP
   43          READ 14,R,THETA,SIGMA
   44       14 FORMAT(3F12.4)
   45          PRINT 15,R,THETA,SIGMA
   46       15 FORMAT(12H FIELD POINT,10X,8HDISTANCE,E15.6,5X,7HAZIMUTH,E15.6,
              1 5X,9HELEVATION,F15.4,//20X,8HHARMONIC,10X,14HSOUND PRESSURE,
              2 11X,11HSPL (DB)RMS)
   47          THETA=THETA*RAD
   48          SIGMA=SIGMA*RAD
   49          DO 999 M=1,NHAR
   50          DO 20 KK=1,NT
   51          HARM=M
   52          PHASE(KK)=HARM*RBN*(MACH*COSF(SIGMA)*COSF(ANRAD(KK))-ANRAD(KK))
   53          FUNCRE(KK)=EQLOD(KK)*COSF(PHASE(KK))*(COSF(SIGMA)*SINF(BETA)*
              1 SINF(ANRAD(KK)-THETA)+COSF(BETA)*SINF(SIGMA))
   54          FUNCIM(KK)=EQLOD(KK)*SINF(PHASE(KK))*(COSF(SIGMA)*SINF(BETA)*
              1 SINF(ANRAD(KK)-THETA)+COSF(BETA)*SINF(SIGMA))
   55       20 CONTINUE
   56          FUNCRE(NP)=FUNCRE(1)
   57          FUNCIM(NP)=FUNCIM(1)
   58          CALL INTGRL(NP,ANRAD,FUNCRE,SPRE)
   59          CALL INTGRL(NP,ANRAD,FUNCIM,SPIM)
   60          SP=((CPS*RADIUS*RBN)/(518.4*R))*SINF(((HARM*RBN*CHORD)/
              1 (1.2*RADIUS)))*SQRTF(SPRE**2+SPIM**2)
   61          SPL=127.6+20.0*.4343*ALOGF(ABSF(SP))
   62          PRINT 40,M,SP,SPL
   63       40 FORMAT(25X,I2,5X,2E20.8)
   64      999 CONTINUE
   65          IF (NEND) 9999,9999,111
   66     9999 GO TO EXIT
   67          END
LINE                                ATLAS  FORTRAN                    11/06/70        VERSION 7
NUMBER                          SOURCE ROUTINE LISTING                 10.53.09    COUNTER=     465
                                                                                  LABEL FIELD
    1          SUBROUTINE INTGRL(N,A,Z,AREA)
    2          DIMENSION A(721),Z(721)
    3          AREA=0.
    4          DO 100 MM=2,N
    5          AREA=AREA+(Z(MM-1)+Z(MM))*(A(MM)-A(MM-1))/2
    6      100 CONTINUE
    7          RETURN
    8          END
```

FIG. 20. COMPUTER PROGRAM D.

APPENDIX VII : CALCULATION OF TIME AVERAGES FOR CIRCULAR MOTION

In the case of a moving point source, the relation between the observation time t and the corresponding emission time $[t]$ is given by equation (5.1) as

$$t = \left[t + \frac{R}{c_o} \right] \quad . \tag{1}$$

For uniform rotation in a circle, $\theta = \Omega t$, $R \doteq r - a\cos\theta\sin\psi$ in the far field (see Fig. 5.5). Therefore equation (1) can be written as a relation between $\theta(t)$ and $\theta([t]) = [\theta]$:

$$(\theta - \frac{\Omega r}{c_o}) = \left[\theta - \alpha\cos\theta\right], \quad \text{where } \alpha = M \sin\psi \ . \tag{2}$$

Denoting $[\theta]$ by ϕ and differentiating the above equation gives

$$d\theta = (1 + \alpha\sin\phi)\, d\phi \quad . \tag{3}$$

This result allows an average over t (or θ) to be evaluated as an average over ϕ .

APPENDIX VIII : CORRELATION - SPECTRAL DENSITY TRANSFORMATION

(a) The cross-spectral density $G_{xy}(\nu)$ is defined as the Fourier transform of the cross-correlation function $R_{xy}(\sigma)$,

$$G_{xy}(\nu) = \frac{1}{\pi} \int_{-\infty}^{\infty} R_{xy}(\sigma)\, e^{-i\nu\sigma}\, d\sigma \quad . \tag{1}$$

Differentiating with respect to ν the appropriate number of times gives

$$i\, G'_{xy}(\nu) = \frac{1}{\pi} \int_{-\infty}^{\infty} \sigma\, R_{xy}(\sigma)\, e^{-i\nu\sigma}\, d\sigma \quad , \tag{2}$$

$$-\, G''_{xy}(\nu) = \frac{1}{\pi} \int_{-\infty}^{\infty} \sigma^2 R_{xy}(\sigma)\, e^{-i\nu\sigma}\, d\sigma \quad , \tag{3}$$

$$-\, i\, G'''_{xy}(\nu) = \frac{1}{\pi} \int_{-\infty}^{\infty} \sigma^3\, R_{xy}(\sigma)\, e^{-i\nu\sigma}\, d\sigma \quad , \tag{4}$$

and

$$G^{iv}_{xy}(\nu) = \frac{1}{\pi} \int_{-\infty}^{\infty} \sigma^4\, R_{xy}(\sigma)\, e^{-i\nu\sigma}\, d\sigma \quad . \tag{5}$$

(b) Spectral densities like $G_{\dot{T}\dot{T}}(\nu)$ can be expressed in terms of $G_T(\nu)$ as follows:

The Fourier transform pair of a function T is defined as

$$\hat{T}(\nu) = \frac{1}{2\pi} \int_{-\infty}^{\infty} T(t)\, e^{-i\nu t}\, dt \tag{6}$$

$$T(t) = \int_{-\infty}^{\infty} \hat{T}(\nu)\, e^{i\nu t}\, d\nu \quad . \tag{7}$$

Differentiating (7) with respect to t,

$$\dot{T}(t) = \int_{-\infty}^{\infty} i\nu\, \hat{T}(\nu)\, e^{i\nu t}\, d\nu \qquad (8)$$

and so

$$i\nu\, \hat{T}(\nu) = \frac{1}{2\pi} \int_{-\infty}^{\infty} \dot{T}(t)\, e^{-i\nu t}\, dt \quad . \qquad (9)$$

By definition $$\hat{\dot{T}}(\nu) = \frac{1}{2\pi} \int_{-\infty}^{\infty} \dot{T}(t)\, e^{-i\nu t}\, dt \qquad (10)$$

and therefore, from (9) and (10),

$$\hat{\dot{T}}(\nu) = i\nu\, \hat{T}(\nu) \quad . \qquad (11)$$

Further differentiation of (8) similarly gives

$$\hat{\ddot{T}}(\nu) = -\nu^2\, \hat{T}(\nu) \quad . \qquad (12)$$

Now $$G_{TT}^{\dot{}\ddot{}}(\nu) = \lim_{t_o \to \infty} 2\pi \left\{ \frac{\hat{\dot{T}}^*(\nu) \cdot \hat{\ddot{T}}(\nu)}{t_o} \right\} , \qquad (13)$$

where * signifies complex conjugate, and using (11), (12) this becomes

$$G_{T\dot{T}}^{\ddot{}\dot{}}(\nu) = i\nu^3\, G_T(\nu) \quad . \qquad (14)$$

Similarly, it can be shown that

$$G_{T\dot{T}}^{\dot{}}(\nu) = i\nu\, G_T(\nu) \quad , \qquad (15)$$

$$G_{T\dot{T}}^{\dot{}\dot{}}(\nu) = \nu^2\, G_T(\nu) \quad , \qquad (16)$$

$$G_{T\dot{T}}^{\ddot{}}(\nu) = -\nu^2 G_T(\nu) \quad ; \qquad (17)$$

and $$G_{T\dot{T}}^{\ddot{}\ddot{}}(\nu) = -\nu^4\, G_T(\nu) \quad . \qquad (18)$$

APPENDIX IX : PURE ROTATION EFFECT ON FORCE RADIATION SPECTRUM (M→ 0)

Since M = 0, the periodic functions f, g, h given by equation (5.21) become

$$f = 1 \ , \quad g = \sin \left[\theta\right] \ , \text{ and } h = \cos \left[\theta\right] \tag{1}$$

and the resulting correlations are obtained as

$$\left.\begin{aligned} &R_f(\tau) = 1, \quad R_g(\tau) = 0 \ , \quad R_h(\tau) = \tfrac{1}{2} \cos \Omega \left[\tau\right] , \\ &R_{fg}(\tau) = 0, \quad R_{fh}(\tau) = 0 \ , \quad R_{gh}(\tau) = - \tfrac{1}{2} \sin \Omega \left[\tau\right] . \end{aligned}\right\} \tag{2}$$

Also, since M = 0 , α becomes zero and $\left[\tau\right] = \tau$. The general equation (5.22) then gives, on time-averaging,

$$(4\pi c_o r)^2 \, R_p(\tau) = R_X^{\bullet}(\tau) + \tfrac{1}{2} \cos\Omega\tau \, R_Y^{\bullet}(\tau) + \Omega \sin\Omega\tau \, R_{YY}^{\bullet}(\tau) + \tfrac{1}{2} \Omega^2 \cos\Omega\tau \, R_Y(\tau) \ . \tag{3}$$

Clearly, rotation has no effect on thrust radiation,as would be expected, and from here on we put $R_X^{\bullet}(\tau) = 0$ to investigate the effect of rotation on the drag radiation spectrum. Noting that

$$\left.\begin{aligned} &R_{YY}^{\bullet}(\tau) = R_Y'(\tau) \\ \text{and} \quad &R_Y^{\bullet}(\tau) = - R_Y''(\tau) \ , \end{aligned}\right\} \tag{4}$$

the radiation spectrum can be obtained from (3) as

$$(4\pi c_o r)^2 \, \bar{G}_p(\omega) = \frac{1}{\pi} \int_{-\infty}^{\infty} e^{i\omega\tau} \left\{ - \tfrac{1}{2} \cos\Omega\tau \, R_Y'''(\tau) + \Omega \sin\Omega\tau \, R_Y'(\tau) + \tfrac{1}{2} \Omega^2 \cos\Omega\tau \, R_Y(\tau) \right\} d\tau \ . \tag{5}$$

This integrates by parts and the resulting far field pressure spectrum,

noting $Y = D \sin\psi$, is

$$(4\pi c_o r)^2 \, \bar{G}_p(\omega) = \tfrac{1}{4} \, \omega^2 \left\{ G_D(\omega + \Omega) + G_D(\omega - \Omega) \right\} \sin^2\psi \quad . \tag{6}$$

If (a) $\Omega \to 0$, or (b) the drag spectrum $G_D(\omega)$ is linear in ω , then (6) shows that

$$(4\pi c_o r)^2 \, \bar{G}_p(\omega) = \tfrac{1}{2} \, \omega^2 \, G_D(\omega) \sin^2\psi \quad . \tag{7}$$

APPENDIX X : RADIATION SPECTRUM FROM BROADBAND FORCES IN UNIFORM STRAIGHT-LINE MOTION

The far field spectral densities of the sound power output from single frequency (ν) transverse and longitudinal forces convected uniformly in a straight line at Mach number M are given by Morse and Ingard [6 , p. 734] as

$$\left(\frac{dW}{d\omega}\right)_T = \frac{\nu^2 f_o^2}{32\pi\rho_o c_o^3} \frac{1}{M^3\omega} \left\{(M-1)\frac{\omega}{\nu} + 1\right\}\left\{(M+1)\frac{\omega}{\nu} - 1\right\} \qquad (1)$$

and

$$\left(\frac{dW}{d\omega}\right)_D = \frac{\nu^2 f_o^2}{16\pi\rho_o c_o^3} \frac{1}{M^3\omega} \left(\frac{\omega}{\nu} - 1\right)^2 \qquad (2)$$

respectively. For continuous source spectra, the above results become

$$\left(\frac{dW}{d\omega}\right)_T = \frac{1}{16\pi\rho_o c_o^3} \int_o^\infty \frac{\nu^2 G_T(\nu)}{M^3\omega} \left\{(M-1)\frac{\omega}{\nu} + 1\right\}\left\{(M+1)\frac{\omega}{\nu} - 1\right\} d\nu \qquad (3)$$

and

$$\left(\frac{dW}{d\omega}\right)_D = \frac{1}{8\pi\rho_o c_o^3} \int_o^\infty \frac{\nu^2 G_D(\nu)}{M^3\omega} \left(\frac{\omega}{\nu} - 1\right)^2 d\nu \quad . \qquad (4)$$

Now a uniformly convected force of frequency ν radiates at acoustic frequencies in the range

$$\frac{\nu}{1+M} \leq \omega \leq \frac{\nu}{1-M} \quad , \qquad (5)$$

and so the radiation at frequency ω is the total contribution from forces in the frequency range

$$\omega(1-M) \leq \nu \leq \omega(1+M) \quad . \qquad (6)$$

Thus equations (3) and (4), for $G_T(\nu)$, $G_D(\nu) \propto \nu^{-2}$, become

$$\frac{12\pi\rho_o c_o^3}{\omega^2 G_T(\omega)} \left(\frac{dW}{d\omega}\right)_T = \frac{3}{4M^3\omega} \int_{\omega(1-M)}^{\omega(1+M)} \left\{ (M^2-1)\frac{\omega^2}{\nu 2} + 2\frac{\omega}{\nu} - 1 \right\} d\nu \qquad (7)$$

and

$$\frac{12\pi\rho_o c_o^3}{\omega^2 G_D(\omega)} \left(\frac{dW}{d\omega}\right)_D = \frac{3}{2M^3\omega} \int_{\omega(1-M)}^{\omega(1+M)} \left(\frac{\omega^2}{\nu^2} - 2\frac{\omega}{\nu} + 1 \right) d\nu \quad ; \qquad (8)$$

upon integration, these give

$$\frac{12\pi\rho_o c_o^3}{\omega^2 G_T(\omega)} \left(\frac{dW}{d\omega}\right)_T = \frac{3}{M^3} \left\{ \tfrac{1}{2} \ln \left(\frac{1+M}{1-M}\right) - M \right\} \qquad (9)$$

and

$$\frac{12\pi\rho_o c_o^3}{\omega^2 G_D(\omega)} \left(\frac{dW}{d\omega}\right)_D = \frac{3}{M^3} \left\{ \frac{M(2-M^2)}{(1-M^2)} - \ln \left(\frac{1+M}{1-M}\right) \right\} \quad . \qquad (10)$$

APPENDIX XI : RADIATION SPECTRUM FROM BROADBAND SOURCES IN UNIFORM STRAIGHT-LINE MOTION

The far field spectral density of the sound power output from a single frequency (ν) monopole, convected uniformly in a straight line at Mach number M, is given by Morse and Ingard [6 , p.732] as

$$\frac{dW}{d\omega} = \frac{Q_o^2}{16\pi\rho_o c_o} \frac{\omega}{M} \quad , \quad M < 1.0 \quad . \tag{1}$$

For a continuous source spectrum, this becomes

$$\frac{dW}{d\omega} = \frac{1}{8\pi\rho_o c_o} \int_o^\infty G_Q(\nu) \frac{\omega}{M} \, d\nu \quad . \tag{2}$$

Now a uniformly convected monopole of frequency ν radiates at acoustic frequencies in the range

$$\frac{\nu}{1 + M} \leq \omega \leq \frac{\nu}{1 - M} \quad , \tag{3}$$

and so the radiation at frequency ω is the total contribution from sources in the frequency range

$$\omega(1 - M) \leq \nu \leq \omega(1 + M) \quad . \tag{4}$$

Thus equation (2), for $G_Q(\nu) \propto \nu^{-2}$, becomes

$$\frac{4\pi\rho_o c_o}{\omega^2 G_Q(\omega)} \frac{dW}{d\omega} = \frac{\omega}{2M} \int_{\omega(1-M)}^{\omega(1+M)} \frac{1}{\nu^2} \, d\nu \quad . \tag{5}$$

Upon integration, this gives

$$\frac{4\pi\rho_o c_o}{\omega^2 G_Q(\omega)} \frac{dW}{d\omega} = \frac{1}{1 - M^2} \quad . \tag{6}$$

APPENDIX XII : CORRELATION FUNCTIONS

The cross-correlation function is defined as

$$R_{xy}(\tau) = \langle x(t)\, y(t+\tau) \rangle \quad . \tag{1}$$

Upon differentiation with respect to τ , this gives

$$R'_{xy}(\tau) = \langle x(t)\, y'(t+\tau) \rangle \quad , \tag{2}$$

which can be written as

$$R'_{xy}(\tau) = \langle x(t-\tau)\, y'(t) \rangle \quad . \tag{3}$$

Differentiating (2) and (3) again gives

$$R''_{xy}(\tau) = \langle x(t)\, y''(t+\tau) \rangle = \langle - x'(t-\tau)\, y'(t) \rangle \quad . \tag{4}$$

From (4), putting $\tau = 0$, we obtain

$$R''_{xy}(0) = - R''_{xy}(0) \quad . \tag{5}$$